Core-collapse supernova physics in the multi-messenger era

Thesis by
Sarah E. Gossan

In Partial Fulfillment of the Requirements for the
Degree of
Doctor of Philosophy

Caltech

CALIFORNIA INSTITUTE OF TECHNOLOGY
Pasadena, California

2019
Defended 22 February 2019

Acknowledgements

Where better to begin with acknowledging those who have shaped my life than with my parents. To Mum and Dad, this thesis is a testament to your boundless support throughout my life. It's because of you that I never hesitated I could do anything I set my mind to. You always encouraged any interest or curiosity, and allowed me to make my own mistakes along the way. Thank you for your unconditional love and support. Thanks are also due to my sister, Rachel Gossan, for (among many other things) first introducing me to Criminal Minds back in 2006 (more below), and for consistently introducing me and Mum to bingeworthy TV shows (my stalwart!) during the 00s. Thanks to my brother, Tom Gossan, for (again, among many other things!) indulging in various shared obsessions with me (Pokémon, Super Mario, and physics, to name a few) over the years as we grew up together.

To my St. Tom's crew! Mr Callaghan, Mr Leleivre; thanks for letting me hide out in your classrooms at lunch. Our chats got me through a difficult time. Mr Otlet, your art classes were my favourite part of the week! You always had my back, and never failed to bring me right back to earth when I was being mouthy. I chose astrophysics first, but fashion and interior design are NEXT! Mr Edwards, thank you for letting me hide in the back of the class with my AS-level maths books – distracting myself working through problem after problem has remained my calm place ever since. To Mrs Kerslake; writing was my therapy, and your English classes gave me the opportunity to express myself and let out the pain. While this is a PhD thesis in theoretical astrophysics (!) rather than murder mystery or gothic poetry stained with angst, I took your advice and never stopped writing; thank you for your mentorship and guidance. To Mr Deplechin, thank you for teaching me about the French language and Camus. Thank you to Ismini Ginis, Sadia, Lakhjeet Kaur, Nadine Badresingh, Diley Banh, Lisa Hong, Natasha Hobbs, Francesca D'Abramo, India Farrell, Matthew, Clare Moscowicz, Sarah Evans, Nathan Barrett, Liam Fitzgerald, and Knuthai Edwards, for the fun times and friendship; you were rays of hope in a very dark place, and I miss you lots.

Thank you to the St Brendan's sixth form college folks; to Rachael Crowe, my tattoo sister, to Anna Wardell, Lauren Falloon, Lucas Fedyniak-Hopes, Kerry Parker, Austin Ball, thank you for introducing me to the world and, to name but a few, Keri Hudson, James Nelson, and Oliver Denton-Turner. Thank you Jammy, one of my oldest and dearest friends, for always believing in me. Oliver, you are magical and a true kindred spirit; thank you for keeping me grounded, I hope our worldlines intersect soon. Thank you Richard, my A-level maths++ teacher; for encouraging me at every turn, for indulging my competitive side, and for challenging me to follow my dreams.

My time as an undergrad at Cardiff University was formative for my academic development, and I had the fortune to interact with many wonderful people who helped shape the person I am today. To Carole Tucker, my personal tutor; thank you for your mentorship and support over the years, and for indulging my competitive streak. Thank you for pushing me to go beyond my comfort zone and explore new things. You encouraged me to apply for the LIGO summer research position, something I'd never considered before. For the first time, I learned how to *learn*, and the experience opened doors that I previously didn't even know existed. Thank you for changing my life, and being an endless inspiration. To Bangalore Sathyaprakash, my academic advisor. Thank you, Sathya, for introducing me to black hole ringdowns and the prospect of getting a PhD in astrophysics - something I'd never seriously considered before meeting you. You are an endless inspiration and I would not be where I am today without your continued support, guidance, mentorship, teaching, and collaboration. Thank you for bearing with me over the years, and for always believing in me.

To Patrick Sutton, who helped me learn Matlab and grapple with X-Pipeline during my first summer research position at Cardiff before later teaching me general relativity (and writing an exam that was legimate joy to take); thank you, thank you, thank you - for all the things. Over the past nine years (!), you have taught me so much. From high-performance computing to searching for gravitational waves from long gamma-ray bursts and core-collapse supernovae to name just a couple, thank you for being such a genuine person who supports your students, and for continuing to have my back over the years. To John Veitch and Chris Messenger, thank you for being my baseline for advising students. John, thank you for teaching me how to write a paper and navigate applying for PhD positions. LALNest was truly a baptism of fire (particularly given that I'd never coded in C before), but working with you was the first time I really developed a passion for coding, and I use computing skills you taught me back in 2011 to this day. Thanks for not laughing at me as I stumbled (random walked?) through many baby researcher follies. Chris, thank you for teaching me about matter! Neutron stars have always been my jam[1], so studying gravitational waves from the hypermassive magnetars formed when two neutron stars merge was an absolute dream. Thank you for always being a kind and helpful advisor, and for (repeatedly) having my back. I hope we can work together again soon!

I also want to thank several other outstanding teachers I had during my time at Cardiff; Haley Gomez, Phil Mauskopf, Steve Fairhurst, Ed Gomez, Chris van der Broeck, Bernard Richardson, Mark Hannam, and Mike Edmunds. To the rest of the Cardiff gravy waves group, thank you for welcoming me so warmly into your world. To Valeriu Predoi, thank you for your enduring friendship. Sharing an office with you was unmatchable, and our weekend pub adventures got me through countless tough times. Collaboration meetings were highlighted (or, indeed, made bearable) by meeting up with you for a brewski or three. To more of my office mates (at one time or another) in Cardiff; Gareth Jones, Craig Robinson, James Clark, Thomas Dent, Jereon Meidam, Mark Edwards, and Ian McKechan. Thank you for the camaraderie; I have learned so much about research, academia, and life from you. To Laura Nuttall, Duncan Macleod, Patricia Schmidt, Geraint Pratten, and Ian Harry; I met you as grad students and today you're at the top of your fields and running the LIGO world! Thank you for being so friendly and inviting to the overachieving undergrad in your midst. Your excellence and scientific badassery continue to be incredibly motivating and inspiring.

To the Cardiff Astrophysics class of 2012, thank you for the four unforgettable years of camaraderie and kinship. From Mondays at Fun Factory and

---

[1] Citing here the magnetar poster I made when I was seventeen for my A-level Physics course (Gossan 2007), and the Chandrasekhar mass tattoo on my left wrist (Gossan 2010) I got a couple of days before my twentieth birthday.

Wednesday at Metros, thank you for making 9am lectures on Tuesdays and Thursdays less painful. Chaos forever! To Gregg Evans, Danielle Gardiner, and Aaron Bryant; thank you for the fun roomie times and dear friendship - I cherish the time we lived together. To David Sullivan, Tom Wilson, Llywelyn Gale, Harriet Parfitt, Rebecca Pinhorne; our exam study sessions were the highlights of my year. Chaos forever! To the postgrad TAs: Tom Hughes, Adam Rykala, Sara Carver, Sarah Harry, thank you for making lab afternoons a fun experience and for being such warm, friendly, patient (!), and kind-hearted people. To Julie Gould, Vicky Evans, Jackie Webb, Alrun Guenther, Lianne Coulbeck, and Helen Johnson; your academic excellence was a constant source of motivation. Thank you for (inadvertently!) pushing me to work harder and learn more.

Moving to Pasadena for grad school was like nothing I could have imagined. Though my time at Caltech has been, ahem, turbulent[2], I will cherish it forever. This place has been my Hogwarts (complete with its own chamber of secrets), and I understand the universe (and the physics governing it) indescribably much better having completed this PhD. I have also learned a lot about people, not to mention having taken a veritable crash course on many-body interactions in a high pressure environment[3]. To Felicia Hunt; thank you for having faith in me when I had lost faith in myself. Caltech is a safer place for your work there. To Kristina Larson, thank you for your help and advice (both legal and otherwise!) over the past three years. You are an incredible person who does such important work. Thank you for amplifying my voice.

Thank you to Samaya Nissanke, Chiara Mingarelli, Patricia Schmidt, and Jess McIver, for reminding me of what it looks like to have self-respect and for supporting my fight to get it back. Samaya, your strength, grace, and boundless enthusiasm for high energy astrophysics are a constant inspiration. Thank you for repeatedly hosting me at GRAPPA both before and after my defense; you helped me back from the depths of despair, and are also a big part of the reason I have been able to write this thesis. I'm forever grateful for both your existence and to be your friend. You are a superstar!

To Alan Weinstein, my advisor; thank you for welcoming me into the fold,

---

[2] Sorry, not sorry.

[3] Both literally and metaphorically.

supporting my decisions, and giving me the freedom to research what interested me. You offered me a route out of TAPIR that kept me at Caltech, and have always wanted the best for me; I will forever be thankful for that. To Jim Fuller, my thesis committee chair; thank you for your endless patience over the past three and a half years, and for introducing me to the many applications of wave physics. Your ongoing support is a significant part of why I'm able to sit here (officially doctored!) and have a completed thesis for which to be writing an acknowledgements section. To Rana Adhikari, Yanbei Chen, and Phil Hopkins, who comprised the rest of my thesis committee; thank you for your guidance and patience with me on my journey from candidacy (way back in November 2015) to defense and thesis submission. Rana, so many of my favourite Caltech moments have either involved or been organised by you; thank you for seeing my sparkle from the start, and for always having faith in me.

To my fellow Physics grad students incoming fall 2012, special mentions to the Friday pub crew; Tony Bartolotta, Dustin Anderson, Daniel Brooks, Jason Pollack, Jon Blackman, Kevin Barkett, Evan Hall, and Nick Hunter-Jones. Kevin, thank you for being you. Having you as an office mate and fellow TAPIR was a blessing I'll never forget, and I'll always fondly remember the awesome summer with Natalie and Thibault - go team dinos! Evan, you are a true kindred soul, and there is no-one I'd rather have grown up with (academically and otherwise) as LIGO grad siblings. Thank you for the sugar-free adventures and Starbucks, for Silverlake, for winter 2017, and last (but definitely not least) for being you. I'm excited for what's next to come. To Yoni BenTov, thank you for the sparkle bae times at Copa. Looking forward squirrel adventures with smoked salmon and berries in the frozen place soon. To JoAnn Boyd, you are the soul and backbone of TAPIR. Between our hallway chats, impromptu fashion shows, and whine and wine, you anchored me in a brutal storm. Thank you for pushing me to stand up for myself and move on with my life. To Dan Hemberger, Ernazar Abdikamalov, Philipp Mösta, Chris Mach, Matt Giesler, David Tsang, Vicky Scowcroft, Tony Piro, Jeandrew Brink, Leo Stein, Aaron Zimmerman, Fan Zhang, John Wendell, and Abhilash Mishra; thank you for making a hopeless place less hopeless. To Casey Handmer, thank you for using your voice.

To my LIGO Caltech family; who better to start with than Julie Hiroto, whose support and positive influence has helped push me through to the finish line[4]. Julie, your cross-stitch will forever have a place on my fridge for morning (and any time) motivation. To Alex Urban, thank you for being you. Over the eight years since I first met you, you've always unconditionally offered your support and friendship. Thank you for holding me down in Pasadena, for Baton Rouge, for loving little sweets like your own, for everything. May we chronicle meow meow kitty adventures (starring Indica, in the role of a lifetime) forever and always. To Brittany Kamai, thank you for being a breath of fresh air in an often suffocatingly toxic work environment. Our check-ins on signal kept me on pace while writing up, and brought light to often otherwise dull days. I deeply appreciate you and your sparkle, and am constantly inspired by you. You are a wonderful and powerful human fighting for long-overdue change, and the field (not to mention my life) is so much better for you in it. To my fellow LIGO grad siblings in 364 W. Bridge, Craig Cahillane, Max Isi, Surabhi Sachdev, and Aaron Markowitz; thank you for the fun adventures and office mate kinship. To my postdoc office mates Rory Smith and Michael Coughlin, thank you for your friendship. I've known you since the start of my (our?) LIGO days, and it has been a joy to watch you grow up academically and move to faculty (!!!) positions. You are two of the kindest hearted and talented researchers I know, and I can't wait to see the amazing things you'll continue to do. To Eric Gustafson and Syd Meshkov, talking with you about core-collapse supernovae after some of my LIGO seminars is a really happy and positive experience from Caltech that I'll always cherish. Thank you for the advice, chats, and friendship. To Mary Massinger, Jamie Rollins, TJ Massinger, Eric Quintero, Zach Korth, Andrew Wade, and Aidan Brooks; thank you for the (reliably very interesting) chats at Wednesday beer hour and Friday coffee, which were always high points of my week. To Cody Messick, thank you for the truly magical three months in early 2016 when you visited Pasadena - you are awesome.

To Fiona Harrison, your leadership and compassion have changed PMA, and with Sofie Leon, Mika Walton, and the PMA grad program office, the Caltech experience for the typical Physics grad student has been transformed for the better. Thank you for your all for your support, and for helping me get to where I needed to be. To Cora Went, Ivanna Escala, Gina Duggan, Alicia Lanz, Jacob Jencson, Sean Carroll, Mansi Kasliwal, Lynne Hillenbrand,

---

[4] Much like a stalled shock being revived to drive a successful explosion.

Gregg Hallinan, Melany Hunt, and Maria Spiropulu; thank you for pushing for much needed change. To France Cordova, thank you for (among many things) setting up the Garmire Scholar prize. Being awarded this by you in 2017 was the highlight of my career, and the prize fund allowed me to purchase the laptop I wrote this thesis with.

To Jasmine Gill, Laksh Bhasin, Alex DeMaio, Tony Rojko, and Yun-Ting Cheng, all of whom I had the pleasure of meeting and briefly mentoring through student programs at Caltech; thank you for reminding me of why I got into science. Your brilliance and passion for learning never ceased to be infectious, and I'm so proud of everything you've accomplished and continue to accomplish.

Thank you to Deirdre Shoemaker and Pablo Laguna for hosting me at Georgia Tech in October 2015, giving me some (space)time ring down after the Title IX investigation came to a local minimum and the poop really started to hit the fan. To Norna Robertson, Fred Raab, Jocelyn Read, Bruno Giacomazzo, Tyson Littenberg, Chris Pankow, Josh Smith, Geoffrey Lovelace, Anna Watts, Sera Markoff, Jean-Michel Désert, Chanda Prescod-Weinstein, Alessondra Springmann, Sarah Tuttle, Jorge Moreno, Laura Lopez, Jessica Kirkpatrick, Karan Jani, Satya Mohapatra, Lionel London, Shane Larson, and others, thank you for reaching out and offering truly buoyant support during early 2016 and beyond. Thank you to the Ladies Science Collective for the wonderful care package you sent me that year, which moved me to tears and I have kept to this day. To Nicole Yamzon, thank you for existing. Thank you to the wonderful people I've met at COFI, UvA, KCL, and FOE2019 over the past few months; Katie Breivik (see you soon, CITA friend!), Jillian Bellovary, Laura Blecha, Tanja Hinderer, David Nichols, Athira Menon, Amruta Jaodand, Geert Raaijmakers, Tom Edwards, Ralph Wijers, Malcolm Fairbairn, Eugene Lim, and Helvi Witek for welcoming me so warmly into your world, and propelling me to the finish line.

To Elle Woods and Reese Witherspoon, thank you for inspiring me for the past sixteen years. Watching Legally Blonde a transformative experience for me, and was one of the first times I'd seen a glamorous, unapologetically femme woman succeeding academically and proving everyone wrong. You reminded me that I really loved science, and soon after, I started to look into how to work towards a degree in astrophysics. Further shoutouts are warranted to Penelope Garcia (Kirsten Vangsness) and Spencer Reid (Matthew Gray Gubler), for playing such compelling, wholly relatable characters that I have so closely identified with while growing up, moving through uni and grad school, and now onto the next f rontier - with the final season approaching, it's really the end of an era. Thank you for first introducing me to Caltech, and for the unmatchable escapism. Thank you To Cody Johnston, Katy Stoll, and their podcast Even More News, to Nicole Byer and her delightful podcast Why Wont You Date Me?, and to Tim Blais' A Capella Science, all of which have helped me keep hold of (admittedly by this point only some semblance of) my sanity in Louisiana these past eight months. Thanks of course are also due here to Alex (Urban), who continues to recommend outstanding podcasts, shows, and other assorted media.

All plots in this thesis were produced using Python, NumPy [1], SciPy [2], and Matplotlib [3]. Special thanks to Color Oracle and Color Brewer for allowing me to indulge my love for making beautiful and accessible plots here. I am a member of the LIGO Laboratory. LIGO was constructed by the California Institute of Technology and Massachusetts Institute of Technology with funding from the National Science Foundation and operates under cooperative agreement PHY-0757058. I carried out the work presented here as a member of the LIGO Scientific Collaboration (LSC).

With this section rapidly becoming a veritable tome (although likely one still too short!), I'll start to wrap up by referencing a quote;

> *I used to want the words 'She tried' on my tombstone. Now I want 'She did it.'*
>
> —Katherine Dunham

which has driven me forward and brought me solace on countless occasions since I first finding it through Chanda Prescod-Weinstein in 2017. I've leave you with this:

I hope you will disdain mediocrity and aim to excel in whatever you do. I hope you will love your work as I love doing astronomy. I hope that you will fight injustice and discrimination in all its guises. I hope you will value diversity among your friends, among your colleagues, and, unlike some of your regents, among the student body population. I hope that when you are in charge, you will do better than my generation has. In 1993, U.S. universities awarded Ph.D. degrees in physics and Astronomy to a total of nine black Americans. You do better.

—Vera Rubin, *1996 UC Berkeley Commencement Address*

Throughout this thesis, I recommend a number of excellent review articles for the interested reader to learn more. To that end, let me begin by heartily encourage all to read the Decolonising Science Reading List [4] and references therein. Please take note, and work to make a meaningful, ongoing commitment to equity and inclusion in physics and astronomy.

I’m not sad, but the boys who are looking for sad girls always find me.
I’m not a girl anymore and I’m not sad anymore.
You want me to be a tragic backdrop
so that you can appear to be illuminated
so that people can say
‘Wow, isn’t he so terribly brave to love a girl who is so obviously sad?’
You think I’ll be the dark sky so you can be the star?
I’ll swallow you whole.

—Warsan Shire

For Mum, Carole, Felicia, and Samaya.
And me.

Abstract

Eighty-five years following the historic proposal that core-collapse supernovae accompanied the transition of evolved massive stars to neutron stars [5], the mechanism through which these collapsing stars explode remains uncertain. While supernovae are observed on a daily basis across the electromagnetic spectrum, neutrinos and gravitational waves, emitted from the very heart of the core-collapse supernova central engine, provide a direct glimpse of the dynamics driving the explosion. The joint gravitational wave and electromagnetic observations of a colliding neutron star binary system on 17th August 2017 heralded a new era for multi-messenger astronomy [6]. The next galactic core-collapse supernova presents an unparalleled opportunity to directly probe core-collapse supernova physics and the explosion mechanism.

This thesis explores a number of topics in multi-messenger astronomy and core-collapse supernova physics. First, it tackles the observation problem; detailing an astrophysically motivated search protocol for gravitational waves from core-collapse supernovae triggered by observations of neutrino and/or electromagnetic counterparts. Applying these methods to a number of hypothetical observational scenarios, it presents sensitivity estimates for the second generation of gravitational wave interferometric detectors to both realistic and speculative emission mechanisms associated with core-collapse supernovae. Next, it addresses the prospects for post-detection inference; developing a Bayesian toolkit to interpret gravitational wave observations from core-collapse supernovae and augment current understanding of the explosion mechanism. A proof-of-principle study is also presented, using tailor-made simulations to demonstrate the viability of extracting the angular momentum distribution of nascent millisecond proto-neutron stars from their gravitational wave echoes. Thereafter, it considers the ramifications of failure to accurately capture proto-neutron star hydrodynamics in core-collapse supernova simulations; exploring the influence on the explosion mechanism of gravito-acoustic waves generated by convection in the proto-neutron star mantle. Finally, it ponders the impact of advances in multi-messenger astronomy and source modelling over the next twenty years on the understanding of core-collapse supernova physics.

Published Content and Contributions

[1] R. X. Adhikari, P. Ajith, et al. Astrophysical science metrics for next-generation gravitational-wave detectors. ArXiv e-prints, 1905.02842 (2019). Submitted to Class. Quantum Grav., available at `https://arxiv.org/abs/1905.02842`.
SEG performed all calculations related to stellar collapse, and wrote all manuscript text in the supernova sections.

[2] S. E. Gossan, J. Fuller, and L. F. Roberts. On the role of waves in the core-collapse supernova explosion mechanism (2019). In preparation; to be submitted to Mon. Not. Roy. Astron. Soc..
SEG used simulation outputs produced by LFR to carry out all post-processing calculations, as led by JF who also guided matters of interest. SEG produced all figures, and wrote the manuscript text alongside JF.

[3] B. P. Abbott, R. Abbott, T. D. Abbott, et al. First targeted search for gravitational-wave bursts from core-collapse supernovae in data of first-generation laser interferometer detectors. Phys. Rev. D 94 (10), 102001 (2016).
SEG led the waveform model choice and astrophysically-motivated source orientation distribution. Much manuscript text, tables, and formatting is taken directly from Gossan et al. (2006).

[4] S. E. Gossan, P. Sutton, A. Stuver, et al. Observing gravitational waves from core-collapse supernovae in the advanced detector era. Phys. Rev. D 93 (4), 042002 (2016).
SEG designed the observational study and ran the analysis, with crucial X-Pipeline expertise and support from PS. SEG produced all figures and wrote the majority of the manuscript text.

[5] J. Powell, S. E. Gossan, et al. Inferring the core-collapse supernova explosion mechanism with gravitational waves. Phys. Rev. D 94 (12), 123012 (2016).

SEG led the project for three years and originally wrote the SMEE2G pipeline in Python, but had to step back towards the end due to health concerns. SEG made the figures, directed the observing cases considered, and wrote around half of the manuscript.

[6] E. Abdikamalov, S. Gossan, et al. Measuring the angular momentum distribution in core-collapse supernova progenitors with gravitational waves. Phys. Rev. D 90 (4), 044001 (2014).
SEG led the signal analysis and detectability studies using waveforms produced by simulations ran by EA and AM, and wrote around one third of the manuscript.

TABLE OF CONTENTS

LIST OF ILLUSTRATIONS

LIST OF TABLES

1 Introduction to core-collapse supernovae

The nitrogen in our DNA, the calcium in our teeth, the iron in our blood, the carbon in our apple pies were made in the interiors of collapsing stars. We are made of star stuff.
—Carl Sagan, *Cosmos*

Core-collapse supernovae (CCSNe) have been observed throughout history, with the earliest recorded sightings of these magnificent stellar explosions preceding the invention of the modern telescope by over a millenium. Accompanying the gravitational collapse of massive stars (greater than $8 - 10\,M_\odot$ at birth) at the end of their nuclear burning lifetimes, CCSNe release some 10^{53} erg of energy across the electromagnetic (EM) spectrum, neutrinos, and gravitational waves (GWs). From nuclear interactions and neutrino physics in the collapsing core to shock interaction with the stellar surface and circumstellar medium, CCSNe are fantasically complex multi-scale astrophysical laboratories, with length scales associated with relevant physical processes spanning almost 20 orders of magnitude and encompassing all four fundamental forces. Computationally modelling CCSNe is thus, to no surprise, an involved task of Gordian proportions. In the absence of unlimited computational resources, even state-of-the-art simulations are beholden to approximate treatment of source physics. A problem arises, however, as many simulations fail to reproduce the stellar explosions observed, and thus known to occur, in nature. Could it be that our theoretical understanding of the mechanism through which collapsing massive stars explode be wrong?

As yet, a robust answer to this question remains out of reach. The basic picture for core collapse, generally agreed upon by the CCSN community, is as follows. As a massive star evolves, a heavy, degenerate core is gradually formed from the products of nuclear burning in the stellar interior. The core mass increases, with the central temperature soaring as the maximum (Chandrasekhar) mass supportable by electron degeneracy pressure grows near. Heavy nuclei in the centre of the core begin to break apart under the intense temperature and pressure there, driving electron capture on free protons and accelerating gravitational collapse. The core, initially in free-fall, separates; the inner core (usually around $M_{\rm ic} \sim 0.6 - 0.8\,M_{\odot}$), which remains in sonic contact, collapses homologously[1], while the outer core (typically around $M_{\rm oc} \sim 0.6\,M_{\odot}$) continues to infall subsonically. As the density of the inner core approaches that of nuclear matter, the nucleon-nucleon potential becomes repulsive, providing support against further gravitational collapse. The inner core rebounds, driving a shock wave outwards. As the shock travels through the outer core, it loses energy both through superheating the infalling material (breaking up heavy nuclei into free nucleons) and through increased neutrino losses as high temperatures drive increased rates of electron capture. For all but the lightest stars ($8 - 9\,M_{\odot}$ progenitors, for which the degenerate core is comprised of oxygen, magnesium, and neon), the shock stalls within $50 - 100\,$ms of core bounce (typically around $r_{\rm sh} \sim 150 - 250\,$km), forming an accretion boundary supported against collapse by thermal pressure and neutrino heating. The shock must then be "revived" to explode the progenitor star before accretion of infalling material onto the PNS drives the nascent remnant's mass above the maximum supportable against gravitational collapse, leading to black hole (BH) formation on a timescale of $\sim 1 - 3\,$s. While it's expected that some BHs formed via stellar collapse, many CCSNe (for which the inferred progenitor mass is larger than $12\,M_{\odot}$) have been observed, suggesting that there is some mechanism through which the shock is revived (in a timely manner) to successfully explodes the star.

So what do we know about the CCSN explosion mechanism? It's likely some complex interplay between neutrino heating, turbulent hydrodynamics, and fluid instabilities. Beneath the shock, a *gain region* (of order several tens of kilometres thick) develops, where net neutrino heating occurs. In contrast, a region of net cooling emerges above the the proto-neutron star

---

[1] i.e. velocity is proportional to the radius, and the collapse dynamics are effectively scale-free.

(PNS) “surface”[2] as the PNS cools (via neutrinos) and contracts. Between the neutrino-cooled region above the PNS (which is, relatively speaking, fairly low entropy and lepton-poor) and the (shock-heated, lepton-rich) gain region, neutrino-driven convection develops by $\sim 150-200\,\mathrm{ms}$ post-bounce and rapidly becomes turbulent, contributing an additional source of pressure behind the shock and pushing it outwards. Large neutrino heating rates across the gain region persist only for a few hundreds of milliseconds, so this typically can’t revive the shock alone if an explosion isn’t seen within 500 ms or so. Turbulent pressure behind the shock (due to vigorous convective motion across the gain region) can also contribute to shock revival, although this is subject to the caveat that much of the convective power here too dies down after around 500 ms. The standing accretion-shock instability (SASI; see, e.g., [7]), where global fluid sloshing in the cavity between the PNS and the stalled shock is driven by acoustic waves coupling to “advected waves” of entropy and vorticity perturbations produced at the shock (due to physical displacement) dragged down with the infalling accretion flow towards the PNS. Advective waves rapidly decelerate as they approach the PNS surface, generating outgoing acoustic waves that propagate to the shock, where they partially reflect and impart momentum upon the shock, driving it outwards and producing new pertubations which then in turn get advected down towards the PNS with the accretion flow. This “advective-acoustic” cycle can be a powerful feedback mechanism when the shock stalls at large radii, creating a larger cavity over which global fluid modes can develop without being (completely) disrupted by turbulent motion. Furthermore, wave-driven energy transport from the convective PNS mantle out to the shock can contribute an important source of pressure behind the shock, and may favour development of the SASI by providing an additional source of outgoing acoustic flux from the PNS surface. PNS convection persists over several seconds as the PNS contracts and cools, so wave-driven energy transport from here can contribute heating and pressure behind the shock out to late times (long after neutrino heating and turbulent convection have calmed; see Chap. 7 for quantitative study on the impact of wave heating from PNS convection).

---

[2] Often taken very loosely to be where $\rho \sim 10^{11}\,\mathrm{g\,cm^{-3}}$. The *neutrinosphere*, which is often discussed analogously with the PNS surface, is defined as where the optical depth to neutrinos $\tau_\nu = 1/3$ (i.e. where neutrinos decouple from nuclear matter and can escape).

Pragmatically, CCSN explosions are likely to be driven by some combination of these effects or, indeed, by something entirely different. While successful explosions are starting to be seen by state-of-the-art simulations, a consensus across the CCSN simulation community is a distant prospect likely decades away. Observationally, we are yet to constrain much as, despite routine observation of CCSNe across the EM spectrum, we have yet to directly probe the CCSN central engine. EM emission originates far from the collapsed core, produced through nuclear decay and interaction of the SN shock with the circumstellar medium after it has broken through the surface of the progenitor star. As such, only second-hand information on what drives these stellar explosions is yielded by EM observations, limited for the most part to details on explosion asymmetry and outflow velocities. On the contrary, GWs and neutrinos are emitted from the very heart of the CCSN, offering an unparalleled opportunity to witness the birth of compact objects and the mechanism through which CCSN explosions are powered. The scant few neutrinos observed from SN1987A, a CCSN in the Large Magellanic Cloud (LMC) over thirty years ago, confirmed the basic theoretical picture of the so-called CCSN explosion mechanism established previously [8, 9]. A more recent opportunity, however, to perform precision astronomy on CCSNe with neutrinos and GWs has yet to manifest.

The joint observation of GWs and light from a binary neutron star merger [6, 10] heralded the dawn of a new multi-messenger era including GWs. With the second-generation of GW detectors in place and the next galactic CCSN already exploded, the importance of the first joint observation of GWs, neutrinos, and light from a CCSN cannot be overstated. An unprecented opportunity to peer directly into the CCSN central engine, GW and neutrino observations will allow us to probe both the explosion mechanism and natal properties of compact objects. To truly harness the scientific potential of the next galactic CCSN, we must have a thorough understanding of how to optimally conduct a multi-messenger search for CCSNe, investigate the observational prospects given existing detectors, and establish the astrophysical information that can be inferred from post-detection analysis of observations.

With these considerations in mind, the primary goal of this thesis is to provide a clear and coherent discussion of the prospects for exploring CCSN physics through multi-messenger astronomy over the next thirty years. Explicitly, we aim to lay out a roadmap through detection, source inference, and development of a science case for next-generation observatories in the context of GWs from CCSNe for the budding astronomer interested, but perhaps not yet well-versed, in these brilliant cosmic explosions. To this end, we present a comprehensive search procedure which will later be released as open-source package of signal analysis tools that may be employed to not only reproduce the research presented here, but may also be further developed to augment one's own research by the interested reader.

The rest of this thesis is organised as follows. In Chapter 2, we seek to provide a broad overview of general relativity (GR) and GWs, neutrino radiation hydrodynamics, and the nuclear matter equation of state (EOS); three (of many!) key topics unlying the dynamics of stellar collapse and compact object formation. In Chapter 3, we discuss the observational signatures of CCSNe, before contextually discussing detection techniques for GWs and neutrinos. Chapter 4 outlines an astrophysically-motivated protocol for externally-triggered searches for GWs from CCSNe, employing these methods to explore the prospects for observing GWs from CCSNe with the second-generation of ground-based interferometers. In Chapter 5 and Chapter 6, we address the post-detection problem: inference of source physics. We demonstrate, in Chapter 5, the ability to establish, for a given GW observation, whether the CCSN explosion was driven predominantly by either multidimensional hydrodynamic instabilities or rotational effects. Following this, we run a suite of tailor-made CCSN simulations for rapidly rotating progenitors in Chapter 6 and develop a proof-of-principle concept study on the ability to constrain the angular momentum distribution of the pre-collapse core from GW observations alone. Acknowledging the uncertainty in the particulars of the CCSN explosion mechanism, we turn our attention in Chapter 7 to the impact of approximations used in CCSN simulations on the fundamental physical processes driving the explosion, establishing the viability of wave-driven energy transport from PNS convection as a subdominant feature driving the CCSN central engine. Looking forward in Chapter 8, we explore the prospects for multi-messenger astronomy with CCSNe over the next thirty years, focusing predominantly on the impact of third-generation GW detector design on sensitivity to GWs from CCSNe. Finally in Chapter 9, we reflect on the impact of the work presented in this thesis on the field, and discuss future directions crucial to maximising the scientific potential yielded from observing the next galactic CCSN through the multi-messenger lens.

2 Fundamental physics of core-collapse supernovae

These violent delights have violent ends.

—Dolores Abernathy, *Westworld*

As prefaced in Chap. 1, CCSNe are fantastically complicated phenomena; astrophysical laboratories for a broad range of fundamental physics in extreme conditions. While here we seek to provide a more detailed discussion of only three topics particularly pertinent to the topics addressed in this thesis, we highly recommend Thorne & Blandford [11], Shapiro & Teukolsky [12], Creighton & Anderson [13], Chapters 1-3 of Sherwood Richers' thesis [14], pretty much all of Evan Hall's thesis [15], and the Ay190 Computational Astrophysics notes to the interested reader.

2.1 General relativity and gravitational waves

Background math

In general relativity, massive particles traverse paths in spacetime (a Riemannian manifold characterised by metric $g_{\mu\nu}$) along which their proper time τ is extremised. Mathematically, this can be stated through an equation of motion, the geodesic equation, which can be solved for the set of allowed particle trajectories (known as geodesics) $x^{\mu}\left(\mathcal{P}(\tau)\right)$.

In the absence of external forces, the geodesic equation takes the following form;

$$\frac{d^2 x^{\sigma}}{d\tau^2} - \Gamma^{\sigma}_{\mu\nu} \frac{d\,x^{\mu}}{d\,\tau} \frac{d\,x^{\nu}}{d\,\tau} = 0\,, \tag{2.1}$$

where connection coefficients $\Gamma^{\sigma}_{\mu\nu}$ are defined

$$\Gamma^{\sigma}_{\mu\nu} = \frac{1}{2} g^{\sigma\lambda} \left(\partial_{\nu} g_{\lambda\mu} + \partial_{\mu} g_{\lambda\nu} - \partial_{\lambda} g_{\mu\nu} \right) , \tag{2.2}$$

where the notation $\partial_{\mu} = \partial / \partial x_{\mu}$ is employed. External forces such as electromagetism contribute to an additional source term on the right hand side of the geodesic equation.

The curvature of a spacetime manifold is encoded in the Riemann tensor $R^{\sigma}_{\mu\rho\nu}$, defined as

$$R^{\sigma}_{\mu\rho\nu} = \partial_{\rho} \Gamma^{\sigma}_{\nu\mu} - \partial_{\nu} \Gamma^{\sigma}_{\rho\mu} + \Gamma^{\sigma}_{\rho\lambda} \Gamma^{\lambda}_{\nu\mu} - \Gamma^{\sigma}_{\nu\lambda} \Gamma^{\lambda}_{\rho\mu} , \tag{2.3}$$

Repeated contraction of the Riemann tensor yields the Ricci tensor $R_{\mu\nu}$ and scalar curvature R;

$$R_{\mu\nu} = R^{\lambda}_{\mu\lambda\nu} , \tag{2.4}$$

$$R = R^{\nu}_{\nu} . \tag{2.5}$$

In general relativity (GR), gravity manifests through spacetime curvature, which induces relative acceleration between initially parallel points in space. This acceleration can be quantified by considering two test particles, initially separated by space-like vector s^{μ}, traversing geodesics with identical four-velocity $u^{\nu} = dx^{\nu} / d\tau$. The relative acceleration between the two particles is given by the equation of geodesic deviation;

$$\frac{d^2 s^{\sigma}}{d\tau^2} = R^{\sigma}_{\mu\lambda\nu} u^{\mu} u^{\lambda} s^{\nu} , \tag{2.6}$$

which underscores the effect of spacetime curvature on particle trajectories.

Curvature is manifestly due to the distribution of matter and energy across spacetime. Given a distribution characterised by stress-energy tensor $T_{\mu\nu}$, the resultant metric can be found by solving the Einstein field equations:

$$G_{\mu\nu} + \Lambda g_{\mu\nu} = \frac{8\pi G}{c^4} T_{\mu\nu} , \tag{2.7}$$

where $G_{\mu\nu} = R_{\mu\nu} - g_{\mu\nu} R / 2$ is the Einstein tensor, and Λ is a cosmological constant related to the vacuum energy of empty space.

Linearised gravity and gravitational waves

In many terrestrial and astrophysical contexts (i.e. for a source that is slowly moving and non-relativistic), spacetime curvature is small, and approximations to vastly simplify the Einstein equations can be applied. In this weak field limit, the metric is approximately flat and can be written as a Minkowski background $\eta_{\alpha\beta}$ plus some small tensor perturbation $h_{\alpha\beta}$:

$$g_{\mu\nu} = \eta_{\mu\nu} + h_{\mu\nu} + \mathcal{O}\left(|h|^2\right) , \tag{2.8}$$

where $\left|h_{\mu\nu}\right| = \left|g_{\mu\nu} - \eta_{\mu\nu}\right| \ll 1$.

Gauge freedom can be exploited to simplify the form of the equations to solve. Commonly employed is the Lorentz gauge condition;

$$\partial_\mu h^\mu_\nu - \partial_\nu h = 0 , \tag{2.9}$$

where $h = h^\alpha_\alpha$ is the trace of the perturbation. Requiring further that we work in the transverse-traceless (TT) gauge, in which $h_{\alpha 0} = 0$ and $h = 0$, the Einstein equations in vacua (i.e $T_{\mu\nu} = 0$) simplify to

$$\Box h_{\mu\nu} = 0 , \tag{2.10}$$

where $\Box$ is the d'Alembertian operator. This set of equations admits solutions of plane-wave form $h_{ij}(t, \mathbf{x})$, denoted GWs. Two degrees of freedom in h_{ij} remain, which are typically interpreted as distinct polarisations, denoted $+$ (plus) and $\times$ (cross);

$$h_{ij} = h_+ e^+_{ij} + h_\times e^\times_{ij} . \tag{2.11}$$

Here, the polarisation tensors are defined

$$\mathbf{e}^+ = \vec{e}_1 \otimes \vec{e}_1 - \vec{e}_2 \otimes \vec{e}_2 , \tag{2.12}$$

$$\mathbf{e}^\times = \vec{e}_1 \otimes \vec{e}_2 - \vec{e}_2 \otimes \vec{e}_1 , \tag{2.13}$$

where orthonormal spatial basis vectors $\vec{e}_1$ and $\vec{e}_2$ form the fundamental plane perpendicular to wave propagation direction $\vec{e}_3$. We save an in-depth discussion of the principles of GW detection and features of GW observatories for Sec. 3.2.

Numerical relativity

To solve for the dynamic evolution of a general-relativistic system, one must construct an initial value problem from the Einstein equations. In pursuit of this goal, a $(3+1)$-D spacetime decompositon is typically employed (see, e.g., [16]). In such a system, spatial coordinates x^j are defined on 3D space-like hypersurfaces Σ_t, where each hypersurface is specified by constant $t = x^0$. For normal observers (i.e. those moving with four-velocity n^μ, where n^μ is a timelike vector normal to Σ_t), the difference in time coordinate between the same spatial position on two hypersurfaces is given by

$$dt^\mu = d\tau \left(\alpha n^\mu + \beta^\mu\right) . \tag{2.14}$$

Here, the lapse function α accounts for the different rates of change of coordinate time and proper time for observers, while the shift vector β (tangent to Σ_t) allows the spatial coordinates to slide normally with t between hypersurfaces. On each hypersurface, the spatial metric $\gamma_{\mu\nu}$ applies

$$\gamma_{\mu\nu} = g_{\mu\nu} + n_\mu n_\nu , \tag{2.15}$$

from which the Lorentz factor W and three-velocity v^j of an object moving with four-velocity u^μ measured by a normal observer can be obtained

$$\begin{aligned} W &= \alpha u^0 , \\ v^j &= \frac{u^j}{W} + \frac{\beta^j}{\alpha} . \end{aligned} \tag{2.16}$$

The extrinsic curvature K_{ij} describes how the hypersurfaces deform with coordinate time

$$K_{ij} = \nabla_\nu n_\mu \, e^\mu_i \, e^\nu_j , \tag{2.17}$$

where e^μ_i are the spatial components of basis vector and ∇_μ is the covariant derivative. Setting α and β through gauge choices, the evolution of γ_{ij}, K_{ij}, and the constraint equations must be solved for on each time slice [17];

$$\begin{aligned} \partial_t \gamma_{ij} =& -2\alpha K_{ij} + \nabla_i \beta_j + \nabla_j \beta_i , \\ \partial_t K_{ij} =& -\nabla_i \nabla_j \alpha + \alpha \left(R_{ij} - 2K_{ik}K^k_j\right) \\ & + \beta^k \nabla_k K_{ij} + K_{ik}\nabla_j \beta^k + K_{jk}\nabla_i \beta^k - 8\pi\alpha \left(S_{ij} - \frac{\gamma_{ij}}{2}\left(S^k_k - \rho_H\right)\right) , \\ 0 =& \; R - K_{ij}K^{ij} - 16\pi\rho_H , \\ 0 =& \; \nabla_i K^{ij} - 8\pi S^j . \end{aligned} \tag{2.18}$$

Here, S_{jk} are the spatial components of stress-energy tensor $T_{\mu\nu}$, S^j the momenta, and $\rho_H = \alpha^2 T^{00}/\rho$ the total energy. We leave the specifics of stress-energy source terms from radiation hydrodynamics to Sec. 2.2.

The conformal-flatness condition (CFC, also known as the Isenberg, Wilson, and Mathews condition; see, e.g., [18]) is often used to implement approximate general-relativistic effects in numerical studies. In this, the spatial 3-metric γ_{ij} may be written as flat multiplied by some scalar factor;

$$\gamma_{ij} = \psi^4 \eta_{ij}\,. \tag{2.19}$$

While satisfied irrespectively in spherical symmetry, the approximation is only valid in two or three spatial dimensions when gravitational waves are not present. While this may seem problematic to discuss in a thesis concerned with gravitational waves from core-collapse supernovae, it is often a good approximation for the general-relativistic behaviour of the hydrodynamics in systems (such as simulations of core-collapse supernovae in which black holes are not formed) without strong field effects [17, 19]. This approximation greatly simplifies the numerical task to be solved, removing any explicit time derivatives in the equations above, and reducing the problem to a set of elliptic equations. While GWs cannot be extracted from simulations using CFC, the signal expected can be estimated using the quadrupole approximation [20]

$$h_{ij}(t,r) \approx \frac{2G}{c^4 r}\ddot{I}^{\mathrm{TT}}_{ij}\left(t - \frac{r}{c}\right)\,, \tag{2.20}$$

where $\ddot{I}^{\mathrm{TT}}_{jk}$ is the second time derivative of the quadrupole moment tensor in the transverse-traceless gauge, and

$$\ddot{I}_{ij} = \frac{\partial}{\partial t}\int d^3x\,\rho W\sqrt{\gamma}\left(v_i x_j + v_j x_i - \delta_{ij} v_k x^k\right)\,. \tag{2.21}$$

This approximation is reasonable assuming slow motion (i.e. the curvature source is confined to a region much smaller than the wavelength of gravitational radiation emitted) and a weak gravitational field, which has shown to be valid in the case of core-collapse supernovae [21]. In Chap. 6, we present GW signals estimated from simulations of core-collapse supernovae implementing CFC for treatment of general relativistic effects.

2.2 Neutrino radiation hydrodynamics

General-relativistic hydrodynamics

It is typical in classical fluid dynamics to describe a fluid in terms of its mass density ρ, three-velocity v^j, pressure P, and energy density e. The hydrodynamic evolution of a relativistic perfect fluid is constrained by the set of local conservation equations for mass, momentum, and stress-energy;

$$\begin{aligned} \nabla_\mu \left(\rho u^\mu\right) &= 0\,, \\ \nabla_\mu T^{\mu\nu} &= 0\,, \end{aligned} \tag{2.22}$$

where u^μ is the fluid four-velocity and the stress-energy tensor $T^{\mu\nu}$ takes the form

$$T^{\mu\nu} = \rho h u^\mu u^\nu + P g^{\mu\nu}\,, \tag{2.23}$$

and $h = 1 + e + P/\rho$ is the specific enthalpy. For the purpose of solving these equations numerically, it is useful to recast them into conservative form. This is done by introducing a set of conserved variables $(D,\, S_j,\, \tau)$ in terms of primitive variables $(\rho,\, v_j,\, e)$ [22];

$$\begin{aligned} D &= \rho W\,, \\ S_j &= \rho h W^2 v_j\,, \\ \tau &= \rho h W^2 - p - D\,, \end{aligned} \tag{2.24}$$

where D, S_j, and τ are the rest-mass density, j^{th} component of the momentum, and total energy density minus rest-mass density, respectively. From the conserved variables, the evolution equations take the simple form

$$\partial_t \left(\sqrt{\gamma}\mathbf{U}\right) + \partial_j \left(\sqrt{-g}\mathbf{F}^j\right) = \mathbf{S}\,, \tag{2.25}$$

where state vector $\mathbf{U}$, flux vector $\mathbf{F}^j$, and source vector $\mathbf{S}$ are defined

$$\begin{aligned} \mathbf{U} &= \left[D,\, S_j,\, \tau\right]\,, \\ \mathbf{F}^i &= \left[D\hat{v}^i,\, S_j\hat{v}^i + \delta^i_j P,\, \tau\hat{v}^i + Pv^i\right]\,, \\ \mathbf{S} &= \left[0,\, T^{\mu\nu}\left(\partial_\mu g_{\nu j} - \Gamma^\lambda_{\mu\nu} g_{\lambda j}\right),\, \alpha\left(\partial_\mu (\log\alpha) - T^{\mu\nu}\Gamma^0_{\mu\nu}\right)\right]\,, \end{aligned} \tag{2.26}$$

where $\hat{v}^i = v^i - \beta^i/\alpha$. This first-order hyperbolic set of equations is closed through the equation of state (EOS) governing the fluid, $P = P(\rho, s)$, where s

is the specific entropy. In the case of core-collapse supernovae, the EOS must be valid over a large parameter space including (but not limited to) nuclear densities. This is a topic of active research and discussed in more depth in Sec. 2.3.

Neutrino transport

According to the Standard Model, there are six species of neutrino; ν_e, $\bar{\nu}_e$, ν_μ, $\bar{\nu}_\mu$, ν_τ, and $\bar{\nu}_\tau$, each of which are Dirac fermions. The distribution of energy and momentum within a population is dictated by the neutrino distribution function $f(x^\mu, p^\mu)$, which describes the number density of neutrinos in phase space;

$$dN = -\frac{1}{hc} p_\mu u^\mu f(x^\mu, p^\mu) \left(W\sqrt{-g} d^3x\right) \left(\frac{\sqrt{-g}}{-h^2}\frac{d^3p}{p}\right) . \tag{2.27}$$

Here, the expressions in the first and second sets of parentheses are the invariant volume element and invariant momentum-space element, respectively. The evolution of the neutrino distribution function is governed by the general-relativistic Boltzmann equation (also known as the Lindquist equation) [23];

$$p^\mu \nabla_\mu f = \left(\frac{df}{d\lambda}\right)_{\text{coll}} , \tag{2.28}$$

where λ is an affine parameter, and the collision term on the right hand side encompasses production and destruction of neutrinos from absorption, emission, and scattering processes. In core-collapse supernovae, the collision term is dominated by scattering of neutrinos off free nucleons and heavy nuclei, absorption of ν_e and $\bar{\nu}_e$ on free nucleons, and pair production/annihilation and nucleon-nucleon bremsstrahlung. We discuss the details of these processes with respect to calculation of neutrino opacities for supernova simulations in more detail in Sec. 3.3.

The stress-energy tensor from neutrino radiation is given by

$$T^{\mu\nu}_{\text{neutrinos}} = \int \frac{d^3p}{p} \frac{\sqrt{-g}}{-h^2} p^\mu p^\nu f , \tag{2.29}$$

which obeys $\nabla_\mu T_{\mu\nu} = 0$ as f is invariant. In the reference frame of an observer travelling with four-velocity u^μ (i.e. in a Lagrangian fluid frame), $T^{\mu\nu}_{\text{neutrinos}}$

can be written in terms of the first three angular moments of the neutrino distribution function;

$$T^{\mu\nu}_{\text{neutrinos}} = \frac{E}{c^2} u^\mu u^\nu + \frac{1}{c}\left(F^\mu u^\nu + F^\nu u^\mu\right) + P^{\mu\nu} \,. \tag{2.30}$$

Here, energy-integrated moments M are obtained from their energy-dependent counterparts $M_{(\epsilon)}$ using [14]

$$M = \frac{1}{(hc)^3} \int d\left(\frac{\epsilon^3}{3}\right) M_{(\epsilon)} \,, \tag{2.31}$$

and $M_{(\epsilon)}$ are defined

$$\begin{aligned} E_{(\epsilon)} &= \epsilon \int d\Omega f \,, \\ F^\mu_{(\epsilon)} &= \epsilon \int d\Omega f \, l^\mu \,, \\ P^{\mu\nu}_{(\epsilon)} &= \epsilon \int d\Omega f \, l^\mu l^\nu \,, \end{aligned} \tag{2.32}$$

given vector l^μ defined to separate the timelike and spacelike components of the neutrino momenta [14].

The evolution of the moments is dependent on higher order moments. State-of-the-art neutrino transport for core-collapse supernova simulations uses a local two-moment scheme which evolves only E and F^μ, using a closure scheme to obtain radiation pressure $P^{\mu\nu}$ and higher-order moments (see, e.g. [24–27]). In the simulation presented in Chap. 7, the energy-dependent pressure tensor is obtained by interpolating between the optically thick and optically thin limits given in [28], and employs the closure scheme $\chi_{(\epsilon)}$ from [29];

$$P^{ij}_{(\epsilon)} = \left[\frac{3\left(1 - \chi_{(\epsilon)}\right)}{2}\right] P^{ij}_{(\epsilon),\,\text{thick}} + \left[\frac{3\chi_{(\epsilon)} - 1}{2}\right] P^{ij}_{(\epsilon),\,\text{thin}} \,, \tag{2.33}$$

$$\chi_{(\epsilon)} = \frac{1}{3} + \frac{2}{15}\xi^2_{(\epsilon)}\left(3 - \xi_{(\epsilon)} + 3\xi^2_{(\epsilon)}\right) \,, \tag{2.34}$$

where $\xi_{(\epsilon)} = \sqrt{\mathbf{F}_{(\epsilon)} \cdot \mathbf{F}_{(\epsilon)} / E^2_{(\epsilon)}}$ is the flux factor.

In Sec. 3.3, we outline the particulars of neutrino emission from core-collapse supernovae and the methods used to observe them.

2.3 Nuclear matter equation of state

The equation of state (EOS) for matter at densities above the nuclear saturation density n_{sat}[1] is highly uncertain, not least because recreating such high density environments in the laboratory is highly unfeasible. While such conditions are commonplace in neutron stars, opportunities to directly probe the nuclear matter EOS have been few and far between. Observations of neutron stars with inferred masses of $\sim 2M_\odot$ (see, e.g., [30–32]) have set constraints on the lower limit of the maximum mass supportable by the nuclear matter EOS, ruling out some of the more speculative propositions for nuclear matter containing, for example, strange matter and free quarks. While we provide a brief overview of the dense matter EOS here as relevant to core-collapse supernovae, we direct the interested reader to [33–35] and references therein for in-depth and informative reviews.

The properties of the nuclear matter EOS are often discussed with respect to the internal energy density $E(n_{\text{B}}, Y_e, T)$, as a function of the density, temperature and composition of the fluid. Here, n_{B} is the number density of baryons, T the temperature, and Y_e is the electron fraction. For the purposes of core-collapse supernova simulations, the EOS must be valid over the parameter space constrained by $n_{\text{B}} \in [10^{-5}, 10]\text{fm}^{-3}$, $Y_e \in [0, 0.6]$, and $T \in [0, 150]\text{MeV}$ [33].

The binding energy per nucleon for cold ($T = 0$), symmetric ($Y_e = 0.5$) matter at $n_B = n_{\text{sat}}$, E_0, is well constrained experimentally to $E_0 \approx 16\,\text{MeV}$ [36]. One way to approach this problem is to construct a functional in small changes from this point using a Taylor expansion. Given parameters $x = (n_B - n_0)/n_0$ and $\beta = 1 - 2Y_e$, the binding energy per nucleon for small x and β can be approximated

$$E(x, \beta) = -E_0 + \frac{K}{18}x^2 + \frac{K'}{162}x^3 + \ldots + \mathcal{S}(x, \beta)\,, \tag{2.35}$$

where K is the incompressibility of nuclear matter, K' is skewness parameter, and $\mathcal{S}(x, \beta)$ is the symmetry term, which encompasses EOS effects due to changes in composition:

$$\mathcal{S}(x, \beta) = \mathcal{S}_2(x)\beta^2 + \mathcal{O}(\beta^4)\,. \tag{2.36}$$

---

[1] n_{sat} defined as where $dE/dn_B|_{n_B = n_{\text{sat}}} = 0$

Here,

$$\mathcal{S}_2(x) = J + Lx + \mathcal{O}(x^2)\,, \tag{2.37}$$

where J is the symmetry energy at saturation, and L is the symmetry slope parameter.

While an EOS for cold nuclear matter isn't a great approximation for the hot proto-neutron star created after core collapse, it is physically relevant for many evolved neutron stars. Using this approximation, observations (indirect or direct) of systems containing neutron stars can be used to put constraints on the behaviour of matter at such densities. Commonly used for this purpose is the maximum neutron star mass that can be supported by a particular equation of state. In Fig. 2.1, we show the mass-vs-radius relations for cold neutron stars in neutrinoless β-equilibrium for a variety of EOS proposals as obtained from `CompOSE` [37], overlaying observational constraints on the maximum neutron star mass from PSR J0348+0432 [31] and PSR J1614+2230 [30].

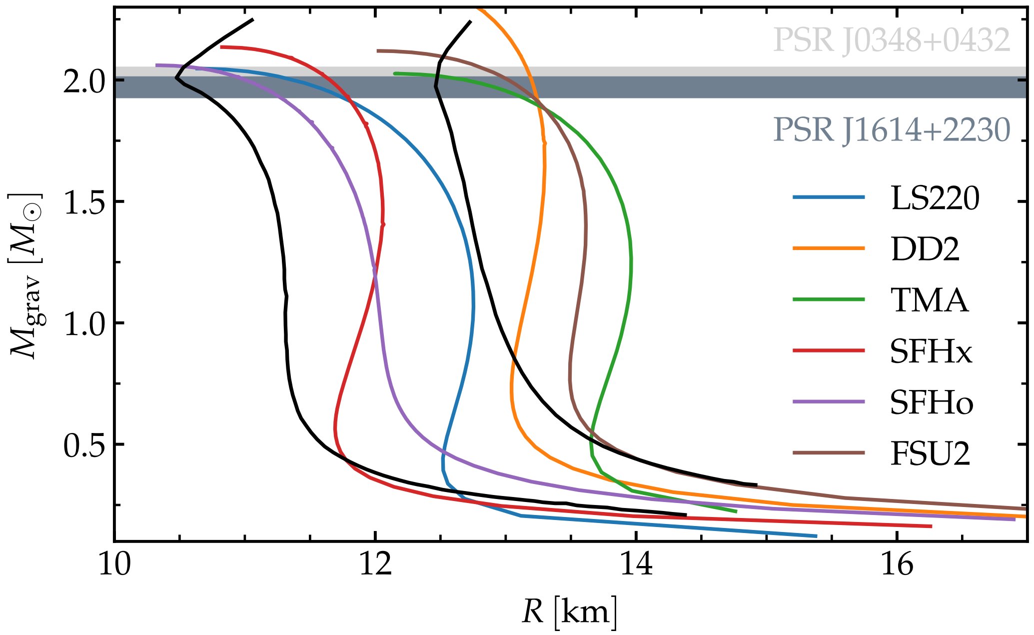

Figure 2.1: Mass vs radius plot for cold neutron stars in neutrinoless beta-equilibrium for different EOSs as obtained from `CompOSE` [37]. The constraints placed on the maximum neutron star (NS) mass by observations of PSR J0348+0432 [31] and PSR J1614+2230 [30] are indicated by shaded panels in light gray and slate gray, respectively.

3 Multimessenger astronomy and the observational signatures of core-collapse supernovae

Though my soul may set in darkness,
it will rise in perfect light;
I have loved the stars too fondly
to be fearful of the night.

—Sarah Williams, *The Old Astronomer*

3.1 Observational signatures

A colossal reservoir of some few 10^{53} ergs of energy is made available as the degenerate core built up within a massive star throughout its nuclear burning lifetime undergoes gravitational collapse. Over 99% is spent in neutrinos, while less than 1% is emitted in GWs and across the electromagnetic (EM) spectrum. Appreciable neutrino emission begins as the degenerate precollapse core approaches collapse, continuing while the nascent proto-neutron star (PNS) cools and deleptonises through an intense neutrino-driven wind. GW emission is sourced by the formation and evolution of the PNS, where quadrupolar deformation can for the most part be attributed to PNS oscillations excited by core bounce, ringdown, development of hydrodynamic fluid instabilities in the cavity between the PNS and stalled shock, and rotational instabilities. Constrastingly, EM emission originates far from the so-called CCSN central engine, with signatures across the spectrum related to shock breakout through the progenitor star, nuclear decay, and interaction of the shock with the circumstellar medium.

To put into context the various phases of GW and neutrino emission, we hereafter discuss phases of the dynamics governing core collapse and stellar explosion [38, 39]:

- **Onset of core collapse.** The central temperature T_c of the degenerate core (formed at the centre of a massive star over its last nuclear burning stages; typical mass is between $(1.3 - 2)\,M_\odot$ and progenitor dependent.) increases as the core grows and slowly contracts. As $T_c \rightarrow 1\,\mathrm{MeV}$, Fe-group nuclei begin to fall victim to partial dissociation by thermal photons, producing α particles and free nucleons. This reduces the effective adiabatic index $\Gamma_1 < 4/3$, which accelerates collapse. Increased Fermi energy renders electrons more susceptible to capture on nuclei (see, e.g., [40, 41]). In these initial stages of collapse, ν_e emission from electron capture is able to free-stream outwards and escape the collapsing core.
- **Neutrino trapping in the core.** Neutrinos become trapped in the collapsing core as the density approaches $10^{12}\,\mathrm{g/cm^3}$. This occurs predominantly due to neutral current scattering on heavy nuclei as, at such densities, their nucleons interact coherently as a single body off which neutrinos scatter [38]. In this scenario, electron neutrinos produced by electron capture cannot escape, and are instead dragged ever further inwards with gravitational collapse. The collapsing core separates into two regions. The inner core, where most electrons have already captured on nucleons, is rich with entropy and lepton number due to trapping effects and collapses homologously. In the outer core, where electron capture (now for the most part onto free protons) proceeds, collapse accelerates further still and approaches freefall ($\lesssim 0.3c$).
- **Core bounce and shock formation.** As the central density reaches that of nuclear matter, a phase transition transforms heavy nuclei to a uniform nuclear medium of sorts. The EOS of this material stiffens as internucleon forces become repulsive, resisting further compression. Collapse of the inner core grinds to an abrupt halt, with a shock formed around 10 km as the supersonically infalling outer core strikes the in-

ner core and rebounds. The mass of the inner core is dependent on the electron fraction, $Y_e = n_e/n_{\mathrm{B}}$, where n_e and n_{B} are the number densities of electrons and baryons respectively, and is approximately bounded by the instantaneous Chandrasekhar mass M_{ch};

$$M_{\mathrm{ch}} \sim 1.457(Y_e)^2 \, M_{\odot} \, , \tag{3.1}$$

which is typically around $0.5\, M_{\odot}$ at the time of bounce.

- **Shock propagation and breakout.** The shock propagates outwards, driving through the ever-infalling outer core and buoyed by trapped neutrinos. Electron capture abounds in the post-shock region as the shock travels outwards through material where free protons still exist, producing ν_e in monumental numbers that remain trapped while the shock propagates faster than ν_e can diffuse. As the shock breaks out into material where neutrinos are no longer trapped, an ultraluminous burst of ν_e is emitted (often called the neutrino burst at shock breakout), causing the lepton fraction $Y_{\mathrm{L}} = (n_{\nu} + n_e)/n_{\mathrm{B}}$, where n_{ν} is the number density of neutrinos, in the post-shock region to plummet.

- **Stalling of the shock.** The shock continues to propagate through the infalling outer core, behaving as a thermal transducer of sorts as it dissipates the kinetic energy of the infalling material into thermal energy, causing rapid deceleration, compression, and heating of the post-shock flow. Heavy nuclei are dissociated into free nucleons as the shock passes through, draining the shock of its might. Assuming a pre-collapse core comprised of iron-group nuclei, the shock burns through some 10^{51} ergs for every tenth of a solar mass it passes through. Combined with reduced post-shock pressure following the prior escape of trapped neutrinos, the shock stalls around an enclosed mass of $\sim 1\, M_{\odot}$ (typically between $(100 - 150)$ km). The infalling outer core persists, feeding an accretion flow onto the PNS.

- **PNS accretion and shock revival.** Following shock stagnation, infalling material accretes onto the PNS at a rate of several $0.1\, M_{\odot}/\mathrm{s}$. Temperature and composition gradients between the inner core and the hot, puffy accretion layer drives convection in the PNS mantle. A gain region, where neutrino heating exceeds neutrino cooling, develops behind the stalled shock due to the differences in temperature dependence of neutrino emission and absorption rates. Charged-current neutrino capture on free nucleons dominates energy deposition rates. Convective instability sets in between the stalled shock and PNS surface, driving overturn and turbulence there. Non-radial motions expand the shock and increase the efficiency of neutrino heating. A combination of these effects, the so-called delayed neutrino-heating mechanism, is thought to revive the shock and drive a successful explosion. While laid out here as canon, it is important to note that many questions relating to this process remain to be answered (see, e.g., [42, 43]). Confirmation of the CCSN explosion mechanism will require both observational evidence and assertion through robust computational modelling, facets of which this thesis aims to address.

- **PNS cooling and the neutrino-driven wind.** Following shock revival, accretion onto the PNS can persist for several hundreds of milliseconds, simultaneous to shock expansion. After accretion ends, the PNS undergoes Kelvin-Helmholtz cooling, during which any remaining gravitational binding energy is radiated away over a neutrino diffusion timescale. Energetic neutrinos emitted near the neutrinosphere deposit energy in the cooler, outer layers of the PNS (predominantly through charged-current absorption on free nucleons), driving dilute but persistent mass outflows (initially around $\sim 10^{-2}\,M_{\odot}/\mathrm{s}$ from the surface of the nascent NS - a neutrino-driven wind.

We hereafter discuss the observational signatures of CCSNe.

Gravitational waves

The GW signatures of CCSNe are diverse, evidencing the complex physical processes driving stellar explosions, and are strongly dependent on the properties of the progenitor stars from whence they came.

For the most part, GW emission is dominated by the dynamics of the nascent PNS. For progenitor stars with precollapse cores with rotational periods exceeding a few tens of seconds, the strongest GW emission comes from PNS oscillations excited by convective plumes and hydrodynamic waves striking the PNS and causing it to ring up (see, e.g., [44–47]). The peak frequency of emission naturally follows the dominant PNS surface g-mode frequency, which increases quasi-linearly with time from $\sim (100-200)$ Hz to over 1 kHz as the PNS accretes fallback material, contracts, and deleptonises, although it has been shown that a broad and complex spectrum of oscillations is typically excited (see, e.g., [48–50]). GW emission from prompt convection, which develops within a few tens of milliseconds of core bounce but dies down before ~ 100 ms has passed, is typically at frequencies $100-300$ Hz due to the puffy nature of the PNS surface at these early times. Conversely, neutrino-driven convection in the gain region at later times sources GW emission between $\sim 300-1000$ Hz (increasing with time) as it drives oscillations of an ever-contracting PNS. Strong fluid downflows from development of the standing accretion-shock instability (SASI) can modify the accretion rate at the PNS, inducing quadrupolar oscillations around $(100-200)$ Hz at later times (after a few hundred milliseconds), where the emission frequency is related to the characteristic frequency of the advective-acoustic cavity in which the SASI develops [25, 42, 44, 45]. While the frequency evolution of the GW signature is robust, it is perhaps not surprising that the phase is decidedly stochastic due to the chaotic nature of turbulent convection and the SASI (see, e.g., [51]).

For illustrative purposes, we show in Fig. 3.1, the time-domain GW strain and time-frequency evolution of the GW energy spectrum for model `15_3.7` from Murphy *et al.* [44].

In precollapse cores with appreciable angular momentum, increased centrifugal support around equatorial regions leads to pronounced oblate deformation of the inner PNS core as collapse proceeds. Strong quadrupole radiation is produced as the inner core rapidly decelerates and rebounds, resulting in a pronounced spike in the GW signal at core bounce, followed by ringdown of the PNS as it settles to its new equilibrium state (see, e.g., [52–54] for a detailed discussion). Unsurprisingly, the GW signal is dependent on the mass of the inner core, its angular momentum distribution, and the equation of state of nuclear matter (see, e.g. [54–62]). In precollapse cores characterised by extremely rapid rotation and/or strong differential rotation, nonaxisymmetric rotational instabilities driven by rotational shear (see, e.g., [19, 63–67]) may develop, resulting in a significant enhancement of GW emission after ~ 50 ms or so post-bounce.

While we spoke previously on pre- and post-explosion dynamics for CCSNe,

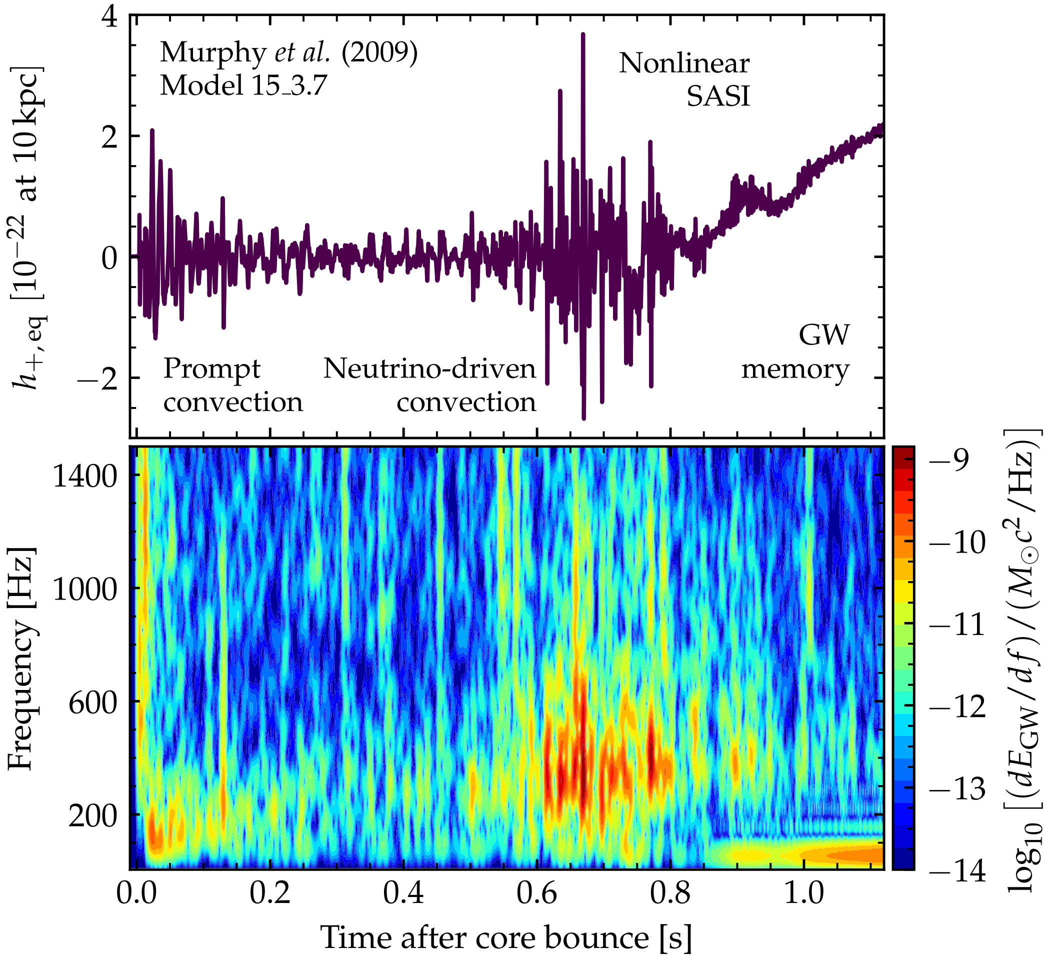

Figure 3.1: In the context of an equatorial observer at 10 kpc, the time domain strain (top panel) and time-frequency evolution of the spectral GW energy (bottom panel) for model `15_3.7` from Murphy *et al.* [44]. We highlight regions where emission originates from prompt convection, neutrino-driven convection, non-linear SASI, and GW memory.

it is indeed possible that no explosion occurs. Should the stalled shock not be revived before PNS accretion increases the PNS mass beyond the maximum permissible by the nuclear matter EOS, BH formation will occur. The timescale on which this happens is dependent on the accretion rate onto the PNS (influenced by the properties of the progenitor star), the angular momentum of the PNS, and the nuclear matter EOS, but is typically around $\sim (0.5 - 3)$ s (see, e.g, [49, 68–70]). The GW signature of BH formation is a characteristic short burst and ringdown. The peak ringdown frequency is inversely proportional to the mass of the nascent BH, with typical ringdown spectra for stellar mass BH formation peaking around several kilohertz [27, 49, 71, 72]. For very massive progenitors (i.e. Population III stars with zero-age main sequence (ZAMS) $M_{\text{ZAMS}} \gtrsim 100\,M_{\odot}$), an intermediate PNS stage may not occur at all, with prompt BH formation occuring instead (see, e.g., [73]). For the reader interested in the probability of BH formation given progenitor mass and structure, we recommend [69, 74, 75] and references therein.

Neutrinos

We provide here a broad overview of neutrino signatures from CCSNe, drawn heavily from reviews by Janka [38], Roberts & Reddy [76], and Mirizzi *et al.* [77], which we highly recommend to the interested reader.

The vast majority of neutrinos from CCSNe are emitted within ~ 10 seconds of the initial core collapse, and the resultant observational signature is characterised by three distinct periods;

- **Neutrino burst at shock breakout.** A high-luminosity ν_e burst emitted as the shock breaks through the neutrinosphere, allowing trapped ν_e produced prior from electron-capture on nuclei and free neutrons during core collapse to escape. Peak luminosities are of order $\sim 10^{53}$ erg/s, with mean neutrino energy around $(12 - 13)$ MeV. Following breakout through the neutrinosphere, luminosities of $\bar{\nu}_e$ and heavy-lepton neutrinos ν_x increase as their creation becomes possible in the shock-heated material through pair-production processes.
- **Post-bounce accretion.** After the shock stalls, accretion of fallback material onto the PNS gives rise to generous production of ν_e and $\bar{\nu}_e$ through charged-current processes, the expected luminosities of which are related to the accretion rate and mass of the growing PNS. Large-scale temporal and spatial variations in the luminosity are expected as convective plumes and turbulent downflows disrupt accretion at the PNS surface. As GW emission is also impacted by this, it has been shown that the GW and neutrino signatures during this time are likely to be correlated (see, e.g., [67, 78]). Though considerably lower in luminosity than for ν_e and $\bar{\nu}_e$, heavy-lepton neutrino emission attributed to pair production from nucleon-nucleon bremsstrahlung occurs in the core.

- **PNS cooling and deleptonisation.** After accretion has ceased, Kelvin-Helmholtz cooling of the nascent PNS commences as it contracts and deleptonises to its final state as a cold NS. During this phase, luminosities from all neutrino types become comparable (i.e. within $\sim 10\%$ of eachother), with total luminosity around a few 10^{52} erg/s which persists for several seconds.

In Fig. 3.2, we show the temporal evolution of the luminosity and mean energy in neutrinos from the CCSN simulation presented in Roberts [79].

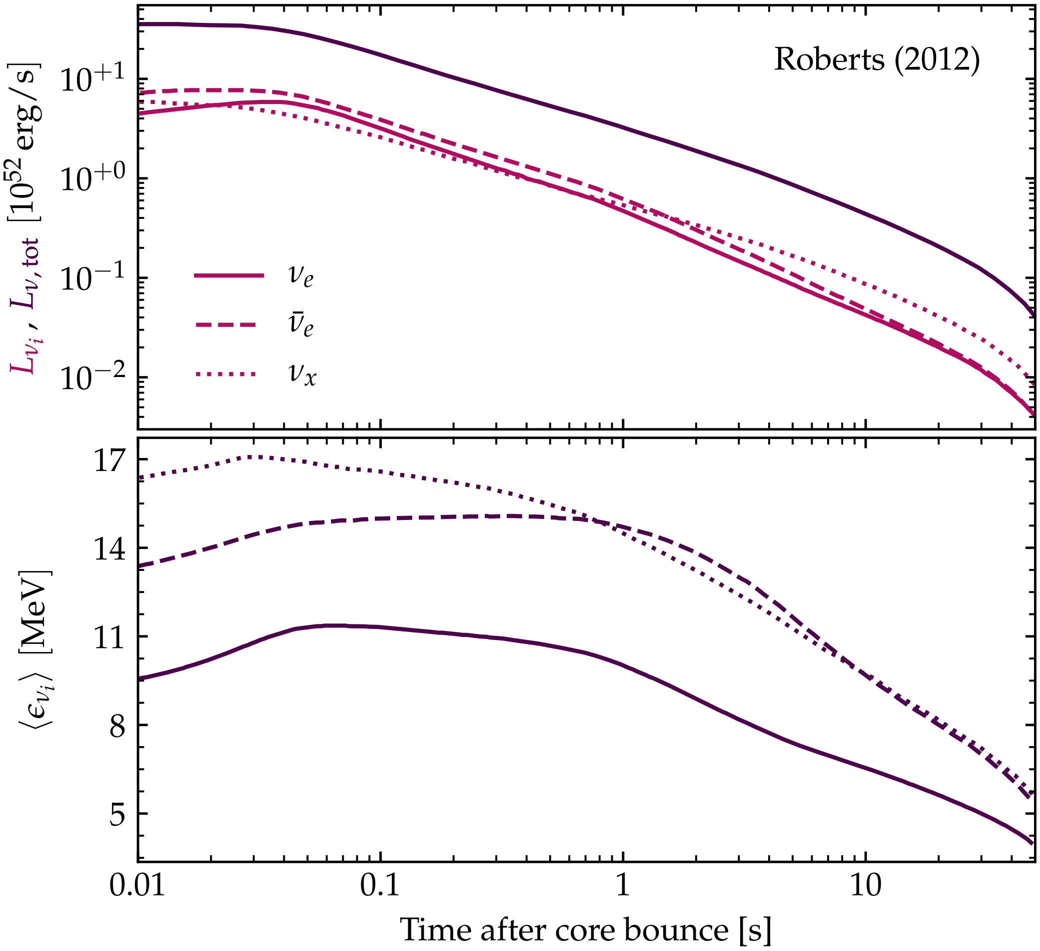

Figure 3.2: Temporal evolution of the neutrino luminosity (top panel) and mean neutrino energy (bottom panel) for the CCSN model presented in Roberts [79].

Electromagnetic

CCSNe are typically classified by the morphology of their optical light curves, which are dependent on the structure and composition of both the progenitor star and the circumstellar medium. Broadly, CCSNe with spectra rich in hydrogen are categorised as Type II. Of hydrogen-poor Type I SNe, CCSN spectra containing helium lines are denoted Type Ib, while CCSNe with spectra absent of helium are categorised Type Ic. Type Ia SNe, characterised by ionised silicon lines, are borne of thermonuclear explosions rather than core collapse, and are thus hereafter not considered. Beyond Type II, Type Ib, or Type Ic, further subclassification according to light curve morphology is typical.

Of the progenitor stars for CCSNe, Type II explosions are borne from supergiant stars with most, if not all, of their hydrogen envelope intact. Type I CCSNe originate from more compact progenitors, where Type Ib progenitors have lost their hydrogen envelopes through either an intense stellar wind or interaction with a binary companion. Type Ic progenitors are more compact still, having lost both their hydrogen and helium envelopes. In the interest of brevity we keep this discussion on CCSN progenitors concise, but refer the interested reader to an excellent review by Smartt [80].

The first EM observable from CCSNe occurs as the shock breaks through the surface of the progenitor star, which peaks in the ultraviolet (UV) band. Inspired by Fig. 2 of Kistler *et al.* [81], we show in Fig. 3.3 the time to shock breakout after core bounce against the duration of the shock breakout UV signature for a number of Wolf-Rayet, blue supergiant, and red supergiant CCSN progenitors.

3.2 Gravitational wave detection

As discussed briefly in Chapter 2, the propagation of GWs distorts the background metric, stretching and squeezing spacetime itself as the GW passes through. The effects of this are very minute as a consequence of the incredibly weak coupling between gravity and matter, but is measurable through precision laboratory techniques. In this Section we focus on providing a broad overview of the principles of ground-based interferometric detection, and direct the interested reader to [82] for a thorough and in-depth review.

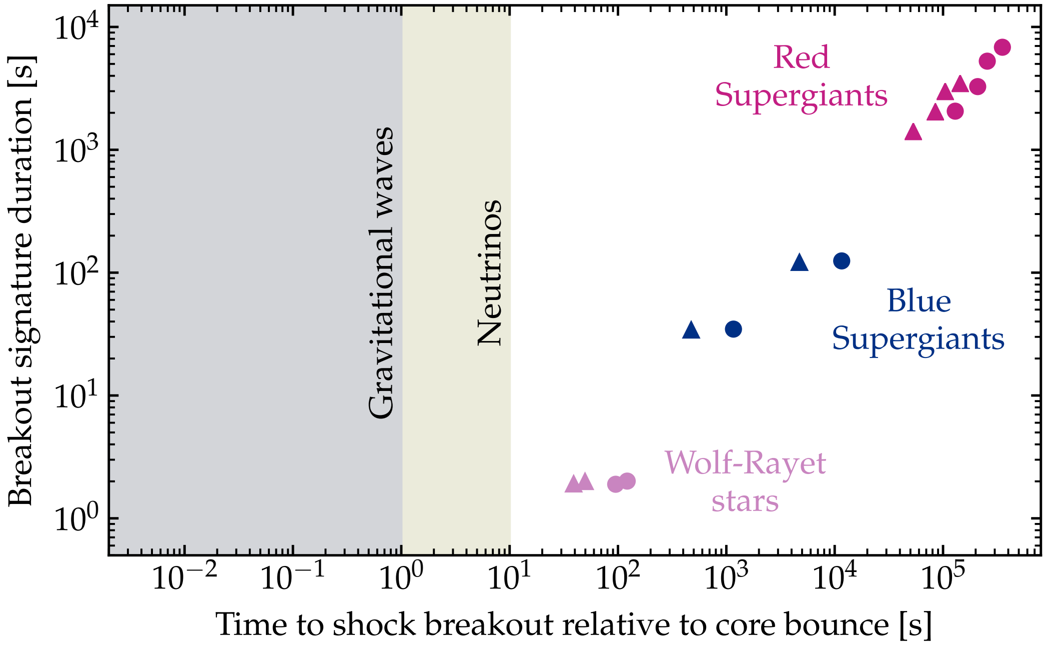

Figure 3.3: Time to shock breakout, relative to core bounce, against the duration of the UV shock breakout signature for a variety of Wolf-Rayet, blue supergiant, and red supergiant progenitor stars, in the style of Fig. 2 from Kistler *et al.* [81]. Circular and triangular markers indicate CCSNe characterised by explosion energies of 5×10^{50} erg and 10^{51} erg, respectively, while each triangle/circle pair represented a particular progenitor mass.

Fundamentals of laser interferometry

Laser interferometry permits precision length measurement through minute phase shifts between outgoing and returning laser beams. For illustrative purposes, we consider an apparatus comprised of two free test masses in the plane $y = z = 0$, positioned at coordinates $x = 0$ and $x = L$ respectively. Placing a laser at the origin, the distance betwen the two masses can be measured by sending a beam out from the origin to the second mass, then measuring the phase difference of the reflected beam relative to the outgoing beam as it reaches the origin. Phase shifts can be interpreted as distance variations, meaning that changes in the apparent arm length can be measured. For GWs with period much longer than the light travel time, this can be used to measure the effect of GWs as they pass through the detector. The GW strain produces a fractional change in the original arm length, i.e. $\Delta L/L \sim h$.

The current generation of ground-based detectors are Michelson interferometers employing Fabry-Pérot optical cavities, using laser light with wavelength λ to traverse orthogonal arms of length L. For a linearly polarised wave, the difference in phase shift $\Delta\Psi$ between beams traversing each arm is approximately

$$\Delta\Psi \approx \frac{4\pi L h_+}{\lambda} . \tag{3.2}$$

Physical arm lengths are typically limited to a few km due to spatial and financial constraints, while laser wavelengths of order micrometers are typical. Given optimistic astrophysical GW strains of order 10^{-21}, this results in expected phase shifts of just 10^{-11} radians. Hypothetical third-generation detectors with arm length of order 10 km and above have been proposed, a discussion of which is saved for Chap. 8. Employing a Fabry-Pérot cavity in each arm can greatly increase the effective arm length and hence theoretical sensitivity of an interferometer over its Michelson counterpart. Instead of a single test mass, the Fabry-Pérot cavity is composed of a partially transmissive input test mass (ITM) and a highly reflective end test mass (ETM). The distance between the two test masses is tuned so optical power can build up within the cavity as the beam traverses the arm many times. The factor by which the phase shift is amplified by traversing the Fabry-Pérot cavity, the arm cavity gain G_{arm}, is related to the optical properties of the ITM [13];

$$G_{\text{arm}} = \frac{t_{\text{ITM}}^2}{(1 - r_{\text{ITM}})^2} , \tag{3.3}$$

where r_{ITM} and t_{ITM} are the reflection and transmission coefficients of the ITM, respectively.

Further imporovement in sensitivity can be gained by careful placement of mirrors on the symmetric and anti-symmetric sides of the beamsplitter to utitlise power recycling and signal extraction techniques, respectively [82].

Antenna response

The response of a given interferometer (positioned with orthogonal x and y arms in the direction of unit vectors $\vec{X}$ and $\vec{Y}$, respectively) can be quantified through detector tensor $\overleftrightarrow{D}$, defined as

$$\overleftrightarrow{D} = \frac{1}{2}(\vec{X} \otimes \vec{X} + \vec{Y} \otimes \vec{Y}) . \tag{3.4}$$

In the TT-gauge, the GW strain on said detector due to metric perturbation h_{ij} (c.f. Sec. 2.1) is just

$$h = D^{ij} h_{ij} \,, \tag{3.5}$$

which can be written in terms of the the detector response to each polarisation;

$$\begin{aligned} h &= F_+ h_+ + F_\times h_\times \,, \\ F_+ &= D^{ij} e^+_{ij} \,, \\ F_\times &= D^{ij} e^\times_{ij} \,. \end{aligned} \tag{3.6}$$

Here, F_+ and $F_\times$ are the antenna response patterns of the detector, and polarisation vectors $\mathbf{e}^{+,\times}$ are defined previously as in Sec. 2.1.

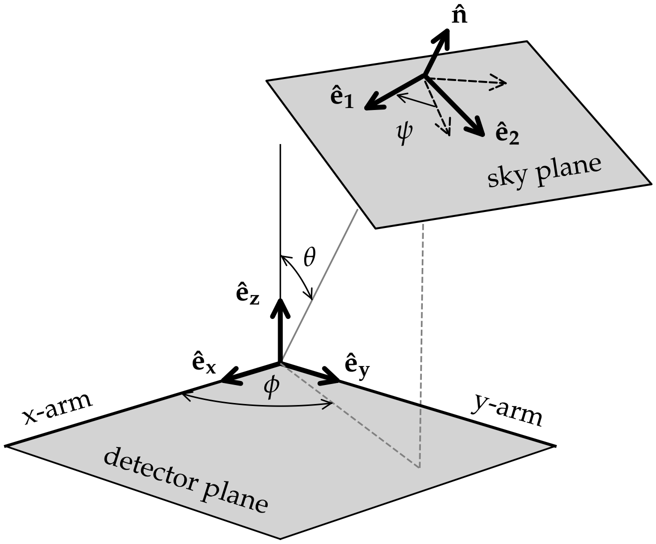

Figure 3.4: The detector frame and sky frame, in the style of Fig. 3 of [83].

For a hypothetical detector aligned with arms along x and y axes, the antenna response to a source at location characterised by Euler angles (θ, ϕ, ψ) is just [83, 84]

$$F_+ = \frac{1}{2}\left(1+\cos^2\theta\right)\cos 2\phi \cos 2\psi - \cos\theta \sin 2\phi \sin 2\psi \,, \tag{3.7}$$

$$F_\times = \frac{1}{2}\left(1+\cos^2\theta\right)\cos 2\phi \sin 2\psi - \cos\theta \sin 2\phi \cos 2\psi \,, \tag{3.8}$$

where we illustrate the definition of said angles in Fig. 3.4.

Noise sources

The sensitivity of the detector is limited by a number of sources which cause fluctuations in either the phase of the optical field used to read out the GW strain (oft denoted sensing noise or optical readout noise) or directly move the test mass (displacement noise). We provide a short discussion of sensing and displacement noise sources in ground-based interferometers following [13, 15, 82] and references therein.

Displacement noise, which originates from the stochastic fluctuation of forces, has most power at low frequencies. Sensitivity at low frequencies is limited by the seismic noise floor, a consequence of ground motion from earthquakes, wind, waves, and human activity. The impact of seismic noise in ground-based interferometers is mitigated through a combination of active isolation platforms (with seismic vibration sensors) and a passive isolation system using a series of mass-spring layers and multiple-pendulum suspensions which isolate the final test mass from the active isolation system. Seismic fluctuations, as well as fluctuations in atmospheric pressure, can also source so-called Newtonian noise; displacement due to changing the gradient of the local Newtonian gravitational potential at the test masses which cannot be mitigated through isolation systems. Seismometers may be used to estimate the Newtonian noise contribution for offline subtraction in the future [85].

At intermediate frequencies up to around 100 Hz, thermal noise in the mirrors and suspensions is dominant. Losses in a system give rise to fluctuations in physical coordinates through the fluctuation-dissipation theorem. Fluctuations in the mirror surface position are dominated by Brownian noise in the mirror coatings, while thermal effects from bulk mirror motion are negligible for the current generation of detectors. Suspension thermal noise is dominated by structural losses in the suspension fibres where they bend as they connect to the mirror.

Above $\sim$ 100 Hz, quantum noise dominates. Quantum noise is a combination of effects from radiation pressure noise (which causes test mass displacement) and shot noise (phase fluctuations due to uncertainty in photon arrival times). Radiation pressure noise, negligible above 100 Hz, is largest at low frequencies, but is not yet the dominant source of noise there in Advanced LIGO-type detectors. At higher frequencies, shot noise is dominant. Increasing laser power reduces shot noise but increases radiation pressure noise. Increasing the test mass reduces radiation pressure noise. Laser power can be optimised to maximise sensitivity. Assuming amplitude and phase fluctuations from the vacuum fields are uncorrelated, it can be shown that a minimum noise floor is set by the Standard Quantum Limit (SQL) [86]. Groundbreaking work by Buonanno and Chen [87, 88] and Kimble *et al.* [89] showed that significant correlations can be built up through use of high laser power and a signal recycling cavity, which can then be used to reduce the noise floor across certain frequency domains. Tuning the detector configuration can then be used to optimise the frequency-dependent sensitivity for your favourite astrophysical source [82, 90–92].

In Chap. 8, we discuss the quantitative impact of mitigative techniques on the sensitivity of the prospective third-generation of ground-based detectors, focusing particularly on how different configurations affect the detectability of GWs from CCSNe.

Historical overview of ground-based GW interferometry

The first-generation of GW interferometric detectors comprised five observatories. Initial LIGO [93] was comprised of three interferometers; two detectors with 4 km arms in Hanford, WA and Livingston, LA (denoted H1 and L1, respectively), and second detector in Hanford, WA with 2 km arms (denoted H2). H2 was decommissioned in 2011 at the end of the initial LIGO observing runs. The Virgo detector (denoted V1) is an interferometer with 3 km arms located in Cascina, Italy [94]. GEO 600 (oft denoted G1) is an interferometer with 600 m arms located in Hanover, Germany [95]. The detector was augmented to improve high frequency sensitivity, thereafter known as GEO-HF [96]. TAMA 300 was an interferometer with 300 m arms located in Mitaka, Japan [97], before being decommissioned in preparation for construction of second-generation detector KAGRA.

Of the so-called second-generation of ground-based GW detectors, the two Advanced LIGO (aLIGO) detectors [98] began operation in late 2015 at approximately one-third of their final design sensitivity. Advanced Virgo (Ad-

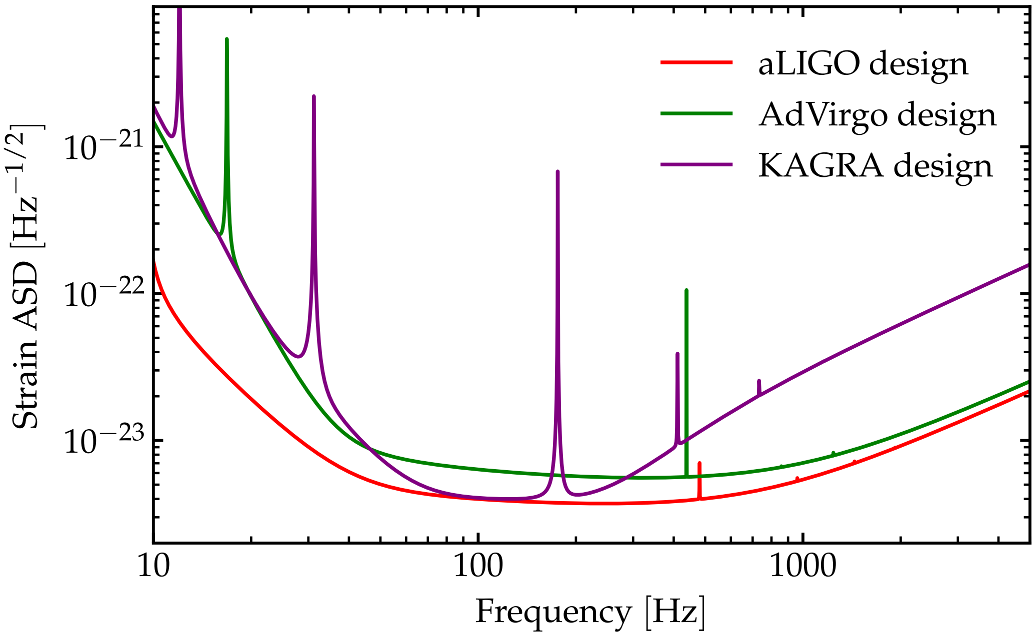

Figure 3.5: Amplitude spectral density (ASD) of the noise floor for Advanced LIGO (aLIGO), Advanced Virgo (AdVirgo), and KAGRA at design sensitivity.

Virgo) [94, 99] came online in August 2017, officially joining the O2 science run with the two aLIGO detectors.

KAGRA [100, 101], a detector with 3 km arms located deep in the Kamioka mine, first operated in an initial configuration with a Michelson interferometer in March 2016 [102]. Having undergone upgrades to its baseline design configuration, KAGRA will be cryogenically cooled to reduce thermal noise. KAGRA is due to start taking observational data alongside Advanced LIGO and Advanced Virgo for the O3 science run, scheduled to begin in April 2019.

LIGO India [103] is under construction, and may begin operations c. 2025.

In Fig. 3.6, we show the predicted timeline for observating runs O1 through O5 for aLIGO, AdVirgo, KAGRA, and LIGO India, employing the approximate run dates provided in Fig. 2 of [104].

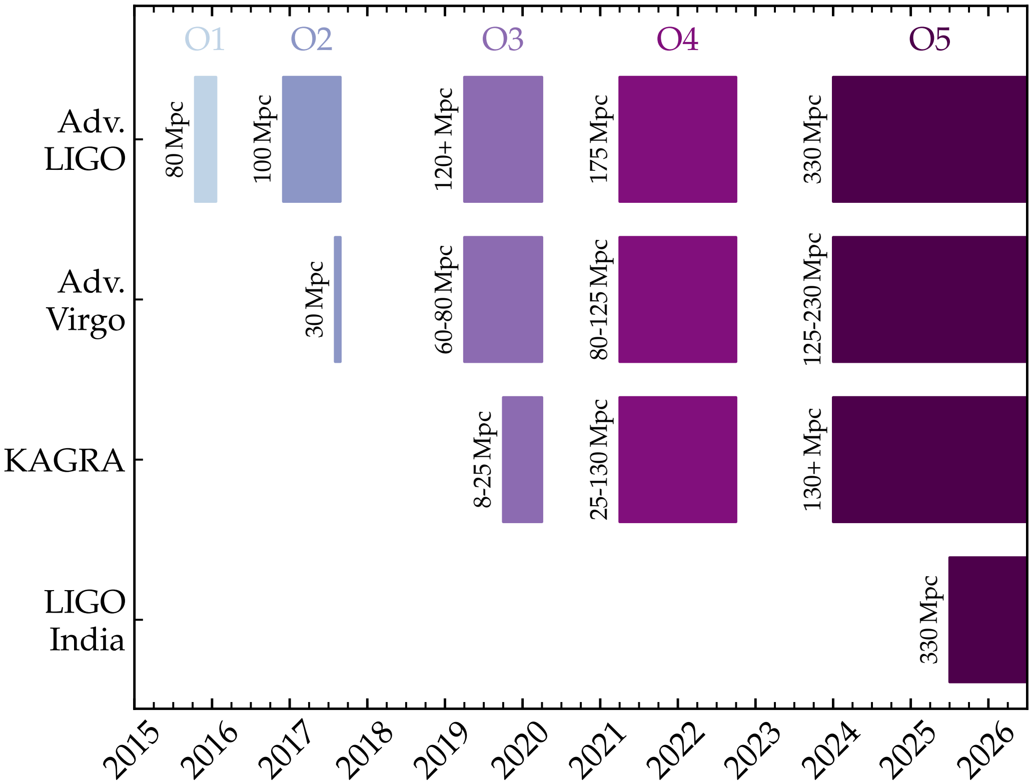

Figure 3.6: Timeline for observing runs O1 through O5 for aLIGO, AdVirgo, KAGRA, and LIGO India. For each observing run, the approximate sensitivity of the instruments is given in the context of the observational horizon distance for the coalescence of a canonical $1.4M_{\odot}$-$1.4M_{\odot}$ BNS system.

3.3 Neutrino detection

There exist numerous types of neutrino detectors, but all operate on the principle of detection of particles (be those photons, charge buildup, neutrons, etc to name a few) produced by interaction of detector material with incident neutrinos. In this Section, we provide the reader a brief overview of the four main types of detectors used to observe neutrinos from CCSNe, namely; liquid scintillator, water Cerenkov, liquid argon, and lead. We encourage the interested reader to peruse [105, 106] and references therein for further information.

Detector types

We discuss the principles of these four types of neutrino detector below.

Liquid scintillator

Large-mass scintillator detectors are typically comprised of large vats of hydrocarbons C_nH_{2n}, surrounded by photomultiplier tubes (PMTs). Photon emission from deexcitation of molecular energy levels signifies energy loss of charged particles. Interaction rates are dominated by inverse beta decay (IBD), with incoming anti-electron neutrinos captured on free protons;

$$\bar{\nu}_e + p \rightarrow e^+ + n\,. \tag{3.9}$$

Neutrons produced by IBD are thermalised and capture on free protons on a timescale of $\sim 200\,\mathrm{ms}$ [105];

$$n + p \rightarrow {}^2d + \gamma(2.2, \mathrm{MeV})\,. \tag{3.10}$$

Compton scattering of the the 2.2 MeV photon produced can be observed, as well as the production of two 0.511 MeV photons from positron annihilation. Detection efficiency can be improved by dissolving elements with a large cross-section to neutron capture (e.g., Galidonium; symbol Gd) in the scintillator. Positron production followed by delayed neutron capture is a clear signature of IBD.

Less prolific but still observable are neutrino interactions on carbon-12 (^{12}C). Neutral current excitation of ^{12}C prompts emission of a 15.1 MeV photon, which can be used to infer the total neutrino flux if the energy resolution of the detector is sufficient. Elastic scattering is also expected to contribute to the event rate at a low level.

Fine energy resolution and low background rates, characteristic of large-mass scintillator detectors, are achieved by collecting large numbers of photoelectrons. Interaction vertices can be reconstructed using photon arrival times, from which some directional information can be gleaned by separating sites of neutron capture and positron emission.

Water Cerenkov

Similar to hydrocarbons, water is rich with free protons. Huge detectors, comprised of vast homogeneous bodies of water with PMTs installed, are viable due to the relative inexpense of the fluid. Relativistic charged particles exceeding the speed of light in water emit Cerenkov radiation, which is then detected. Emitted in a characteristic cone with opening angle 42°, the Cerenkov ring pattern can be used to glean information on directionality of the neutrino source.

Interaction rates are dominated by IBD, but photon yields from these detectors are approximately 50 times smaller than for their liquid scintillator counterparts. Given index of refraction $n \sim 1.34$ for water, the Cerenkov thresholds for electrons and protons are 0.8 MeV and 1.4, GeV, respectively [105]. The mean energy of neutrinos from CCSNe is around a few tens of MeV, and so it is not suprising that protons created by neutrino capture on neutrons from CCSNe are not detectable here, and that detection efficiency is comparatively low. Interactions with oxygen nuclei can also contribute to the interaction rate, but detection efficiency is also low due to the Cerenkov threshold. Gd can be used to improve neutron tagging which is useful when considering signal components from each neutrino species, although some interactions with oxygen nuclei produce neutrons so it can lead to increased IBD false-alarms.

Another type of water Cerenkov detector employs arrays of long vertical strings of PMTs hung in ice. While designed to observe very high energy neutrinos (of order TeV and above), these detectors may be able to detect neutrinos from CCSNe should the background rate be reduced sufficiently. While unsuited for extracting spectral or directional information, large photon statistics means the temporal structure of the signal can be mapped with superior accuracy.

Liquid argon

Liquid argon detectors are predominantly large time projection chambers (TPCs), using an electric field to guide charged particles to wire planes where charge is collected and read out.

Unlike scintillation detectors and water Cerenkov detectors, liquid argon detectors are most sensitive to electron neutrinos. Interaction rates are dominated by neutrino capture on argon-40 (symbol ^{40}Ar);

$$\nu_e + {}^{40}\mathrm{Ar} \rightarrow e^- + {}^{40}\mathrm{K}^* \,, \tag{3.11}$$

which is tagged via photon emission as $^{40}\mathrm{K}^*$ deexcites. The charged current reaction with $\bar{\nu}_e$ also occurs;

$$\bar{\nu}_e + {}^{40}\mathrm{Ar} \rightarrow e^+ + {}^{40}\mathrm{Cl}^* \,, \tag{3.12}$$

which can be tagged by deexcitation of $^{40}\mathrm{Cl}^*$ and photons from positron annihilation. Neutral current reactions and elastic scattering of neutrinos occur on smaller scales.

Arrival times at the collection plane can be used to reconstruct detailed particle tracks, with position resolution set by the spacing of the wires. As $^{40}\mathrm{Ar}$ is prone to scintillation, PMT signals can be used to improve event localisation. Energy resolution is also good.

Lead

Interaction rates in lead ($^{A}\mathrm{Pb}$) detectors are dominated by electron-neutrino capture and scattering;

$$\nu_e + {}^{A}\mathrm{Pb} \rightarrow e^- + {}^{A}\mathrm{Bi}^* \,, \tag{3.13}$$

$$\nu_x + {}^{A}\mathrm{Pb} \rightarrow \nu_x + {}^{A}\mathrm{Pb}^* \,, \tag{3.14}$$

where the nuclei produced typically deexcite through emission of one or more neutrons. Pauli blocking due to the neutron-rich nature of $^{A}\mathrm{Pb}$ strongly suppresses $\bar{\nu}_e$ capture reactions.

The low cross-sections to neutron capture make $^{A}\mathrm{Pb}$ ideal for studying neutron production, as neutrons emitted will pass through the detector until reaching the neutron-sensitive sensor. The strong dependence of neutron ejection on neutrino energy allows for spectral information on the neutrino source to be inferred.

Overview of past and current neutrino detectors

Neutrinos from SN 1987A, a CCSN in the Large Magellanic Cloud (50 kpc from Earth) were observed by three detectors. Kamiokande-II, located deep in the Kamioka mine, is a Japanese water Cerenkov detector which operated between 1985 and 1990 [8], and the Irvine-Michigan-Brookhaven detector (IMB [9]; a water Cerenkov detector in Lake County, Ohio by the shore of

Lake Erie which took data between 1982-1991) detected 19 neutrino events over 13 seconds between them. The Baksan Neutrino Observatory (BNO; a scintillator detector located in the Baksan river gorge in the Russian Caucasus mountains, operational since 1986) also reported observations [107].

Most neutrino detectors operational today that are sensitive to CCSN neutrinos are liquid scintillators. The Large Volume Detector (LVD; a kiloton-scale experiment [108]) and Borexino (a smaller detector first built to study solar neutrinos [109]), both located in the Italian Gran Sasso laboratory, have been taking data since 1992 and 2009, respectively, while KamLAND (a kiloton-scale detector located in the Kamioka mine, Japan [110]) first came online in 2002. All these experiments are underground to greatly reduce background rates from cosmic-rays. Surface scintillator detectors are characterised by larger noise floors, but some are still expected to be able to observe neutrinos from nearby CCSNe. Of note are NOνa (a fifteen kiloton segmented detector at Fermilab near Chicago [111]) and Daya Bay (a sub-kiloton experiment in China [112]).

The most sensitive detector to CCSN neutrinos is Super-Kamiokande (Super-K), a 32 kiloton water Cerenkov detector in the Kamioka mine, Japan [113]. Approximately 8000 events are expected for a CCSN at 10 kpc, and Super-K will be able to detect neutrinos from a CCSN out to 100 kpc [113].

A long-string water Cerenkov detector, IceCube is a gigaton-scale experiment set into Antarctic ice [114]. While designed for the detection of TeV-scale neutrinos, IceCube will be able to detect CCSN neutrinos from a source in the LMC at 6σ confidence.

Other detectors of interest are HALO (a small-scale helium-lead detector at the SNOLAB in Canada [115]), and MicroBooNE (a surface liquid argon detector at Fermilab [116]).

A number of next-generation neutrino detectors have been proposed, which are discussed in Chap. 8.

Directionality

As the ground-based GW interferometers are antennae, their ability to localise a GW source without a priori information is poor. For neutrino detectors, the prospects for gleaning directionality from detection is dependent on the type of detector and the strength of the signal. Electron scattering, where the electron is knocked in the direction of neutrino propagation, is the most promising reaction for recovering source direction;

$$\nu_x + e^- \rightarrow \nu_x + e^- \,, \tag{3.15}$$

for which localisation to a cone with half-opening-angle $\Delta\theta \sim 25^\circ/\sqrt{N}$ (where N is the number of events) can be achieved in the absence of background noise.

Water Cerenkov detectors can use the shape of the Cerenkov ring to infer direction, but as electron scattering comprises just a small fraction of the expected events from a CCSN, the ability to reconstruct source location relies upon reducing the dominant (mostly isotropic) IBD signature through neutron tagging. For Super-K, localisation to $\sim 8^\circ$ for a CCSN at 10 kpc is expected, but this can be improved to $\sim 3^\circ$ by implementating optimised neutron tagging [117, 118]. Triangulation using timing information from multiple detectors can also be used to improve localisation [119].

4 Observational prospects in the advanced detector era

*If you're going to let one stupid p**** ruin your life, you're not the girl I thought you were.*

—Professor Stromwell, *Legally Blonde*

[1] S. E. Gossan, P. Sutton, A. Stuver, et al. Observing gravitational waves from core-collapse supernovae in the advanced detector era. Phys. Rev. D 93 (4), 042002 (2016).
SEG designed the observational study and ran the analysis, with crucial X-Pipeline expertise and support from PS. SEG produced all figures and wrote the majority of the manuscript text.

4.1 Motivation

The true dawn of transient multimessenger astronomy came with the joint EM and neutrino observations of SN 1987A [8, 9], a Type II-pec SN in the Large Magellanic Cloud (LMC), roughly 52 kpc from Earth [120]. While CCSNe are routinely observed across the EM spectrum out to great distances by astronomers, neutrinos from CCSNe have not been observed since that fateful day thirty-two years ago. The joint EM and GW observations of a binary neutron star merger, GW170817, marked a new era of multi-messenger astronomy with GWs [6, 10]. While GWs from CCSNe have yet to be observed, the promise of the next galactic CCSN has astronomers eager for the possibility of joint observations in GWs, EM, and neutrinos for the first time.

As introduced previously in Chap. 3, GW and neutrino observations of CCSNe offer unprecedented opportunities to directly observe the dynamics of the supernova central engine. While EM observations suggest that many, if not most, CCSN explosions exhibit asymmetric features (see, e.g., [121–125]), they originate far from the collapsed core, and can thus only provide second-hand information on the dynamics driving the explosion. This assertion is backed up by results of multidimensional CCSN simulations (see, e.g., [126–134] and references therein). It has been shown in previous studies that signatures of the PNS structure, composition, and angular momentum distribution are imprinted on the GW emission from core collapse (see, e.g., [135]), and indeed we later discuss opportunities to do so in Chap. 5 and Chap. 6 of this thesis. Before signal analysis can be done, however, one must first detect a signal; a decidedly non-trivial task.

Astronomers searching for short-duration GW transients emitted from CCSNe face multiple challenges. First and foremost, the expected event rate is incredibly low. Given realistic GW emission predictions from state-of-the-art simulations (see Chap. 3 for an overview), simple estimates of signal-to-noise ratio (SNR) suggest that the second-generation detectors currently online will be unable to detect GWs from CCSNe beyond the galaxy and Magellanic Clouds. We are long overdue for a galactic CCSN, but the best estimates of the CCSN rate in the Milky Way are just $(0.6-10.5)\times10^{-2}$ CCSNe/yr (see, e.g., [136–141]), while the combined CCSN rate in the Magellanic Clouds is $(1.9-4.0)\times10^{-3}$ CCSNe/yr [136, 138, 142]. Extending our attention to even the most speculative of GW emission models for CCSNe, similar SNR estimates predict detectability is limited to a few Mpc. Within the Local Group ($D \lesssim 3\,\mathrm{Mpc}$), the CCSN rate is $\sim 9\times10^{-2}$ CCSNe/yr, with major contributions from Andromeda (M31), Triangulum (M33), and the dwarf irregular galaxies IC 10, IC 1613, and NGC 6822 [136, 138, 143, 144]. External to this, the CCSN rate increases to ~ 0.15 CCSNe/yr within $D \sim 5\,\mathrm{Mpc}$, including IC 342, the M81 group, M83, and NGC 253 as significant contributors to the CCSN rate [81, 145–149]. Within $D = 10\,\mathrm{Mpc}$, the CCSN rate is ~ 0.47 CCSNe/yr, while it increases to ~ 2.1 CCSNe/yr within $D = 20\,\mathrm{Mpc}$ [145, 147–149].

Beyond a breathtakingly low event rate, the GW emission expected from CCSNe is decidedly uncertain. While it is expected that the GW signal is dominated by oscillations of the nascent PNS, said oscillations are thought to be excited by turbulent fluid downflows, convective plumes, and complex hydrodynamic instabilities striking the PNS. The unmistakably stochastic nature of these processes means that while modelling of GW emission frequencies may be reasonably robust, the phase evolution of the GW signal can neither be accurately predicted or accounted for by a single constant phase shift. This is problematic, because the optimal method for extracting signal from data (matched, or Weiner, filtering [150]) requires robust knowledge of the amplitude and phase evolution for the target signal. As such, this technique is not appropriate for the case at hand and cannot be used. The "excess-power" approach [151–153], an alternative method for extracting signals of uncertain morphology from noise, searches for statistically significant excesses of power in detector data across the time-frequency plane. It can be shown that, in the absence of any knowledge of the signal other than its duration and frequency bandwidth, the excess-power method is Neyman-Pearson optimal in the context of Gaussian noise [151]. While searches of this type for unmodelled GW transients must typically scan the entire GW detector data set for signals incident from any direction on the sky (e.g., [154, 155] and references therein), the coincident observation of an EM or neutrino counterpart can provide timing and/or sky position information to localize the prospective signal in time-frequency space (see, e.g., [156–158] and references therein). Prior information on the sky position, time of arrival, and polarisation of the targeted GW source can be exploited to reduce the noise background and, consequently, the detection false alarm rate. It has been shown that utilizing localisation information gleaned from external triggers can improve the sensitivity of such a search by up to a factor of ~ 2 [156, 159].

It is important to note, however, that excess-power searches typically require a signal to be coincidentally observed in two or more detectors. The duty cycle (fraction of time a detector is operating and taking science-quality data) is limited by several factors. In addition to commissioning work to improve detector sensitivity and stability, interference due to environmental noise is a concern. During Initial LIGO's fifth science run (S5) for example, which lasted almost two years between November 15 2005 through November 02 2007, the H1, H2, and L1 detectors had duty cycles of 75%, 76%, and 65%, respectively. The duty cycle for double coincidence (two or more detectors taking data simultaneously) was 60%, and the triple coincidence duty cycle was 54% [160, 161]. While resonant bar and sphere detectors provide limited backup [162–164], a larger network of detectors mitigates the risk of observing GWs from the next galactic CCSN in only one detector, or indeed none at all.

Even then, noise in GW detectors arises from a combination of instrumental, environmental, and anthropogenic noise sources that are extremely difficult to characterize precisely [82, 93, 165, 166] (see Sec. 3 for an overview of said noise sources). Non-Gaussianities such as instrumental "glitches" can lead to large excursions over the time-averaged noise and may mimic the expected time-frequency content of an astrophysical signal [93, 167]. While mitigation strategies against such noise artefacts include

1. Coincident observation with multiple, geographically separated detectors
2. Data quality monitoring and the recording of instrumental and environmental vetos derived from auxiliary data channels such as seismometers, magnetonometers, etc.
3. Glitch-detection strategies based on Bayesian inference (e.g., [168, 169]) or machine learning (e.g., [169, 170]),

the existence of glitchy data further reduces the viability of GW detection from CCSNe. This provides another reason why using external triggers from EM or neutrino observations to inform the temporal "on-source window" over which to search can reduce the probability of noise transients being present in the (shorter) time period searched. This, however, causes its own problems for GW searches employing ground-based detectors, as the sensitivity of searches over on-source windows much shorter than a sidereal day will be strongly dependent on the antenna response of the detectors to the source location at that particular GPS time.

Considering all these variables, it may seem at first that searching for GWs from CCSNe is an extremely challenging task. While undeniably so, the development of astrophysically-motivated search protocols can help in tackling this problem. The goal of this Chapter is to do just that; outline an astrophysically motivated search procedure for GWs from CCSNe, and investigate how the sensitivity of a three-detector network of second-generation ground-based GW detectors to GWs from CCSNe evolves from 2015 to 2019 for a variety of observational scenarios. The rest of this Chapter is organised as follows. In Sec. 4.2 we outline four observational scenarios considered for a nearby ($d < 5\,\mathrm{Mpc}$) CCSN. In Sec. 4.3, we summarise the GW emission models considered for this study, and discuss the data analysis procedures employed in Sec. 4.4. In Sec. 4.5, we explore the sensitivity of our search method for nearby CCSNe (within $\sim 100\,\mathrm{kpc}$, for which a neutrino trigger is expected) in the context of realistic GW emission models produced by multidimensional hydrodynamic simulations. In Sec. 4.6, we explore the prospects to observationally constrain speculative emission models associated with long GRBs for more distant CCSNe (out to a few Mpc, where only an EM transient is likely to be observed). To conclude, we discuss in Sec. 4.7 the implications of this study and future research directions.

4.2 Observational scenarios

In this section, we outline the particulars of different observational scenarios for which we aim to estimate the detectability of GWs from CCSNe.

Location of supernovae

As mentioned in Sec. 4.1, optimal SNR calculations suggest that detectability for the most realistic predictions for GW emission from CCSNe are limited to the Galaxy and Magellanic Clouds.

The Milky Way, a barred spiral galaxy, is home to our solar system. For the purposes of this study, we consider a hypothetical CCSN in the direction of the galactic center, at right ascension (RA) $17^{\mathrm{h}}47^{\mathrm{m}}21.5^{\mathrm{s}}$ and declination (Dec) $-5^{\circ}32^{'}9.6^{''}$ [171], located $\sim 9\,\mathrm{kpc}$ from Earth. This is motivated by the work of Adams *et al.* [141], in which the probability distribution for the distance of galactic CCSN from Earth is shown to peak around $\sim 9\,\mathrm{kpc}$, and the CCSN location distribution is assumed to trace the disk of the galaxy. Best estimates place the galactic CCSN rate between $(0.6-10.5)\times10^{-2}$ CCSNe/yr [141], and the youngest known galactic CCSN remnant, Cassiopeia A, is believed to be $\sim 330\,\mathrm{yrs}$ old [172].

The Large Magellanic Cloud (LMC) is home to the most active star-formation region in the Local Group, the Tarantula Nebula [173]. Located at RA $5^{\mathrm{h}}23^{\mathrm{m}}34.5^{\mathrm{s}}$ and Dec $-69^{\circ}45^{'}22^{''}$ [174], the LMC is an irregular galaxy located $\sim 50\,\mathrm{kpc}$

Galaxy name	(RA, Dec)	Distance [Mpc]	CCSN rate [10^{-2}/yr]	References
Milky Way	(266.42, -29.01)	0.01	0.6 – 10.5	[141]
LMC	(80.89, -69.76)	0.05	0.1 – 0.3	[136, 138, 174, 176]
M31	(10.69, 41.27)	0.77	0.2	[136, 138, 177, 178]
M82	(148.97, 69.68)	3.52	2.1 – 20	[180–183]

Table 4.1: Summary of the location (RA, Dec), distance, and host galaxy CCSN rate for the four hypothetical CCSNe.

from Earth [175, 176], and is estimated to have a CCSN rate of $(1.5 - 3.1) \times 10^{-3}$ CCSNe/yr [136, 138]. The last CCSN observed in the LMC was SN1987A, a type II-pec SN first detected on February 23, 1987, by Kamiokande II via its neutrino burst [8].

More speculative emission scenarios linked to more extreme core collapse events and long gamma-ray bursts (LGRBs) may be detectable out to a few Mpc. To this end, we consider hypothetical CCSNe in M31 and the more distant starburst galaxy M82 for which to estimate the detectability of these more uncertain models.

The M31 galaxy, Andromeda, is the most luminous galaxy in the Local Group. Located at RA $0^{h}42^{m}44.4^{s}$ and Dec $41°16'8.6''$ [177], M31 is a spiral galaxy whose distance is ~ 0.77 Mpc from Earth [178], and it is estimated to have a CCSN rate of $\sim 2.1 \times 10^{-3}$ CCSNe/yr [136, 138]. No CCSNe have yet been observed in M31.

The M82 galaxy, five times brighter than the Milky Way, exhibits starburst behaviour as a consequence of gravitational interaction with neighbouring galaxy M81 [179]. Located at RA $9^{h}55^{m}52.7^{s}$ and Dec $69°40'46''$ [180], M82 is an irregular starburst galaxy at a distance ~ 3.52 Mpc from Earth [181]. Its CCSN rate is estimated to be $\sim (2.1 - 20) \times 10^{-2}$ CCSNe/yr [182, 183]. While the most recent CCSN in M82 was SN2008iz, a Type II SN first observed on May 3, 2008 [184], the recent Type Ia SN named SN2014J was also located in M82 (see, e.g., [185, 186]).

We summarise the relevant information on the Milky Way, LMC, M31, and M82 in Table 4.1.

Analysis times

For CCSNe within $\sim 100\,\text{kpc}$, the neutrino burst originating from the shock breaking out through the neutrinosphere is expected to be detectable (see Chap. 3 for an in-depth discussion). The SuperNova Early Warning System (SNEWS) [187] Collaboration aims to provide a rapid alert for a nearby CCSN to the astronomical community, as triggered by neutrino observations. Pagliaroli *et al.* [188] were the first to make quantitative statements on the use of neutrino detection from CCSNe as external triggers for an associated GW search, in the context of an analytical approximation for the anti-electron neutrino luminosity, $L_{\bar{\nu}_e}$, as a function of time. More realistic models for L_ν (see, e.g. [77, 189]) suggest that over $\sim 95\%$ of the total energy in neutrinos is emitted within $\sim 10\,\text{s}$ of core bounce. Given the neutrino observation time, t_0, we consider a 60 s on-source window, aligned $[-10, 50]$ s about t_0 for our hypothetical SNe in the galactic plane and LMC. We note that a more detailed neutrino light curve will allow the time of core bounce to be localized to $\sim$ few ms [190]. This would permit the use of a much shorter on-source window, resulting in a lower background rate and higher detection sensitivity.

For CCSNe beyond $\sim 0.5\,\text{Mpc}$, it is unlikely a neutrino signature will be detected. An EM counterpart, however, will likely be observed. The on-source window derived from the EM observation time is dependent on characteristics of the progenitor star (i.e. radius, shock velocity), as well as the observational cadence on the host galaxy. The first EM signature of a CCSN comes at the time of shock breakout, t_{SB}, when the shock breaks through the stellar envelope.

Compact CCSN progenitors with stellar radii of $R_* \sim$ few $(1 - 10)R_\odot$ (i.e. Type Ib/Ic SN progenitors) have been stripped of their stellar envelopes through either intense stellar winds (i.e. Wolf-Rayet stars), or mass transfer to a binary companion [80, 191]. Li [192] studied the properties of shock breakout for a variety of type Ibc SN progenitor models in the context of semianalytic density profiles and found shock breakout times in the range $t_{\text{SB}} \in [1, 35]$ s. As a conservative estimate, we choose $t_{\text{SB,min}} = 60\,\text{s}$.

For type II SNe, however, their supergiant progenitors are much more extended. Type II-pec SNe, such as SN1987A, have blue supergiant progen-

Galaxy name	Observational counterpart	Minimal on-source window [s]	Maximal on-source window [s]
Milky Way	Neutrino, EM	n/a	[-10,+50]
LMC	Neutrino, EM	n/a	[-10,+50]
M31	EM	[-60,+3600]	[-180000,+3600]
M82	EM	[-60,+86400]	[-180000,+86400]

Table 4.2: Summary of the observational counterpart used to derive the on-source window, in addition to the associated on-source window, for the four hypothetical CCSNe considered.

itors, with typical stellar radii of $\sim 25\,R_\odot$. More typically, the progenitors are red supergiant stars, with typical stellar radii of $\sim$ (100-1000) $R_\odot$ [80, 191]. While theoretical shock breakout times for these progenitors are typically of order a few hours, observed breakout times have been significantly longer [193, 194]. As a conservative estimate, we employ $t_{\mathrm{SB,max}} = 50\,\mathrm{h}$, based upon consideration of the unstripped Type II-P progenitor from the hydrodynamic simulations performed by Morozova *et al.* [195], and use $t_{\mathrm{SB,max}} = 50\,\mathrm{h}$.

Beyond theoretical predictions of the time to shock breakout, the observational cadence of observations of the CCSN host galaxy must be considered when deriving the on-source window. For actively observed galaxies, we expect to have no greater than $\sim$ 24 h latency between pre- and post-CCSN observations. We consider two observational scenarios in which the time scale between pre- and post-CCSN images are $t_{\mathrm{obs}} \sim 1\,\mathrm{h}$ and 24 h, for sources in M31 and M82, respectively. We construct the on-source window assuming that shock breakout occurs immediately after the last pre-SN image. Given the time of the last pre-SN observation, the EM trigger time t_0, we consider an on-source window of length $t_{\mathrm{SB}} + t_{\mathrm{obs}}$, aligned $[-t_{\mathrm{SB}}, t_{\mathrm{obs}}]$ about t_0.

We summarize the on-source windows used for all observational scenarios considered in Table 4.2.

As briefly touched upon in Sec. 4.1, the antenna response of the detector network to a particular location on the galactic sphere is a function of time, with variability characterised by period one sidereal day. While the on-source windows we consider for a hypothetical CCSN in M82 exceed this timescale, those employed for CCSNe in the Milky Way, LMC, and the shorter on-source window in M31 do not. For representative purposes, we wish to choose a central trigger time t_0 for which the antenna sensitivity is approxi-

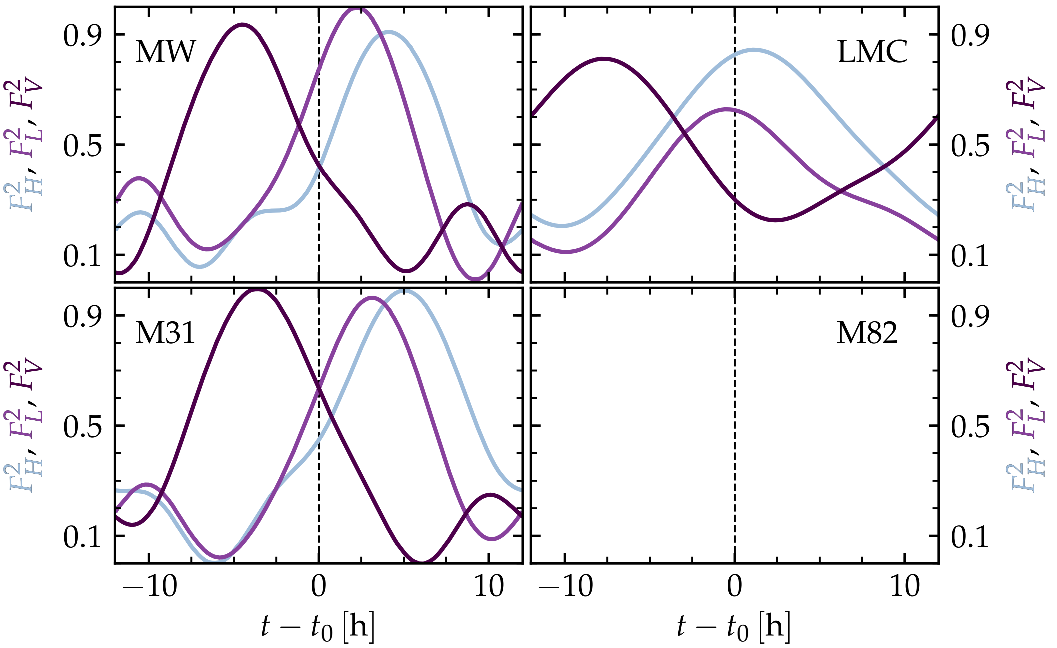

Figure 4.1: The sum-squared antenna response $F^2 = F_+^2 + F_\times^2$ over one mean sidereal day for the two Advanced LIGO detectors (H,L), and the Advanced Virgo detector, V, for sources located toward the Galactic center (top left), LMC (top right), M31 (bottom left), and M82 (bottom right). For each galaxy, we indicate the chosen GPS trigger time t_0 with a dashed black line.

mately average over the time variability for a given sky location. In Fig. 4.1, we show the sum-squared antenna response for each detector over one sidereal day for sources located at the Galactic center, LMC, and M31.

To our end of representing the time-averaged sensitivity of the detector network, we choose GPS trigger times of $t_0 = 871645255$, $t_0 = 871784200$, and $t_0 = 871623913$ for the Galactic, LMC, and M31 sources, respectively. As mentioned previously, the on-source windows considered for M82 are greater than a sidereal day, and thus the particular trigger time is less important from an antenna response standpoint. For practical purposes, we choose GPS trigger time $t_0 = 871639563$ for the M82 source, such that the 74 h on-source window is covered by the 100 h stretch of S5 data recolored for this study.

Detector networks

As mentioned previously, the GW detector noise will be non-Gaussian and nonstationary. To this end, we use real GW data from the fifth LIGO science run (S5) and the first Virgo science run (VSR1), recolored to the target noise amplitude spectra densities (ASDs)[1]. for the considered observational scenarios. See Sec. 4.4 for technical details on the recoloring procedure used.

We consider a subset of the observing scenarios outlined in Aasi *et al.* [166] to explore how the sensitivity of the Advanced detectors to CCSNe will evolve between 2015 and 2019. For all these cases, we characterize the detector sensitivity by the single-detector binary neutron star (BNS) range, d_{R}. The BNS range is the standard figure of merit for detector performance, and is defined as the sky location- and orientation-averaged distance at which a $(1.4, 1.4)\, M_{\odot}$ BNS system can be detected with an SNR, $\rho \geq 8$. The 2015 scenario assumes a two-detector network comprised of the two Advanced LIGO detectors (H,L) operating with BNS range $d_{\mathrm{R;HL}} = 54\,\mathrm{Mpc}$ and is hereafter referred to as the `HL 2015` scenario. The 2017 scenario assumes a three-detector network comprised of the two Advanced LIGO detectors (H,L) operating with BNS range $d_{\mathrm{R;HL}} = 108\,\mathrm{Mpc}$, and the Advanced Virgo detector operating with BNS range of $d_{\mathrm{R;V}} = 36\,\mathrm{Mpc}$, and is hereafter referred to as the `HLV 2017` scenario. In 2019, we consider a three-detector network, HLV, with the two Advanced LIGO detectors operating with BNS range $d_{\mathrm{R;HL}} = 199\,\mathrm{Mpc}$, and the Advanced Virgo detector operating with BNS range $d_{\mathrm{R;V}} = 154\,\mathrm{Mpc}$, referred to as the `HLV 2019` observational scenario [99, 166]. Fig. 4.2 shows the one-sided ASDs $\sqrt{S_h(f)}$ of Advanced LIGO and Advanced Virgo as used to recolor the data for each observational scenario considered.

4.3 Gravitational waveforms

As we discussed in more detail in Chap. 3, a broad range of multidimensional hydrodynamic processes may contribute to GW emission during core collapse and the subsequent evolution of the nascent PNS. Most GW emission from CCSNe lies in the most sensitive frequency band of ground-based GW detectors ($\sim 50-1000\,\mathrm{Hz}$). Notable exceptions are black hole formation

---

[1] The one-sided amplitude spectral density is the square root of the one-sided power spectral density, $S_h(f)$.

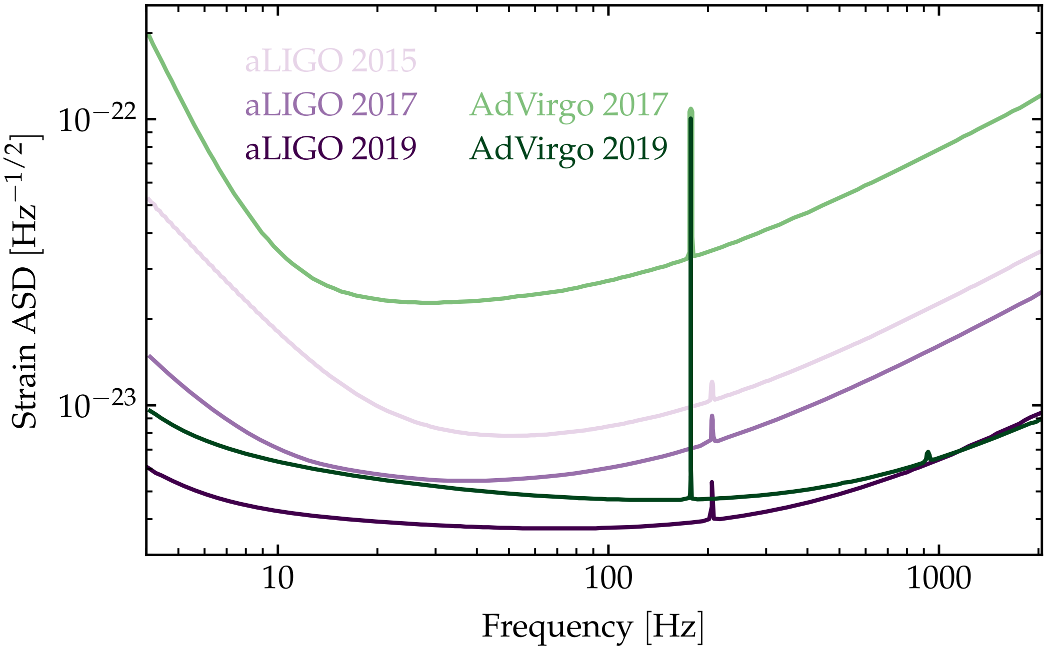

Figure 4.2: The predicted strain noise ASDs $\sqrt{S_h(f)}$ for the Advanced LIGO (aLIGO) and Advanced Virgo (AdVirgo) detectors in the context of the `HL 2015`, `HLV 2017`, and `HLV 2019` networks considered.

($f_{\mathrm{peak}} \sim$ few kHz), asymmetric neutrino emission, and asymmetric outflows ($f_{\mathrm{peak}} \lesssim 10\,\mathrm{Hz}$), which are not considered here.

For the purpose of this study, we consider a representative sample of GW waveforms from two-dimensional (2D) and three-dimensional (3D) CCSN simulations discussed in Chap. 3. For clarity, we note that we refer to these waveforms as numerical waveforms in the following. In addition, we draw a sample of analytical phenomenological waveforms for emission from more speculative scenarios, with the goal of establishing the degree to which we may constrain extreme GW emission models given more distant CCSNe.

In Tables 4.3 and 4.4, we summarize key properties of the selected numerical and phenomenological waveforms, respectively, including the total energy emitted in GWs, E_{GW}, the angle-averaged root-sum-squared GW strain, $\langle h_{\mathrm{rss}} \rangle$, and the peak GW frequency, f_{peak}. We define f_{peak} as the frequency at which the spectral energy density in GWs, $\mathrm{d}E_{\mathrm{GW}}/\mathrm{d}f$, peaks. We compute E_{GW} as in [20] from the spectral GW energy density $\mathrm{d}E_{\mathrm{GW}}/\mathrm{d}f$;

$$E_{\mathrm{GW}} = \int_0^{\infty} \mathrm{d}f\, \frac{\mathrm{d}E_{\mathrm{GW}}}{\mathrm{d}f}\,, \tag{4.1}$$

where

$$\frac{\mathrm{d}E_{\mathrm{GW}}}{\mathrm{d}f} = \frac{2}{5}\frac{G}{c^5}\left(2\pi f\right)^2 \left|\tilde{\ddot{I}}_{jk}\right|^2 , \tag{4.2}$$

and

$$\tilde{\ddot{I}}_{jk}(f) = \int_{-\infty}^{\infty} \mathrm{d}t\, \ddot{I}_{jk}(t)\, e^{-2\pi i f t} , \tag{4.3}$$

is the Fourier transform of $\ddot{I}_{jk}(t)$, the second time derivative of the mass-quadrupole tensor in the transverse-traceless gauge.

To construct the strain for different internal source orientations, we present the projection of GW modes, $H_{lm}(t)$, onto the -2 spin-weighted spherical harmonic basis, ${}^{-2}Y_{\ell m}\left(\iota, \phi\right)$ [196]. Using this, we may write

$$h_+ - i h_\times = \frac{1}{D} \sum_{l=2}^{\infty} \sum_{m=-l}^{l} H_{lm}(t)\, {}^{-2}Y_{\ell m}\left(\iota, \phi\right) , \tag{4.4}$$

where (ι, ϕ) are the internal source angles describing orientation. For the numerical waveforms considered here, the quadrupole approximation (see Chap. 2 for a discussion as pertains to the validity of this approximation with respect to CCSN simulations) is used to estimate the GW emission. The mode expansion here, considering only $\ell = 2$, can be constructed using

$$\begin{aligned} H_{20}^{\mathrm{quad}} &= \sqrt{\frac{32\pi}{15}} \frac{G}{c^4} \left(\ddot{I}_{zz} - \frac{1}{2}\left(\ddot{I}_{xx} + \ddot{I}_{yy}\right)\right) , \\ H_{2\pm1}^{\mathrm{quad}} &= \sqrt{\frac{16\pi}{5}} \frac{G}{c^4} \left(\mp \ddot{I}_{xz} + i \ddot{I}_{yz}\right) , \\ H_{2\pm2}^{\mathrm{quad}} &= \sqrt{\frac{4\pi}{5}} \frac{G}{c^4} \left(\ddot{I}_{xx} - \ddot{I}_{yy} \mp 2i \ddot{I}_{xy}\right) , \end{aligned} \tag{4.5}$$

and

$$\begin{aligned} {}^{-2}Y_{20} &= \sqrt{\frac{15}{32\pi}} \sin^2 \iota , \\ {}^{-2}Y_{2\pm1} &= \sqrt{\frac{5}{16\pi}} \sin \iota \left(1 \pm \cos \iota\right) e^{\pm i \phi} , \\ {}^{-2}Y_{2\pm2} &= \sqrt{\frac{5}{64\pi}} \left(1 \pm \cos \iota\right)^2 e^{\pm 2 i \phi} . \end{aligned} \tag{4.6}$$

The root-sum-square strain, h_{rss}, is defined as

$$h_{\mathrm{rss}} = \left[\int_{-\infty}^{\infty} \mathrm{d}t \left[h_+^2(t; \iota, \phi) + h_\times^2(t; \iota, \phi) \right] \right]^{1/2} , \tag{4.7}$$

which can be analytically averaged over source angles using

$$\langle h_{\mathrm{rss}} \rangle = \iint \mathrm{d}\Omega \, h_{\mathrm{rss}} \, , \tag{4.8}$$

to obtain

$$\langle h_{\mathrm{rss}} \rangle = \frac{G}{c^4} \frac{1}{D} \left[\frac{8}{15} \int_{-\infty}^{\infty} \mathrm{d}t \left[\ddot{I}_{xx}^2 + \ddot{I}_{yy}^2 + \ddot{I}_{zz}^2 - \right.\right.$$
$$\left.\left. (\ddot{I}_{xx}\ddot{I}_{yy} + \ddot{I}_{xx}\ddot{I}_{zz} + \ddot{I}_{yy}\ddot{I}_{zz}) + 3 \left(\ddot{I}_{xy}^2 + \ddot{I}_{xz}^2 + \ddot{I}_{yz}^2 \right) \right] \right]^{1/2} . \tag{4.9}$$

Numerical waveforms

Gravitational waves from convection and SASI

We draw sample waveforms for GWs from nonrotating core collapse from three numerical studies [46, 128, 197]. Yakunin *et al.*[46] performed 2D simulations of neutrino-driven CCSNe. We choose a waveform obtained from the simulation of a 15 $M_{\odot}$ progenitor star (referred to as `yak` in the following). Due to axisymmetry, the extracted waveform is linearly polarized. Müller *et al.* [197] performed 3D simulations of neutrino-driven CCSNe with a number of approximations to make the simulations computationally feasible. Importantly, they started their simulations after core bounce and assumed a time-varying inner boundary, cutting out much of the PNS. Prompt and PNS convection do not contribute to their waveforms, and higher frequency GW emission is suppressed due to the artificial inner boundary. As the simulations are 3D, the waveforms produced by this study have two polarizations. We use waveform models L15-3, W15-4 (two different 15 $M_{\odot}$ progenitors), and N20-2 (a 20 $M_{\odot}$ progenitor), to which we hereafter as `müller1`, `müller3`, and `müller2`, respectively. Ott *et al.* performed 3D simulations of neutrino-driven CCSNe. The simulations are general-relativistic and incorporate a three-species neutrino leakage scheme. We employ the GW waveform from model $s27f_{\mathrm{heat}}1.05$ (a 27 $M_{\odot}$ progenitor), which we hereafter refer to as `ott`. We plot the GW signal for the `ott` model in the top panel of Fig. 4.3, and summarise properties of these waveforms in Tab. 4.3.

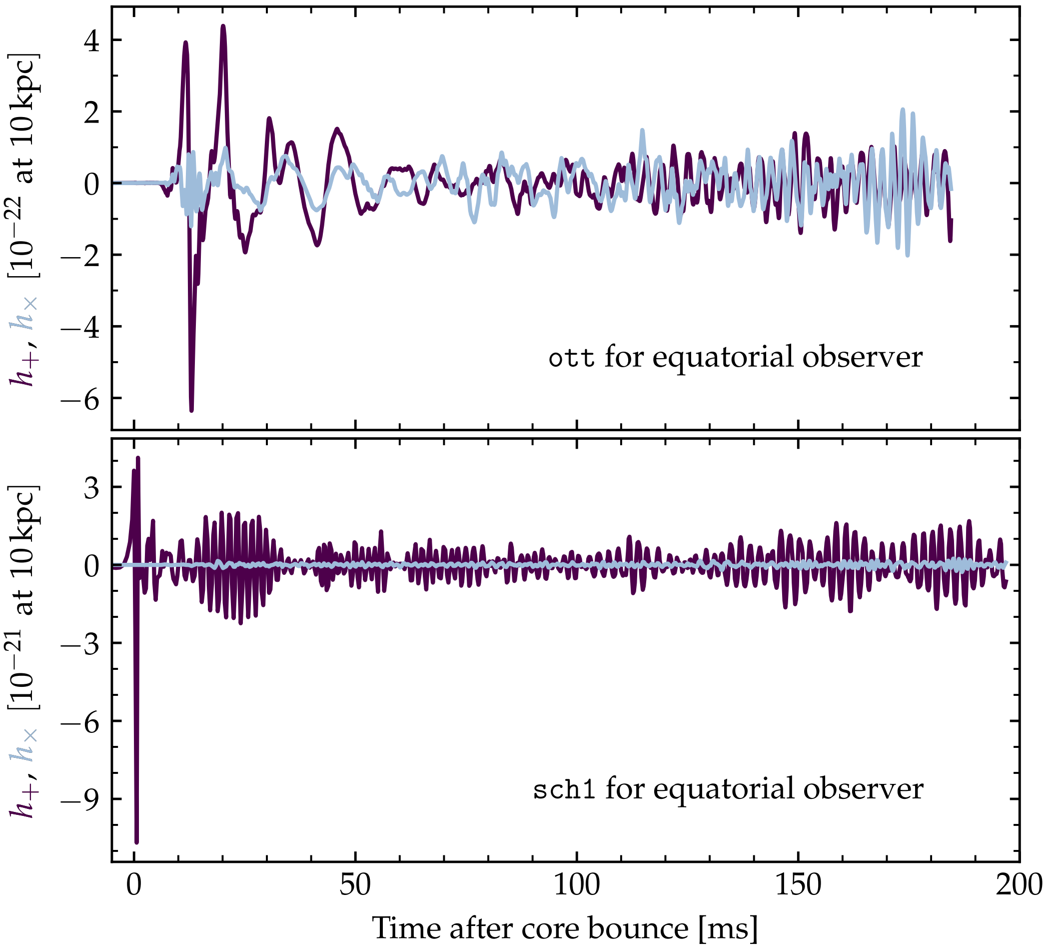

Figure 4.3: The time domain GW strain for representative models of CCSNe from non-rotating and rapidly rotating progenitor cores (`ott` in the top panel, and `sch1` in the bottom panel, respectively) as seen by an equatorial ($\iota = \pi/2$; $\phi = 0$) observer at 10 kpc. We note that the typical GW strain from rotating core collapse is roughly an order of magnitude larger than the typical GW strain from neutrino-driven explosions. In addition, the typical GW signal duration of bounce and ringdown of the PNS is $\sim$ few 10 ms, compared to the typical GW signal duration of $\sim$ few 100 ms for neutrino-driven explosions. Nonaxisymmetric rotational instabilities, however, may persist for a few hundreds of milliseconds.

Waveform name	$\langle h_{\rm rss} \rangle$ [10^{-22} at 10 kpc]	$f_{\rm peak}$ [Hz]	$E_{\rm GW}$ [$M_\odot c^2$]	Ref.
`yak`	1.89	888	9.08×10^{-9}	[46]
`müller1`	1.66	150	3.74×10^{-11}	[197]
`müller2`	3.85	176	4.37×10^{-11}	[197]
`müller3`	1.09	204	3.25×10^{-11}	[197]
`ott`	0.24	1019	7.34×10^{-10}	[128]
`dim1`	1.05	774	7.69×10^{-9}	[52]
`dim2`	1.80	753	2.79×10^{-8}	[52]
`dim3`	2.69	237	1.38×10^{-9}	[52]
`sch1`	5.14	465	2.25×10^{-7}	[65]
`sch2`	5.80	700	4.02×10^{-7}	[65]

Table 4.3: Key characteristics of waveforms from multidimensional CCSN simulations considered for this study. $E_{\rm GW}$ is the energy emitted in GWs, $\langle h_{\rm rss} \rangle$ is the angle-averaged root-sum-square strain, and $f_{\rm peak}$ is the frequency at which the spectral GW energy $dE_{\rm GW}/df$ peaks.

Gravitational waves from rotating core collapse and bounce

We draw three sample waveforms from the axisymmetric general-relativistic (conformally flat) simulations of Dimmelmeier *et al.* [52], all of which employed a $15\,M_\odot$ progenitor star and the Lattimer-Swesty EOS [198]. The three linearly polarized waveforms chosen differ primarily by their initial rotation rate and angular momentum distribution. Explicitly, we choose models s15A2O05-ls, s15A2O09-ls, and s15A3O15-ls (so named in [52]), which we hereafter refer to as `dim1` through `dim3`. For the purposes of including GWs from nonaxisymmetric rotational instabilities, we choose two sample waveforms from the 3D Newtonian, magnetohydrodynamical simulations of Scheidegger *et al.* [65], which use a neutrino leakage scheme. All were performed with a $15\,M_\odot$ progenitor star, and the Lattimer-Swesty EOS [198]. Due to the 3D nature of the simulations, the Scheidegger *et al.* waveforms have two polarizations. We employ waveforms for models R3E1AC$_{\rm L}$ and R4E1FC$_{\rm L}$ (so named in [65]), which we hereafter refer to as `sch1` and `sch2`, respectively. In the bottom panel of Fig. 4.3, we show the time-domain strain for the `sch1` model. We summarise the properties of the waveforms introduced in this subsection in Tab. 4.3.

Phenomenological waveforms

Gravitational waves from long-lived rotational instabilities

PNSs with ratio of rotational kinetic energy T to gravitational energy $|W|$, $\beta = T/|W| \gtrsim$ 25-27% become dynamically unstable to nonaxisymmetric deformation (with primarily $m = 2$ bar shape). If $\beta \gtrsim 14\%$, an instability may grow on a secular (viscous, GW backreaction) time scale, which may be seconds in PNSs (e.g., [199]). Furthermore, PNSs are born differentially rotating (e.g., [200]) and may thus be subject to a dynamical shear instability driving nonaxisymmetric deformations that are of smaller magnitude than in the classical instabilities, but are likely to set in at much lower β. Since this instability operates on differential rotation, it may last for as long as accretion maintains sufficient differential rotation in the outer PNS (e.g., [19, 64–66, 201, 202] and references therein).

For simplicity, we assume that the net result of all these instabilities is a bar deformation, whose GW emission we model in the Newtonian quadrupole approximation for a cylinder of length l, radius r and mass M in the x-y plane, rotating about the z axis. We neglect spin-down via GW backreaction. The second time derivative of the bar's reduced mass-quadrupole tensor is given by

$$\ddot{I}_{jk} = \frac{1}{6} M (l^2 - 3r^2)\, \Omega^2 \begin{pmatrix} -\cos 2\Omega t & \sin 2\Omega t \\ \sin 2\Omega t & \cos 2\Omega t \end{pmatrix} , \tag{4.10}$$

where $\Omega = 2\pi f$ is the angular velocity of the bar (see, e.g., [203] for details). The GW signal can then be estimated using the quadrupole formula [196, 204].

We generate representative analytic bar waveforms by fixing the bar length to 60 km, its radius to 10 km and varying the mass in the deformation M, the spin frequency f, and duration of the bar mode instability Δt. In practice, we scale the waveforms with a Gaussian envelope $\propto \exp(-(t-\Delta t)^2/(\Delta t/4)^2)$ to obtain nearly zero amplitudes at start and end of the waveforms, resulting in waveforms of sine-Gaussian morphology. In this study, we consider three bars of mass $M = 0.2\, M_\odot$, with $(f, \Delta t) = (400\,\mathrm{Hz}, 0.1\,\mathrm{s})$, $(400\,\mathrm{Hz}, 1\,\mathrm{s})$, and $(800\,\mathrm{Hz}, 0.1\,\mathrm{s})$ (hereafter referred to as `longbar1`, `longbar2`, and `longbar3`, respectively), and three bars of mass $M = 1\, M_\odot$ with $(f, \Delta t) = (400\,\mathrm{Hz}, 0.1\,\mathrm{s})$,

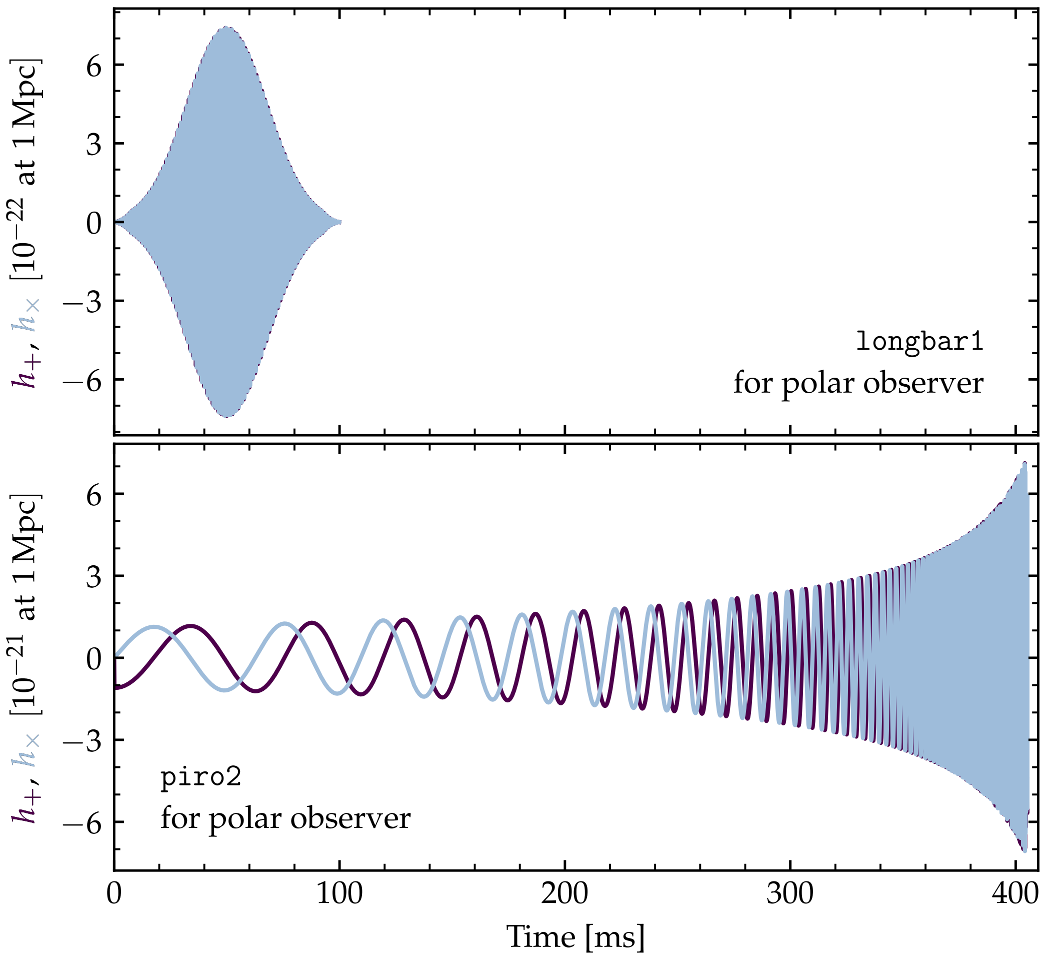

Figure 4.4: Time domain GW strain for representative models of bar-mode instability (`longbar1`; top panel) and disk fragmentation instability (`piro2`; bottom panel), as seen by a polar ($\iota = 0$; $\phi = 0$) observer at 1 Mpc.

(400 Hz, 1 s), and (800 Hz, 0.025 s) (hereafter referred to as `longbar4` through `longbar6`, respectively). We choose these parameters to explore the regime of strong bar-mode GW emission with the constraint that the strongest signal must emit less energy than is available in collapse, $E_{\mathrm{GW}} \lesssim 0.15 M_\odot c^2$. Values of $\langle h_{\mathrm{rss}} \rangle$, f_{peak}, and E_{GW} for the six representative waveforms used in this study are shown in Table 4.4, and the time-domain strain seen by a polar observer at 1 Mpc for model `longbar1` is shown in the top panel of Fig. 4.4

Disk fragmentation instability

If the CCSN mechanism fails to reenergize the stalled shock (see, e.g., [205]), the PNS will collapse to a BH on a time scale set by the accretion rate (e.g., [68]). Provided sufficient angular momentum, a massive self-gravitating accretion disk/torus may form around the nascent stellar-mass black hole with mass $M_{\rm BH}$. This scenario may lead to a collapsar-type GRB or an engine-driven SN [206].

The inner regions of the disk are geometrically thin due to efficient neutrino cooling, but outer regions are thick and may be gravitationally unstable to fragmentation at large radii [207, 208]. We follow work by Piro and Pfahl [207], and consider the case in which a single gravitationally bound fragment forms in the disk and collapses to a low-mass neutron star with $M_f \sim 0.1 - 1 M_\odot \ll M_{\rm BH}$. We then obtain the predicted GW signal using Eq. (4.5) [196, 204], assuming the fragment is orbiting in the (x-y)-plane, such that

$$\ddot{I}_{jk} = 2\frac{M_{\rm BH} M_f}{(M_{\rm BH} + M_f)} r^2\,\Omega^2 \begin{pmatrix} -\cos 2\Omega t & -\sin 2\Omega t \\ -\sin 2\Omega t & \cos 2\Omega t \end{pmatrix} . \tag{4.11}$$

For more technical details, including the waveform generation code, we direct the reader to [207, 209]. We consider waveforms from four example systems with $(M_{\rm BH}, M_f) = (5\,M_\odot, 0.07\,M_\odot)$, $(5\,M_\odot, 0.58\,M_\odot)$, $(10\,M_\odot, 0.14\,M_\odot)$, and $(10\,M_\odot, 1.15\,M_\odot)$ (hereafter denoted `piro1`, `piro2`, `piro3`, and `piro4`, respectively). Values of $\langle h_{\rm rss} \rangle$, $f_{\rm peak}$, and $E_{\rm GW}$ for the four representative waveforms used in this study are shown in Table 4.4, and the time domain strain seen by a polar observer at 1 Mpc for `piro2` is shown in the bottom panel of Fig. 4.4.

Ad hoc signal models

It is possible that there are GW emission mechanisms from CCSNe that we have not considered. In this case, it is instructive to determine the sensitivity of our GW search to short, localized bursts of GWs in time-frequency space. For this reason, we include *ad-hoc* signal models in our signal injections, in addition to the aforementioned physically motivated signal models. We take motivation from the all-sky, all-time searches for GW bursts performed in

Waveform name	$\langle h_{\mathrm{rss}} \rangle$ [10^{-20} at 10 kpc]	f_{peak} [Hz]	E_{GW} [$M_{\odot} c^2$]	Ref.
`longbar1`	1.48	800	2.98×10^{-4}	[203]
`longbar2`	4.68	800	2.98×10^{-3}	[203]
`longbar3`	5.92	1600	1.90×10^{-2}	[203]
`longbar4`	7.40	800	7.46×10^{-3}	[203]
`longbar5`	23.41	800	7.45×10^{-2}	[203]
`longbar6`	14.78	1600	1.18×10^{-1}	[203]
`piro1`	2.55	2035	6.77×10^{-4}	[207]
`piro2`	9.94	1987	1.03×10^{-2}	[207]
`piro3`	7.21	2033	4.99×10^{-3}	[207]
`piro4`	28.08	2041	7.45×10^{-2}	[207]

Table 4.4: Key characteristics of the considered waveforms from phenomenological models. E_{GW} is the energy emitted in GWs, $\langle h_{\mathrm{rss}} \rangle$ is the angle-averaged root-sum-square strain, and f_{peak} is the frequency at which the spectral GW energy density $\mathrm{d}E_{\mathrm{GW}}/\mathrm{d}f$ peaks.

the intial detector era [154, 210], and consider linearly and elliptically polarized sine-Gaussian GW bursts. Characterized by central frequency, f_0, and quality factor, Q, the strain is given by

$$\begin{aligned} h_+(t) &= A\left(\frac{1+\alpha^2}{2}\right)\exp(-2\pi f_0^2 t^2/Q^2)\sin(2\pi f_0 t)\,, \\ h_\times(t) &= A\alpha\exp(-2\pi f_0^2 t^2/Q^2)\cos(2\pi f_0 t)\,, \end{aligned} \tag{4.12}$$

where A is some common scale factor, and α is the ellipticity, where $\alpha = 0$ and 1 for linearly and circularly polarized waveforms respectively. Assuming isotropic energy emission, we may compute the energy in GWs associated with a sine-Gaussian burst as

$$E_{\mathrm{GW}} = \frac{\pi^2 c^3}{G} d^2 f_0^2 h_{\mathrm{rss}}^2\,, \tag{4.13}$$

where d is the distance at which h_{rss} is computed. In Table 4.5, we list the f_0, Q, and α values for all sine-Gaussian waveforms considered in this study.

4.4 Analysis procedure

X-Pipeline: A search algorithm for gravitational wave bursts

`X-Pipeline` is a coherent analysis pipeline used to search for GW transient events associated with CCSNe and GRBs, which has a number of features

Model Name	f_0 [Hz]	Q	α
`sglin1,sgel1`	70	3	0,1
`sglin2,sgel2`	70	9	0,1
`sglin3,sgel3`	70	100	0,1
`sglin4,sgel4`	100	9	0,1
`sglin5,sgel5`	153	9	0,1
`sglin6,sgel6`	235	3	0,1
`sglin7,sgel7`	235	9	0,1
`sglin8,sgel8`	235	100	0,1
`sglin9,sgel9`	361	9	0,1
`sglin10,sgel10`	554	9	0,1
`sglin11,sgel11`	849	3	0,1
`sglin12,sgel12`	849	9	0,1
`sglin13,sgel13`	849	100	0,1
`sglin14,sgel14`	1053	9	0,1
`sglin15,sgel15`	1304	9	0,1

Table 4.5: Key characteristics of the *ad-hoc* sine-Gaussian waveforms employed in this study. f_0 is the central frequency, Q is the quality factor, and α is the ellipticity. See Eq. (4.12) in Sec. 4.3 for details.

designed specifically to address the challenges associated with searching for unmodelled, short-duration GW transients. For example, since the signal duration is uncertain, `X-Pipeline` uses multiresolution Fourier transforms to maximize sensitivity across a range of possible signal durations. The pixel clustering procedure applied to time-frequency maps of the data is designed to find arbitrarily shaped, connected events [211]. The potentially nonstationary data is whitened in blocks of 256 s duration, removing the effect of variations in background noise levels which typically happen on longer time scales. Short-duration noise glitches are removed by comparing measures of interdetector correlations to a set of thresholds that are tuned using simulated GW signals from the known sky position of the CCSNe and actual noise glitches over the on-source window. The thresholds are selected to satisfy the Neyman-Pearson optimality criterion (maximum detection efficiency at fixed false-alarm probability), and are automatically adjusted for the event amplitude to give robust rejection of loud glitches. We provide a brief overview of the functionality of `X-Pipeline` here, specifically in the context of CCSN searches, and direct the reader to the `X-Pipeline` technical document for a more in-depth description [212].

As previously introduced in Sec. 4.2, an external EM or neutrino trigger at time t_0 can be used to define an astrophysically motivated on-source window, such that the expected GW counterpart associated with the external trigger is expected to be enclosed within the on-source window. The on-source windows employed in this study are outlined in detail in Sec. 4.2.

Given a specified external source location, $(\alpha; \delta)$, the N data streams observed from an N-detector network are time-shifted, such that any GW signals present will arrive simultaneously in each detector. The time-shifted data streams are then projected onto the dominant polarization frame, in which GW signals are maximized, and null frame, in which GW signals do not exist by construction [213, 214]. The data streams in the dominant polarization frame are processed to construct spectrograms, and the 1% of time-frequency pixels with the largest amplitude are marked as candidate signal events. For each cluster, a variety of information on the time and frequency characteristics is computed, in addition to measures of cluster significance, which are dependent on the total strain energy $|h|^2$, of the cluster. For the purposes of this study, a Bayesian likelihood statistic is used to rank the clusters. We direct the reader to [159, 212] for detailed discussion of the cluster quantities used by X-Pipeline.

For statements on the detection of GWs to be made, we must be able to show with high confidence that candidate events are statistically inconsistent with the background data. To do this, we consider the loudest event statistic, where the loudest event is the cluster in the on-source with the largest significance; we hereafter denote the significance of the loudest event $\mathcal{S}_{\max}^{\text{on}}$ [215, 216]. We estimate the cumulative distribution of the loudest significances of background events, $\mathcal{C}\left(S_{\max}\right)$, and set a threshold on the false alarm probability (FAP) that the background could produce an event cluster in the on-source with significance $\mathcal{S}_{\max}^{\text{on}}$. If $\mathcal{C}\left(\mathcal{S}_{\max}^{\text{on}}\right)$ is greater than the threshold imposed, we admit the loudest event as a potential GW detection candidate. For the purposes of this study, we impose FAP=0.1%, which corresponds to $\sim 3.3\sigma$ confidence.

For Gaussian noise, the significance distribution of background events can be estimated analytically, but noise transients in glitchy data produce excess-power clusters in the data that may be mistaken for a GW event. However, the method used by X-Pipeline to construct the dominant polarization frame results in strong correlations between the incoherent energy I (from the individual data streams) and the coherent energy E (from the combined data streams) for glitches [217]. A comparison of I and E for candidate events can thus be used to veto events that have the same statistical properties as the background noise. A threshold curve in $(I; E)$ space is defined, and veto tests may be one-sided (all events on one side of the curve are vetoed), or two-sided (events within some band centered on the $I = E$ diagonal are vetoed). The threshold curve is chosen to optimize the ratio of glitch rejection to signal acceptance.

In practice, the statistics of the distribution of background events in the data are determined by applying unphysically large time-shifts, hereafter referred to as "lags", to the detector streams. Additionally, we generate known signal events by injecting simulated GW signals into the data streams. The background and signal events are split into two sets, used for pipeline tuning and testing detection perfor- mance, respectively. A large range of trial threshold cuts are applied for the background rejection test, and the statistics of the background events computed. The minimum injection amplitude for which 50% of the injections (1) survive the threshold cuts and (2) have a FAP $\leq 0.1\%$, $h_{\text{rss}}^{50\%}$, for a given family of GW signal models is computed. This is known as the upper limit on h_{rss} at 50% confidence—see Sec. 4.4. The optimal threshold cut is defined as that for which $h_{\text{rss}}^{50\%}$ is minimized at the specified FAP. Unbiased statements on the background distribution and waveform detectability can then be made by processing the tuning set events with the thresholds obtained previously.

Recoloring of GW detector data

The many methods used to detect GW transients can often be proven to be near optimal in the case of stationary, Gaussian noise. Data from the GW detectors, however, is not expected to be stationary or Gaussian, and as such, it is important to test the efficacy of one's detection method in nonstationary and non-Gaussan noise. To this end, we utilize observational data taken by the Hanford and Livingston LIGO detectors during the S5 science run, in addition to data taken by the Virgo detector during the VSR1 science run. The S5 data is now publicly available via the GW Open Science Center (GWOSC) [218].

Recoloring of these data to the predicted power spectral densities (PSDs) of the Advanced detectors during different stages during the next five years (see Sec. 4.2) permits a more realistic estimation of the sensitivity of the advanced detectors to CCSNe. We recolor the GW data using the gstlal software packages [219, 220], following the procedure outlined below:

- Determine PSD of original data.
- Whiten data using a zero-phase filter created from the original PSD.
- Recolor whitened data to desired PSD.

This method provides non-Gaussian, nonstationary detector data including noise transients, tuned to any sensitivity desired. For specific details on the detector networks, and noise PSDs considered, see Sec. 4.2 III C. For the purposes of this study, we recolor 100 hours of data from the H1 and L1 detectors during the S5 science run, and the V1 detector during the VSR1 science run.

Injection of known signal events

As discussed previously in Sec. 4.4, it is a well established practice to inject known signal events into detector data for analysis (see, e.g., [154]). This process permits the estimation of detection efficiency for GWs from signal models of varying time-frequency characteristics.

As discussed in Chap. 3, a GW source can be characterized by five angles—$(\iota, \phi; \theta, \Phi, \psi)$, where (θ, Φ, ψ) describe the sky location and polarization of the source, while (ι, ϕ) describe the orientation of the source frame with respect to the observer's line of sight. In this study, the source location in Earth-centered coordinates (θ, ϕ) are fixed by right ascension α, and declination δ of the source, as well as the GPS time at geocenter of the injected signal—see Sec. 4.2 for more detailed information. The polarization angle ψ relating the source and detector reference frames is distributed uniformly in $[1, \ldots, 2\pi]$ for all injections. For CCSNe systems, the inclination angle ι and azimuthal angle ϕ are known a priori only in exceptional cases. To represent this, we inject signals with many different (ι, ϕ), to average over all possible observer orientations.

As alluded to previously in Sec. 4.3, we may construct the strain for differently oriented observers by projecting the mode coefficients $H_{\ell,m}(t)$ onto the -2 spin-weighted spherical harmonics, ${}^{-2}Y_{\ell m}(\iota, \phi)$. Making use of geometric symmetries for different astrophysical systems permits the use of polarization factors to describe $h_{+,\times}(\iota, \phi)$ as a function of $h_{+,\times;0}(\iota, \phi) = h_{+,\times}(\iota = 0, \phi = 0)$. Defining polarization factors $n_{+,\times}(\iota, \phi)$, we may write the strain for an arbitrarily oriented observer as

$$h_{+}(\iota, \phi) = n_{+}(\iota, \phi)\, h_{+;0}\,, \tag{4.14}$$

$$h_{\times}(\iota, \phi) = n_{\times}(\iota, \phi)\, h_{\times;0}\,, \tag{4.15}$$

where the form of $n_{+,\times}(\iota, \phi)$ is dependent on the symmetries of the system considered.

For linearly polarized signals (e.g., linear sine-Gaussian injections), we apply

$$n_{+}^{\mathrm{lin}} = 1\,, \tag{4.16}$$

$$n_{\times}^{\mathrm{lin}} = 0\,. \tag{4.17}$$

For elliptically polarized signals (e.g., bar-mode instability, disk fragmentation instability, and elliptical sine-Gaussian injections), we apply

$$n_{+}^{\mathrm{el}} = \frac{1}{2}\left(1 + \cos^{2}\iota\right)^{2}\,, \tag{4.18}$$

$$n_{\times}^{\mathrm{el}} = \cos\iota\,. \tag{4.19}$$

For the 2D CCSN emission models, the axisymmetric system results in a linearly polarized GW signal. The system has azimuthal symmetry, resulting in zero amplitude for all modes except H_{20}. The strain h_{+} varies with ι as

$$h_{+} = h_{+}^{\mathrm{eq}} \sin^{2}\iota\,, \tag{4.20}$$

where h_{+}^{eq} is the strain as seen by an equatorial observer. We thus apply SN polarization factors:

$$n_{+}^{\mathrm{SN}} = \sin^{2}\iota\,, \tag{4.21}$$

$$n_{\times}^{\mathrm{SN}} = 0\,. \tag{4.22}$$

For the 3D CCSN emission models, the GW signal is nontrivially related to the observer's orientation, and as such, the h_{+} and $h_{\times}$ strains must be computed for specific observer orientations. For these waveforms, no additional polarisation factors are applied.

For all emission models for which $n_{+,\times}$ can be defined, we inject signals uniform in $\cos\iota \in [-1, 1]$. For the 3D CCSN emission models, we inject signals uniformly drawn from a bank of 100 realizations of $(\cos\iota, \phi)$, where $\cos\iota \in [-1, -7/9, \ldots, 1]$ and $\phi \in [0, 2\pi/9, \ldots, 2\pi]$. For each observational scenario, we inject 250 injections across the considered on-source window.

Upper limits and detection efficiencies

To make detection statements and set upper limits on the GWs emitted from CCSNe, we must compare the cumulative distribution of background event significance, $\mathcal{C}\left(\mathcal{S}_{\text{max}}\right)$, estimated from off-source data, to the maximum event significance in the on-source data $\mathcal{S}_{\text{max}}^{\text{on}}$. If no on-source events are significant, we may instead proceed to set frequentist upper limits on the GWs from the CCSN of interest, given the emission models considered.

As alluded to previously in Sec. 4.4, we may define the 50% confidence level upper limit on the signal amplitude for a specific GW emission model as the minimum amplitude for which the probability of observing the signal, if present in the data, with a cluster significance louder than $\mathcal{S}_{\text{max}}$ is 50%. In this study, we aim to determine the 50% on upper limit, as defined here, as a function of

- Source distance d, in the context of astrophysically motivated signal models.
- Root-sum-square amplitude $h_{\text{rss}}^{50\%}$, in the context of linear and elliptical sine-Gaussian waveforms. It is more relevant, astrophysically to consider the corresponding 50% upper limit on the energy emitted in GWs, $E_{\text{GW}}^{50\%}$, which we compute from $h_{\text{rss}}^{50\%}$ using Eq. 4.13.

After the on-source data has been analysed and $\mathcal{S}_{\text{max}}^{\text{on}}$ computed, we inject a large number of known signal events for families of waveforms for which $h_{\text{rss}}^{50\%}$ and $d^{50\%}$ (where applicable) are desired. For a single waveform family, we outline the upper limit procedure:

- Inject many waveforms at different times during the on-source window and with a broad range of polarization factors.

- Compute the largest significance $\mathcal{S}$ of any clusters associated with the injected waveforms (observed within 0.1 s of the injection time) that have survived after application of veto cuts.
- For all injections, compute the percentage of injections for which $\mathcal{S} > \mathcal{S}^{\mathrm{on}}_{\mathrm{max}}$. This is called the "detection efficiency," $\mathcal{E}$.
- Repeat procedure, modifying the injection amplitude of each waveform by a scaling factor.

The final goal is to produce a plot of the detection efficiency as a function of h_{rss} or distance d for each waveform family, such that one may place upper limits on the GW emission models considered. From the efficiency curve, one may determine $h^{50\%}_{\mathrm{rss}}$ as

$$\mathcal{E}\left(h_{\mathrm{rss}} = h^{50\%}_{\mathrm{rss}}\right) = 0.5\,. \tag{4.23}$$

Given an astrophysical signal injected at $h^{\mathrm{inj}}_{\mathrm{rss}}$ corresponding to fiducial distance d^{inj}, we may define $d^{50\%}$ as

$$d^{50\%} = \left(\frac{h^{50\%}_{\mathrm{rss}}}{h^{\mathrm{inj}}_{\mathrm{rss}}}\right) d^{\mathrm{inj}}\,. \tag{4.24}$$

We note that X-Pipeline rescales the detection efficiency to account only for injections placed at times at which detector data is available. Without this correction, the efficiencies computed asymptote to the duty cycle fraction for the on-source window considered. For the data considered in this study, the total duty cycle is typical of the S5 and VSR1 science runs, which is described in detail in Sec. 4.2.

Systematic uncertainties

The uncertainties in the efficiencies, upper limits and exclusion capabilities of our analysis method are related to non-Gaussian transients in the data, in addition to calibration uncertainties. There are a number of systematic uncertainties present in this study that will non-negligibly affect the results. We consider only a short period of recolored data from LIGO's S5 and Virgo's VSR1 data-taking runs, over which the frequency and character of non-Gaussian transients changed non-negligibly. The noise transients in advanced LIGO data are also significantly different to those in initial LIGO data, and the non-Gaussianities are not yet understood well enough to make quantitative statements on the statistical behavior of the data. For these reasons, we only quote results to two significant figures in this study. The statistical uncertainty in detector calibration can be characterized by the 1σ statistical uncertainty in the amplitude and phase of the signal. Uncertainties in phase calibration can be estimated by simulating its effect on the ability to recover test injections. We direct the reader to Kalmus [221], in which it is shown that phase uncertainties contribute negligibly to the total systematic error, and thus we only consider amplitude uncertainties in this study. The target design amplitude uncertainties in the frequency range 40–2048 Hz for Advanced LIGO and Advanced Virgo are 5% at 2σ confidence [165]. As such, the upper limits for $h_{\rm rss}^{50\%}$ and $d^{50\%}$ obtained from a search for GWs from CCSNe in the will have intrinsic $\sim$ 5% uncertainties. For comparison, typical amplitude uncertainties due to calibration in S5 were below 15% [161].

4.5 Results: Neutrino-triggered searches

We consider realistic waveform models from numerical simulations of core collapse. For the 'garden-variety' CCSN models considered (`müller1`, `müller2`, `müller3`, `ott`, and `yak`), convection and SASI are the dominant GW emission processes. For rotating core collapse, we choose models where bounce and ringdown of the rapidly rotating PNS (`dim1`, `dim2`, and `dim3`), and non-axisymmetric rotational instabilities (`sch1` and `sch2`) are the dominant GW emission processes. As these waveforms will only be detectable from CCSNe at close distances ($d \lesssim 100$ kpc), we consider CCSNe in the direction of the Galactic center and LMC, for which the coincident neutrino signal will be detected. We use a conservative on-source window of [-10,+50]s about the time of the initial SNEWS trigger.

We present the distances $d^{50\%}$ at which 50% detection efficiency is attained (the measure we use for "detectability") for the considered numerical waveforms in Table 4.6, for CCSNe in the direction of the Galactic center and LMC, in the context of a 60-second on-source window.

For CCSNe in the direction of the Galactic center, we see that emission from neutrino-driven convection and SASI is detectable out to $\sim$ (1.0-2.4) kpc with

	$d^{50\%}$ [kpc] for Galactic center			$d^{50\%}$ [kpc] for LMC		
Waveform	`HL 2015`	`HLV 2017`	`HLV 2019`	`HL 2015`	`HLV 2017`	`HLV 2019`
`müller1`	2.3	3.3	4.7	2.5	3.8	5.3
`müller2`	1.0	1.5	2.2	1.2	1.8	2.5
`müller3`	1.2	1.5	2.4	1.4	1.6	2.7
`ott`	2.4	3.4	5.5	3.2	4.9	7.2
`yak`	1.5	1.8	5.1	1.6	2.1	6.2
`dim1`	7.0	9.1	17	7.4	10	18
`dim2`	11	17	29	13	20	32
`dim3`	13	21	38	18	32	50
`sch1`	31	43	78	36	48	90
`sch2`	35	50	98	45	56	120

Table 4.6: The distance in kpc at which 50% detection efficiency is attained, $d^{50\%}$ for the numerical core-collapse emission models considered using the `HL 2015`, `HLV 2017`, and `HLV 2019` detector networks, for CCSNe in the direction of the Galactic center and the LMC.

the `HL 2015` detector network. This increases to ~ (1.5-3.4) kpc and ~ (2.2-5.5) kpc with the `HLV 2017` and `HLV 2019` detector networks, respectively.

Similarly, we see that emission from bounce and ringdown of the central PNS core is detectable out to ~ (7.0-13.4) kpc for CCSNe in the direction of the Galactic center with the `HL 2015` detector network. This increases to ~ (9.1-21) kpc and ~ (17-38) kpc with the `HLV 2017` and `HLV 2019` detector networks, respectively.

Emission from nonaxisymmetric rotational instabilities from CCSNe in the direction of the galactic center is detectable out to ~ (31-35) kpc with the `HL 2015` detector network. This increases to ~ (43-50) kpc and ~ (78-98) kpc with the `HLV 2017` and `HLV 2019` detector networks, respectively.

Assuming the fiducial distance of a galactic CCSN to be ~ 9 kpc, this suggests that we will be able to detect emission from the more extremely rapidly rotating CCSN waveforms considered with the `HL 2015` detector network, while all considered rapidly rotating waveforms will be detectable for CCSNe in the direction of the Galactic center with the `HLV 2017` and `HLV 2019` detector networks. We will be limited to detection of nonrotating CCSNe within 5.5 kpc with the most sensitive `HLV 2019` detector network.

Considering CCSNe in the direction of the LMC, we see that emission from neutrino-driven convection and SASI is detectable out to ~ (1.2-3.2) kpc with the `HL 2015` detector network. This increases to $\sim$(1.6-4.9) kpc and $\sim$(2.5-7.2) kpc with the `HLV 2017` and `HLV 2019` detector networks, respectively. Given the LMC is around 50 kpc away, GW emission from neutrino-driven convection and SASI is likely not detectable from CCSNe there.

Emission from bounce and ringdown of the central PNS core is detectable out to $\sim$(7.4-18) kpc and $\sim$(11-32) kpc for CCSNe in the direction of the LMC with the `HL 2015` and `HLV 2017` detector networks, respectively. This increases to $\sim$(18-50) kpc with the `HLV 2019` detector network. This suggests that emission from the bounce and subsequent ringdown of the PNS may not be detectable from CCSNe in the LMC for even the most rapidly rotating waveform considered with the `HLV 2019` detector network.

We see that emission from nonaxisymmetric rotational instabilities from CCSNe in the direction of the LMC is detectable out to $\sim$(36-45) kpc with the `HL 2015` detector network. This increases to $\sim$(48-56) kpc and $\sim$(90-120) kpc with the `HLV 2017` and `HLV 2019` detector networks, respectively. This suggests we will be able to detect emission from nonaxisymmetric rotational instabilities for CCSNe in the LMC with the `HLV 2017` detector network.

Fig. 4.5 presents the detection efficiency as a function of distance, for the numerical waveforms considered, for CCSNe directed toward the Galactic center and the LMC.

4.6 Results: Electromagnetically-triggered searches

For more distant CCSNe, we consider more speculative, extreme phenomenological GW emission models for long-lived bar-mode instabilities (using waveforms `longbar1` through `longbar6`) and disk fragmentation instabilities (with `piro1` through `piro4`). More distant CCSNe (beyond around M31) will not be detectable via neutrinos with the current class of neutrino detectors, but the EM counterpart is likely to be observed. We consider CCSNe in M31 and M82, and use on-source windows assuming a compact, stripped progenitor star of 61 minutes and 24 hour 1 minute, respectively. For an extended, red supergiant progenitor, we use on-source windows of 51 hours and 74 hours for M31 and M82, respectively.

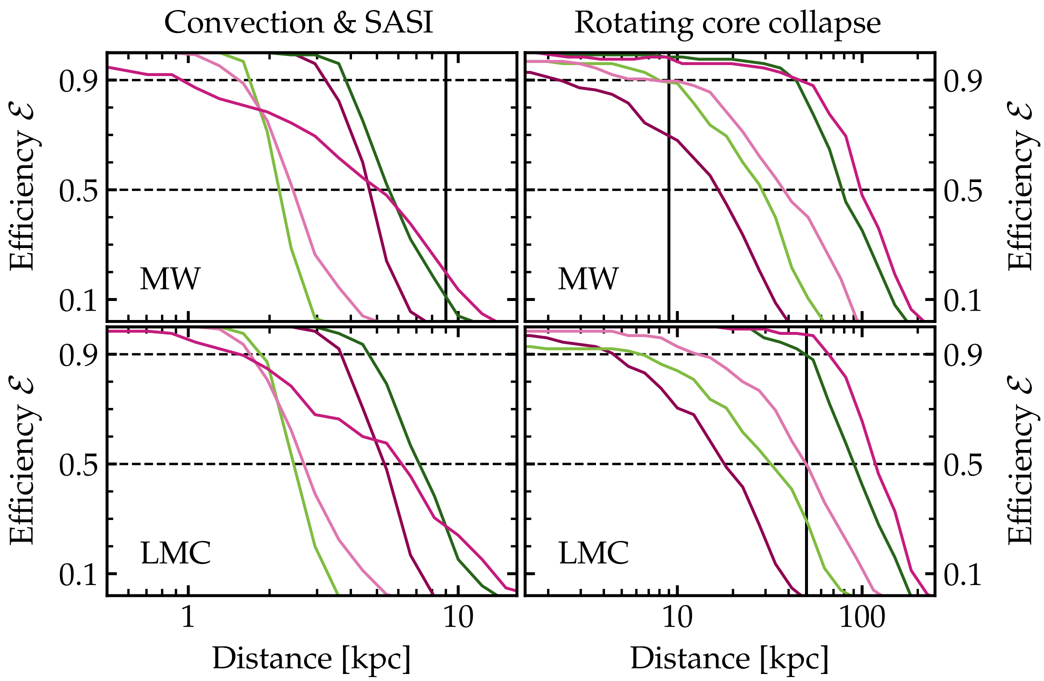

Figure 4.5: The detection efficiency $\mathcal{E}$ as a function of distance for waveforms from neutrino-driven explosions (left column; labelled Convection & SASI) and rotating core collapse (right column) for a search using a sixty second on-source window and a three-detector network at design sensitivity. Panels in the top row consider sources in the direction of the galactic center (labelled MW), while panels in the bottom row conversely employ sources in the direction of the Large Magellanic Cloud (labelled LMC). In each panel, 50% and 90% detection efficiency is marked with a dashed horizontal black line, and the assumed distance to the source is marked with a solid vertical black line.

In Tab. 4.7, we present the distances at which 50% detection efficiency is attained $d^{50\%}$ (the measure we use for "detectability") for the considered phenomenological waveforms in the context of a hypothetical CCSN in M31 using 61-minute and 51-hour on-source windows.

For CCSNe in the direction of M31, we see that emission from long-lived bar-mode instabilities will be detectable out to ~ (0.5-5.2) Mpc [~ (0.2-2.7) Mpc] when using a 61-minute [51-hour] on-source window, with the `HL 2015` detector network. The distances at which 50% detection efficiency is reached, $d^{50\%}$, increase to ~ (0.8-8.6) Mpc [~ (0.3-3.4) Mpc] and ~ (1.6-18) Mpc [~ (0.8-9.9) Mpc] when using a 61-minute [51-hour] on-source window, with the `HLV 2017` and `HLV 2019` detector networks, respectively.

	$d^{50\%}$ with `HL 2015`		$d^{50\%}$ with `HLV 2017`		$d^{50\%}$ with `HLV 2019`	
Waveform	61m	51h	61m	51h	61m	51h
`longbar1`	0.5	0.2	0.8	0.3	1.6	0.8
`longbar2`	1.5	0.7	2.5	0.9	4.8	2.8
`longbar3`	1.0	0.6	1.6	0.6	3.6	2.2
`longbar4`	2.0	1.1	2.8	1.2	6.0	3.8
`longbar5`	5.2	2.7	8.6	3.4	18	9.9
`longbar6`	2.1	1.1	3.4	1.1	6.7	4.7
`piro1`	0.9	0.6	1.3	0.6	2.0	1.4
`piro2`	3.9	2.2	6.3	2.6	9.4	5.8
`piro3`	1.9	1.3	3.4	1.8	4.9	3.7
`piro4`	12	6.5	19	6.1	28	18

Table 4.7: The distance in Mpc at which 50% detection efficiency is attained, $d^{50\%}$ for the extreme phenomenological emission models considered using the `HL 2015`, `HLV 2017`, and `HLV 2019` detector networks in the context of a hypothetical CCSN in M31 using 61-minute and 51-hour on-source windows.

Emission from disk fragmentation instabilities will be detectable out to $\sim$ (0.9-12) Mpc [$\sim$ (0.6-6.5) Mpc] and $\sim$ (1.3-19) Mpc [$\sim$ (0.6-6.1) Mpc] when using 61-minute [51-hour] on-source windows with the `HL 2015` and `HLV 2017` detector networks, respectively, for CCSNe in the direction of M31. These distances increase to $\sim$ (2-28) Mpc [$\sim$ (1.4-18) Mpc] when using a 61-minute [51-hour] on-source window, with the `HLV 2019` detector network.

Assuming a fiducial distance of 0.77 Mpc for a CCSN in M31, this suggests that we will be able to detect emission from all considered long-lived bar-mode instability waveforms with the `HLV 2019` detector network, while the detectable fraction of considered waveforms with the `HL 2015` and `HLV 2017` detector networks is strongly dependent on the on-source window length. Taking the 51-hour on-source window as the most pessimistic scenario, $\sim$ 50% and $\sim$ 67% of the considered bar-mode instability waveforms are detectable with the `HL 2015` and `HLV 2017` detector networks, respectively.

Similarly, emission from the considered disk fragmentation instabilities waveforms will be detectable for a CCSN in M31 with the `HLV 2019` detector network for all considered on-source windows. For the 51-hour on-source window, we see that $\sim$ 75% of the considered disk-fragmentation instability waveforms are detectable with both the `HL 2015` and `HLV 2017` detector networks.

We note that, for some models, the $d^{50\%}$ values computed for the M31 source, when using a 51-hour on-source window, are smaller for the `HLV 2017` detector network than the `HL 2015` network. While this might at first seem counter-intuitive, this is due to the requirement for coincident data between detectors to run a coherent analysis. The lower sensitivity of the `HV` and `LV` detectors for the data analyzed, compared with the sensitivity of the `HL` detectors, reduces the effective total sensitivity of the network. We include the third detector, however, as it increases the overall duty cycle of the network.

In Tab. 4.8, we present the $d^{50\%}$ distances for the considered phenomenological waveforms in the context of a hypothetical CCSN in M82 using 24-hour 1-minute and 74-hour on-source windows.

	$d^{50\%}$ with `HL 2015`		$d^{50\%}$ with `HLV 2017`		$d^{50\%}$ with `HLV 2019`	
Waveform	24h1m	74h	24h1m	74h	24h1m	74h
`longbar1`	0.3	0.4	0.3	0.4	1.0	0.7
`longbar2`	0.9	1.1	1.0	1.2	3.0	2.1
`longbar3`	0.8	0.8	0.7	0.8	2.4	1.8
`longbar4`	1.1	1.5	1.4	1.5	3.9	2.8
`longbar5`	3.0	4.3	3.4	5.2	9.7	8.3
`longbar6`	1.4	1.9	1.4	1.7	4.4	3.7
`piro1`	0.5	0.7	0.7	0.8	1.3	1.3
`piro2`	2.2	3.2	3.0	3.8	5.7	5.8
`piro3`	1.1	1.3	1.5	1.9	2.8	3.1
`piro4`	6.4	7.5	8.6	9.5	16	15

Table 4.8: The distance in Mpc at which 50% detection efficiency is attained, $d^{50\%}$ for the extreme phenomenological emission models considered using the `HL 2015`, `HLV 2017`, and `HLV 2019` detector networks in the context of a hypothetical CCSN in M82 using 24-hour 1-minute and 74-hour on-source windows.

For CCSNe in the direction of M82, we see that emission from long-lived bar-mode instabilities will be detectable out to $\sim$ (0.3-3) Mpc [$\sim$ (0.4-4.3) Mpc] and $\sim$ (0.3-3.4) Mpc [$\sim$ (0.4-5.2) Mpc] using a 24-hour 1-minute [74-hour] on-source window, with the `HL 2015` and `HLV 2017` detector networks. This increases to $\sim$ (1-9.7) Mpc [$\sim$ (0.7-8.3) Mpc] for a 24-hour 1-minute [74-hour] on-source window, with the `HLV 2019` detector network.

For emission from disk fragmentation instabilities for CCSNe in the direction of M82, the distance reach is $\sim$ (0.5-6.4) Mpc [$\sim$ (0.7-7.5) Mpc] when using a 24-hour 1-minute [74-hour] on-source window with the `HL 2015` detector network. This increases to ∼ (0.7-8.6) Mpc [∼ (0.8-9.5) Mpc] and ∼ (1.3-16) Mpc [∼ (1.3-15) Mpc] for the `HLV 2017` and `HLV 2019` detector networks, respectively.

Given a fiducial distance of ∼ 3.52 Mpc for CCSNe in M82, we note that only the most extreme waveform considered for both long-lived bar-mode instabilities and disk fragmentation instabilities are detectable with the `HL 2015` detector network. Of the considered long-lived bar-mode instability waveforms, only the most extreme emission model is detectable with the `HLV 2017` detector network, while 50% of the waveforms will be detectable with the `HLV 2019` detector network. For emission from disk fragmentation instabilities, we see that only 50% of the waveforms considered will be detectable out to M82 with the `HLV 2017` and `HLV 2019` detector networks.

We note that the distance reach for these models increases with the larger on-source window for the M82 source. This is due to the properties of the data over the two considered on-source windows. As previously mentioned, real data from GW detectors is not stationary, and as such, the PSD of the data is a function of time. Time periods over which the detector data is glitchy will have locally have significantly decreased sensitivity when compared to a much larger time period over which the detector is more well behaved. This means that if the on-source window derived happens to lie in a glitchy period of detector data, the sensitivity of the detector network will, unfortunately, be decreased. In repeating the search for a larger on-source window, over which the average sensitivity is much greater, the distance reach for the emission models considered may appear to increase. The detectability of the waveforms considered in this study is established by injecting a number of waveforms over the full on-source window considered. The distance reach for the longer on-source window in this case appears to increase because we inject waveforms uniformly across the on-source window, meaning that many “test” signals are placed at times in the data stretch where the sensitivity is greater, in addition to the shorter, more glitchy, time period where the sensitivity is not as great. This is a great example of how realistic noise can significantly affect the detectability of GWs from CCSNe at different times, and is motivation for improving active noise suppression techniques for the detectors.

Fig. 4.6 and Fig. 4.7 present the detection efficiency as a function of distance for the considered phenomenological extreme emission models, for CCSNe in the direction of M31 and M82 for the `HLV 2019` detector network, using on-source windows motivated by type Ibc and type II CCSNe, respectively.

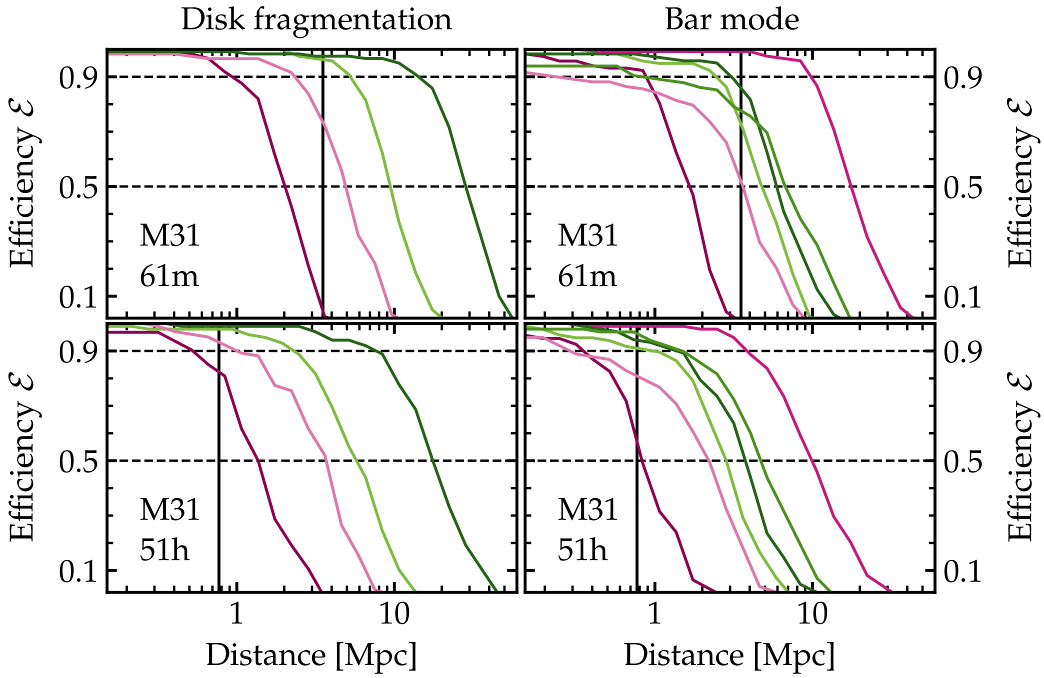

Figure 4.6: The detection efficiency $\mathcal{E}$ as a function of distance for phenomenological waveforms from accretion disk fragmentation in collapsars (left column; labelled Disk Fragmentation) and dynamical bar mode instability in a rapidly-rotating neutron star remnant (right column; labelled Bar Mode) for a search for sources in M31 with a three-detector network at design sensitivity. Panels in the top row consider an on-source window of 61 minutes derived from EM observations of an ultra-stripped progenitor (labelled M31 61m), while panels in the bottom row conversely use an on-source window of 51 hours derived from EM observations of an extended red-supergiant progenitor (labelled M31 51h). In each panel, the 50% and 90% detection efficiency is marked with a dashed horizontal black line, and the distance to M31 (0.77 Mpc) is marked with a solid vertical black line.

Sine-Gaussian waveforms

For all host galaxies, we consider *ad-hoc* sine-Gaussian bursts to assess the sensitivity of our analysis to localized bursts of energy in time-frequency space.

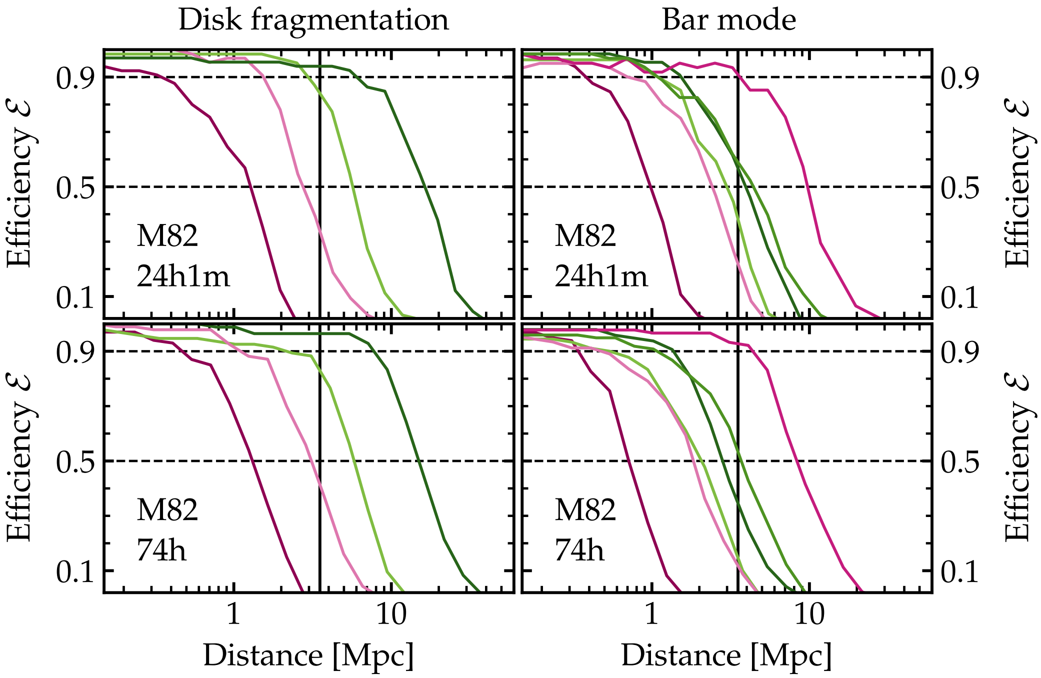

Figure 4.7: The detection efficiency $\mathcal{E}$ as a function of distance for phenomenological waveforms from accretion disk fragmentation in collapsars (left column; labelled Disk Fragmentation) and dynamical bar mode instability in a rapidly-rotating neutron star remnant (right column; labelled Bar Mode) for a search for sources in M82 with a three-detector network at design sensitivity. Panels in the top row consider an on-source window of 24 hours and 1 minute derived from EM observations of an ultra-stripped progenitor (labelled M82 24h1m), while panels in the bottom row conversely use an on-source window of 74 hours derived from EM observations of an extended red-supergiant progenitor (labelled M82 74h). In each panel, the 50% and 90% detection efficiency is marked with a dashed horizontal black line, and the distance to M82 (3.52 Mpc) is marked with a solid vertical black line.

We remind the reader of the large systematic uncertainties associated with these results and, as such, quote all results to two significant figures.

The energy emitted in GW, $E_{\mathrm{GW}}^{50\%}$, required to attain the root-sum-squared strain at 50% detection efficiency, $h_{\mathrm{rss}}^{50\%}$, for the sine-Gaussian bursts considered is presented in Fig. 4.8 for sources in the direction of the Galactic center, LMC, M31, and M82.

For the *ad-hoc* sine-Gaussian bursts considered, we use $E_{\mathrm{GW}}^{50\%}$ as the figure of merit for detection.

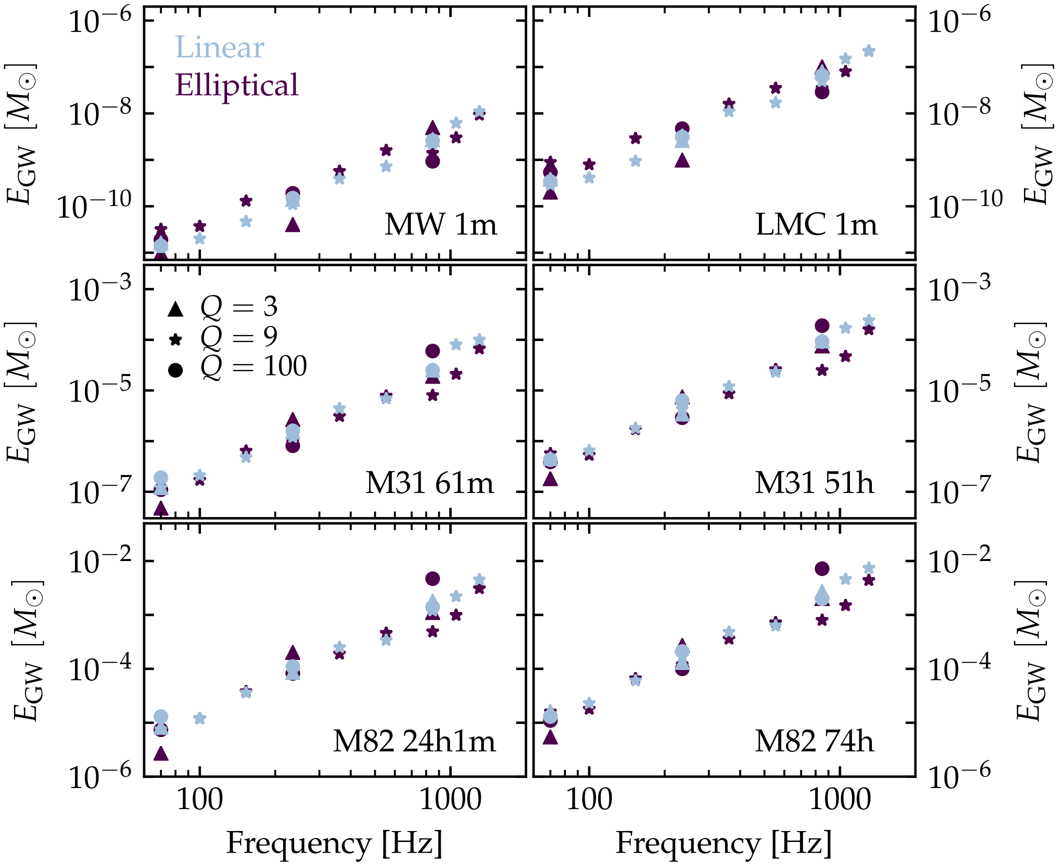

Figure 4.8: The energy emitted in GW, $E_{\mathrm{GW}}^{50\%}$, required to attain the root-sum-squared strain at 50% detection efficiency, $h_{\mathrm{rss}}^{50\%}$, for the sine-Gaussian bursts considered in this study, in the context of the `HLV 2019` detector network. The top row is for sources directed toward the galactic center (left) and the Large Magellanic Cloud (right), for both of which a 1-minute on-source window is used. The middle row is for sources in M31, considering 61-minute and 51-hour on-source windows (left and right plots, respectively). The bottom row is for sources in M82, considering on-source windows of 24 hours and 1 minute, and 74 hours (left and right plots, respectively). Distances of 10 kpc, 50 kpc, 0.77 kpc, and 3.52 Mpc are used to compute $E_{\mathrm{GW}}^{50\%}$ for sources in the galaxy, Large Magellanic Cloud, M31, and M82, respectively.

For CCSNe in the direction of the Galactic center, we see that the typical $E_{\mathrm{GW}}^{50\%}$ values are $\sim$ (8-110)$\times10^{-10}\,M_\odot$ for sine-Gaussian bursts with central frequencies of $\sim$ (554-1304) Hz, the typical frequencies of emission for CCSNe, using a 60-second on-source window with the `HLV 2019` detector network. For CCSNe in the direction of the LMC, we find $E_{\mathrm{GW}}^{50\%} \sim$ (1-20)$\times10^{-8}\,M_\odot$ in the same frequency range. We remind the reader that for the numerical waveforms considered, $E_{\mathrm{GW}} \sim$ (0.1-4000)$\times10^{-10}\,M_\odot$. This is consistent, as `X-Pipeline` is more sensitive to sine-Gaussian bursts, and we find that only the more rapidly rotating models considered are detectable.

For CCSNe in the direction of M31, we find typical $E_{\mathrm{GW}}^{50\%}$ values of $\sim$(7-100)$\times10^{-6}\,M_{\odot}$ across the frequency range considered, using a 51 hour on-source window with the `HLV 2019` detector network. For CCSNe in the direction of M82, we find $E_{\mathrm{GW}}^{50\%}$ $\sim$(3-60)$\times10^{-4}\,M_{\odot}$ across the same frequency range. We remind the reader that for the extreme phenomenological waveforms considered, E_{GW} $\sim$(2-600)$\times10^{-4}\,M_{\odot}$. This is again consistent with our previous results, as we find that all waveforms are detectable for CCSNe in M31 with the `HLV 2019` detector network, but only the more extreme cases are detectable out to M82.

4.7 Discussion

The next galactic CCSN will be of great importance to the scientific community, allowing observations of unprecedented accuracy via EM, GW, and neutrino messengers. Using GW waveform predictions for core collapse from state-of-the-art numerical simulations, and phenomenological waveform models for speculative extreme GW emission scenarios, we make the first comprehensive statements on detection prospects for GWs from CCSNe in the Advanced detector era.

Given a known sky location, we outline a search procedure for GW bursts using `X-Pipeline` , a coherent network analysis pipeline that searches for excess power in time-frequency space, over some astrophysically motivated time period (or on-source window). The GW detector data is non-Gaussian, nonstationary, and often contains loud noise transients. For this reason, it is beneficial to minimize the on-source window to reduce the probability of glitchiness or extreme Gaussian fluctuations being present in the detector data.

For CCSNe within $\sim$ 100 kpc, the coincident neutrino signal will be detected, allowing the time of core collapse to be determined to within a few tens of milliseconds. Using an conservative asymmetric on-source window of $[-10, +50]$ seconds around the start time of the neutrino signal, we consider hypothetical CCSNe in the direction of the Galactic center and the LMC. We find that neutrino-driven CCSN explosions, believed to account for $\sim$ 99%

for CCSNe, will be detectable within 2.4 kpc, 3.5 kpc, and 5.5 kpc in 2015, 2017, and 2019, respectively. Rapidly rotating CCSNe, however, will be detectable throughout the galaxy from 2017, and the most rapidly rotating model considered will be detectable out to the LMC in 2019. Rapidly rotating CCSNe with nonaxisymmetric rotational instabilities will be detectable out to the LMC and beyond from 2015.

More distant CCSNe will not have coincident neutrino observations, and so the on-source window must be derived using EM observations. Using recent studies of light curves for type Ibc and type II CCSNe (see, e.g. [192, 195, 222]), we assume that, if the time of shock breakout t_{SB} is observed, the time of core collapse can be localized to between 1 minute and 50 hours. Unfortunately, shock breakout is rarely observed, and an observation cadence time delay, t_{obs}, between the last pre-CCSN and first post-CCSN images is introduced. Given this, we construct an on-source window of $[-t_{\mathrm{SB}}, t_{\mathrm{obs}}]$ about the time of the last pre-CCSN image. Frequently observed galaxies, such as those for which the CCSN rate is high, are likely to have CCSNe detected within one day of shock break-out. As such, we consider two observational scenarios where $t_{\mathrm{obs}} = 1$ hour and 24 hours for hypothetical CCSNe in M31 and M82, respectively. In the context of EM observations of type Ibc CCSNe, we use on-source windows of 61 minutes and 24 hour 1 minute for CCSNe in M31 and M82, respectively. Correspondingly for type II CCSNe, we use on-source windows of 51 hours and 74 hours for CCSNe in M31 and M82, respectively. We find that most of the extreme GW emission models considered are observable out to M31 with the `HL 2015` detector network when using a 61-minute on-source window, while all models are observable when using the 51-hour on-source window in 2019. Only the most extreme emission models considered are observable out to M82 with the `HL 2015` detector network, but approximately half of the models considered will be detectable out to M82 and beyond in 2019. This allows us to either detect events associated with or exclude such extreme emission models for CCSNe in M31 and M82 with the `HLV 2019` detector network.

In anticipation of unexpected GW emission from CCSNe, we additionally consider sine-Gaussian bursts across the relevant frequency range for all observational scenarios studied. We find, that the sensitivity of our search method is comparable, if not slightly improved, to that found for the realistic waveform models considered. This is to be expected as `X-Pipeline` , and other clustering-based burst search algorithms, are most sensitive to short bursts of GW energy localized in frequency space. It should be noted, however, that such simple waveform morphologies are more susceptible to being confused for noise transients. As such, a more complicated waveform morphology, as found for realistic GW predictions for CCSNe, can actually improve detectability [223].

Detection prospects for GWs from CCSNe can be improved by refining light curve models for CCSNe, and increasing observation cadence, so as to reduce the on-source window as derived from EM observations as much as possible. Improvement of stationarity and glitchiness of detector data, in addition to increasing the detector duty cycle, will improve detectability of GWs from CCSNe. Further to this, more second-generation GW detectors such as KAGRA and LIGO India will improve the overall sensitivity of the global GW detector network and could potentially allow for neutrino-driven CCSN explosions to be observable throughout the Galaxy.

5 Inferring the core-collapse supernova explosion mechanism with gravitational waves

You own everything that happened to you. Tell your stories. If people wanted you to write warmly about them, they should have behaved better.

—Anne Lamott, *Bird by Bird: Some Instructions on Writing and Life*

[1] J. Powell, S. E. Gossan, et al. Inferring the core-collapse supernova explosion mechanism with gravitational waves. Phys. Rev. D 94 (12), 123012 (2016).
SEG led the project for three years and originally wrote the SMEE2G pipeline in Python, but had to step back towards the end due to health concerns. SEG made the figures, directed the observing cases considered, and wrote around half of the manuscript.

5.1 Motivation

More than eighty years have passed since Baade and Zwicky first proposed that supernovae originated from the collapse of evolved stellar cores to neutron stars [5], yet still the mechanism driving these comsic explosions remains poorly understood. While CCSNe are observed on a daily basis across the EM spectrum, only secondary information on the CCSN central engine can be gleaned from such observations as they originate far from the collapsed core. From what can be determined, observations of CCSN ejecta and pulsar kicks are indicative of the multidimensional hydrodynamic instabilities thought to be driving the explosion [42, 127] (see Chap. 3 for a detailed discussion). GWs and neutrinos, originating deep within the exploding SN, offer an unparalleled glimpse into the inner regions of the central engine. While GWs from CCSNe have not yet been directly detected, the few neutrinos detected from SN 1987A were consistent with the broad strokes of current theories regarding the explosion mechanism [8, 9, 224]. Understanding how massive stars explode has consequences far beyond the explosion mechanism itself, with far-reaching effects on fundamental physics, the mass-distribution of compact remnants, the evolution of compact binary systems, and even the origin of the elements, to name a few (see, e. g. [43, 205] and references therein). Having tackled the problem of detection in Chap. 4, we now turn our attention to the prospects for augmenting our understanding of the CCSN explosion mechamism using said observations.

As discussed previously in Chap. 3, the GW signature from core collapse can vary wildly dependent on the characteristics of the progenitor star. The GW emission is sourced predominantly by oscillations of the nascent PNS, but differences in the nature of the hydrodynamics behind the stalled shock and within the inner regions of the evolving PNS alters the expected duration and frequency spectra of emission. For example, while GWs are emitted with core collapse at PNS formation, the asymmetry of collapse (and resultant quadrupole deformation in the PNS) is drastically changed should the pre-collapse core possess appreciable angular momentum (see, e. g., [52, 65, 66]) resulting in several orders of magnitude difference in emitted GW energy. We explore this further in Chap. 6. Furthermore, GW emission at later times (e. g. after $\sim$ 100ms post-bounce) often originates from oscillations of the inner PNS rung up by turbulent fluid downflows and convective plumes in the post-shock flow, the development of which are strongly inhibited by a differential rotation profile in the precollapse core. The nature of these processes is incredibly complex, and developing robust signal models across the vast parameter space of CCSN progenitors is not viable in the absence of unlimited computational resources. To this end, it is beneficial to identify broad characteristics of the GW signals expected in subsets of the progenitor parameter space, say rapidly rotating vs non-rotating precollapse cores, to identify for a given signal which of the limits the progenitor lies closest to.

Logue *et al.* [58] (hereafter referred to as L12) first employed this approach with the `Supernova Model Evidence Extractor` (`SMEE`), considering GW signatures from three "explosion mechanisms": neutrino-driven convection [205], rapidly rotating core collapse [225], and protoneutron star pulsations [226, 227]. Drawing on previous work by Heng [56] and Röver *et al.* [57], principal component analysis (PCA; see, e.g., [228]) was used to construct a basis set for GW signatures associated with each mechanism from signal catalogs amassed from the literature. A proof-of-principle study was conducted using the bases to reconstruct signals in Advanced LIGO Gaussian noise, employing a Bayesian nested sampling algorithm [229] to compute the evidence for each model. Comparison of the evidences was then used to make statements on which explosion mechanism was more likely.

Several limitations to the analysis in L12 were identified by the authors. First and foremost, the antenna response of the detectors was not taken into consideration; instead, it was assumed that the single detector employed was maximally sensitive to linearly polarised GWs. This lead to overestimating the single-detector SNR, an issue compounded by employing only linearly polarised GW signals in the waveform catalogs and for injection purposes. Physically, linearly polarised waves are sourced by quadrupole deformation with azimuthal symmetry, but EM observations suggest that many, if not most, CCSN explosions exhibit asymmetric features [121–125]. Furthermore, 3D simulations of core collapse for progenitor cores with pre-collapse periods greater than a second show that GWs from most CCSNe are expected to be unpolarised, due to asymmetric flow structures set up by turbulent convection and the SASI [19, 47, 51, 66, 128, 230–234]. Finally, using Gaussian noise as an injection medium for test signals meant that the effect of non-Gaussianities and non-stationary behaviour in detector data could not be studied.

The goal of this Chapter is to address these limitations, chiefly by developing the `SMEE` algorithm to consider more realistic observational scenarios, as well as implementing test signals from more sophisticated simulations developed since L12 was published. We develop `SMEE2G`, currently implemented in LALInference [235] and soon to be released as part of an open-source Python framework for GW signal analysis for CCSNe with the aim of championing reproducibility within the CCSN GW community, and encouraging participation in developing inference studies for GWs from CCSNe in the future. For continuity with Chapter 4, we implemet functionality to employ a three-detector network with realistic antenna sensitivity, and inject signals into non-Gaussian, non-stationary detector noise, recolored to the design sensitivity of the Advanced LIGO and Advanced Virgo detectors. With these improvements, we make updated statements on `SMEE2G`'s ability to discern between explosions driven by either convection and SASI or magnetorotational effects with GW observations of CCSNe. We also discuss the fundamental limitations in using an approach such as this for post-detection source inference, and detail alternative perspectives from which to tackle the problem in future studies.

This chapter is organised as follows. In Sec. 5.2, we discuss the principles upon which the SMEE pipeline is founded and provide a broad overview of the concepts of Bayesian model selection. In Sec. 5.3, we provide the technical details of the analysis for the interested reader, focusing particularly on the waveform catalogs employed, before presenting our results for hypothetical sources within the Galaxy and Magellanic Clouds in Sec. 5.4. We discuss our results and highlight caveats associated with our method in Sec. 5.5, concluding with a summary of the implications of this analysis as well as improvements to be carried out future studies in Sec. 5.6.

5.2 SMEE2G

In this Section, we provide an introduction to the concepts of PCA and Bayesian model selection, and discuss how they are applied in the `SMEE2G` code.

Principal Component Analysis

Principal component analysis (PCA) isolates dominant features of waveforms into linearly independent principal components, ordered by their relevance. Mathematically, utilizing matrix C containing a given waveform catalog, one can factorize C as

$$C = U \, \Sigma \, V^T \, , \tag{5.1}$$

where U and V are matrices comprised of the eigenvectors of $C\,C^T$ and $C^T\,C$, respectively, and Σ is a diagonal matrix, composed of the square roots of corresponding eigenvalues. The PCs, U, are organized according to their corresponding eigenvalues, such that the more dominant PCs (characterized by larger eigenvalues) are shifted to the first few columns of U.

Waveform approximations can then be constructed from a linear combination of PCs;

$$h_i \approx \sum_j U_{ij}\epsilon_j \,, \tag{5.2}$$

where h is the desired waveform approximation, and $\vec{\epsilon}$ are the PC coefficients, and the sum runs over the PC basis. For catalog waveforms, $\vec{\epsilon}$ contains projections of the original catalog onto the PCs, but in theory any waveform can be approximated (albeit perhaps not well) by projecting onto the PC basis.

For the purposes of this study, we consider two models; `C&S` (short for convection and SASI, which dominates the GW signature for CCSNe from non-rotating progenitors) and `RotCC` (for rotating core collapse). In the following, we outline the properties of the waveform catalogs employed and PCs constructed for the `C&S` and `RotCC` models.

`C&S` catalog

Following L12, we use the 16 waveforms presented in Murphy *et al.* [44] to construct the `C&S` PCs. These waveforms were produced using the quadrupole approximation ([20]; see Chap. 2 for a discussion) on outputs from axisymmetric Newtonian CCSN simulations using BETHE-hydro, an arbitrary Lagrangian-Eulerian (ALE) code [236]. Neutrino treatment was employed through a local heating and cooling scheme parameterised by the temperature and luminosity of electron neutrinos to minimise computational expense. Four non-rotating progenitors from [237] were considered, characterised by ZAMS mass $M_{\mathrm{ZAMS}} \in \{12, 15, 20, 40\}\, M_{\odot}$. For each progenitor, waveform models were produced for four different neutrino luminosities. A representative waveform from the `C&S` catalog is shown in the upper panel of Fig. 5.1 for a source at 10 kpc, while the first four `C&S` PCs are shown in the left column of Fig. 5.2.

While there is no doubt that the explosion dynamics of CCSNe driven by multidimensional hydrodynamic instabilities are significantly different in two and three dimensions, the dearth of large waveform catalogs produced by 3D CCSN simulations for non-rotating progenitors motivates the choice to employ the catalog used in the L12 study. The implications of this are discussed in Sec. 5.5.

`RotCC` catalog

As for the `C&S` catalog, we follow L12 and employ the 128 waveforms from the Dimmelmeier *et al.* [52] catalog to produce the `RotCC` PCs. The simulations are performed in axisymmetry using `CoCoNuT` (see, e.g., [238, 239]), which implements general-relativistic hydrodynamics using the conformal flatness approximation, while treating deleptonisation and its effects through the collapse phase using a parameterised scheme. Pressure from neutrino stress is included in the evolution equations. The `CoCoNuT` code used to perform these simulations is discussed in more detail in Chap. 6. Waveforms were produced using the quadrupole approximation.

Four non-rotating progenitors from [237] were considered, parameterised by ZAMS mass $M_{\mathrm{ZAMS}} \in \{11.2, 15, 20, 40\}\, M_{\odot}$. For each progenitor, several 'rotating' progenitors were produced by imposing a rotation profile parameterised by initial central angular velocity $\Omega_{c,i}$ and differential rotation length scale A. This rotation profile is used in Chap. 6, and is discussed in more detail there. Simulations were considered across the parameter space in $(\Omega_{c,i}, A)$, choosing $A \in \{5 \times 10^2, 10^3, 5 \times 10^4\}$ km to represent strongly differential, moderately differential, and almost uniform rotation profiles, respectively. Across A, sixteen central angular velocities $\Omega_{c,i} \in \{0.45, 13.31\}$ rad/s were considered. For each rotating progenitor, two simulations employing either the Lattimer-Swesty EOS (with incompressibility $K = 180\,\mathrm{MeV}$; see [198]) or H. Shen EOS (with incompressibility $K = 281\,\mathrm{MeV}$; see [240, 241]) were performed to assess the variability with soft and hard nuclear EOS, respectively. A representative waveform from the `RotCC` catalog is shown in the lower panel of Fig. 5.1, while the first four `RotCC` PCs are shown in the right column of Fig. 5.2.

While using a waveform catalog produced using 2D rather than 3D simulations is likely to cause some differences in the explosion dynamics, our study here is limited to modelling the signal from rotating core collapse with the bounce and ringdown signature associated with millisecond PNS formation. We discuss the implications of this in Sec. 5.5.

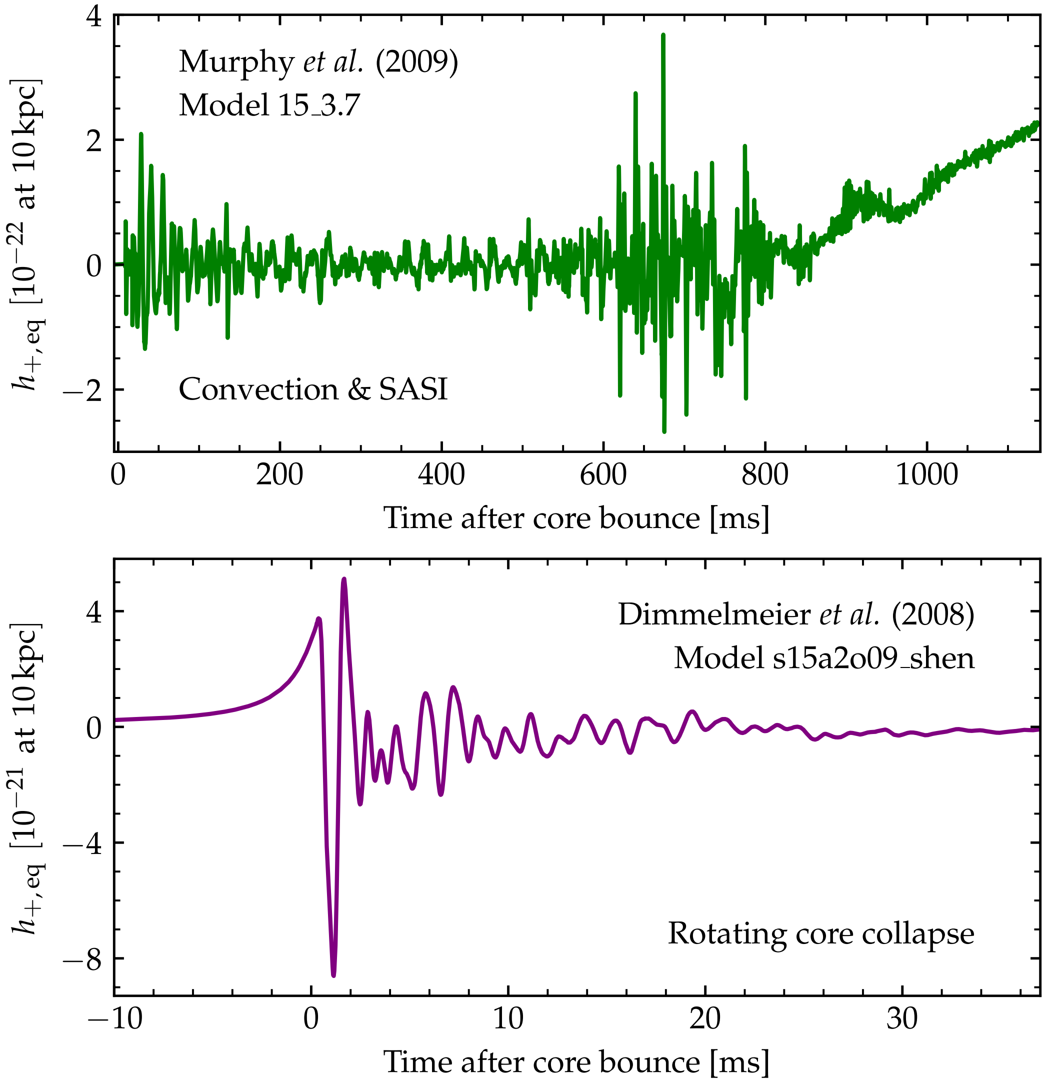

Figure 5.1: (Time domain GW strain for representative models of neutrino-driven explosions (top panel) and rotating core collapse (bottom panel), as seen by an equatorial observer at 10 kpc, drawn from the `C&S` and `RotCC` waveform catalogs, respectively [44, 52]. We note that the typical GW strain from rotating core collapse is roughly an order of magnitude larger than the typical GW strain from neutrino-driven explosions. In addition, the typical GW signal duration is more than an order of magnitude longer for neutrino-driven explosions than for rotating core collapse.

It is clear that the time domain structure of the `C&S` model is far more complex than that for the `RotCC` model.

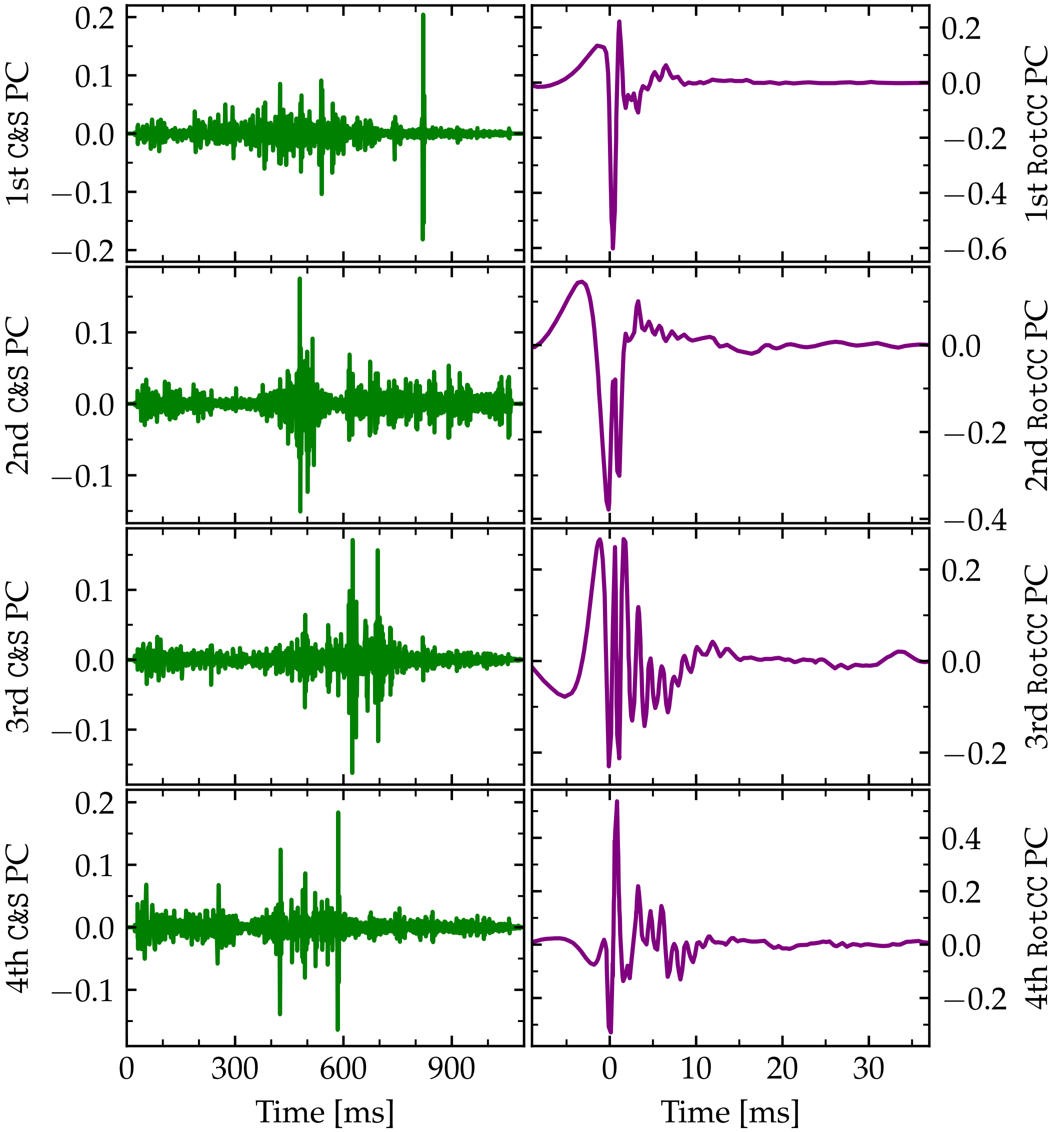

Figure 5.2: The first four PCs for the `C&S` model (left column) and `RotCC` model (right column) as a function of time.

Bayesian model selection

Given a data stream containing a GW signal from a CCSN buried in detector noise, our goal is to establish whether that signal is more likely to have originated from a CCSN borne of a non-rotating or rapidly rotating progenitor. In practice, we do this by attempting to reconstruct the unknown signal using either the `C&S` or `RotCC` PCs, and compute the evidence (or marginal likelihood) for each model. Explicitly, the evidence for the model $\mathcal{M}$ is given by

$$p\,(d|\mathcal{M}) = \int_{\vec{\mu}} \mathrm{d}\vec{\mu}\, p\,(d|\vec{\mu};\mathcal{M})\; p\,(\vec{\mu}|\mathcal{M})\;, \tag{5.3}$$

where $p\,(\vec{\mu}|\mathcal{M})$ is the prior distribution on the parameters $\vec{\mu}$ characterising the signal model $\mathcal{M}$, and $p\,(d|\vec{\mu};\mathcal{M})$ is the likelihood function for the data. The Bayes factor $B_{\mathcal{M}_1;\mathcal{M}_2}$ is the ratio of evidences for models $\mathcal{M}_1$ and $\mathcal{M}_2$. Numerically evaluating the evidence integral, particularly for a model characterised by a large number of parameters, is a computationally expensive task. `SMEE` tackles this problem by using nested sampling to calculate the evidence. In the interests of brevity, we don't discuss the particulars of nested sampling here, and instead direct the interested reader to L12, [228, 229, 235] and references therein.

Working in log-space for convenience, we first compute the Bayes factor for signal against noise;

$$\log B_{S,N} = \log[p\,(d|\mathrm{M}_S)] - \;log[p\,(d|\mathcal{M}_N)]\,, \tag{5.4}$$

where $\log B_{S,N} > 0$ and $\log B_{S,N} < 0$ indicate the signal model is preferred over noise and vice versa, respectively. The Bayes factor comparing the two signal models, $\log B_{\texttt{RotCC}-\texttt{C\&S}}$, then follows;

$$\log B_{\texttt{RotCC}-\texttt{C\&S}} = \log B_{\texttt{RotCC},N} - \log B_{\texttt{C\&S},N}\,. \tag{5.5}$$

If $\log B_{\texttt{RotCC}-\texttt{C\&S}} > 0$, the signal is represented more faithfully on the `RotCC` basis than the `C&S` basis and, by extension, we posit is more likely to have originated from the core collapse of rapidly rotating progenitor and magnetorotationally-driven explosion. Conversely if $\log B_{\texttt{RotCC}-\texttt{C\&S}} < 0$, the signal is better represented on the `C&S` basis than the `RotCC` basis, and is (hypothetically) more likely to have originated from the core collapse of a non-rotating progenitor and explosion driven by neutrino heating and hydrodynamic instabilities. The caveats of this approach are discussed in detail in Sec. 5.5.

Signal model

Trial signals produced by the `C&S` and `RotCC` models are parameterised by PC coefficients $\vec{\epsilon}$, sky location $(\alpha,\,\delta)$, distance D, and arrival time at geocenter t_c. GW strain is first constructed on one of the bases using Eq. 5.2, drawing $\vec{\epsilon}$ from within the prior ranges. In this study, we employ uniform priors across the range set by the catalog waveforms, padded by 10% to account for uncertainty due to the incompleteness of the bases. In L12, evidences were computed using both three and seven PCs to compare 'sparse' and 'dense' representations respectively. Here, we calibrate the number of PCs to maximise the reeconstruction ability while avoiding the Occam's razor penalty incurred by an overcomplex model. We discuss this calibration process in Sec. 5.3.

The other parameters mentioned adapt the trial GW strain to account for antenna response of the detectors, source distance, and different signal arrival times in multiple detectors. As a nearby CCSN is expected to have both observed EM and neutrino counterparts, we fix the sky location of the source to be a known parameter. As `SMEE2G` is intended as a follow-up analysis rather than a detection pipeline, a time of arrival will be known within some small uncertainty window from the external trigger. While it is not expected that GWs from CCSNe would be found by an online search for GW bursts unless the source is within $\sim 1kpc$ or so, the SNEWS alert triggered by the neutrino signature will establish a window of uncertainty over which to scour with offline GW searches [242]. It has also been shown that the time of core bounce can be established from the neutrino counterpart to within a few tens of milliseconds [190], which can further reduce the uncertainty in arrival time. Uniform priors in distance and arrival time are employed.

5.3 Analysis

In this section, we discuss the specifics of the analysis procedure used for the results presented in this Chapter. We detail calibration of the number of PCs for `C&S` and `RotCC` models, discuss the noise model and injection procedure, and investigate `SMEE2G`'s response to realistic noise.

Calibration

In L12, the relative complexity of the `C&S` and `RotCC` models was not taken into consideration when choosing the number of PCs to use. Here, we discuss calibration of these models to optimise the choice of number of PCs; maximising reconstruction ability while not self-penalising for unnecessary complexity.

It is customary to achieve this by studying the individual and cumulative variance encompassed in the PCs, opting for the quantity which contains some fraction of the total variance [243]. This method, however, only considers influence from the catalog waveforms, ignoring the implications of Occam's razor penalties imposed by Bayesian model selection methods. Should the waveform catalogs be incomplete (discussed in Sec. 5.5), signal SNR be low, or data stream contaminated by noise transients, unnecessary errors may be introduced [228]. To this end, we use the behaviour of $\log B_{S;N}$ for each model as a function of the number of PCs as a metric for establishing the optimal basis size. In Fig. 5.3, we show $\log B_{S;N}$ as a function of the number of PCs used to reconstruct the catalog waveforms for the `RotCC` and `C&S` models, in the context of catalog waveforms injected at SNR=20 into simulated Gaussian noise.

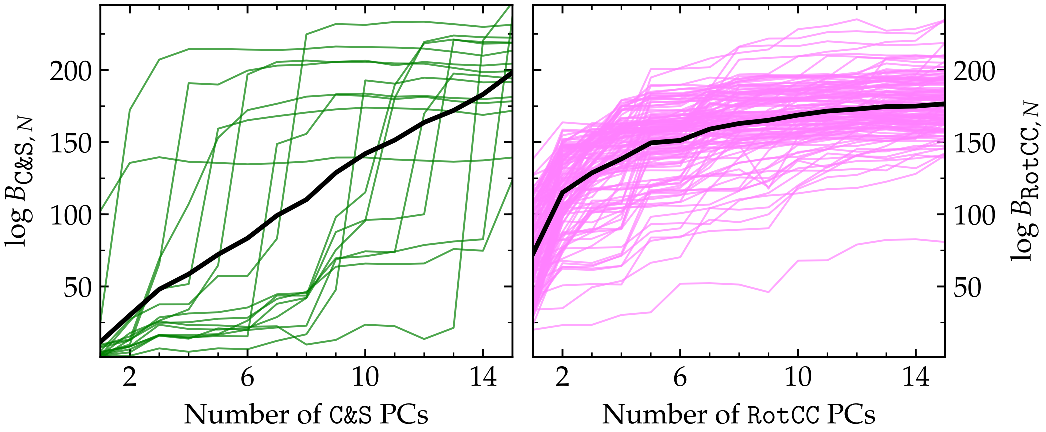

Figure 5.3: $\log B_{S;N}$ as a function of increasing number of PCs for the `C&S` model (left panel) and `RotCC` model (right panel) as calculated using catalog waveforms (colored traces), with the mean behaviour across the catalog overlaid with a thick black line.

As the number of PCs increases, a more complex signal can be reconstructed to match that present in the data, and consequently $\log B_{S;N}$ increases. After the ideal number of PCs has been exceeded, the improved signal match is outweighed by the penatly for a more complex model, and the Bayes factor will plateau or even begin to decrease.

We see that the variance in $\log B_{S;N}$ across the catalog is much smaller for the `RotCC` model than the `C&S` model. This is to be expected for two reasons. First, the dominant features of the signal itself from rotating core collapse are far simpler; bounce and ringdown of a rotating fluid body as opposed to the complex and detailed structure in the time domain signal from the `C&S` model. Furthermore, the catalog size is far greater for the `RotCC` model than the `C&S` model, compounding the complexity issue; not only is the signal simpler for rotating core collapse, but a larger sample of waveforms means the PC basis produced is much closer to complete. With the `C&S` model, the time domain evolution of the waveforms are fantastically messy; the result of turbulent hydrodynamic instabilities, manifestly stochastic in nature, that do not scale in any simple way with ZAMS mass or neutrino luminosity. The signal requires a greater number of PCs to reconstruct the complex structure, but the waveform catalog is also woefully incomplete. This is an unfortunate but unavoidable problem, as the large scale parameter studies with 3D general-relativistic simulations implementing faithful neutrino transport and accurate microphysics simply do not yet exist. The consequences of this, as well as potential research directions to explore to circumvent this issue, is explored in detail in Sec. 5.5.

The ideal number of PCs for the `RotCC` model is clearly much smaller than for the `C&S` model. Using one model dependent on significantly more parameters than the other, however, can unfairly penalise the more complex model for low SNR signals or glitchy data even when it more faithfully reconstructs the observations. Being mindful of this concern, we conservatively choose six PCs for the `RotCC` model, and nine PCs for the `C&S` model.

Injection procedure

In L12, a single Advanced LIGO (aLIGO) detector with simulated Gaussian noise and maximal antenna response to linearly polarised signals was considered. Here, we explore a three-detector network comprised of the two aLIGO detectors and Advanced Virgo (AdVirgo) detector, hereafter referred to as H1, L1, and V1, respectively. We employ non-Gaussian, non-stationary detector noise as taken by H1 and L1 during the S5 science run, recolored to aLIGO design sensitivity, in addition to real data taken by V1 during the VSR1 science run, recolored to AdVirgo design sensitivity. The procedure used to recolor these data is outlined in Chap. 4, while the raw data from S5 and VSR1 are publicly available for the interested reader via the GW Open Science Center (GWOSC) [218].

In addition to more realistic noise, we also use accurate antenna response functions for the detectors considered. As previously discussed in Chap. 4, the antenna response of the detectors is periodic with an associated time scale of one sidereal day, due to the rotation of the Earth. As this analysis considers data stretches far shorter than this, the antenna sensitivity to a particular sky position is strongly dependent on the time of day. To account for this, we repeat this analysis at ten different GPS times spread throughout a sidereal day, and average over the results.

We inject signals into realistic noise considering two sources; one in the direction of the galactic center, and one in the direction of the LMC. We first establish the sensitivity of our method using catalog waveforms to assert analysis viability. We then repeat the analysis using additional waveforms drawn from the catalogs employed for the sensitivity study in Chap. 4. Specifically, we use waveforms `yak`, `müller1`, `müller2`, `müller3`, and `ott` to test the `C&S` model. For the `RotCC` model, we use `sch1`, `sch2`, and three waveforms drawn from the waveform catalog produced by Abdikamalov *et al.* [60] (denoted `abd1`,`abd2`, and `abd3`), which is presented in Chap. 6.

Response to Noise

In L12, the response of `SMEE` to simulated Gaussian noise was studied to more accurately quantify the Bayes factor between two models when run on data containing signals. We calculate the response of `SMEE2G` to simulated Gaussian noise for aLIGO and AdVirgo at design sensitivity using six PCs for the `RotCC` model and nine PCs for the `C&S` model, accounting for the relative complexity of the models. We then repeat this analysis using recolored noise to compare and contrast how `SMEE2G`'s response to noise changes in the present of glitchy data.

In Fig. 5.4, we show $\log B_{S;N}$ for the `C&S` and `RotCC` models as run on 1000 instances of simulated Gaussian noise and recolored S5/VSR1 noise for a three-detector network at design sensitivity. For the Gaussian and recolored noise respectively, we see that the mean $\log B_{S;N}$ for the `C&S` model are -23 and -19. For the `RotCC` model, the mean $\log B_{S;N}$ for the Gaussian and recolored noise are -12 and -9, respectively. We see that for both the `C&S` and `RotCC` models, the distributions of $\log B_{S;N}$ characterising `SMEE2G`'s response to recolored S5/VSR1 noise are less negative and more broadly distributed. This is to be

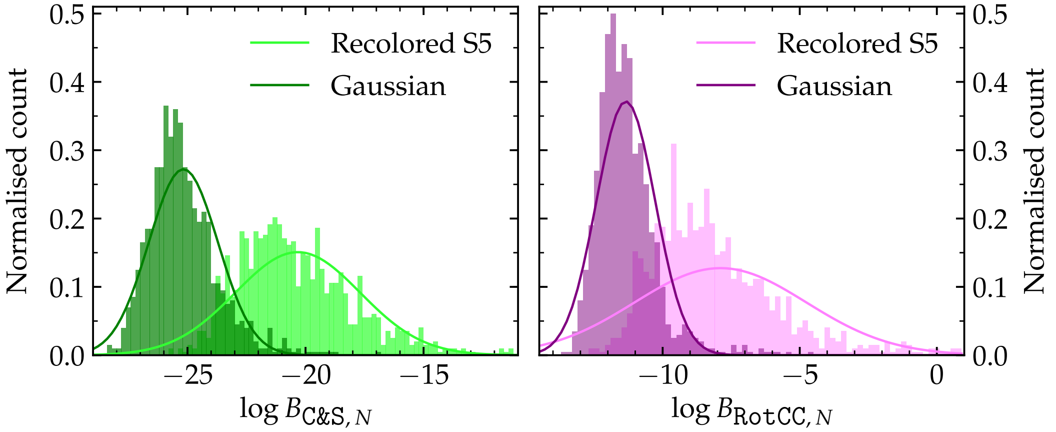

Figure 5.4: (Left panel) Histograms of $\log B_{S;N}$ as obtained by running `SMEE2G` on one thousand instances of simulated Gaussian noise (forest green) and recolored S5/VSR1 noise (neon green) for a three-detector network at design sensitivity using six PCs from the `C&S` model. Overlaid are normalised Gaussians characterised by mean and variance of the histogrammed $\log B_{S;N}$ data for simulated noise (solid forest green trace) and recolored noise (solid neon green trace). (Right panel) As for the left panel but using nine PCs from the `RotCC` model. Histograms and overlaid Gaussian traces for simulated and recolored noise are shown in deep purple and baby pink, respectively.

expected, as short duration noise transients and lines in the data can be mistaken for signals. Over the thousand instantiations of recolored noise, the broadened distribution is representative of how time-varying noise characteristics can alter `SMEE2G`'s response. To account for this, we increase the threshold on $\log B_{S;N}$ for correct identification to 10 from the threshold of 5 employed in L12.

5.4 Results

In this section, we put `SMEE2G` into practice; first, testing the ability to recover catalog waveforms correctly within the galaxy and the LMC, before using non-catalog waveforms to establish the model selection capabilities of our method.

Catalog waveforms

We inject all waveforms from the `C&S` and `RotCC` catalogs into recolored data from the S5/VSR1 science runs for a three-detector network at design sensitivity, considering sources in the direction of the galactic centre at distances 2 kpc, 10 kpc, and 20 kpc, and a single source in the direction of the LMC at 50 kpc away. We compute Bayes factors comparing the evidence for `C&S` and `RotCC` models to establish which better describes the data at hand. We repeat the analysis at ten different GPS times over a sidereal day to account for time-variability of the detectors' antenna response, before averaging the results over the times considered. We require $\log B_{S;N} > 10$ to consider the signal model preferred over noise. Comparing evidences for the `RotCC` and `C&S` models, we require $\log B_{\texttt{RotCC}-\texttt{C\&S}} > 10$ to consider the `RotCC` model chosen over the `C&S` model. Conversely, we require $\log B_{\texttt{RotCC}-\texttt{C\&S}} < -10$ to consider the `C&S` model preferred over the `RotCC` model. Should $-10 < \log B_{\texttt{RotCC}-\texttt{C\&S}} < 10$, we determine it is not possible using this method to definitively distinguish between the two models.

In Fig. 5.5, we show histograms of $\log B_{\texttt{RotCC}-\texttt{C\&S}}$ for catalog waveforms from the `RotCC` and `C&S` models injected in the direction of the galactic center at distances of 2 kpc, 10 kpc, and 20 kpc, in addition to injections in the direction of the LMC at 50 kpc.

For sources at 2 kpc in the direction of the galactic centre, we see that all catalog waveforms are correctly identified. In the same spatial direction but at a greater distance of 10 kpc, most `RotCC` waveforms and $\sim$ 82% of `C&S` waveforms are correctly identified, but neither model is preferred for over a quarter `C&S` waveforms and a couple of `RotCC` waveforms. This is to be expected when comparing to the detectability results presented in Chap. 4, which shows that 50% detection efficiency for GWs from CCSNe driven by neutrino heating and hydrodynamic instabilities is reached at just a few kpc. At 20 kpc, this trend is continued with less than 30% of `C&S` waveforms correctly identified. Despite the 50% detection efficiency being far exceeded at this distance, the `C&S` model is still preferred for a small fraction of these waveforms. While this may at first seem counter intutitive, we remind the reader that these waveforms are all optimally-oriented (i.e. as seen by an equatorial observer) and that for linearly polarised waveforms, the polarisation factor $\sin^2 \iota$ is degenerate with distance. Furthermore, this analysis

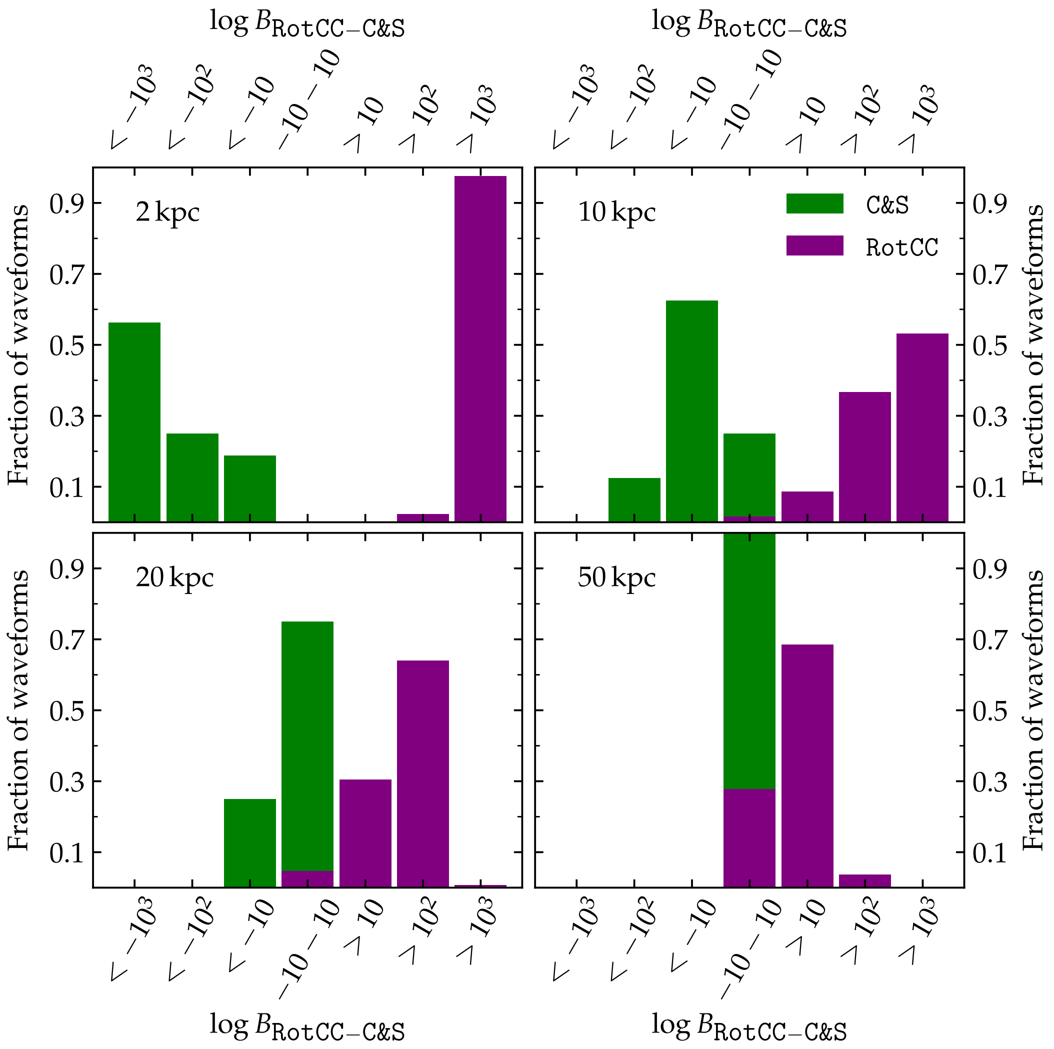

Figure 5.5: Histograms of $\log B_{\texttt{RotCC}-\texttt{C\&S}}$ for waveforms from the `RotCC` and `C&S` catalogs, shown in deep purple and dark green, respectively. Sources in the direction of the galactic centre at a distance of 2 kpc (top left panel), 10 kpc (top right panel), 20 kpc (bottom left panel) are considered, in addition to a source at 50 kpc in the direction of the LMC (bottom right panel). $\log B_{\texttt{RotCC}-\texttt{C\&S}} > 10$ indicates the `RotCC` model is favoured, $\log B_{\texttt{RotCC}-\texttt{C\&S}} < -10$ indicates the `C&S` model is favoured, while $-10 < \log B_{\texttt{RotCC}-\texttt{C\&S}} < 10$ indicates neither model is preferred.

employs information on the waveform morphology to reconstruct signals buried in noise, which is a far more sensitive signal extraction method than the excess-power approach used in Chap. 4. While it may seem puzzling then that this method is not preferred over an excess-power search when aiming to observe GWs from CCSNe, we emphasise that due to the stochastic nature of the dynamics driving GW emission in CCSNe (particularly for non-rotating progenitors), the GW phase is not robustly predictable. This means that while signal analysis methods can in principle be used to carry out time domain template-inspired searches for GWs from CCSNe driven by neutrino heating and hydrodynamic instabilities, it is a fruitless endeavour as GWs from the next CCSN will not have the same phase evolution. This lies at the heart of the limitations associated with this analysis, and are discussed in depth in Sec. 5.5.

Conversely for the `RotCC` waveforms, we see that over 90% are still correctly identified for a hypothetical galactic source at 20 kpc, while around $\sim 75\%$ are correctly identified for a source at 50 kpc in the LMC. These results are consistent with the detection efficiencies for rotating core collapse presented in Chap. 4, with the same caveat regarding degeneracy between polarisation factor $\sin^2 \iota$ and source distance applicable. While the GW signature from rapidly rotating core collapse is expected to have at least some stochastic component from prompt convection, this occurs after around 30 ms, and so the first $\sim$ 25 ms of the GW signature (associated with bounce and ringdown of a millisecond PNS) is thought to be fairly robust. This forms the basic motivation for the work presented in Chap. 6, thus a broader discussion is saved for there.

Testing robustness with non-catalog waveforms

As touched upon briefly in Sec. 5.4, it is very likely that the waveforms comprising the `RotCC` and `C&S` catalogs will not exactly match the GW emission from the next nearby CCSN. As such, it is important to test the robustness of this method by using `SMEE2G` on non-catalog waveforms. Using the extra waveforms introduced in 5.3, we repeat the analysis outlined in Sec. 5.4 to establish if the `RotCC`, `C&S`, or indeed neither model is preferred.

In Fig. 5.6, we show histograms of $\log B_{\texttt{RotCC}-\texttt{C\&S}}$ for the non-catalog `C&S` waveforms (`yak`, `müller1`, `müller2`, `müller3`, and `ott`, shown in dark green) and non-catalog `RotCC` waveforms (`sch1`, `sch2`, `abd1`, `abd2`, and `abd3`, shown in deep purple) for hypothetical sources in the direction of the galactic center at distances of 2 kpc, 10 kpc, and 20 kpc, and at 50 kpc in the direction of the LMC.

We see that all non-catalog `RotCC` waveforms are correctly identified for hy-

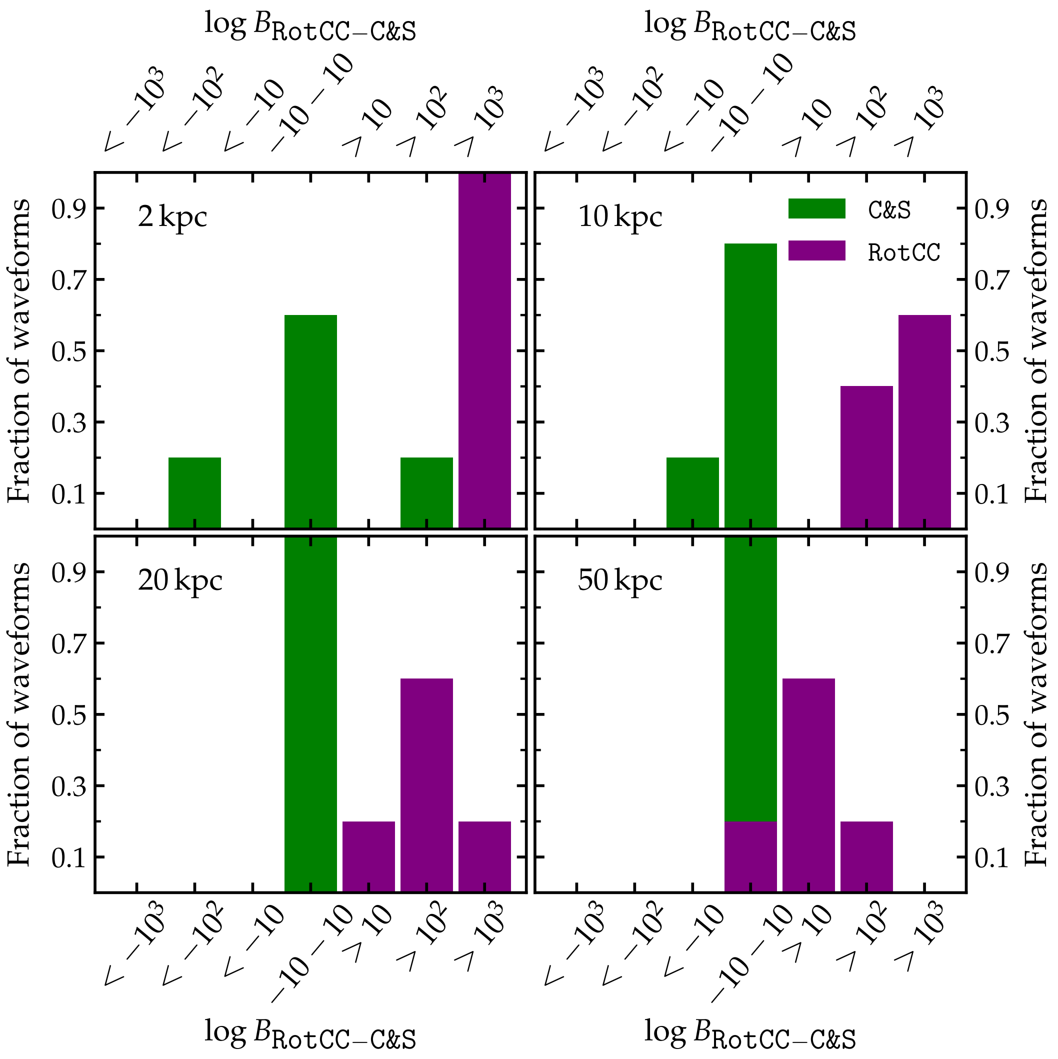

Figure 5.6: Histograms of $\log B_{\texttt{RotCC}-\texttt{C\&S}}$ for non-catalog waveforms for `RotCC` and `C&S` explosion mechanisms shown in deep purple and dark green, respectively. Sources in the direction of the galactic centre at a distance of 2 kpc (top left panel), 10 kpc (top right panel), 20 kpc (bottom left panel) are considered, in addition to a source at 50 kpc in the direction of the LMC (bottom right panel). $\log B_{\texttt{RotCC}-\texttt{C\&S}} > 10$ indicates the `RotCC` model is favoured, $\log B_{\texttt{RotCC}-\texttt{C\&S}} < -10$ indicates the `C&S` model is favoured, while $-10 < \log B_{\texttt{RotCC}-\texttt{C\&S}} < 10$ indicates neither model is preferred.

pothetical sources throughout the galaxy. At 50 kpc, $\sim$ 80% of non-catalog `RotCC` waveforms respectively are identified correctly.

For the non-catalog `C&S` waveforms, a far less successful tale is told. At 2 kpc, only $\sim$ 20% of injected waveforms are correctly identified. We note that all these waveforms were of type `yak`. Of the three `müller` waveforms, neither `C&S` or `RotCC` model was preferred. The `ott` injections, however, were misidentified with the `RotCC` model. While unfortunate, this is certainly not surprising. Addressing first the `müller` injections, we showed in Chap. 4 that their 50% detection efficiency distances were only a couple of kiloparsecs or so. Aiming to reconstruct these unpolarised signals on a linearly polarised basis, not to mention one with different time domain structure, is a tall order indeed. As most GW energy in these waveforms is emitted at later times (after ~ 500 ms or so), little overlap with the shorter `RotCC` waveforms could be found. Contrastingly, the `yak` waveform originates from a 2D simulation and so is linearly polarised, has a similar morphology to at least some of the `C&S` catalog waveforms, and was shown to be detectable out to ~ 8 kpc with the excess-power analysis in Chap. 4. It is thus plausible that these waveforms could be successfully identified using the `C&S` basis, even for a source at 10 kpc. Given that the explosion dynamics and, consequently, the time-domain GW emission are so disparate between 2D and 3D simulations for CCSNe from these non-rotating progenitors, it suggests that constructing PC bases from time-domain signals is not really viable for realistic `C&S` signals. We discuss this more in Sec. 5.5. Finally for the `ott` waveform, which is misidentified by the `RotCC` model at 2 kpc and thereafter indistinguishable from noise, we note again that this waveform originates from a 3D simulation. Unlike the `müller` waveforms however, the simulations were only followed for a couple hundred milliseconds after core bounce due to computational limitations. This meant that GW power from turbulent downplumes striking the PNS and wave trapping from PNS convection was muted, and certainly not dominant as seen in the `C&S` catalog, `müller`, and `yak` waveforms. GW emission at early times from prompt convection, however, was strong. While this feature is seen in the `C&S` basis, the lack of power at later times downweighted the probability that this waveform belonged to the `C&S` model. While GW power seen in this waveform after ~ 200 ms could not be matched by the `RotCC` basis simultaneously with early GW emission, partial reconstruction of GW emission either associated with prompt convection or neutrino driven convection meant the `RotCC` model was ultimately chosen by `SMEE2G` as more probable. This again brings us back to the problematic issue of differences in dynamics and waveform morphology seen between 2D and 3D simulations of CCSNe, which is pondered upon in Sec. 5.5.

5.5 Discussion

We have revisited the `SMEE` pipeline introduced in L12 to develop the refined post-detection analysis pipeline `SMEE2G`, and applied the updated method to realistic observational scenarios. In this Section, we address uncertainties and assumptions impacting our results, discuss fundamental limitations inherent to this type of post-detection inference pipeline, and ponder future directions for study.

We use the same waveform catalogs for `C&S` and `RotCC` models as employed in L12, acknowledging the limitations associated with the employ of linearly polarised waveforms from axisymmetric simulations rather than their three-dimensional counterparts. In the context of the `C&S` model, there is no doubt that the multidimensional hydrodynamic instabilities driving CCSNe from non-rotating progenitors exhibit markedly different behaviour in two- and three- dimensions (see, e.g., [244–246]), but large scale studies studying the model dependence of GWs for CCSNe from non-rotating progenitors in three dimensions simply do not exist. While waveform catalogs could in theory be amassed from results from a number of different simulations, the dependence of the GW signal on different approximations and implementation of source physics is decidedly unknown. Indeed, only recently have studies exploring the impact of approximations on simulation dynamics and between differnt simulation codes begun to enter the foray (see, e.g. [26, 71, 247, 248]). Furthermore, use of two-polarisation waveforms from three-dimensional simulations to produce PCs introduces another concern, namely observer dependence of the GW signature. Aside from the obvious changes associated with phase evolution (although this brings up its own questions regarding the suitability of an analysis assuming a stochastic signal's phase evolution can be modelled), it has also been shown that even the GW spectrum may be markedly observer dependent (see, e.g. [67]). For the `RotCC` model, we note the dynamics of collapse, bounce, and ringdown approach axisymmetric for precollapse cores with rapid rotation. While triaxial deformation may well develop after timescales of $\sim 100\,\mathrm{ms}$ or more in millisecond PNSs from secular instabilities (see, e.g., [65]), we save consideration of these effects to future studies.

Addressing now concerns arising from use of incomplete waveform catalogs, we recall that the use of PCA implicitly assumes that the catalog used to produce the PCs encompasses all possible variations. While this is true for neither the `RotCC` or `C&S` catalogs, the complex signal and minute catalog size for the `C&S` catalog amplifies the impact. This is seen when computing the Bayes factor as a function of number of PCs for `C&S` catalog waveforms, where we see the evidence for the `C&S` model relative to noise continues to grow linearly with each added PC. This effect is compounded by the (admittedly well motivated) choice to use fewer PCs for the `C&S` model to avoid penalties for model complexity when compared with the `RotCC` model. Noting that, due to computational limitations, three-dimensional simulations are often only run for a few hundred milliseconds post-bounce resulting in an artificially short signal, it is perhaps not surprising that the `ott` waveform was misidentified with the `RotCC` model.

Discussion of the aforementioned issues naturally leads to considerations on the overall suitability of this method to the problem at hand. It is crucial to note that the phase evolution of GW emission sourced by stochastic processes, such as for example PNS oscillations excited by convective plumes and turbulent downflows striking the PNS surface, is not robustly predictable. While signal reconstruction techniques in either the time- or frequency-domain can be applied in principle to a particular instantiation of a stochastic GW signal, the exercise is little more than academic, as the phase evolution will be different for each simulation. Taking this into account, the use of PCs constructed from time-domain or frequency-domain waveforms is really not applicable for GWs from garden-variety CCSNe. While the signal evolution in the time-frequency plane is thought to be robustly predictable, the issue of observer-dependent spectra complicates matters. Indeed, it would seem that the logical way to proceed would be to consider the GW emission from first principles; estimate the temporal evolution of PNS oscillation modes. This approach is expected to be far more robust than constructing basis vectors from incomplete waveform catalogs with poorly understood systematic errors, and much research on PNS oscillations has been pursued (see, e.g., [249–252]). This approach is discussed more in Sec. 8. Beyond waveform modelling, we note the opportunity to improvement to any analysis concerning signals in non-Gaussian noise by incorporating a model for noise transients [169, 253].

5.6 Conclusions

We have augmented the `SMEE` analysis pipeline presented in L12 to consider realistic observational scenarios. Implemented in LALInference, and rewritten in Python in preparation for open-source release, `SMEE2G` boasts functionality to inject unpolarised signals into realistic non-Gaussian, non-stationary data for a three-detector network, employing accurate antenna response patterns as a function of temporal and spatial source location. Using waveform catalogs amassed from CCSN simulations of non-rotating progenitors (`C&S` model; GW emission is dominated by stochastic excitation of PNS oscillations by convection and SASI) and rotating progenitors (`RotCC` model; GW emission dominated by formation and ringdown of millisecond PNS), we construct PCs encompassing the dominant waveform features of each catalog. We use `SMEE2G` to project a given dataset (comprised of noise and unknown signal) onto each set of basis vectors, using Bayesian model selection methods to establish whether the `RotCC` or `C&S` models best represent the observations.

We calibrate our analysis, optimising the number of PCs used for each model, and exploring the pipeline response to non-Gaussian noise. We choose the number of PCs for each model to faithfully encompass dominant waveform features while avoiding penalties for superfluous model complexity. For the `RotCC` model, contructed from an extensive waveform catalog covering large swathes of the parameter space describing angular momentum distribution of the precollapse core, features of the simple signal morphology from core collapse, bounce and ringdown are captured with the first few PCs. For the `C&S` model, produced from a woefully undersampled (but largest publicly available) catalog, the complex waveform morphology is not well captured without employ of all PCs. Systematic penalty from using one model far more complex than the other is sidestepped by opting for three additional PCs than chosen for the `RotCC` model, at the expense of more faithful waveform reconstruction. To account for the wider distribution of pipeline responses to non-Gaussian noise, we increase the threshold for statistical significance imposed on the Bayes factor from 5 (as used in L12 for Gaussian noise) to 10.

For a hypothetical galactic CCSN at 2 kpc, we find all catalog waveforms correctly identified with their respective models. At 10 kpc, many of the `C&S`

catalog waveforms and the vast majority of the `RotCC` waveforms are correctly identified. At 20 kpc, less than a quarter of the `C&S` catalog waveforms are correctly identified, while around 90% of the `RotCC` catalog waveforms remain distinguishable. At 50 kpc for a CCSN in the LMC, no `C&S` waveforms are identified, but 75% of the `RotCC` catalog waveforms can be distinguished.

Considering then non-catalog waveforms assorted from a mélange of two- and three-dimensional simulations, we find disparate results. For the additional `RotCC` waveforms, all are correctly identified for galactic sources, while 80% are still distinguished for a source at 50 kpc. For the additional `C&S` waveforms, only the linearly polarised waveform (`yak`) is correctly identified, at 2 kpc and 10 kpc. Of the waveforms from three-dimensional simulations, neither `RotCC` or `C&S` model is preferred for waveform at 10 kpc and beyond. At 2 kpc, neither model is preferred for the `müller` waveforms, while the `ott` waveform is incorrectly identified with the `RotCC` model.

Differences in the nature of turbulent convection and the SASI in two- and three-dimensions are profound, causing marked discrepancies between the GW signatures. While constructing the `C&S` model instead from an array of three-dimensional simulations is one approach to pursue, this does not address fundamental limitations associated with this method from (i) sparse population of waveform catalogs, (ii) the manifestly stochastic phase evolution of GW emission from PNS oscillations excited by convective plumes, turbulent fluid downflows, and bulk motion associated with the SASI, and (iii) observer dependence of waveform polarisation. Similarly, constructing PCs from spectrograms may well address points (i), (ii), but do not overcome issue (iii). We conclude instead that modelling the time-frequency evolution of the PNS oscillation modes using semi-analytic techniques is the most promising approach to extract astrophysical information from observations of GWs from garden-variety CCSNe.

6 Measuring the angular momentum distribution of the pre-collapse core

The meaner Regina was to her, the more Gretchen tried to win Regina back. She knew it was better to be in the plastics, hating life, than to not be in at all. Because being with the plastics was like being famous... people looked at you all the time and everybody just knew stuff about you.

—Cady Heron, *Mean Girls*

[1] E. Abdikamalov, S. Gossan, et al. Measuring the angular momentum distribution in core-collapse supernova progenitors with gravitational waves. Phys. Rev. D 90 (4), 044001 (2014).
SEG led the signal analysis and detectability studies using waveforms produced by simulations ran by EA and AM, and wrote around one third of the manuscript.

6.1 Motivation

Garden-variety CCSNe typically have characteristic explosion energies of order 10^{51} erg (see Chap. 3 for a detailed discussion). There exists, however, a small subset of the CCSN population (roughly $\sim 1-2\%$; see [123]) with inferred explosion energies of up to 10^{52} erg. Quibbles with respect to the fine details of the so-called neutrino mechanism aside, such large explosion energies require a central engine able to convert the gravitational binding energy available from PNS formation much more efficiently into explosive outflow.

One favoured theory is the formation of a millisecond magnetar, where rotational energy and winding of magnetic field lines drive jet-like outflows (see, e.g., [131, 227, 254–258]), and onset of the magnetorotational instability (MRI) may power an associated LGRB (see, e.g., [206, 259]). We note that many of these super energetic CCSNe were identified as belonging to spectral class Type Ic-BL, characterised by compact progenitors absent of hydrogen and helium, and strongly Doppler-broadened spectral lines from relativistic outflows (see, e.g. [260, 261]). Indeed, all CCSNe associated with LGRB counterparts have been of Type Ic-BL (see, e.g., [262, 263]). It is worth mentioning, however, that a few energetic outliers have been of type II, originating from stars with substantial hydrogen envelopes. It may be that appreciable pre-collapse rotation is what unites these otherwise disparate evolved stars.

A caveat, however; stellar evolution calculations and estimates of pulsar natal spins suggest that most massive stars are thought to possess precollapse cores with rotational periods in excess of $\sim 10\,\mathrm{s}$. Angular momentum losses through stellar winds and angular momentum redistribution through magnetic torques are typically cited as justification for these assertions (see, e.g., [200, 264]). Stellar evolution calculations however are for the most part one dimensional, and studies treating rotation in a self-consistent way are only now being published. Estimates of pulsar natal spins are typically based on magnetic dipole radiation, and may be subject to large errors if early spindown occured through rotational energy being sapped by magnetic field winding and the MRI (see, e.g., [265–267]).

Furthermore, it has been shown that wave-driven angular momentum transport in massive stars during the silicon/oxygen burning phase may spin up the core, setting up a strongly differential rotation profile and ensuring the rotation rate of the precollapse core is uncorrelated with that of the outer envelope [268]. Such methods are not expected to reduce the core rotational period beyond that cited above, and precollapse cores rotating extremely rapidly may require chemically homogeneous evolution at low metallicity (see, e.g. [269, 270]) or extended interaction with a binary companion to develop in nature [271]. Turning instead to post-collapse evolution, it has been shown that spiral modes of the SASI may spin up PNS in the time before the shock is revived and successful explosion launched [66, 272]. Rotating core collapse also naturally leads to differential rotation in the outer PNS and post-shock region [200, 273]. It is thus not unconceivable that rotational effects may impact on the core collapse and explosion dynamics of CCSNe that are not accompanied by LGRBs or don't exhibit ultrarelativistic outflows.

EM observations can be used to estimate the rotation rate of the stellar envelope in massive stars through astroseismology, while Doppler-broadening of spectral lines in CCSNe can be used to measure angular momentum in outflows. Both these techniques, however, yield only second-hand information at best on the angular momentum distribution of the precollapse core and nascent PNS. GWs however, as discussed in depth in Chap. 3, are a direct probe of the angular momentum distribution in NSs and CCSNe. Oblate deformation of the collapsing core naturally sources strong quadrupole emission, a characteristic GW signature associated with the collapse, bounce, and ringdown of the PNS. Strong differential rotation in the PNS may lead to the development of nonaxisymmetric fluid instabilities, notably the corotation instability, which results in extended quasiperiodic GW emission that lasts for timescales of a few hundred milliseconds (see, e.g., [19, 66, 135, 274, 275]). The GW signature from rotating core collapse is potentially observable out to the Magellanic Clouds (see Chap. 4). Previous studies (see, e.g., [52, 78, 276]) have demonstrated that the peak GW strain from PNS formation is dependent on the mass and angular momentum of the inner core at bounce, although little effect is attributed to the nuclear matter EOS. Furthermore, for PNSs with natal spin periods $\lesssim 5\,\mathrm{ms}$, the GW signal morphology is determined predominantly by the total angular momentum of the core, with little impact seen by varying its structure [78]. This is to be expected somewhat, as for precollapse cores forming such rapidly rotating PNSs, convection is significantly inhibited. Consequently, in this limit the GW signal from core collapse and early PNS evolution will take on an almost deterministic morphology that can be modelled as a function of angular momentum distribution in the core.

The goal of this Chapter is to expand upon previous studies to explore the dependence of the GW signature from rapidly rotating core collapse, bounce, and ringdown on the angular momentum distribution of the precollapse core. Furthermore, we develop a proof-of-principle concept study to investigate the potential to extract this information from the GW signal given observations of nearby CCSNe. To this end, we carry out a large set of axisymmetric general-relativistic CCSN simulations employing many progenitor cores with parameterised rotation profiles imposed to explore the impact across the parameter space of angular momentum distribution on the GW signal. Using the GW signals obtained from these simulations, we employ a template-based analysis inspired by numerical template banks for binary-black hole observations to explore the waveform variance across angular momentum parameter space. We then employ a Bayesian model selection analysis inspired by the study presented in 5 to explore the potential for identifying differential rotation in the precollapse core from the GW signature.

The rest of this Chapter is organised thus. In Sec. 6.2, we discuss the models for precollapse rotation employed and describe the simulations used to follow the dynamics through core collapse and early PNS evolution. In Sec. 6.3, we present the simulation data and waveforms produced, while we explore a proof-of-principle concept for extracting the angular momentum distribution of the precollapse core from the GW signature in Sec. 6.4. In Sec. 6.5, we discuss the implications of our results and highlight shortcomings of our analysis, before concluding and pondering future directions to be explored in Sec. 6.6.

6.2 Simulations

In this section, we discuss the simulation code used for core collapse and post-bounce evolution, in addition to the rotating progenitor models used to systematically study differences in evolution dynamics and GW signatures across the parameter space of angular momentum distribution.

Progenitor models

Evolution of presupernova stellar models including rotational effects are few and far between, while those that do exist typically employ spherically symmetric codes assuming shellular rotation (see, e.g., [264, 269, 277]). Recent work has studied the impact of wave-driven angular momentum transport on the rotation rate in the precollapse cores [268], but the undoubtably important effects of interaction with binary companions (see, e.g. [271]) are generally ignored.

The angular momentum distribution in the precollapse core is far from certain, which complicates a comprehensive study of the expected distribution in nature and the resultant impact on explosion dynamics and GW signature to no end. We opt to employ a single non-rotating progenitor model (a $12\,M_\odot$ progenitor with solar metallicity from [237] denoted s12WH07; we note that this progenitor was one of the four considered by Dimmelmeier *et al.* [52] to produce the 128 waveform catalog used in Chap. 5) and generate many 'rotating' progenitors through imposing a parameterised rotation profile. This provides simple control over the total angular momentum and its distribution throughout the precollapse core while performing a systematic parameter space study. We choose the cylindrical rotation law first proposed by Zwerger & Müller [278], which has since been employed by a number of studies concerning rotating core collapse (see, e.g. [26, 52, 65] to name a few). Parameterised by central angular velocity Ω_c and differential rotation length scale A, the angular velocity at cylindrical radial coordinate ϖ is;

$$\Omega(\varpi) = \Omega_\mathrm{c}\left[1 + \left(\frac{\varpi}{A}\right)^2\right]^{-1} , \tag{6.1}$$

which yields constant specific angular momentum where $\varpi \gg A$. While unclear how realistic this rotation law is, it doesn't violate any physical principles or constraints, and allows simple construction of many rotating progenitors. The validity of this approach was studied in [278], and has been the standard method to study impacts of angular momentum in the CCSN simulation community. For the discerning reader unconvinced by our hand-waving arguments, we note that this rotation law reproduces the radial angular momentum distribution seen in the inner $2\,M_\odot$ of rapidly rotating progenitor models 16TI and 16OM from Woosley & Heger [269] with reasonable accuracy. Imposing this rotation profile on the spherically symmetric progenitor we previously introduced, the core is rapidly subject to oblate deformation due to centrifugal effects as collapse proceeds.

We consider five model sets characterised by different length scales for differential rotation, $A \in \{A1, \ldots, A5\}$, where $A1 = 300\,\mathrm{km}$, $A2 = 417\,\mathrm{km}$, $A3 = 634\,\mathrm{km}$, $A4 = 1268\,\mathrm{km}$, and $A5 = 10000\,\mathrm{km}$. In Fig. 6.1, we show the angular velocity Ω as a fraction of Ω_c with enclosed mass coordinate for $A \in \{A1, \ldots, A5\}$ as imposed on the s12WH07 progenitor model.

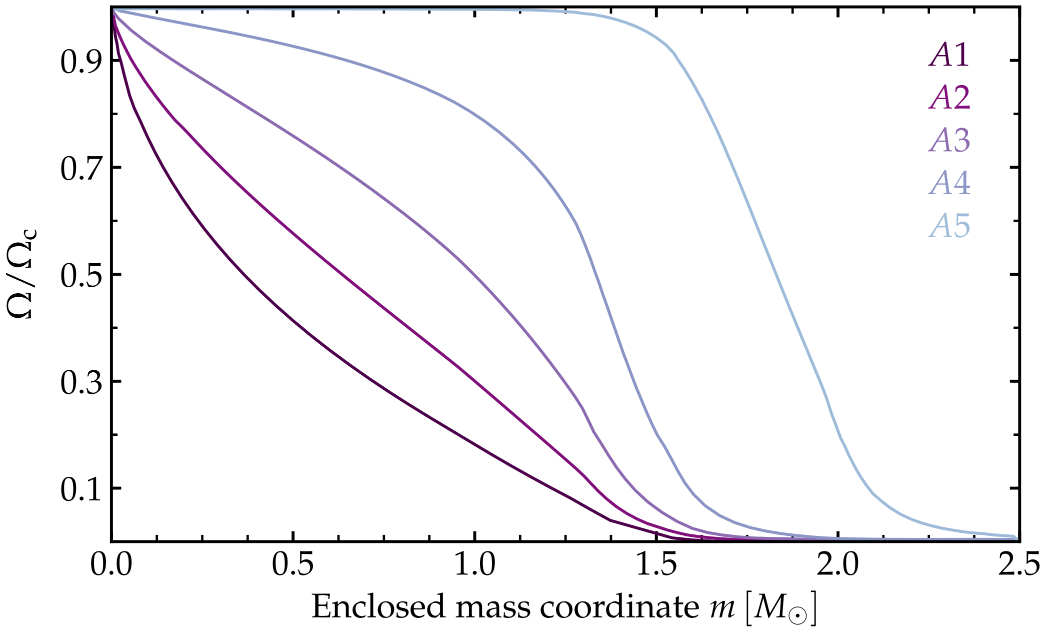

Figure 6.1: The ratio of angular velocity Ω to the central angular velocity Ω_c as a function of enclosed mass coordinate along the equatorial plane for the five differential rotation length scales $A \in \{A1, \ldots, A5\}$ considered in this study (see Tab. 6.1), as imposed on progenitor model s12WH07 from [237].

Here, $A1$ is chosen to represent strongly differential rotation, and $A3$ (as used in [78]) produces an angular momentum profile where Ω at enclosed mass coordinate of $1\,M_\odot$ is equal to $\Omega_c/2$. Of the remaining, $A2$ lies halfway between $A1$ and $A3$, $A4$ is twice that of $A3$, and $A5$ ensures close to uniform rotation across the inner $1.5\,M_\odot$.

For each A model, we generate sequences of progenitors with increasing central angular velocity $\Omega_c \in \{1, 1.5, \ldots, \Omega_{c,\,\mathrm{max}}\}$ rad/s, where $\Omega_{c,\,\mathrm{max}}$ set dependent on A. For models with strong differential rotation ($A1$ and $A2$), we choose $\Omega_{c,\,\mathrm{max}}$ such to obtain the global maximum of $\beta_{\mathrm{ic,\,b}} = (T/|W|)_{\mathrm{ic,\,b}}$, the ratio of rotational kinetic energy to gravitational potential energy of the inner core at bounce, where we compute $T/|W|$ using the expression in [279]. The choice to focus on the inner core is motivated by studies (see, e.g. [52, 276]) that show the GW signal and the dynamics of core bounce are dependent on the mass and spin of the inner core. For models characterised by moderate to weak differential rotation ($A3$, $A4$, and $A5$), $\Omega_{\mathrm{c,max}}$ is chosen by the maximum central anguglar velocity at which collapse will still occur.

Model sequence	A [km]	$\Omega_{\mathrm{c,min}}$ [rad/s]	$\Omega_{\mathrm{c,max}}$ [rad/s]	$\beta_{\mathrm{ic,b,min}}$ [10^{-2}]	$\beta_{\mathrm{ic,b,max}}$	Number of models
$A1$	300	1	15.5	1.62	0.21	30
$A2$	417	1	11.5	3.13	0.19	22
$A3$	634	1	9.5	3.58	0.18	18
$A4$	1268	1	6.5	4.66	0.13	12
$A5$	10000	1	5.5	5.15	0.11	10

Table 6.1: Summary of the key parameters defining our model sequences in differential rotation length scale A and central angular velocity Ω_{c}. Here, $\Omega_{\mathrm{c,\,min}}$ and $\Omega_{\mathrm{c,\,max}}$ are the minimum and maximum central angular velocities considered for a particular A, while $\beta_{\mathrm{ic,\,b,\,min}}$ and $\beta_{\mathrm{ic,\,b,\,max}}$ are minimum and maximum values of the ratio of rotational kinetic energy to gravitational potential energy obtained for the inner core at bounce. For strongly differentially rotating models $A1$ and $A2$, $\Omega_{\mathrm{c,\,max}}$ is chosen according to where $\beta_{\mathrm{ic,\,b,\,max}}$ exists. For models exhibiting moderate or weak differential rotation ($A3$, $A4$, and $A5$), $\Omega_{\mathrm{c,\,max}}$ is set by the maximum central angular velocity for which collapse still proceeds.

In Tab. 6.1, we summarise the key parameters characterising the model sequences we construct in A and Ω_{c}.

CoCoNuT

We perform simulations using `CoCoNuT` , an axisymmetric hydrodynamic evolution code (extensively described in [52, 238, 239, 276]) that implements general relativistic effects through the conformal flatness approximation. It has been shown extensively that methods employing the CFC approximate full general relativity in the context of rotating core collapse to millisecond PNS formation, particularly in the regime concerning strongly differential rotation [280–282]. Indeed, for the short timescales following core bounce considered in this study, systematic errors introduced through use of the CFC are far dwarfed by those associated with uncertainties in the nuclear matter EOS and approximate neutrino transport. The particular version of `CoCoNuT` implemented for this study is as described in [276], with improved treatment of neutrino microphysics and realistic nuclear matter EOS.

For the EOS, we use the tabulated finite-temperature Lattimer-Swesty EOS with incompressibility $K = 220\,\mathrm{MeV}$ [198], generated using [283]. To study the impact of the nuclear matter EOS on the waveforms and collapse dynamics, we repeat a small subset of the models outlined above employing the tabulated EOS from H. Shen *et al.* [240, 284]. Both of these EOS are available for download in tabulated form via the `CompOSE` website [37].

For the neutrino treatment, we use routines provided by open-source software package `GR1D` [68, 283]. During the collapse phase, we treat deleptonisation effects on the electron fraction Y_e following Liebendörfer *et al.* [285];

$$\begin{aligned} Y_e =& \frac{1}{2}\left(Y_{e,1} + Y_{e,2}\right) + \frac{x}{2}\left(Y_{e,1} - Y_{e,2}\right) \\ &+ Y_{e,c}[1 - |x| + 4|x|(|x| - 1/2)(|x| - 1)]\,, \end{aligned} \tag{6.2}$$

where

$$x = \max\left[-1,\, \min\left(1,\, \frac{2\log\rho - \log\rho_2 - \log\rho_1}{\log\rho_2 - \log\rho_1}\right)\right], \tag{6.3}$$

and $\rho_1 = 10^7\,\mathrm{g\,cm^{-3}}$, $\rho_2 = 10^{13}\,\mathrm{g\,cm^{-3}}$, $Y_{e,1} = 0.5$, $Y_{e,2} = 0.29$, and $Y_{e,c} = 0.035$ (as used in [78]). For $\rho > \rho_2$, we correct Y_e using;

$$Y_e = Y_e(\rho_2) + \frac{\log\rho - \log\rho_2}{\log\rho_{\mathrm{cor}} - \log\rho_2}\left[Y_{e,\mathrm{cor}} - Y_e(\rho_2)\right], \tag{6.4}$$

where $\rho_{\mathrm{cor}} = 2.55 \times 10^{14}\,\mathrm{g\,cm^{-3}}$ and $Y_{e,\mathrm{cor}} = 0.2717$. To crudely study the impact of deleptonisation on the dynamics and GW signatures, we repeat a subset of our models employing two perturbed deleptonisation treatments. Explicitly, we consider a 'reduced' parameterisation in which $Y_{e,\mathrm{cor}}$ is reduced by 5%, and conversely an increased parameterisation in which $Y_{e,\mathrm{cor}}$ is increased by 5%.

Following core bounce, we use the neutrino leakage and heating scheme in `GR1D` as outlined in [283], which approximates neutrino effects through parameterised deleptonisation, neutrino cooling, and heating schemes. Optical depths are calculated along radial rays aligned with the radial zones in `CoCoNuT` , and the default scaling factor for neutrino heating $f_{\mathrm{heat}} = 1$ is used. Neutrino pressure and contribution to the stress-energy tensor is treated via the ideal Fermi gas approximation where $\rho > 2 \times 10^{12}\,\mathrm{g/cm^3}$, the fiducial neutrino trapping density.

Our simulations follow evolution from the onset of core collapse through 25 ms after core bounce. Within this timescale, PNS ringdown following bounce has concluded, and the PNS has settled into a quasi-stationary state.

Beyond this, oscillations of millisecond PNSs are expected to be driven by prompt convection, wave excitation from neutrino-driven and PNS convection, and potentially secular instabilities. As simulations employing the CFC do not contain GWs by construction (as discussed in Chap. 2), we estimate the GW signature using the quadrupole formula which has been show to be very accurate for CCSN simulations considering GWs from PNSs, resulting in negligible phase error and systematic amplitude errors of order a few percent compared with GW signals extracted using Cauchy-Characteristic Extraction (CCE) in full general-relativistic simulations [21].

We use the naming convention *AxOyy* for our models, where *Ax* denotes the differential rotation length scale employed ($A \in \{A1, \ldots, A5\}$), while *Oyy* is the initial central angular velocity imposed (see Tab. 6.1 for ranges in Ω_c considered for each A model). This naming convention implies the use of the LS220 EOS, and fiducial deleptonisation treatment. Use of the H. Shen *et al.* EOS [240, 284] is denoted by adding *s* to the end of the name (i.e. *AxOyy* uses the LS220 EOS, while *AxOyys* uses the H. Shen EOS). Similarly for simulations employing the reduced and increased deleptonisation parameterisations, the model name is ended with *m* or *p*, respectively. The GW signals from all simulations carried out in this study are available for download from `stellarcollapse.org/gwcatalog`.

6.3 Dynamics and waveforms

In Fig. 6.2, we show the temporal evolution of the central density ρ_c, ratio of rotational kinetic energy to gravitational potential energy of the inner core β_{ic}, and GW strain as seen by an equatorial observer $h_{+,eq}$ at 10 kpc for model *A3O6* (for which the imposed rotation profile is defined by differential rotation length scale $A = 634$ km and initial central angular velocity $\Omega_c = 6$rad/s). We show time relative to the time of core bounce which, throughout this study, we define as when the specific entropy at the edge of the inner core in the equatorial plane reaches $3\,k_B$/baryon.

We see that the central density rapidly increases as core collapse ensues. As nuclear density is reached, the EOS rapidly stiffens, abruptly decelerating collapse. The inner core overshoots its equilibrium configuration, reaching a maximum central density around $\rho_c \sim 3.5\times10^{14}$ g/cm^3 before rebounding.

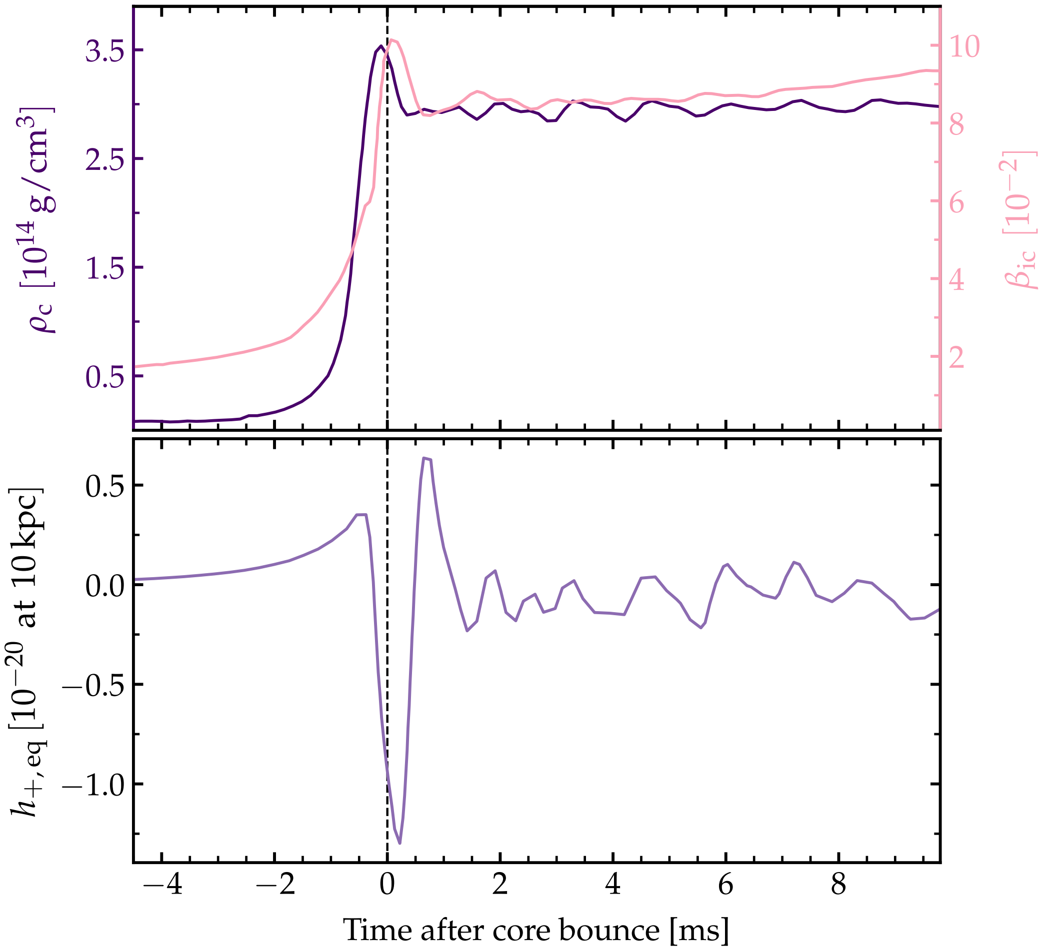

Figure 6.2: Evolution of central density ρ_c (top panel, left axis), ratio of rotational kinetic energy to gravitational potential energy of the inner core β_{ic} (top panel, right axis), and GW strain as seen by an equatorial observer $h_{+,eq}$ at 10 kpc (bottom panel) with time for model *A3O6*. The time of core bounce, defined as when the specific entropy at the edge of the inner core in the equatorial plane reaches $3\,k_B$/baryon, is indicated in both panels with a dashed black line.

The post-bounce core settles to a quasi-equilibrium state with post-bounce central density $\rho_{c,pb} \sim 3 \times 10^{14}$ g/cm^3, following ringdown oscillations that persist for $\sim (10-15)$ ms which are clearly seen as quasi-periodic variations in ρ_c. These trends are also seen reflected in β_{ic}, which we see increase as collapse proceeds, before reaching a maximum around 0.1 just after core bounce, and settling to $\beta_{ic} \sim 0.08$ following ringdown. In the GW strain, the two positive maxima coincide with the sharp deceleration of the core as $\rho_c \sim \rho_{nuc}$ and then as the core decelerates once more after the shock wave has passed through. The negative peak in-between originates from the outward acceleration as the core rebounds after overshooting equilibrium. PNS oscillations as the core rings down post-bounce to a quasi-equilibrium state are reflected in both β_{ic} and the GW strain.

In Fig. 6.3, we show the ratio of rotational kinetic energy to gravitational potential energy of the inner core at the time of core bounce $\beta_{\mathrm{ic,\,b}}$ as a function of initial central angular velocity Ω_{c} for all models simulated.

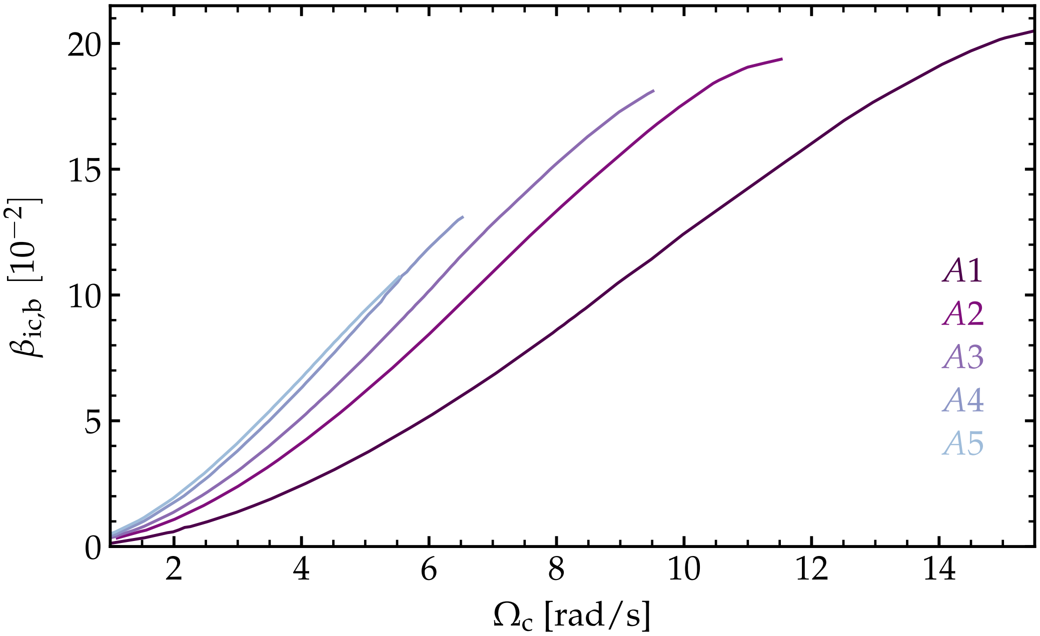

Figure 6.3: Ratio of rotational kinetic energy to gravitational potential energy of the inner core at bounce $\beta_{\mathrm{ic,\,b}}$ as a function of central angular velocity Ω_{c} for all simulated models. We note that the mapping $(A,\, \Omega_{\mathrm{c}}) \rightarrow \beta_{\mathrm{ic,\,b}}$ is dependent on the structure of the progenitor.

For a given Ω_{c}, we note that $\beta_{\mathrm{ic,\,b}}$ is larger for models characterised by less differential rotation. This matches expectations as, for these models, the rotation profiles are far less steep, resulting in signficant centrifugal support throughout the PNS. It follows that for each A sequence there exists a limiting Ω_{c} beyond which centrifugal support prevents gravitational collapse, which decreases as A increases. As discussed briefly in Sec. 6.2, this motivates the maximum Ω_{c} simulated for a model sequence with given A (see Tab. 6.1). It is notable that the maximum $\beta_{\mathrm{ic,\,b}}$ observed in the terminal model for each A sequence increases with decreasing A, i.e. precollapse cores characterised by strongly differential rotation profiles are able to have larger Ω_{c}

and still be able to collapse, resulting in reaching larger $\beta_{\mathrm{ic,b}}$. For sequences $A3$, $A4$, and $A5$, the maximum $\beta_{\mathrm{ic,b}}$ achievable are 0.18, 0.13, and 0.11, respectively.

We caution, however, that this doesn't allow for arbitrarily large $\beta_{\mathrm{ic,b}}$ for strongly differential rotation. For sequences $A1$ and $A2$, which terminate at $\beta_{\mathrm{ic,b}} = 0.21$ and 0.19 respectively, the terminating values for Ω_{c} are chosen precisely because they are where the global maximum of $\beta_{\mathrm{ic,b}}$ for those values of A exist. At higher Ω_{c}, $\beta_{\mathrm{ic,b}}$ would decrease as the bounce occurs at lower density, resulting in a smaller degree of spin-up. We refer the curious reader to extensive discussions in, e.g. [200, 276, 286]. The maximum value of $\beta_{\mathrm{ic,b}}$ attainable is of interest because β often characterises the threshold beyond which a rotating fluid body becomes unstable to rotational hydrodynamic instabilities, which would source GW emission (see discussion in Chap. 3). As such instabilities are not thought to develop until well after the 25 ms cutoff we are concerned with in this study, we postpone discussion of this to Sec. 6.5

The central goal of this study is to establish the impact of the angular momentum distribution in the precollapse core on the dynamics of collapse and early post-bounce evolution, and how this imprints upon the GW signature from bounce and prompt ringdown of the millisecond PNS. While $\beta_{\mathrm{ic,b}}$ is a useful quantity to consider here, it is perhaps not the only one. As the GW emission is sourced by the bounce and ringdown of the inner core of the PNS, it is also useful to consider the total angular momentum and mass of the inner core at bounce, $J_{\mathrm{ic,b}}$ and $M_{\mathrm{ic,b}}$ respectively, which have beens hown in previous studies to determine the GW signature [52, 287]. While $M_{\mathrm{ic,b}}$ is set by the trapped lepton fraction in the inner core for non-rotating progenitors (see, e.g. [288]), rotation increases $M_{\mathrm{ic,b}}$ by slowing down the collapse. A longer collapse timescale means a greater proportion of the precollapse core is in sonic contact, which consequently increases $M_{\mathrm{ic,b}}$ (see, e.g., [52, 276, 289]).

In Fig. 6.4, we show the central density at bounce ρ_{c}, the mass of the inner core at bounce $M_{\mathrm{ic,b}}$, and the angular momentum of the inner core at bounce $J_{\mathrm{ic,b}}$ as a function of $\beta_{\mathrm{ic,b}}$ for all models simulated.

For $\beta_{\mathrm{ic,b}} \lesssim 0.13$, we see that $M_{\mathrm{ic,b}}$ and $J_{\mathrm{ic,b}}$ increase approximately linearly with $\beta_{\mathrm{ic,b}}$ and are roughly independent of the differential rotation length

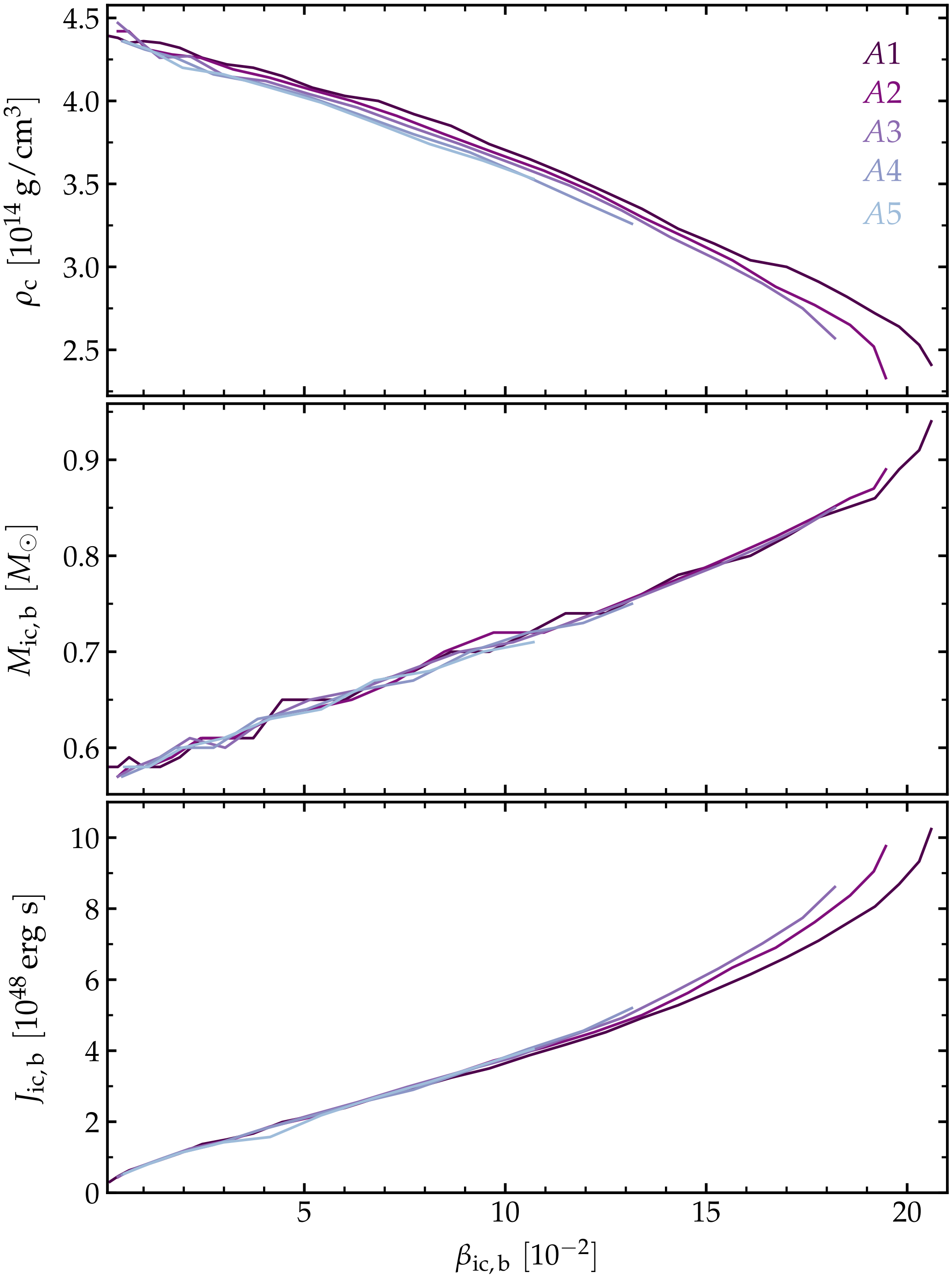

Figure 6.4: As a function of $\beta_{\rm ic,b}$, the central density at bounce $\rho_{\rm c,b}$ (top panel), mass of the inner core at bounce $M_{\rm ic,b}$ (center panel), and total angular momentum of the inner core at bounce $J_{\rm ic,b}$ (bottom panel) for all models simulated.

scale A. Nonlinear behaviour in the mapping $\beta_{\rm ic,b} \rightarrow J_{\rm ic,b}$ is seen above

$\beta_{\mathrm{ic,b}} \sim 0.13$ for sequences $A1$, $A2$, and $A3$. For fixed $\beta_{\mathrm{ic,b}}$ and $M_{\mathrm{ic,b}}$, more differentially rotating models (i.e. larger differential rotation length scale A) will have smaller $J_{\mathrm{ic,b}}$.

For the central density at bounce $\rho_{\mathrm{c,b}}$, we see that while the general evolution with $\beta_{\mathrm{ic,b}}$ follows similar slopes for all A, $\rho_{\mathrm{c,b}}$ is systematically smaller at fixed $\beta_{\mathrm{ic,b}}$ for more uniformly rotating models. We note that ρ_{c} is important for the structure and dynamics of the inner core as, for a given EOS, it determines the structure and spectrum of oscillation modes of the PNS core in the non-rotating low-temperature limit [12]. As we saw in Fig. 6.2, quasi-periodic oscillation in the central density is reflected in the GW strain. In Fig. 6.5, we show the temporal evolution of ρ_{c} for three models ($A1O9$, $A3O6$, and $A5O5.5$) all with $\beta_{\mathrm{ic,b}} \sim 0.1$, but characterised by different differential rotation length scales.

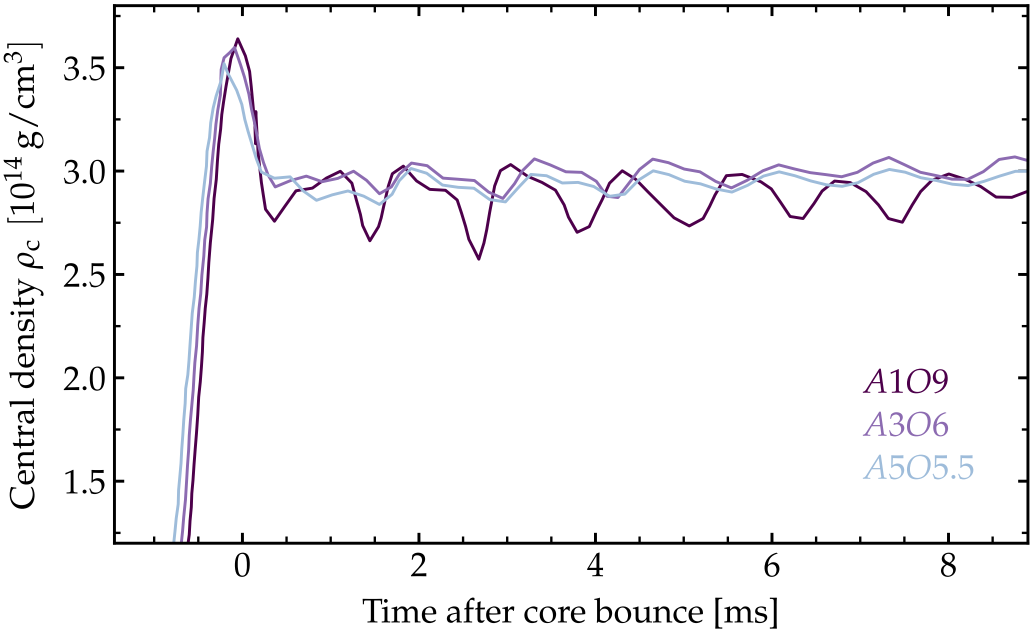

Figure 6.5: Time evolution of the central density ρ_{c} for three models ($A1O9$, $A3O6$, and $A5O5.5$), all with $\beta_{\mathrm{ic,b}} \sim 0.1$ but characterised by different differential rotation length scales.

We see that, at the time of core bounce, the strongly differentially rotating model ($A1O9$) overshoots its post-collapse equilibrium the most, exhibiting the highest maximum central density before bounce. This is consistent with what we have seen previously in Fig. 6.4 where, for a given value of $\beta_{\mathrm{ic,b}}$, models characterised by more uniform rotation reach lower maximum central densities due to stronger centrifugal support throughout the inner core. This model also undergoes stronger post-bounce oscillations than its counterparts, before settling at the lowest post-bounce central density $\rho_{\mathrm{c,\,pb}}$. Conversely for $A3O6$ and $A5O5.5$, we see smaller maximum central densities, weaker rebounds, and less vigorous post-bounce ringdowns.

Relating this to the GW emission, the ringdown signature is a complex superposition of multiple oscillation modes, with rotation coupling ℓ modes into their $\ell \pm 2$ counterparts (see, e.g. [54]). Oblate ($\ell = 2$) deformation is strongest in more differentially rotating models, where spin is concentrated in the central regions. Consequently for fixed $\beta_{\mathrm{ic,\,b}}$, shorter length scales for differential rotation result in larger quadrupole oscillations. We show the GW strain as seen by an equatorial observer $h_{+\,\mathrm{eq}}$ at 10 kpc for models $A1O9$, $A3O6$, and $A5O5.5$ in the lower panel of Fig. 6.6. Interested in how this relationship changes with $\beta_{\mathrm{ic,\,b}}$, we show $h_{+\,\mathrm{eq}}$ at 10 kpc for three models with $\beta_{\mathrm{ic,\,b}} \sim 0.05$ (more moderate rotation; $A1O6$, $A3O4$, and $A5O3.5$) in the top panel of Fig. 6.6.

For moderate rotation ($\beta_{\mathrm{ic,\,b}} \sim 0.05$), we see that the signature at bounce is very similar for the three models shown. Slightly increased emission is seen during ringdown for model $A1O9$ with strongly differential rotation, but there appears to be only a weak dependence at best on the angular momentum distribution for moderately rotating cores. In the rapidly rotating case, we see the strong trends exhibited in the central density evolution (see Fig. 6.5) reflected in the GW signature. The peaks at core bounce are much more pronounced in model $A1O9$ than in its less differentially rotating counterparts $A3O6$ and $A5O5.5$, and strong post-bounce oscillations are observed. This suggests that for rapidly rotating precollapse cores, it may be possible to discern the degree of differential rotation from the GW signal.

To evaluate the dependence of our results on the microphysics, we rerun simulations on the $A1$ sequence of models with: (i) H. Shen *et al.* [240, 284] EOS in place of the Lattimer-Swesty EOS [198], (ii) Y_e parameterisation at nuclear densities decreased by 5%, and (iii) Y_e parameterisation at nuclear densities increased by 5%. We denote models in these sequences $A1s$, $A1m$, and $A1p$, respectively, with the particulars of the implementation outlined in Sec. 6.2. In Fig. 6.7, we show the evolution with time of the central density ρ_{c}

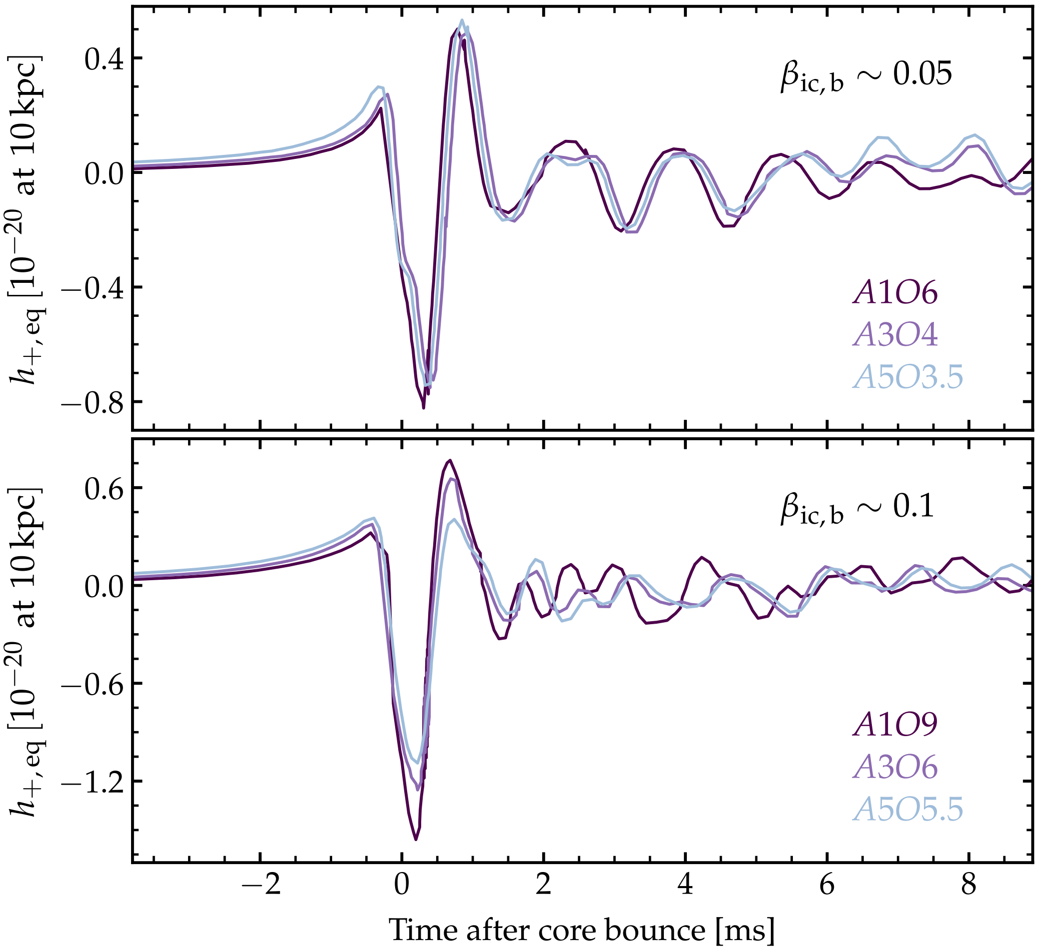

Figure 6.6: (Top panel) The GW strain as seen by an equatorial observer $h_{+,\mathrm{eq}}$ at 10 kpc for three models with $\beta_{\mathrm{ic,b}} \sim 0.05$ (moderate rotation; *A1O6*, *A3O4*, and *A5O3.5*). (Bottom panel) As for top panel, but for three rapidly rotating models ($\beta_{\mathrm{ic,b}} \sim 0.1$; *A1O9*, *A3O6*, and *A5O5.5*.

and GW strain as seen by an equatorial observer $h_{+,\mathrm{eq}}$ at 10 kpc for models *A1O10.25*, *A1O10.25s*, *A1O10.25m*, and *A1O10.25p*.

We see that model *A1O10.25m* reaches the largest ρ_{c} at core bounce, followed in turn by *A1O10.25*, *A1O10.25p*, and *A1O10.25s*, respectively. As the central electron fraction is smaller in *A1O10.25m* and *A1O10.25* than for *A1O10.25p*, reduced core pressure allows the PNS to settle at higher density. Of the four, *A1O10.25s* settles post-bounce at much lower density due to the comparative stiffness of the H. Shen EOS at nuclear densities with respect to the LS220 EOS employed for our fiducial simulations. We refer the interested reader to discussions in Richers *et al.* [26] and Dimmelmeier *et al.* [52] regarding the

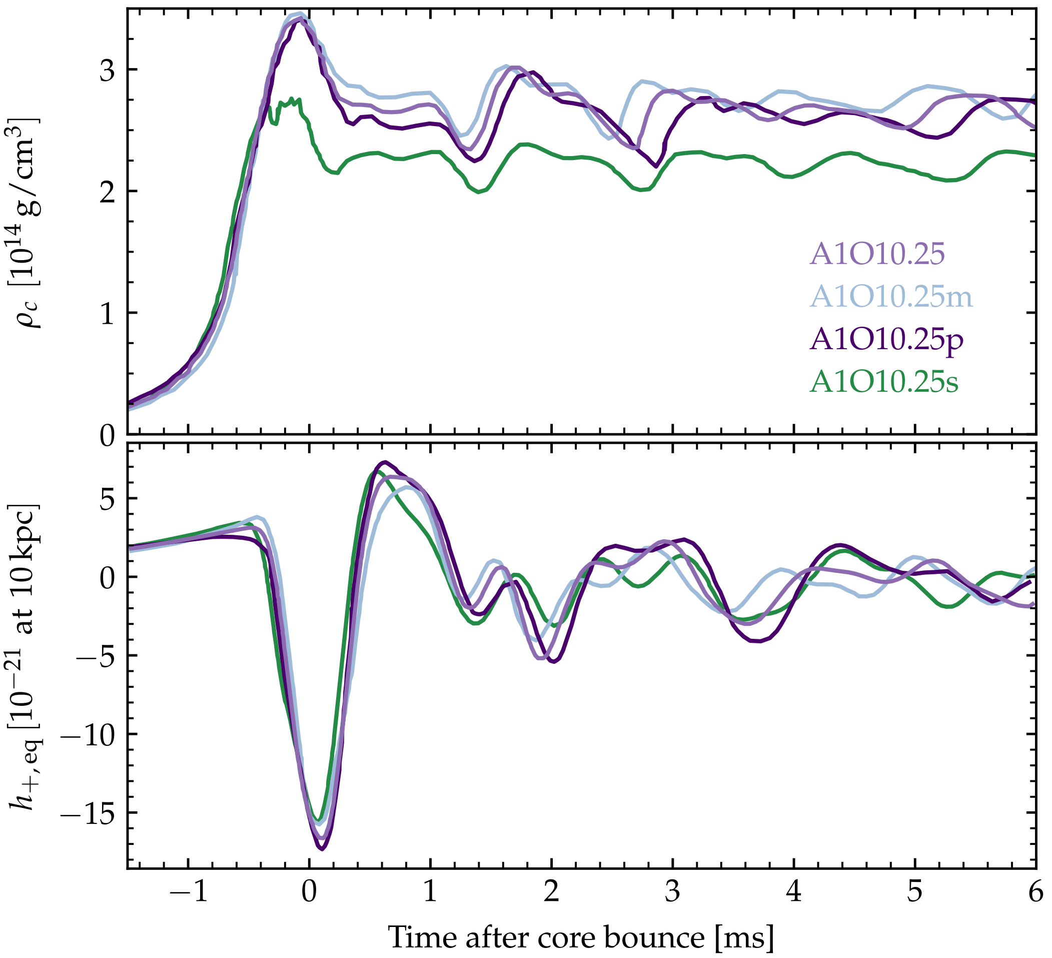

Figure 6.7: Time evolution of the central density ρ_c (top panel) and GW strain as seen by an equatorial observer $h_{+,\mathrm{eq}}$ at 10 kpc (bottom panel) for models *A1O10.25*, *A1O10.25s*, *A1O10.25m*, and *A1O10.25p*.

EOS dependence of the GW signature from rotating core collapse, and to discussions in Abdikamalov. *et al.* [276] on the impact of Y_e parameterisation on GW signals. As we have seen previously, differences seen in the evolution of ρ_c are mirrored in the GW signal. We acknowledge here the qualitative similarities between the GW strain for these four models, but note the non-negligible quantitative differences (which grown with time) originating from changes in the EOS and electron fraction at nuclear density.

Using the waveforms presented in this Section, we now discuss two proof-of-principle concept studies in Sec. 6.4 to explore the viability of extracting the angular momentum distribution of the precollapse core from the GW signature.

6.4 Extracting the angular momentum distribution from gravitational-wave observations

As the simulation results presented in the previous section suggests, many characteristics of both the dynamics and GW emission associated with rotating CCSNe are dependent on both the total rotation and its distribution throughout the precollapse core (as expressed through $\beta_{\mathrm{ic,b}}$ and differential rotation length scale A). In the following, we explore two proof-of-principle concept studies to establish the viability of extracting $(\beta_{\mathrm{ic,b}}, A)$ from GW observations of rotating core collapse.

Numerical Template Bank Analysis: Extracting $\beta_{\mathrm{ic,b}}$

In the case of a known signal in Gaussian noise, it has been shown that matched filtering is the optimal signal extraction technique (see, e.g. [290]). As discussed in Chap. 4, GWs from CCSNe are typically not suitable for a matched filtering analysis, as stochastic components from emission driven by convection make it highly unfeasible to robustly model the phase evolution of the GW signature (see, e.g. [135]). The presence of rapid rotation in the precollapse core, however, suppresses convective instability through a stabilising positive specific angular momentum gradient in the post-shock region (e.g., [291]). As a consequence, the early time GW signature is expected to be fairly deterministic, particularly from rotating core collapse, bounce, and ringdown in the first ten milliseconds or so after bounce. We investigate the ability to extract $\beta_{\mathrm{ic,b}}$ and A in the most optimistic limiting case that matched filtering may be employed to analyse these signals.

We use the waveforms from simulations across the parameter space outlined in Tab. 6.1 to construct a "numerical template bank" of sorts. Labelling each waveform by its characteristic $(\beta_{\mathrm{ic,b}}, \Omega_{\mathrm{c}})$ pair, we compute the match of some dataset containing an unknown signal from rotating core collapse with each 'template', maximising over nuisance parameters. The best-match template across the bank of waveforms most faithfully represents the unknown signal buried in data, from which we posit that the signal is characterised by $(\beta_{\mathrm{ic,b}}, \Omega_{\mathrm{c}})$ of the best-match template. This is an undoubtably crude approximation, but as matched filtering is the optimal method of extracting signal from data (see, e.g. [290]), it is apt for investigating the viability of any such method for extracting the angular momentum distribution from a GW signal in the most optimistic scenario. There are several caveats to this approach that question the suitability of such an analysis for GWs from rotating core collapse, the identity and consequences of which are explored in Sec. 6.5.

As trial waveforms, we inject signals across the parameter space characterised by Ω_c differing by at least 0.25 rad/s from the those of the waveforms populating the template bank. In this way, we aim to mimic the expected scenario where templates exactly corresponding to hypothetical observations are not present in the bank. We consider a source at 10 kpc , and employ a single Advanced LIGO detector at design sensitivity with Gaussian noise [292]. For completeness, we discuss here the full parameter dependence (encoded in vector $\vec{\lambda}$) of a hypothetical signal;

$$\vec{\lambda} = \{D,\, t_c,\, \alpha,\, \delta,\, \iota,\, \phi,\, \psi\} \tag{6.5}$$

Here, D is the source distance, t_c is the arrival time of the signal at geocenter, $(\alpha,\, \delta)$ is the sky position (right ascension and declination), $(\iota,\, \phi)$ describe the orientation of the source frame with respect to the observer's line of sight, and ψ is the polarisation angle. As this study is intended solely as a proof-of-principle concept, we drastically simplify the signal model, assuming the distance is known and that the source is located and oriented such that the detector is maximally sensitive to linearly polarised GWs (i.e. $F_+ = 1$). We assume t_c is known to within one second, which is realistic as for a CCSN at 10 kpc , the neutrino counterpart can be used to estimate the time of core bounce to within tens of milliseconds[1]. For data d (composed of signal and Gaussian noise), we compute the match with template x^j through the noise-weighted inner product $\langle d,\, x^j \rangle$;

$$\langle d,\, x^j \rangle = 2 \max_{t_c} \int_{-\infty}^{\infty} df\, \frac{\tilde{d}(f)\tilde{x}^j(f)^* e^{i2\pi f t_c}}{S_h(f)}\,, \tag{6.6}$$

where $\tilde{a}$ is the Fourier transform of a, and $*$ denotes complex conjugation. We numerically maximise over t_c using fast-Fourier transforms, and normalise $\langle d,\, x^j \rangle$ by the optimal template SNR $\langle x^j,\, x^j \rangle^{1/2}$. We repeat all calculations

---

[1] see Chap. 3 and Chap. 4 for discussion

with ten different realisations of simulated Gaussian noise, and report the averaged result. The 'measured' ($\beta_{\rm ic,b}$, A) are then those belonging to the best-match template x^j.

In Fig. 6.8, we show the measured $\beta_{\rm ic,b}$ and fractional error in this measurement $\Delta\beta_{\rm ic,b}/\beta_{\rm ic,b}$ as a function of true $\beta_{\rm ic,b}$ for all injected waveforms.

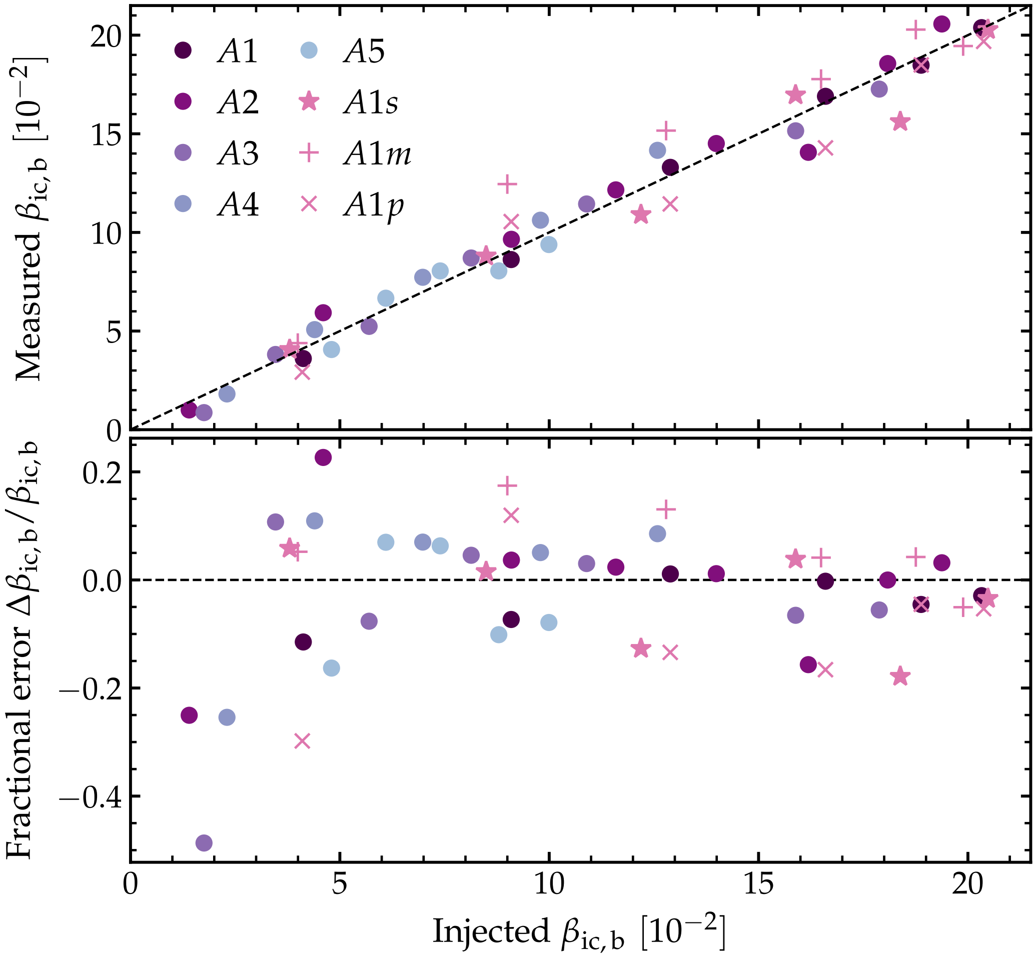

Figure 6.8: (Top panel) Measured $\beta_{\rm ic,b}$ as a function of true $\beta_{\rm ic,b}$ for all injected waveforms. We overlay the track along which measured $\beta_{\rm ic,b}$ and true $\beta_{\rm ic,b}$ are equal with a dashed black line. (Bottom panel) Relative error in measured $\beta_{\rm ic,b}$ with respect to true $\beta_{\rm ic,b}$, $\Delta\beta_{\rm ic,b}/\beta_{\rm ic,b}$, as a function of true $\beta_{\rm ic,b}$ for all injected waveforms. We overlay the track denoting zero fractional error with a dashed black line.

For most injected waveforms, $\beta_{\rm ic,b}$ is recovered within 20% of its true value. Averaging over $\beta_{\rm ic,b}$, the fractional error across all waveforms is $\sim$ 8%. We note that the fractional error is largest for slowly rotating models, which is to be expected as the GW signals from these models contain prominent stochastic features from prompt convection. In spite of this, we see that $\beta_{\mathrm{ic,b}}$ is extracted with good accuracy across a broad range of anguglar momentum distributions.

Focusing on the additional waveforms from the $A1$ set varying the EOS ($A1s$) or electron fraction parameterisation ($A1m$ and $A1p$), we see that this analysis remains robust to changes in microphysics. For the $A1s$ waveforms, produced using the H.Shen *et al.* EOS [240, 284] rather than the Lattimer-Swesty EOS [198], $\beta_{\mathrm{ic,b}}$ is recovered within $\lesssim 15\%$ of its true value over all waveforms, with an average error of $\sim 9\%$. For $A1m$ and $A1p$ waveforms, $\beta_{\mathrm{ic,b}}$ is recovered within $\lesssim 15\%$ for rapidly rotating models ($\beta_{\mathrm{ic,b}} \gtrsim 0.05$), with an average error of just $\sim 10\%$. Outliers at small $\beta_{\mathrm{ic,b}}$ can be attributed to stochastic components in the GW signature for prompt convection.

Based on these observations, we conclude that this proof-of-principle analysis can extract $\beta_{\mathrm{ic,b}}$ with $\lesssim 20\%$ from GW signals from rotating core collapse within the galaxy.

Model selection: inferring A

We consider now an alternative method to investigate the dependence of the GW signal on the differential rotation length scale A, and the ability to infer the degree of differential rotation from GW observations of rotating core collapse. We employ a Bayesian approach, drawing from the PCA analysis presented in Chap. 5. Constructing waveform catalogs for models with common differential rotation length scale A, we are able to isolate dominant waveform characteristics into linearly independent PCs. Using bases constructed for each A, we can compute the evidence that a given data set, comprised of noise and unknown signal, contains a signal best represented on each set of PCs. Comparing the evidences and calculating the model-wise Bayes factors, we can establish the basis set (and hence corresponding value of A) that best models the observed data.

We construct PCs using catalogs from waveforms with $A \in \{A1, \ldots, A5\}$ as described in Tab. 6.1. Limited by the size of the smallest waveform catalog, we use a subset of 10 PCs from each set to approximately reconstruct injected waveforms. We employ the same injection waveforms as outlined in Sec. 6.4, which are distinct from the catalog waveforms used to produce the PC sets.

We use a single Advanced LIGO detector at design sensitivity with simulated Gaussian noise, and assume the sky position and orientation of the source is such that the detector is maximally sensitive to linearly polarised waveforms (i.e. $F_+ = 1$). Placing hypothetical sources at a known distance of 10 kpc , we reduce the parameter space describing the signal to the ten PC components and time of arrival at geocenter t_c.

For each PC set, we compare the single signal model $\mathcal{M}_i$ to the noise model using

$$\log B_i = \log p(d|\mathcal{M}_i) - \log p(d; \text{noise})\,, \tag{6.7}$$

where signal model $\mathcal{M}_i$ here comprises Gaussian noise plus some trial waveform composed from a linear superposition of PCs. We use the python implementation of `SMEE2G` presented in Chap. 5 to compute model-wise evidences.

Of interest is the Bayes factor for model i normalised with respect to the Bayes factor for the correct model, B_{true}, for a given injected signal;

$$\log B_{\text{true},j} = \log B_{\text{true}} - \max[\log B_j]\,, \tag{6.8}$$

where $\max[\log B_j]$ is the maximum logarithmic Bayes factor obtained for A models other than the true one. From this, $\log B_{\text{true};j} > 0$ ($\log B_{\text{true};j} < 0$) states that the correct model for A has (has not) been inferred. Following the conventions discussed in Chap. 5, we impose a confidence threshold such that we require $\log B_{i;j} > 5$ to be statistically significant.

In Fig. 6.9, we show $\log B_{\text{true};j}$ as a function of injected $\beta_{\text{ic, b}}$ for all injected waveforms.

We see that $\log B_{\text{true};j}$ increases with $\beta_{\text{ic;b}}$ and, at a given $\beta_{\text{ic, b}}$, A is inferred correctly with the highest confidence for injections from the most strongly differentially rotating model ($A1$). In the limit of slow rotation ($\beta_{\text{ic;b}} \lesssim 0.05$), the correct model for A is not determined for most injections. Repeating injections for closer sources distances, we find the same results. We thus conclude that this isn't a consequence of low SNR signal, rather likely due to a combination of (i) power in stochastic GW emission from prompt convection is comparable to (or stronger than) power in GWs from collapse, bounce, and ringdown, and (ii) we see little influence on the GW amplitude from collapse,

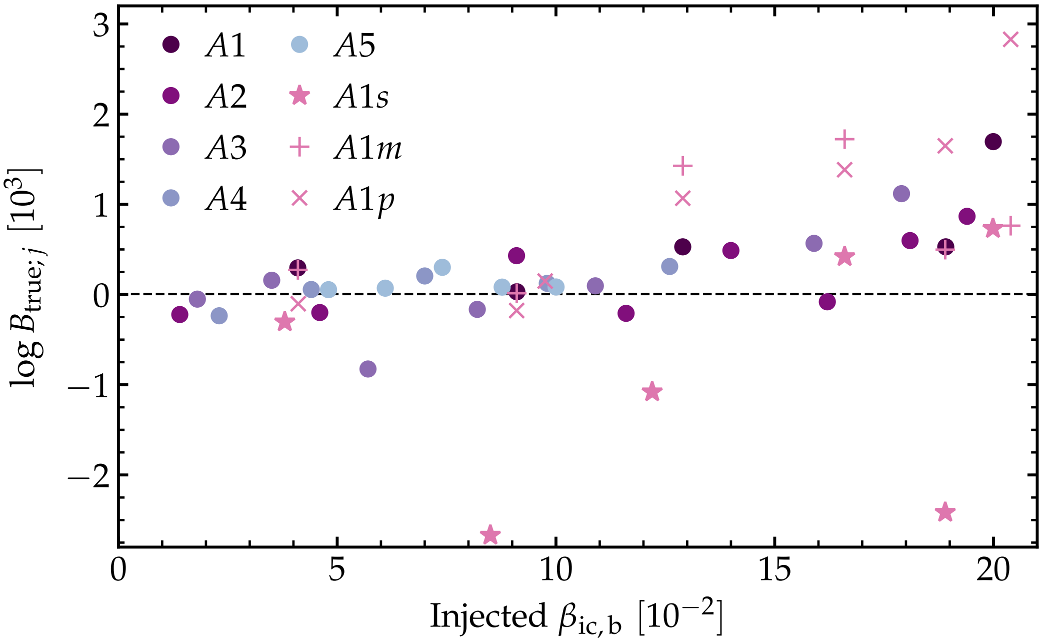

Figure 6.9: Logarithmic Bayes factor $\log B_{\mathrm{true};j}$ as a function of injected $\beta_{\mathrm{ic,b}}$ for all injected waveforms. $\log B_{\mathrm{true};j} > 0$ and $\log B_{\mathrm{true};j} < 0$ imply correct and incorrect inference of A, respectively. Large values of $\log B_{\mathrm{true};j}$ convey that the correct model has been chosen with a high degree of confidence. We overlay a black dashed line at confidence threshold $\log B_{\mathrm{true};j} = 5$.

bounce, and ringdown from A for slowly rotating precollapse cores (see, e.g., Fig. 6.6).

Addressing now the injections from models with different EOS ($A1s$), we find that A is only determined correctly for two models with very rapid rotation (with $\beta_{\mathrm{ic;b}}$ of ~ 0.16 and ~ 0.2). The maximum densities reached in these cases are relatively low, and the two EOS are not very different in this regime. For slowly rotating injections from this set, the incorrect model is inferred and with large negative $\log B_{\mathrm{true};j}$. This suggests that not knowing the nuclear matter EOS with accuracy may make it difficult to infer the angular momentum distribution, but it's important to note that GW signals from strongly differentially rotating models in the slow rotation regime contain non-negligible components from prompt convection which greatly impact the validity of the assumptions made to perform this analysis. Turning now to injections from models with altered electron fraction parameterisation ($A1m$ and $A1p$), we see that the correct model for A is inferred for waveforms from rapidly rotating progenitors, while incorrect models are preferred in the slow rotation limit. Of note is that when $A1$ is correctly identified for injections from $A1m$ or $A1p$, $\log B_{\mathrm{true};j}$ is smaller than for injections from $A1$ corectly associated with $A1$. This suggests that unless Y_e in the inner core is known with reasonable accuracy, our ability to infer the correct model for A greatly suffers.

To conclude this Section, we note that a directly comparable analysis for $\beta_{ic;b}$ is not possible, since, for a given A, many parameters affect $\beta_{ic;b}$, such as Ω_c, EOS, and $Y_e(\rho)$ parametrization. However, a roughly analogous analysis could be constructed in which models describe ranges of $\beta_{\mathrm{ic;b}}$ (e.g., $0 \leq \beta_{\mathrm{ic;b}} \geq 0.05$) rather than discrete values. This blurs the line between model selection and parameter estimation, since the proposed models are just subsets of one model for $\beta_{\mathrm{ic;b}}$, rather than different models. Instead, we try to estimate some range on $\beta_{\mathrm{ic;b}}$, within which it is most likely to be. Well-posed Bayesian methods for parameter estimation typically require a continuous analytical model describing the parameter dependence of the system [229]. Such an analytic model (which could, e.g., be constructed by interpolating between discrete waveforms) is not presently available to us. Hence, we choose to postpone investigation of such a study to future work.

6.5 Discussion

We have extended previous studies to focus on the influence of the angular momentum distribution within the precollapse core on the GW signature of rotating core collapse, bounce, and ring down. To this end, we carried out 124 axisymmetric CCSN simulations with the `CoCoNuT` code [239, 276, 293]. In this Section, we discuss our results, address the uncertainties to which they are subject, then ponder the impact and consequences for future research.

Our results have shown that the overall dynamics governing the formation and post-bounce ringdown of rotating PNSs are somewhat insensitive to the precise distribution of angular momentum within the inner core, instead dominated by its total rotation. Quantifying the total rotation of the inner core through two metrics, $\beta_{\mathrm{ic,b}}$ and $J_{\mathrm{ic,b}}$, we find a simple linear relationship between these measures and the mass of the inner core at bounce $M_{\mathrm{ic,b}}$ throughout the bulk of the explored parameter space. Only in the regime of very rapid rotation ($\beta_{\mathrm{ic,\,b}} \gtrsim 0.13 - 0.15$, $J_{\mathrm{ic,b}} \gtrsim 5 - 6 \times 10^{48}$ erg s), do we find significant differences between models with fixed $\beta_{\mathrm{ic,\,b}}$ and varying A. While unimportant with respect to the overall dynamics, we note that the PNS structure and evolution is affected by the presence of differential rotation. For fixed $\beta_{\mathrm{ic,\,b}}$, differential rotation concentrates oblate deformation in the inner core, as more uniformly rotating cores exhibit global oblateness due to greater centrifugal support at larger radii/enclosed mass coordinates. These structural changes have important consequences for GW emission from more rapidly rotating models ($\beta_{\mathrm{ic,\,b}} \gtrsim 0.05 - 0.08$, $J_{\mathrm{ic,b}} \gtrsim$ 2–3 × 10^{48} erg s), with higher peak strain and more energy emitted in GWs from models characterised by more strongly differential rotation. We note that it is uncertain to what extent the parameterised rotation profiles imposed on our single non-rotating progenitor are realistic and representative of nature. Studies comparing stellar evolution models employing realistic rotation effects to parameterised models such as that employed in this work must be carried out across the parameter space of angular momentum distribution, to establish the existence of any systematic uncertainties. A dearth of the former, combined with it not being possible to determine the angular momentum distribution of the precollapse core through EM observations of evolved stars means that it is difficult to say whether our model is representative of what is seen in nature. Indeed, post-detection inference studies of GWs from rotating core collapse (such as that presented here) are one of the only ways to directly probe the angular momentum of the precollapse core.

We explored potential methods to infer or, at the very least, constrain the angular momentum and differential rotation of the core from GW observations. We presented a proof-of-principle concept study, constructing a crude numerical template bank of sorts from the waveforms produced from our simulations. Simulating additional waveforms with Ω_{c} within the parameter space confines laid out by our templates, we compute the match of each template (maximised over signal arrival time) with some data set comprised of simulated Gaussian noise (for Advanced LIGO at design sensitivity) with an unknown signal injected. Averaging over ten realisations of simulated noise, we compare $\beta_{\mathrm{ic,\,b}}$ of the best-match template with that characterising the injected waveform, and compute the fractional error. We demonstrate the ability to estimate $\beta_{\mathrm{ic,\,b}}$ or $J_{\mathrm{ic,b}}$ to within $\sim 20\%$ for a hypothetical event at 10 kpc , in the context of a single, optimally-oriented detector. This method implicitly assumes that the time domain evolution of the GW signals we are considering are robust and fully deterministic, but this is not necessarily the case. In the limit of rapid rotation, stability against convective overturn hypothetically removes any stochastic components from the GW signal, leaving a deterministic and robustly reproducable signal form collapse, bounce, and post-bounce ringdown. For slowly rotating models, however, stochastic GW emission driven by prompt convection comprises a non-negligible (if not dominant for the most slowly rotating models considered) component of the GW signature. The primary issues with this are twofold; (i) such components cloud the deterministic part of the signal directly related to the total rotation of the inner core, and (ii) computing matches for templates with stochastic components is (at best) a purely academic exercise; the time domain GW signal from such models *is not* robustly predictable, meaning that comparison of two particular instantiations is not representative of the actual ability to recover a GW signal from CCSN observed in nature. Instead, it should be viewed as a(n unattainable) theoretical maximum to our ability to extract such signals. This is discussed more in Chap. 8, where we discuss opportunities for more pragmatic (and less fanciful) directions for so-called CCSN parameter estimation to be explored over the next decade.

Employing now the Bayesian model selection analysis we developed in Chap. 5, we compose basis vectors via PCA from waveform catalogs constructed for each A, aiming to encompass the dominant waveform features for GW signals from each of the five differential rotation length scales considered. Projecting the same data set as considered above (comprised of Gaussian noise plus some unknown GW signal) onto each basis set, we compute the evidence for a signal best represented by the dominant features of the waveform catalog for a particular A. Ratios of the evidences can then be used to establish the most likely model. We showed that for a hypothetical source at 10 kpc , the degree of differential rotation can only be estimated for rapidly rotating models. This analysis is subject to many of the same caveats of the matched-filtering proposal above, not least the presence of stochastic components in some (but not all) catalog waveforms in each model. PCA works by extracting the dominant features from a waveform catalog characteristic of a particular model. Here, we try to extract dominant features from a catalog of, for example, models with strongly differential rotation. Across the catalog, total core rotation $\beta_{\mathrm{ic,\,b}}$ is varied from very slow to extremely rapid rotation. We have already established, however, that the GW signature is strongly dependent on $\beta_{\mathrm{ic,b}}$ and only weakly dependent on A, with effects from A non-negligible only for rapid rotation. As a consequence, the PCs encompass the dominant features averaged across $\beta_{\mathrm{ic,b}}$ in the context of each A. This, for all intents and purposes, blurs out sub-dominant effects associated with differential rotation in favour of features dominating the slow $\beta_{\mathrm{ic,b}}$ and/or extremely rapid β limits of the catalog. A more tailored approach might instead create PCs for each A from catalogs limited to waveforms for which, say, $\beta_{\mathrm{ic,b}} \gtrsim 0.08$. While this would likely result in misindentification for waveforms with small $\beta_{\mathrm{ic,b}}$, it has already been established (see, e.g., discussion in Sec. 6.3 and figures therein) that differential rotation effects impact global dynamics only for rapidly rotating (i.e. large $\beta_{\mathrm{ic,b}}$) models. Realistically, taking such an approach and constructing 'models' for a given A and subset of $\beta_{\mathrm{ic,b}}$ further blurs the already fuzzy lines between whether this constitutes true model selection or just marginalisation over a parameterised fit. If capturing the collapse, bounce, and ringdown of a rotating fluid body is the goal, then modelling the oscillation modes of the PNS may indeed be a better approach. This was first investigated by Fuller *et al.* [251], who computed the hypothetical GW spectra for nascent rotating PNSs simulated in this study using first-order perturbation theory to estimate the oscillation modes excited by core bounce. While semi-analytic GW energy spectra produced showed discrepancies from those for GW emission as computed in this study, the absence of rotational effects (which come in at second-order) are likely to explain at least some of the differences seen. Further study extending this analysis will likely be invaluable to better understanding the GW spectrum from rotating core collapse, and its dependence on the angular momentum distribution of the core.

Returning now to caveats associated with the waveforms from our CCSN simulations, we endeavoured to explore systematic uncertainties associated with the implementation of microphysics. Changing the nuclear matter EOS (from the fiducial Lattimer-Swesty EOS with $K = 220\,\mathrm{MeV}$ [198] to the H. Shen *et al.* EOS [240, 284]), or varying the electron fraction parameterisation by 5% was shown to have a marked effect on the accuracy with which total rotation and the differential rotation length scale can be estimated using the GW analyses discussed above. Exploring uncertainties in the electron fraction in the inner core requires full neutrino radiation-hydrodynamics simulations with state-of-the-art treatment of neutrino-matter interactions. Richers [14, 26] carried out an extensive study on the dependence of the GW signature of rotating core collapse, bounce, and ringdown on the nuclear matter EOS, employing improved electron fraction parameterisation, finding that mismatch between waveforms varying only the EOS decreases strongly as the core becomes more rapidly rotating. It seems likely that the presence of stochastic signal components for slowly rotating precollapse cores requires more heuristic approaches to parameter estimation and signal extraction to be developed. We discuss this further in Chap. 8.

6.6 Conclusion

We have carried out a an extensive set of axisymmetric general-relativistic CCSN simulations to investigate the influence of the angular momentum distribution of the precollapse core on the GW signature from formation and early ringdown of millisecond PNSs. Imposing a cylindrical rotation law governed by central angular velocity Ω_c and differential rotation length scale A onto a single non-rotating presupernova progenitor, we have simulated 124 different models spanning the parameter space (Ω_c, A) to systematically probe the effects of total core rotation (parameterised by either $\beta_{\mathrm{ic,b}}$ or $J_{\mathrm{ic,b}}$) on the dynamics and GW signature of rotating core collapse. Testing for systematic uncertainties, we have also performed simulations in which we vary the nuclear matter EOS and parameterisation of electron fraction in the core.

For rapidly rotating precollapse cores (birthing millisecond PNSs with $\beta_{\mathrm{ic,b}} \gtrsim 0.08$), our simulations show that the GW signature from collapse, bounce, and early ringdown has a strong and systematic dependence on the differential rotation length scale A. For more slowly spinning cores, the GW signal has little to no dependence on the angular momentum distribution, and is instead governed by the total rotation of the core (parameterised in this study via $\beta_{\mathrm{ic,b}}$).

Harnessing the dependence of the GW signature on $(A, \beta_{\mathrm{ic,b}})$, we present two proof-of-principle concept studies to explore the viability of inferring the angular momentum distribution of the precollapse core from GW observations alone. Using a numerical template bank constructed from our simulation waveforms, we demonstrate the ability to measure the total core rotation (via either $\beta_{\mathrm{ic,b}}$ or $J_{\mathrm{ic,b}}$) to within $\sim 20\%$ for unknown GW signals from rotating core collapse in the context of a single Advanced LIGO detector with Gaussian noise optimally-oriented for linearly polarised GWs from a hypothetical source at 10 kpc . Employing a Bayesian model selection analysis inspired by that presented in Chap. 5, we also show that the differential rotation length scale A can be estimated for rapidly rotating cores ($\beta_{\mathrm{ic,b}} \gtrsim 0.08$) with moderate to strong differential rotation, assuming that the nuclear matter EOS and inner-core electron fraction are well understood.

In this study, we have broken new ground by combining precision waveform modelling and GW inference considerations for rotating CCSNe. While our analyses are undeniably subject to limitations, we have shown that information on total core rotation and the degree of differential rotation can be constrained from GW observations of the next galactic CCSN. Future work must address the limitations of this work, namely; (i) The impact of non-axisymmetric dynamics in millisecond PNSs (see, e.g. [65, 66, 294]) on the GW signature from collapse, bounce, and early ringdown in addition to the viability of constraining the angular momentum distribution of the precollapse core. (ii) Comparison of dynamics and GW signatures from this study to simulations using precollapse progenitors evolved with rotational effects. (iii) Extension of proof-of-principle studies to employ multi-detector networks with accurate antenna responses and realistic detector noise. While inoptimal detector alignment will reduce sensitivity, GW observation across multiple detectors increases the network SNR and help mitigate the impact of non-Gaussian noise transients. (iv) Implementation of more realistic neutrino treatment to explore the effects of rapid rotation on core deleptonisation, in addition to the resultant impact of collapse dynamics and GW signature (see, e.g. [26]). (v) Development of heuristic approaches to parameter estimation (see, e.g., semi-analytic prediction of GW spectra [251]) to overcome limitations faced by current techniques for slowly rotating progenitors due to presence of stochastic components in the GW signature.

7 The role of waves in the core-collapse supernova explosion mechanism

"[The sorting hat] only put me in Gryffindor," said Harry in a defeated voice, "because I asked not to go in Slytherin…"

"Exactly," said Dumbledore, beaming once more. "Which makes you very different from Tom Riddle. It is our choices, Harry, that show what we truly are, far more than our abilities."

—J. K. Rowling, *Harry Potter and the Chamber of Secrets*

[1] S. E. Gossan, J. Fuller, and L. F. Roberts. On the role of waves in the core-collapse supernova explosion mechanism (2019). In preparation; to be submitted to Mon. Not. Roy. Astron. Soc..
SEG used simulation outputs produced by LFR to carry out all post-processing calculations, as led by JF who also guided matters of interest. SEG produced all figures, and wrote the manuscript text alongside JF.

7.1 Motivation

The CCSN explosion mechanism is not completely understood. Several mechanisms have been proposed (see, e.g., [43, 127, 295, 296] for broad reviews), but shock revival through delayed neutrino heating is favoured for progenitor cores with pre-collapse rotational periods greater than a few seconds. The ability of the so-called neutrino mechanism to robustly drive SN explosions in a wide range of progenitor stars, however, is far from established. What has become clear is that the development and sustained presence of multidimensional hydrodynamic instabilities in the post-shock accretion flow, such as turbulent neutrino-driven convection and the SASI (see, e.g., [7] and references therein) is crucial for successful explosions. Even when explosions are produced, it is often not clear what the total explosion energy should be, nor how it is dependent on the progenitor properties or the explosion dynamics.

Unsurprisingly, the high-resolution, long-term simulations required to explore this problem present a computationally daunting task. In the interest of reducing computational costs, employing more sparse radial grid resolution has long been a go-to tactic. It has been shown, however, that failure to resolve turbulence across the inertial range reduces turbulent pressure beneath the stalled shock, unintentionally further inhibiting explosions [297–299]. Another strategy employed, particularly by simulations following the evolution of the collapsing star to late times, is evolving the PNS in spherical symmetry. While this increases the Courant limit on the time step, the resultant suppression of non-radial hydrodynamics in the PNS may well sound the death knell for successful shock revival, as we discuss here in this chapter.

Beyond spatial and temporal resolution, the greatest computational cost is often incurred through implementing some treatment for neutrino transport, and/or its effects on composition. Over 99% of the almost $\sim 10^{54}$ erg of energy released during a supernova is emitted in neutrinos. This reservoir originates, for the most part, from the release of gravitational binding energy during core collapse, PNS formation, and early PNS evolution as the nascent remnant cools, which occurs over a timescale of tens of seconds. In simulations concerned only with the "explodability" of a set of progenitor models, neutrino transport is often not put into place at all. Instead, parameterised "light-bulb" models (see, e.g., [300]), which macroscopically describe the effects of weak interactions and neutrino transport (e.g., deleptonisation, entropy changes, and neutrino stress as a function of density and lepton number) are implemented. While these simulations are no doubt far less computationally expensive than their counterparts employing more sophisticated neutrino transport, they rarely see runaway explosions without artificially amplifying the emitted neutrino luminosity to unphysical values [246, 301, 302].

In contrast, state-of-the-art simulations using three-flavour, multi-group neutrino radiation transport in multiple dimensions (see, e.g., [24]) have seen a greater fraction of successful explosions, if not often delayed (more than ~ 500 ms - 1 s after core bounce) and/or less energetic than expected. While failed explosions are still seen with more involved simulations, several studies have shown that the evolutionary track for many models exists near boundary between successful explosion and failed supernova [303–305].

Generally speaking, the impact of the approximations highlighted above on the "explodability" of realistic progenitor stars is poorly understood. As a consequence, it is important to investigate the significance of additional physical processes (or "mechanisms") contributing to the dynamics of shock revival, even if they are sub-dominant. In this chapter, we seek to explore the effect of heating from gravito-acoustic waves excited by PNS convection on shock revival and explosion energy in the context of CCSNe. In the following, we outline the basic concept of our proposed idea in section 7.2, detail the spherically-symmetric simulations employed for this study in section 7.3, and describe our wave energy flux calculations in section 7.4. In section 7.5, we examine wave damping processes and the impact of non-linear wave dynamics, before discussing the implications (and limitations) of our work in light of these effects in section 7.6, and conclude with section 7.7.

7.2 Basic idea

The evolution of the PNS and supernova shock wave during the first few hundred milliseconds after core bounce is, for the most part, agreed upon by simulations. Its energy drained through a combination of neutrino losses and photodissociation of infalling heavy nuclei, the shock stalls (at radius r_{sh}) between 150 km and 250 km. The subsonic material interior to (i.e., beneath) the shock is roughly in hydrostatic equilibrium with the (infalling) stellar layers exterior to the shock. Within around 100 ms of core bounce, regions of net neutrino heating (in the post-shock "gain region") and net neutrino cooling (above the PNS "surface", roughly where the density $\rho \sim 10^{11}\,\mathrm{g\,cm^{-3}}$) develop. The negative entropy gradient that emerges in the gain region drives vigorous convection there, which rapidly becomes turbulent. The gain radius, which marks the inner bound of the net heating region beneath the shock, is typically between 50 km and 100 km. Beneath the gain region exists a radiative layer, stably stratified by net neutrino cooling which creates a positive entropy gradient. This layer extends below the neutrinosphere, interior to which neutrinos are strongly coupled to (i.e. trapped by) the dense matter comprising the inner PNS core. Meanwhile, gradients in composition and entropy develop between the hot, lepton-rich core and the neutrino-cooled, deleptonised outer PNS surface layer drive convection in the PNS mantle. Many simulations confirm the development of a convective layer in the PNS mantle within 150 ms to 200 ms after core bounce, at radii between roughly 10 km and 20 km.

We are concerned with the effects of energy transport via hydrodynamic waves from the PNS mantle out to the post-shock region. As discussed by [306], internal gravity waves are generated by turbulent convection and emitted at convective-radiative interfaces, transporting energy and angular momentum away from the convective zone and depositing it where the waves experience heavy damping. Energy and angular momentum transport through gravity waves generated via this mechanism can be significant, and has been shown to have important ramifications inside low-mass, Sun-like stars (e.g. [268, 307, 308]), intermediate-mass stars [309, 310], and massive stars [54, 311–313].

In the context of the PNS and the evolving supernova shock, gravity waves are expected to be excited in two regions; the optically thick and convective PNS mantle, and secondly in the gain region below the shock due to neutrino-driven convection. The detailed study presented in [314] (see also [315]) examines the properties of the inner PNS convection zone and the gravity waves in the overlying radiative layer, which is neutrino-cooled. They find gravity waves with angular index $\ell = 1 - 3$ and angular frequencies $\omega \sim 10^3\,\mathrm{rad\,s^{-1}}$, though their excitation is primarily attributed by the authors to the (more vigorous) convection present in the outer convective zone. We note, however, that gravity waves are also excited by convection in the PNS mantle. Gravity waves generated here will couple to acoustic waves in the outer PNS, where they then propagate out to the stalled shock. Energy and angular momentum is transported outwards by these waves from the convective zone in the PNS mantle (which is driven, ultimately, by the release of gravitational binding energy as the nascent remnant cools and contracts over the timescale of several seconds), and deposited in regions of heavy damping. Should this damping occur predominantly in the gain region, the increased energy deposition may augment the thermal pressure behind the shock, aiding in its revival. Alternatively, waves that propagate all the way out to the shock will be reflected back inwards, imparting energy and momentum on the shock and driving it outwards. We illustrate this scenario with a stylised cartoon diagram in Fig. 7.1.

We note that this process is related to the *acoustic mechanism* proposed by [226], but with key differences. While the former is powered by energy from accretion of infalling material onto the outer PNS, the acoustic energy we consider comes from the liberation of gravitational binding energy as the PNS deleptonises and contracts. This reservoir, holding almost 10^{54} erg of binding energy at capacity, remains tappable long after accretion onto the PNS has ceased. Consequently, gravity waves excited in this way have the potential to aid shock revival and help to drive the explosion for several seconds after core bounce. The inefficient transport of a small fraction of the PNS binding energy out to the gain region via gravity waves may be considered an aspect of the so-called CCSN "central engine". It follows that effects from these waves may be missed in simulations (for the purposes of reducing computational cost) don't follow PNS evolution either (i) long enough to witness the development of a convective layer in the PNS mantle, or (ii) with sufficient degrees of freedom in long-running simulations, suppressing the development of non-radial hydrodynamic instabilities and, in turn, their effect.

First and foremost, the goal of the study presented here is to determine the extent to which gravito-acoustic waves generated by PNS convection could contribute to shock revival and to, perhaps, increase the fraction of successful explosions seen by simulations evolving CCSNe. We employ spherically-symmetric simulations to estimate the spectral behaviour and energy flux of waves excited by PNS convection, then quantitatively estimate the potential for heating in the gain region from wave energy transport for the first second after core bounce. We discuss the assumptions made to calculate these estimates, and explore how wave damping and non-linear effects could impact our results. Lastly, we consider how wave dynamics can be captured and

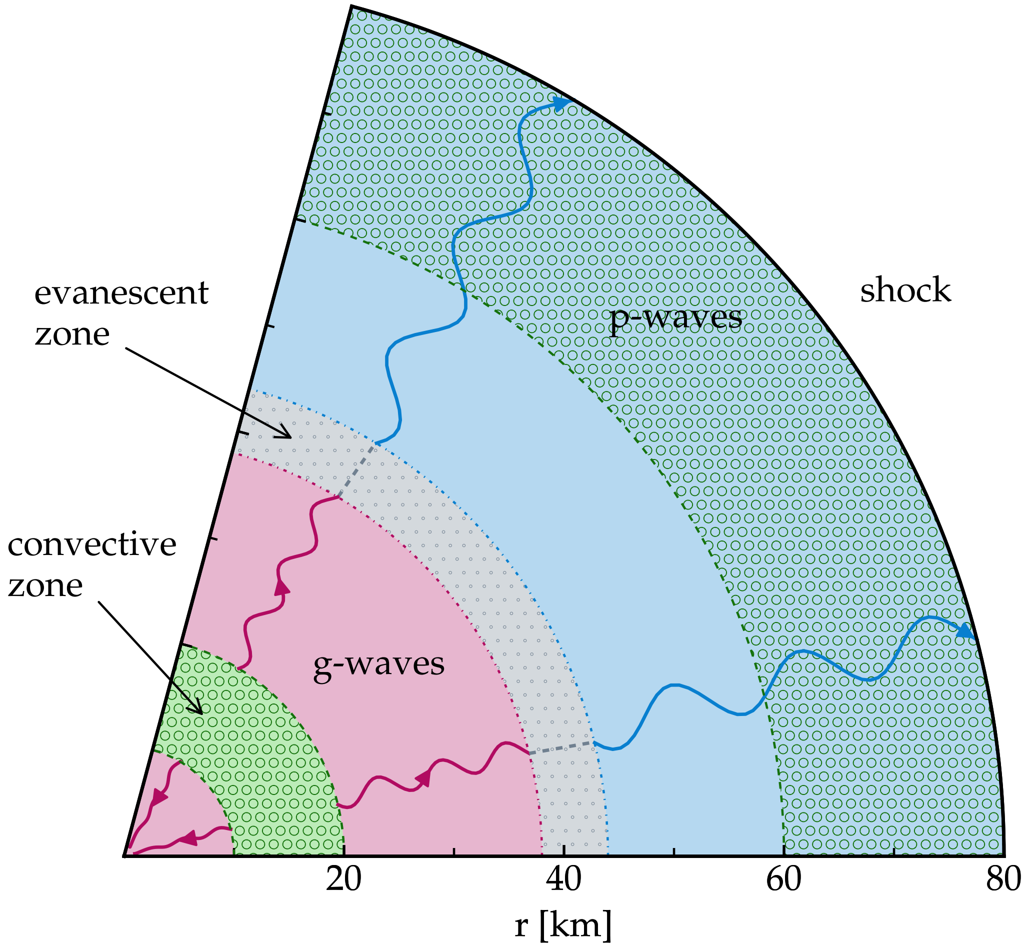

Figure 7.1: Cartoon diagram illustrating the excitation of gravity waves (at angular wave frequency ω) by convective instability in the PNS mantle in the context of our post-shock wave heating hypothesis. Outgoing waves propagate through i the PNS, tunnel out through the evanescent PNS surface, and travel towards the stalled shock as acoustic waves. On reaching the shock boundary, the waves reflect and impart momentum, dissipating energy in the post-shock region and contributing additional pressure there. Here, waves are excited around the inner convective region (shown shaded green with circle hatch). Gravity waves (which propagate where shaded pink) travel outwards, tunnelling through the evanescent PNS surface (shown in light gray with dotted hatch), beyond which they can travel as acoustic waves (region shaded blue) until either damped away or reach the shock (located at the outer edge of the diagram).

heating rates quantified in future simulations.

7.3 Simulations

We employ a spherically symmetric, fully implicit, general relativistic radiation hydrodynamics code, which employs mixing length theory to account for the effect of convective motion [79, 316]. Neutrino transport is treated through a general relativistic moment-wise scheme, employing a variable Eddington factor approach (which retains only the first two moment equations and assumes a closure relation between these and higher order moments; see [317]), with a closure relation derived from a formal solution of the static relativistic Boltzmann equation [79]. The approach, incorporating inelastic scattering and pair production, and treats the spectral behaviour of the neutrinos via energy-integrated groups. Three species of neutrino are considered $\nu_i \in \{\nu_e, \bar{\nu}_e, \nu_x\}$, where ν_x is a characteristic heavy-lepton neutrino employed to encompass the effects of neutrinos ν_μ, ν_τ, and their respective anti-particles. Each neutrino populations is modelled by a distribution of massless Dirac fermions, where neutrinos within a particular energy bin are distributed as for a Fermi blackbody. For each energy group, the effective Planck mean opacity from absorption is computed using a ten-point quadrature to obtain group-averaged opacities, corrected for detailed balance. Group-averaged opacities from scattering, calculated using a five-point quadrature, are not weighted by the local thermal neutrino distribution.

We simulate the core collapse and post-bounce evolution of a $15\,M_\odot$ progenitor star out to 660 ms after core bounce. To close the set of general-relativistic radiation hydrodynamics equations, we employ the Lattimer-Swesty equation of state with incompressibility parameter $K = 220\,\mathrm{MeV}$, with modifications as outlined in [198, 318]. The prescription for energy-dependent neutrino transport uses twenty energy groups spanning the range [0, 200] MeV. Here, nineteen logarithmically-spaced energy bins cover [0, 80] MeV, and a final group spans [80, 200] MeV. In Fig. 7.2, we show snapshots of the radial profiles of interior PNS quantities at four times post-bounce.

We see that entropy in the post-shock region rises from $\sim 12\,k_\mathrm{B}$/baryon to $\sim 22\,k_\mathrm{B}$/baryon between 225 ms and 600 ms post-bounce. In the PNS mantle, gradients in composition and temperature steepen with time, driving convective instability from ~ 200 ms post-bounce through the end of the simulation. The peak temperature, located around the inner boundary of the

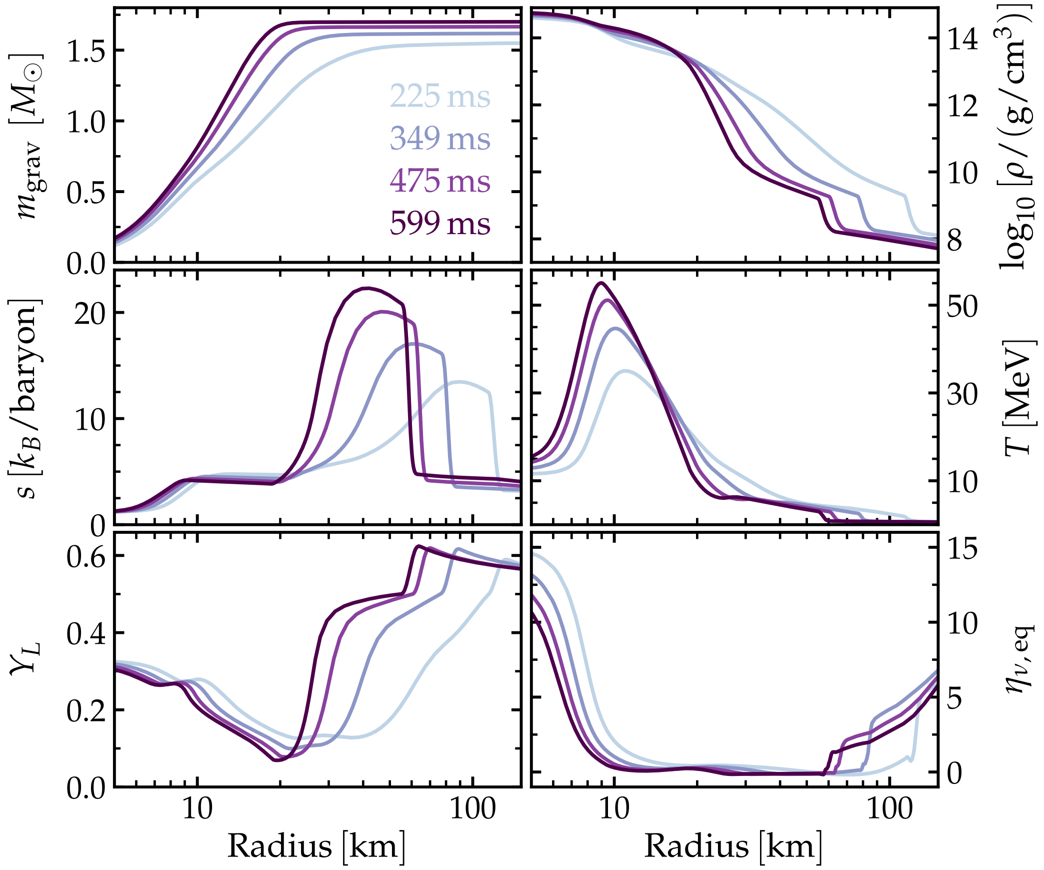

Figure 7.2: Radial snapshots of the enclosed gravitational mass $m_{\rm grav}$ (top left panel), logarithmic mass density $\log_{10}\rho$ (top right panel), specific entropy s (center left panel), temperature T (center right panel), lepton fraction $Y_{\rm L}$ (bottom left panel), and neutrino degeneracy parameter $\eta_{\nu_e,\rm eq}$ (bottom right panel) below the shock radius $r_{\rm sh}$, shown at 225 ms (with a light blue line), 349 ms (with a lavender line), 475 ms (with a rich lilac line), and 599 ms (with an aubergine line) post-bounce.

inner convective zone, rises from $\sim$ 30 MeV to more than 50 MeV between 225 ms and 600 ms post-bounce and the PNS cools and contracts. In the PNS core, comparatively low lepton fractions accompany strongly degenerate ν_e neutrinos. In the range 10 km $\lesssim r \lesssim$ 20 km, a negative lepton gradient combined with a (much shallower) negative entropy gradient both contribute to the onset of convection there.

7.4 Wave generation and energy transport

As previously introduced, gravity waves are excited by turbulent convection at the interface between convective and radiative zones. To establish said boundaries, we use the sign of the squared Brunt-Väisälä (or buoyancy) frequency N^2 as a proxy for the convective stability of a region, where

$$N^2 = -\frac{g}{n_\mathrm{B}}\left(\frac{dn_\mathrm{B}}{dr} - \frac{dP}{dr}\left(\frac{\partial n_\mathrm{B}}{\partial P}\right)_s\right), \tag{7.1}$$

We designate radial grid zones convective where $N^2 < 0$, and conversely radiative where $N^2 > 0$. For plotting purposes, the scaled buoyancy frequency N_p is also an instructive quantity to calculate, where

$$N_p = \mathrm{sign}(N^2)\sqrt{|N^2|}\,. \tag{7.2}$$

In the top panel of Fig. 7.3, we show the temporal evolution of N_p below the shock. We see the emergence of a convectively unstable region around 20 km a little before 200 ms after bounce, which quickly develops into a convective layer between 10 km and 20 km that persists through the end of our simulation. We note that, in the region of interest (the outer boundary of the inner convective region), N_p is of order $\sim 10^3$ rad/s.

The emitted flux in gravity waves L_wave is a small fraction of the convective flux L_con. While there is no doubt some uncertainty in the wave spectrum and energy flux in excited waves, both analytic ([306, 319]) and numerical ([320]) studies suggest that the wave energy flux is approximately

$$L_\mathrm{wave} \sim \mathcal{M}_\mathrm{con}\, L_\mathrm{con}\,, \tag{7.3}$$

where the convective Mach number $\mathcal{M}_\mathrm{con} = v_\mathrm{con}/c_s$ can be calculated using the characteristic convective velocity

$$v_\mathrm{con} = \left[\frac{L_\mathrm{con}}{4\pi r^2 \rho}\right]^{1/3}\,. \tag{7.4}$$

In practice, we can use the total outgoing neutrino luminosity L_ν to estimate v_con as, in the optically thick inner PNS where convection is efficient and carries away almost all of the local neutrino luminosity, $L_\mathrm{con} \sim L_\nu$. Typically, we find $\mathcal{M}_\mathrm{con} \sim 0.1$. We note that the value of L_wave varies within the convective

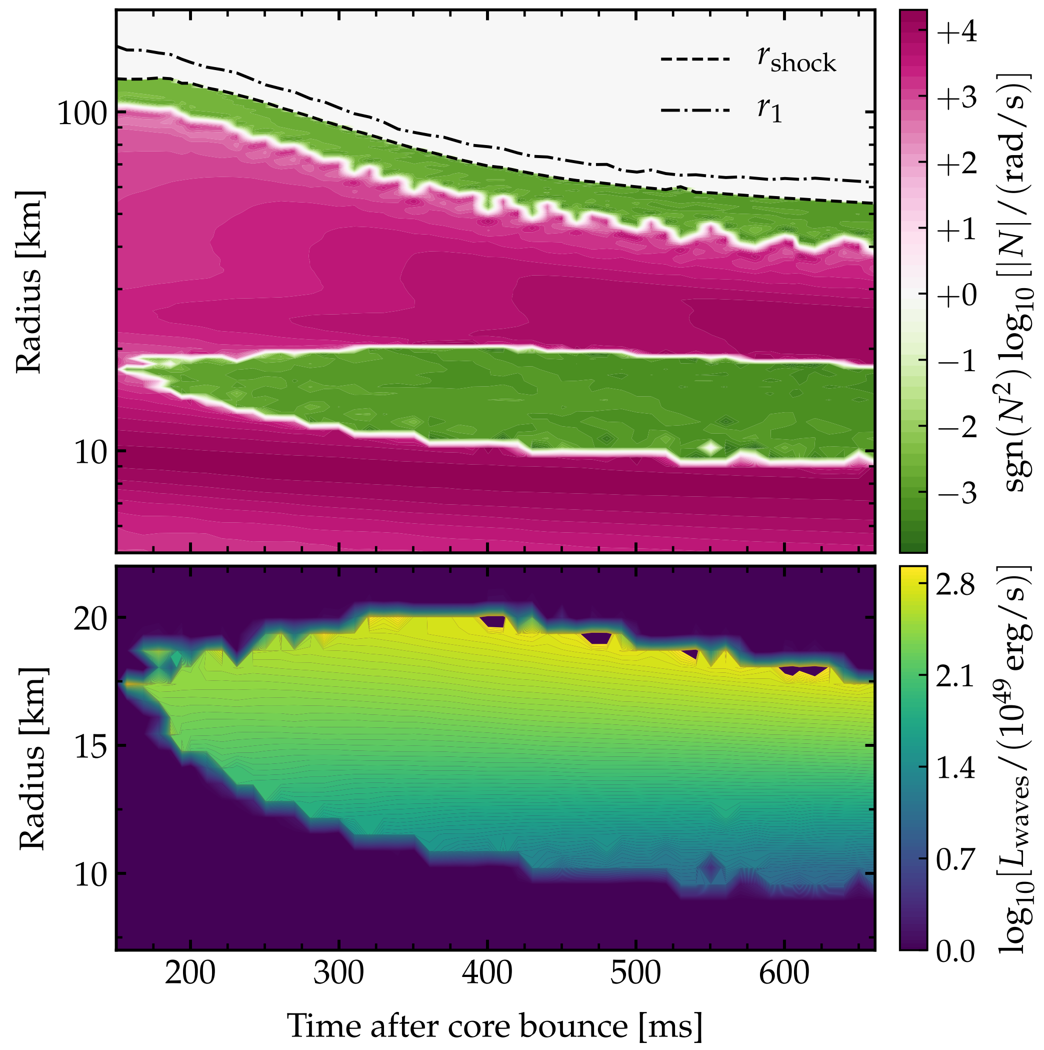

Figure 7.3: (Top panel) Colormap showing the temporal evolution of the radial profile of the scaled buoyancy frequency $N_p = \text{sign}(N^2)\sqrt{|N^2|}$ out to the shock between 200 ms and 660 ms after core bounce. The shock front is bounded by inner radius r_{sh} (shown with a dotted black line) and outer radius r_1 (shown with dot-dashed black line). Convectively unstable regions ($N_p < 0$) are shaded green, while radiative regions ($N_p > 0$, where gravity waves can propagate), are shaded pink. (Bottom panel) Temporal evolution of the wave luminosity L_{wave} generated by turbulent convection across the convective PNS mantle.

zone and so, when estimating wave energy fluxes, we use the maximum value within the convective zone, which is typically found near its upper edge. In the bottom panel of Fig. 7.3, we show the evolution of L_{wave} across the inner convective zone with time. We see wave luminosities in excess of 10^{51} erg/s sustained from around 200 ms after core bounce through the end of our simulation.

We consider waves generated by convective motion within a pressure scale height H_p of the outer boundary of the inner convective region (at radius $r = r_{\rm con}$), where

$$H_p = \frac{P}{g(\rho + P/c^2)} \,. \tag{7.5}$$

Much like the wave energy flux, the frequency and angular wavenumber spectra of waves generated in this scenario are decidedly uncertain [310, 319–321]. Most literature, however, agrees that the wave power drops significantly at frequencies above the local convective turnover frequency $\omega_{\rm con}$, where

$$\omega_{\rm con} = \frac{\pi v_{\rm con}}{2H_p} \,. \tag{7.6}$$

We adopt a flat spectrum across angular modes $\ell \in [1, \ldots, \ell_c]$, where $\ell_c = r_{\rm con}/\Delta r_{\rm con}$ is determined by the physical width of the convection zone, $\Delta r_{\rm con}$. This choice reflects the fact that thin convective zones have smaller eddies that excite waves with smaller horizontal wavelength and, thus, larger angular wavenumber ℓ. Per excited mode, the emitted wave flux $L_{{\rm wave}\,,\ell}$ then follows

$$L_{{\rm wave}\,,\ell} = \frac{L_{{\rm wave}\,,\ell}}{\ell_c} \,. \tag{7.7}$$

In Fig. 7.4, we show the evolution of the convective velocity $v_{\rm con}$, convective turnover frequency $\omega_{\rm con}$, maximum angular wave mode excited ℓ_c, and the wave flux per angular mode $L_{{\rm wave}\,,\ell}$ with time. We find the convective velocity remains roughly constant around $(4 - 4.5) \times 10^8$ cm/s, while the convective turnover frequency steadily increases by a factor of four from $\sim 10^3$ rad/s to $\sim 4 \times 10^3$ rad/s between 200 ms post-bounce and the end of our simulation. At early times, when the physical width of the inner convective zone is thin, modes up to $\ell_c \sim (5 - 6)$ are excited, though $\ell_c \to 3$ by ~ 250 ms post-bounce. From ~ 250 ms through the end of our simulation, the emitted wave luminosity per angular mode exceeds 10^{51} erg/s.

After waves are excited, their propagation within the PNS is largely gogverned by the dispersion relation for gravito-acoustic waves of angular frequency ω,

$$k_{r,\ell}^2 = \frac{(N^2 - \omega^2))(L_\ell^2 - \omega^2)}{\omega^2 c_s^2} \,, \tag{7.8}$$

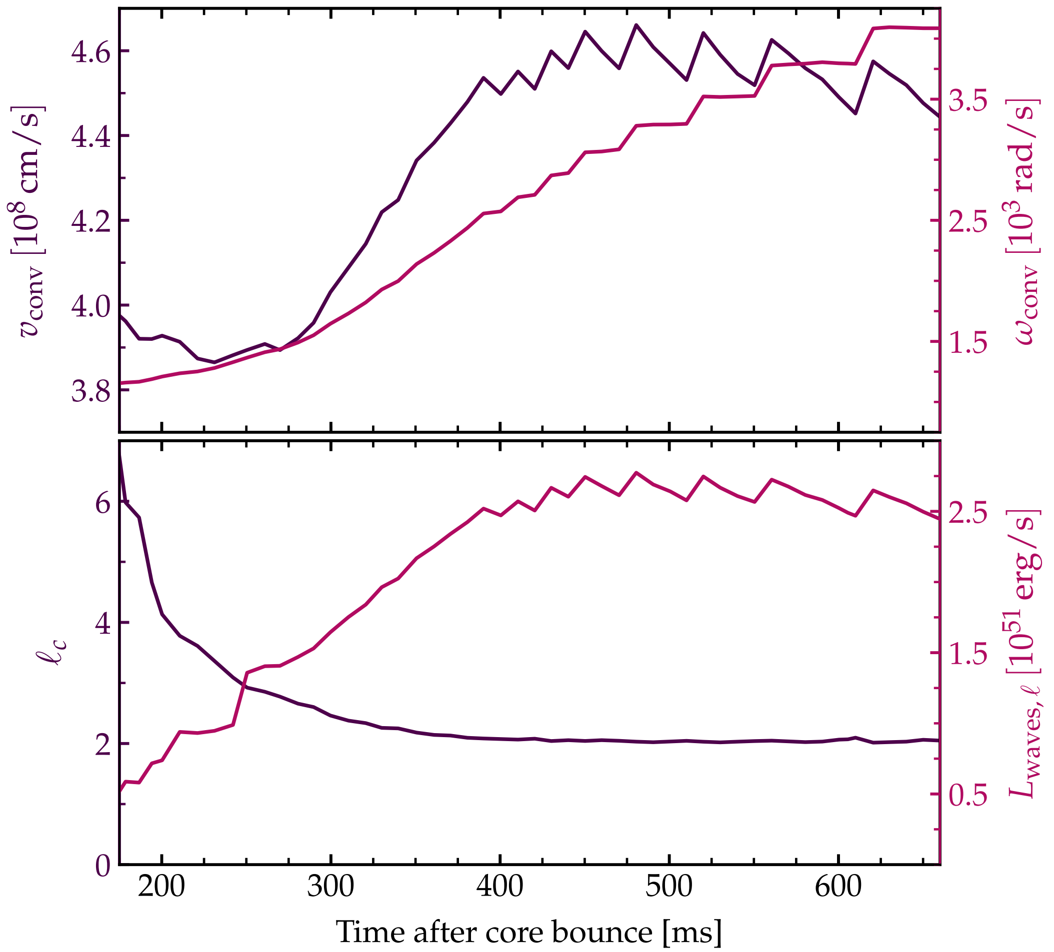

Figure 7.4: (Top panel) Temporal evolution of the convective velocity $v_{\rm con}$ (left axis, deep purple trace) and convective turnover frequency $\omega_{\rm con}$ (right axis, pink trace), measured at the upper edge of the inner convective region. (Bottom panel) Temporal evolution of the maximum angular wavenumber of excited waves, ℓ_c (left axis, deep purple trace), and wave luminosity emitted per angular mode excited $L_{{\rm wave}\,,\,\ell}$ (right axis, pink trace) at the upper edge of the inner convective region with time.

where $k_{r\,,\,\ell}$ is the radial wavenumber for waves of angular mode ℓ, and Lamb frequencies L_ℓ are defined

$$L_\ell^2 = \frac{\ell(\ell+1)c_s^2}{r^2}\,, \tag{7.9}$$

given adiabatic sound speed $c_s^2 = \Gamma_1 P/\rho$, where $\Gamma_1 = (\partial \log P/\partial \log \rho)_s$ is the adiabatic index. Where $\omega < N, L_\ell$, the waves propagate as gravity waves, while they propagate as acoustic waves where $\omega > N, L_\ell$. Where ω lies between N and L_ℓ, the waves cannot propagate and are evanescent. In Fig. 7.5, we show propagation diagrams for $\ell = 2$ waves at 225 ms, 349 ms, 475 ms, and 599 ms post-bounce.

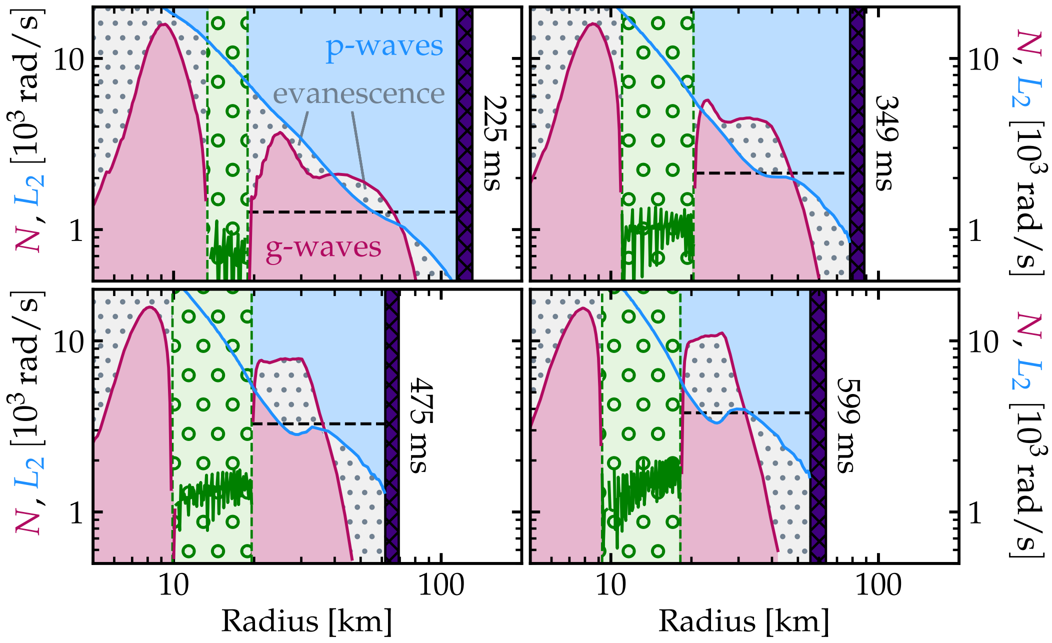

Figure 7.5: Propagation diagrams for $\ell = 2$ gravito-acoustic waves at 225 ms (top left panel), 349ms (top right panel), 475 ms (bottom left panel), and 599 ms (bottom right panel) post-bounce. In each panel, the inner convective region shown with green shading with circle hatch, with the magnitude of the scaled buoyancy frequency $|N_p|$ overlaid. The $\ell = 2$ Lamb frequency L_2 (solid blue line) and scaled buoyancy frequency N_p (solid deep pink line) are also shown. Regions where gravity waves of angular frequency ω can propagate (i.e., where $\omega < N, L_2$) are shaded in pink, while regions in which acoustic waves propagate (i.e., where $\omega > N, L_2$) are shaded in blue. Waves cannot propagate in evanescent regions (where $N < \omega < L_2$ or $N > \omega > L_2$), which are shown with gray shading and dotted hatch. The physical extent of the shock is indicated with dark purple shading and crossed hatch. For waves at frequency $\omega_{\rm con}$, the propagation track is overlaid with a thick dashed green line.

From Fig. 7.5, we see that the width of the evanescent region is highly sensitive to the wave frequency. For $\ell = 2$ waves, the propagation track along $\omega = \omega_{\rm con}$ skims the bottom of a large evanescent region in frequency space. After one pass, a fraction T_ℓ^2 of the incident wave flux is transmitted through the evanescent region (bounded by gravito-evanescent radius $r_{\rm grav-ev}$ and acoustic-evanescent radius $r_{\mathrm{ac-ev}}$), where transmission coefficients T_ℓ^2 are

$$T_\ell^2 = \exp\left[-2\int_{r_{\mathrm{grav-ev}}}^{r_{\mathrm{ac-ev}}} dr\, |k_{r,\ell}|\right]. \tag{7.10}$$

While, in principle, more wave energy could leak through the boundary following multiple reflections within the PNS, we adopt $L_{\mathrm{heat},\ell} = L_{\mathrm{wave},\ell}\, T_\ell^2$ as a conservative lower limit on the wave flux in angular mode ℓ entering the outer PNS.

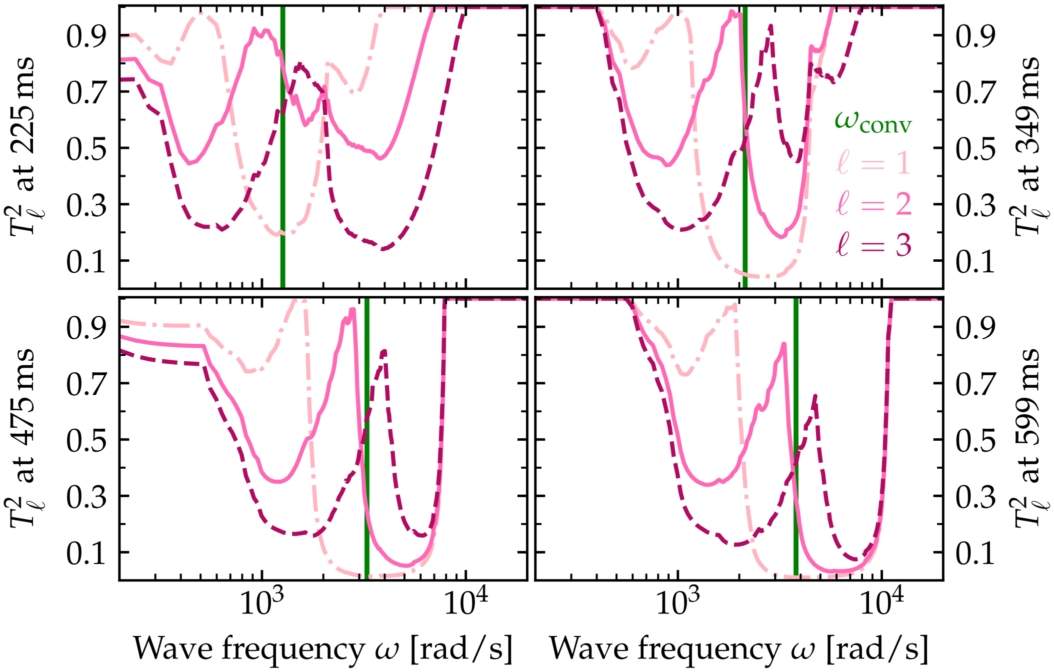

Figure 7.6: Snapshots of the fraction of wave energy transmitted to the post-shock region T_ℓ^2 in $\ell = 1$ (shown with a dash-dotted light pink line), $\ell = 2$ (solid hot pink line), and $\ell = 3$ (dashed deep pink line) waves on angular wave frequency ω at 225 ms (top left panel), 349 ms (top right panel), 475 ms (bottom left panel), and 599 ms (bottom right panel) post-bounce. The convective turnover frequency ω_{con}, at which we assume waves are excited, is overlaid with a solid green line.

In Fig. 7.6, we show snapshots of T_ℓ^2, the fraction of wave energy transmitted out to the post-shock region, for $\ell = 1 - 3$ waves as a function of angular frequency at 225 ms, 349 ms, 475 ms, and 599 ms after core bounce. We see that uncertainty in ω_{con} translates to uncertainties of order unity in the wave flux transmitted through the evanescent region. In reality, a spectrum of waves extending above and below ω_{con} will be generated, and the energy transmitted into acoustic waves of wavenumber ℓ will be $\int d\omega T_\ell^2 (dL_{\mathrm{wave},\ell}/d\omega)$,

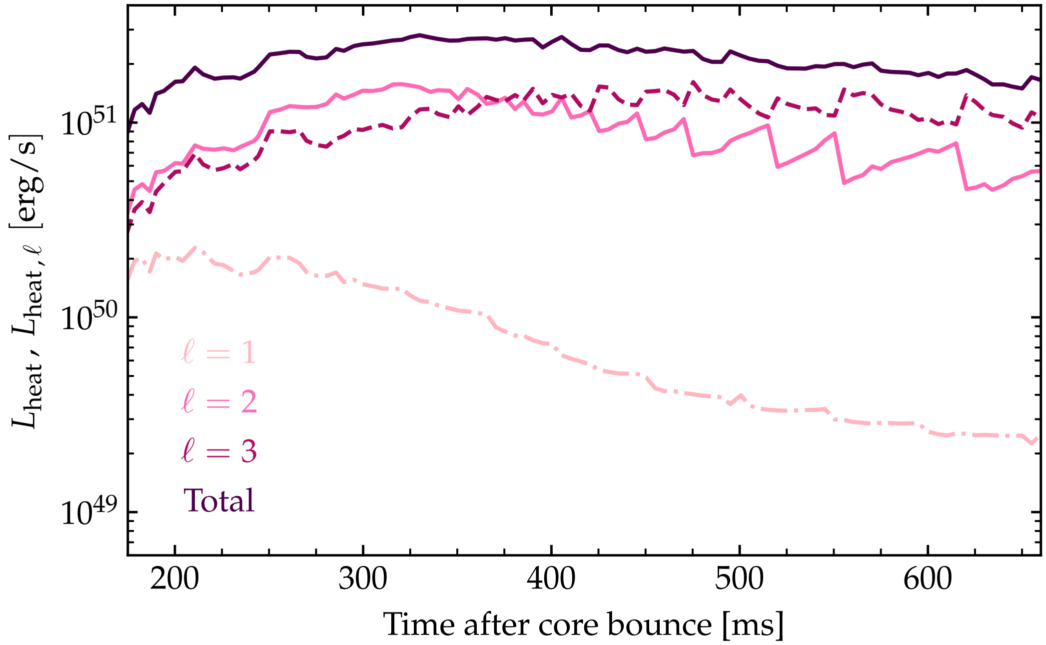

Figure 7.7: Temporal evolution of the heating rates $L_{{\rm heat}\,,\,\ell}$ for $\ell = 1$ (light pink dash-dotted line), $\ell = 2$ (solid hot pink line), and $\ell = 3$ (dashed deep pink line) waves. The total heating rate $L_{\rm heat}$, summed over all excited angular wave modes, is overlaid with a thick dark purple line.

where $(dL_{{\rm wave}\,,\,\ell}/d\omega)$ is the energy flux in waves generated per unit frequency ω. As the wave spectrum is uncertain, it follows that this integral is also uncertain, but Fig. 7.6 demonstrates that we expect transmission fractions of order $T_\ell^2 \sim 0.3$, dependent on the excited wave spectrum and the time after core bounce.

Following their transmission out from the upper edge of the evanescent region, acoustic waves can travel almost unimpeded out to the shock. Consequently, the wave energy transport rate (i.e., "heating rate") beyond the last evanescent region traversed is given by

$$L_{\rm heat} = \sum_{\ell=1}^{\ell_c} L_{{\rm heat}\,,\,\ell}\,. \tag{7.11}$$

In Fig. 7.7, we show the temporal evolution of the heating rate per angular mode ℓ, overlaid with the total heating rate (summed over excited modes) in the post-shock region. Once convection in the PNS mantle develops and begins to generate waves, we find net heating rates $L_{\rm heat}$ in excess of $\sim 10^{51}$ erg/s through the end of our simulation. The power contributed by $\ell = 1$ waves drops significantly with time, with transmitted power in $\ell = 2$ and $\ell = 3$ waves responsible for most of the net heating in the post-shock region. A more accurate calculation that integrates over the wave spectrum may well change the transmission profile. For example, at 349 ms post-bounce, we see that the lower frequency $\ell = 1$ waves and higher frequency $\ell = 3$ waves would be more easily transmitted. While this might yield slightly different net heating rates, we expect our results as presented here to be accurate within a factor of order unity.

7.5 Wave damping and non-linear effects

Until now, our calculations have implicitly assumed that waves generated by PNS convection propagate according to linear perturbation theory, and we have ignored sources of damping. We now address the validity of these assumptions, and work to quantify the effect of wave damping and non-linearity.

Neutrino damping

As discussed in [322], gravity wave attenuation through radiative losses is dominated by increased neutrino diffusion from regions of wave compression. Here, we consider the neutrino damping of gravity waves emitted from the inner convective zone as they propagate from the PNS core out to the stalled shock.

Waves with wavelength $\lambda \sim 2\pi/|k_{r,\ell}|$ will experience neutrino damping in the optically thin limit when the neutrino mean free path $\langle d_\nu \rangle$ exceeds the wavelength, i.e. $\lambda < \langle d_\nu \rangle$. In this scenario, additional neutrinos emitted due to wave-induced compression simply free-stream outwards, with the wave energy loss rate equal to the increased neutrino energy generation rate. In the optically thick limit where $\langle d_\nu \rangle < \lambda_\ell$, the energy loss rate is suppressed by a factor $(\langle d_\nu \rangle |k_{r,\ell}|)^2$ as the energy in neutrinos can only diffuse over a small fraction of the wavelength during the waves' passage. We treat neutrino damping in the quasi-adiabatic limit, where the instantaneous damoing rate γ_ν can be approximated $\gamma_\nu \sim \langle \dot{\varepsilon} \rangle / \varepsilon$. Here, $\langle \dot{\varepsilon} \rangle$ is the energy loss rate per unit mass averaged over one wave cycle, and ε is the wave energy per unit mass (see [313, 322]). Considering both optically thick and optically thin cases, γ_ν is roughly

$$\gamma_{\nu,\ell} = \frac{\delta\epsilon_\nu}{\varepsilon} \times \min\left[1, \left(\frac{|k_{r,\ell}|}{\langle\kappa_{\nu,\mathrm{tot}}\rangle}\right)^2\right], \tag{7.12}$$

where $\delta\epsilon_\nu$ is the Lagrangian perturbation of the net emissivity, and $\langle\kappa_{\nu,\mathrm{tot}}\rangle$ is the total Rosseland mean neutrino opacity.

We approximate an upper bound on the net neutrino emissivity applying the concept of stimulated absorption [323]:

$$\epsilon_\nu = \sum_{\nu_i \in \{\nu_e, \bar{\nu}_e, \nu_x\}} \langle\kappa^*_{\nu_i,\mathrm{abs}}\rangle\, B_{\nu_i}\,, \tag{7.13}$$

where $\langle\kappa^*_{\nu_i,\mathrm{abs}}\rangle$ is the Rosseland mean neutrino opacity from absorption corrected with respect to the local thermal neutrino distribution for neutrinos of flavour ν_i, and B_{ν_i} is the integrated Fermi blackbody intensity. Explicitly,

$$B_{\nu_i} = \frac{4\pi\,(k_B T)^4}{h^3\,c^2} \times \begin{cases} \mathcal{F}_3(\eta_{\nu,\mathrm{eq}}) & \text{for } \nu_e\,, \\ \mathcal{F}_3(-\eta_{\nu,\mathrm{eq}}) & \text{for } \bar{\nu}_e\,, \\ 4\mathcal{F}_3(0) & \text{for } \nu_x\,, \end{cases} \tag{7.14}$$

where

$$\mathcal{F}_3(y) = \int_0^\infty dx\,\frac{x^3}{e^{(x-y)}+1}\,, \tag{7.15}$$

is the standard third-order complete Fermi integral. For the results presented here, we have used the open-source package `fdint` ([324]; see also [325–327]) to calculate Fermi integrals when needed.

In the left column of Fig. 7.8, we show snapshots of the instantaneous damping rate $\gamma_{\nu,\ell}$ for $\ell = 1-3$ waves at 225 ms, 349 ms, 475 ms, and 599 ms post-bounce. Propagating out towards the shock at radius r, the wave flux is attenuated by a factor $\exp[-x_{r,\ell}]$, where $x_{r,\ell}$ is defined

$$x_{r,\ell} = \int_0^r \frac{dr'\,\gamma_{\nu,\ell}(r')}{v_{\mathrm{gr},\ell}}\,. \tag{7.16}$$

Here, $v_{\mathrm{gr},\ell} = |\omega/k_{r,\ell}|$ is the waves' group velocity. In the right column of Fig. 7.8, we show radial snapshots of the cumulative damping experienced, $x_{r,\ell}$, for $\ell = 1-3$ waves at 225 ms, 349 ms, 475 ms, and 599 ms post-bounce.

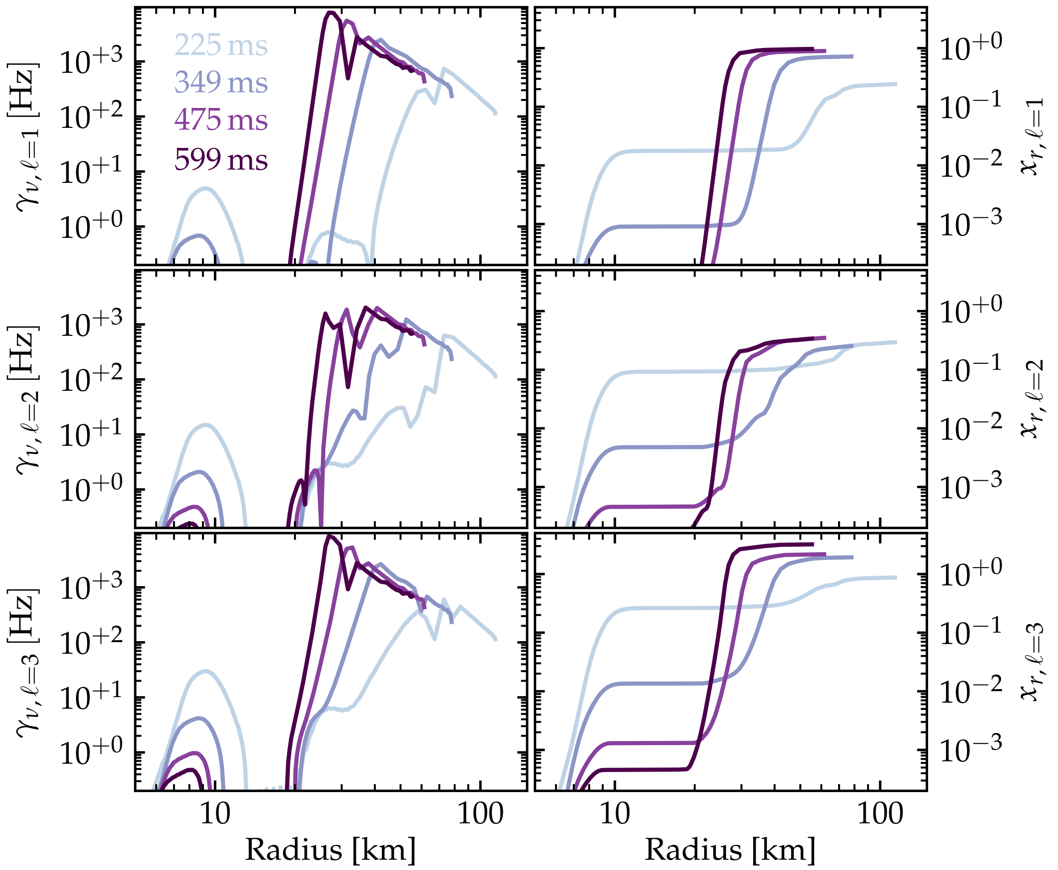

Figure 7.8: Snapshots of the local damping rate from neutrino diffusion $\gamma_{\nu,\ell}$ (left column), and the cumulative damping incurred by waves $x_{r,\ell}$ while propagating out from the PNS core to radius r (right column). For each $\ell = 1$ (top panels), $\ell = 2$ (centre panels), and $\ell = 3$ (bottom panels) waves, radial traces of $\gamma_{\nu,\ell}$ and $x_{r,\ell}$ are shown at 225 ms (in light blue), 349 ms (in lavender), 475 ms (in rich lilac), and 599 ms (in aubergine) post-bounce.

We see that damping rates are highest in the outer PNS for all $\ell = 1 - 3$ waves. This makes sense, as the waves we consider here have wavelengths of order tens of kilometres and, as such, are subject to optically thick neutrino damping until they reach larger radii where the neutrino mean free paths are large, and the neutrinos are close to free streaming. Consequently, the cumulative neutrino damping experienced by the waves is small in the PNS core and mantle (with the exception of $\ell = 3$ waves at early times), but becomes significant as they approach the post-shock region. In line with this hypothesis, we see slightly larger damping rates for $\ell = 3$ waves than $\ell = 1$ waves, which is expected given than $\ell = 3$ waves have smaller group velocities and propagate to larger radii as gravity waves, meaning that they lose more energy as they travel outwards.

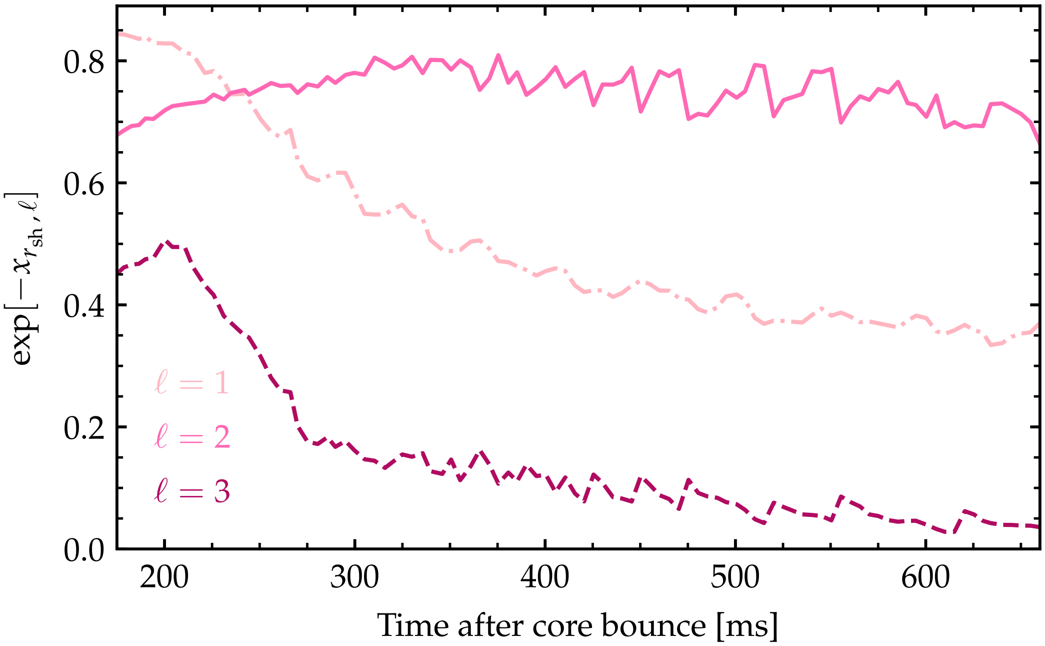

Figure 7.9: Temporal evolution of the fraction of wave luminosity not attenuated through neutrino damping $\exp\left[-x_{r_{\rm sh},\ell}\right]$ (measured at shock radius $r_{\rm sh}$) for $\ell = 1$ (shown with a dash-dotted light pink line), $\ell = 2$ (shown with a solid hot pink line), and $\ell = 3$ (shown with a dashed deep pink line) waves.

The total fraction of wave energy lost through neutrino damping in travelling from the PNS out to the shock is shown as a function of time in Fig. 7.9 for $\ell = 1 - 3$ waves. Beyond ~ 225 ms, we expect neutrino damping to be somewhat important, with a moderate fraction of the wave energy lost in the gain region through neutrino emission. We discuss the ramifications of this, in addition to other potential concerns, in Sec. 7.6.

Non-linear effects

Waves excited by convection will continue to propagate inside the PNS until their energy is dissipated as heat. In the absence of damping, the wave displacement $\vec{\xi}_\ell$ (dependent on the total wave energy) grows as the waves propagate outwards into regions with lower density, and non-linear effects may quickly become non-negligible. A useful measure of wave non-linearity for both gravity waves and acoustic waves is the dimensionless quantity $|\vec{k}_\ell \cdot \vec{\xi}_\ell| \sim |k_{r,\ell}\, \xi_{r,\ell}|$. Previous work (e.g., [328]) has shown that as $|k_{r,\ell}\, \xi_{r,\ell}| \rightarrow 1$, gravity waves overturn via stratification and break, losing energy via Kelvin-Helmholtz instabilities. As acoustic waves enter the non-linear regime, energy is lost as the waves self-shock and dissipate.

In the limit of no damping, it can be shown that the wave amplitude $|\xi_{r,\ell}|$ associated with energy flux $L_{\mathrm{heat},\ell}$ is approximately [329]

$$|\xi_{r,\ell}| \approx \left[\frac{L_{\mathrm{heat},\ell}}{4\pi\rho r^2\omega^2 v_{\mathrm{gr},\ell}}\right]^{1/2} . \tag{7.17}$$

Since the waves propagate in the inner PNS and mantle before coupling to acoustic waves near the prost-shock gain region, we consider both these cases in turn.

For gravity waves, the wave amplitude is $|\xi_\ell| \sim (|k_{r,\ell}/k_{\perp,\ell}|)\,\xi_{r,\ell}$, the group velocity is $v_{\mathrm{gr},\ell} \sim \omega^2 r/(N\sqrt{\ell(\ell+1)})$, and the radial wavevector is $k_{r,\ell} \sim N\sqrt{\ell(\ell+1)}/(\omega r)$. For low-$\ell$ gravity waves, the appropriate non-linearity measure thus follows

$$|k_{r,\ell}\,\xi_{r,\ell}|_{\mathrm{grav}} \approx \left[\frac{L_{\mathrm{heat},\ell}\,N\left(\sqrt{\ell(\ell+1)}\right)^3}{4\pi\rho r^5\omega^4}\right]^{1/2} . \tag{7.18}$$

For acoustic waves, $|\xi_\ell| \sim \xi_{r,\ell}$, $v_{\mathrm{gr},\ell} = c_s$, and $k_{r,\ell} \sim \omega/c_s$. It follows that for low-ℓ acoustic waves,

$$\left|k_{r,\ell}\,\xi_{r,\ell}\right|_{\mathrm{ac}} \approx \left[\frac{L_{\mathrm{heat},\ell}}{4\pi\rho r^2 c_s^3}\right]^{1/2} . \tag{7.19}$$

In Fig. 7.10, we show radial snapshots of $|k_{r,\ell}\,\xi_{r,\ell}|$ for $\ell = 1$–3 waves at 225 ms, 349 ms, 475 ms, and 599 ms after core bounce. Throughout the PNS for the duration of the simulation, $|k_{r,\ell}\,\xi_{r,\ell}| \ll 1$ for $\ell = 1$ waves. On approach to the gain region, $|k_{r,\ell}\,\xi_{r,\ell}| \sim 0.1$ for $\ell = 2$ and $\ell = 3$ waves. In the PNS core at early times, non-linear effects may be important for gravity waves. This suggests that waves propagating through the inner core are moderately non-linear, and may lose some fraction of their energy to non-linear dissipative effects. As we don't take their energy into account when calculating L_{heat}, such dissipation will not affect our main results, but could limit the contribution of such waves to any excess flux above L_{heat}. The main result is that no waves are in the strongly non-linear regime ($|k_{r,\ell}\xi_{r,\ell}| > 1$), so we do not expect

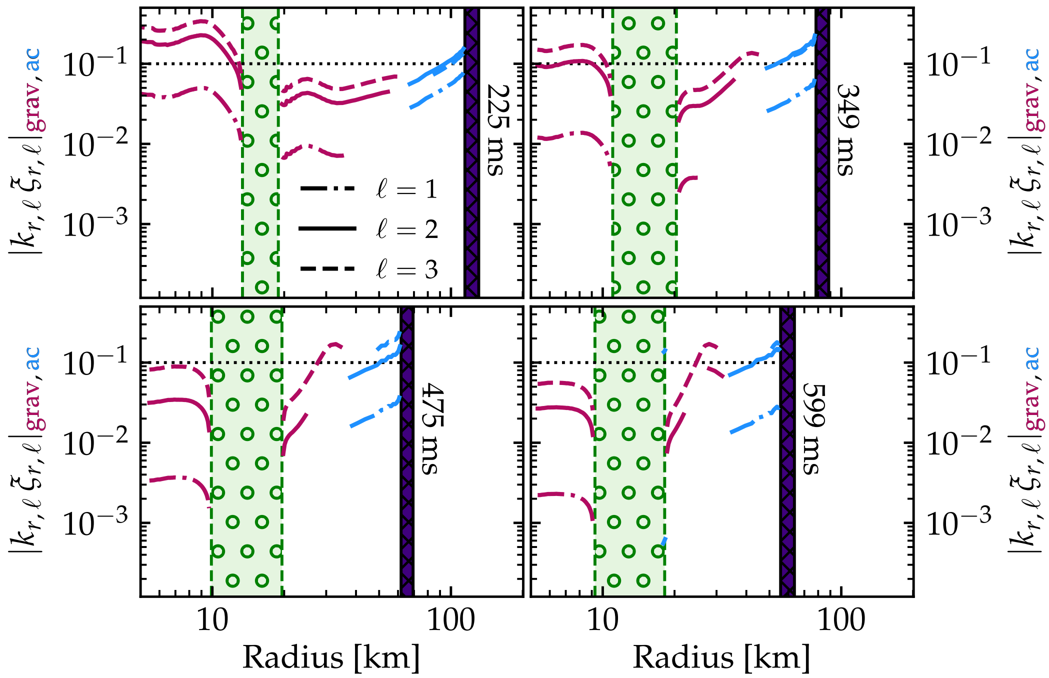

Figure 7.10: Radial snapshots of dimensionless wave non-linearity measure $|k_{r,\ell}\,\xi_{r,\ell}|$ for $\ell = 1$ (dash-dotted line), $\ell = 2$ (solid line), and $\ell = 3$ (dashed line) waves at 225 ms (top left panel), 349 ms (top right panel), 475 ms (bottom left panel), and 599 ms (bottom right panel) post-bounce. Lines are shown in deep pink where gravity waves propagate ($\omega < N, L_\ell$), and shown in blue where acoustic waves travel($\omega > N, L_\ell$). Regions in which the waves are evanescent (i.e., where $N < \omega < L_\ell$ or $L_\ell < \omega < N$) are left blank. For each snapshot, the inner convective region is shaded green with circled hatch, while the shock is shown in deep purple with crossed hatch. In each panel, we overlay dotted lines at $|k_{r,\ell}\,\xi_{r,\ell}| = 0.1$, beyond which non-linear effects are likely to be important for the wave dynamics.

rapid wave damping due to breaking or shock formation. We do find moderately non-linear amplitudes ($|k_{r,\ell}\xi_{r,\ell}| \gtrsim 0.1$) just below the shock, which could cause some wave damping there. When a successful explosion develops, the shock moves out to lower densities, and it is much more likely that acoustic waves will become strongly non-linear, forming weak shocks and depositing their energy as heat within the PNS wind.

It is also important to address the possibility of non-linear three-mode coupling and whether this can quench the wave energy transport, as discussed by [322]. The primary waves excited by convection are low-order (0-2 radial nodes, $\ell = 1-3$) gravity waves in the outer PNS, whereas the acoustic mechanism involves low-order gravity modes in the inner PNS. Due to neutrino damping in the outer PNS, the outgoing convectively excited waves have low quality factors $Q \sim 3$ (see Fig. 7.9), and there are few daughter modes with frequencies $\omega_{\rm d} \sim \omega_{\rm wave}/2$ with which to resonantly couple. Mode coupling likely occurs in the non-resonant limit as given by Eq. 2 of [322], and hence we expect saturation energies of $E_{\rm sat} \sim 10^{49}$ erg. In contrast to lower frequency modes trapped in the inner core, the gravity waves we consider traverse the outer PNS in a wave crossing time $t_{\rm cross} \sim 5\,$ms. The maximum rate at which the oscillating PNS can radiate energy in acoustic waves is $\dot{E} \sim E_{\rm sat} T_\ell^2 / t_{\rm cross} \sim 10^{51}$ erg/s for a transmission coefficient of $T_\ell^2 = 0.5$. As a consequence, our computed energy fluxes are at the limit where non-linear coupling may affect our results, but we don't expect non-linear suppression far below our estimates.

It is worth noting that the wave crossing time is only a few times larger than the wave oscillation periods, and comparable to the daughter mode periods. Hence, we consider it unlikely that non-linear coupling can dissipate the waves faster than the wave crossing time, and thus unlikely it can strongly attenuate the gravity waves before the transition into acoustic waves. This is an important distinction from lower frequency waves or modes trapped in the inner core, which must undergo many more oscillation cycles before their energy leaks out into the envelope.

Our estimates of wave heating are lower limits in the sense that they don't allow for gravity waves to reflect multiple times within the PNS before tunnelling into outgoing acoustic waves. In the absence of damping, multiple reflections could allow the acoustic wave energy flux to approach $L_{\rm wave}$ rather than $L_{\rm wave} T_\ell^2$. Based on the calculations above, however, non-linear coupling likely can prevent gravity waves from reflecting many times and accumulating energy in the outer PNS. With this in mind, it is unlikely that multiple reflections would greatly increase the wave heating rates.

Impact of waves on shock revival

Under the assumption that any wave energy lost through neutrino damping free-streams out through the shock and escapes, an approximate lower limit on the wave energy transport rate to the post-shock region may be obtained simply by multiplying the ideal heating rate by the fraction not attenuated by neutrino damping. Explicitly, an estimate for the corrected heating rate L'_{heat} is just

$$L'_{\mathrm{heat}\,,\ell} = L_{\mathrm{heat}\,,\ell} \exp\left[-x_{r_{\mathrm{sh}},\ell}\right], \tag{7.20}$$

$$L'_{\mathrm{heat}} = \sum_{\ell=1}^{\ell_c} L'_{\mathrm{heat}\,,\ell}\,. \tag{7.21}$$

In the top panel of Fig. 7.11, we show the wave energy tranport rate in the post-shock region, corrected for neutrino damping, as a function of time for $\ell = 1 - 3$ waves, in addition to the total corrected rate summed over all excited angular modes. While slightly reduced relative to Fig. 7.7, we see that corrected wave heating rates are still expected to be substantial, with typical values $L'_{\mathrm{heat}} \sim 4 - 10 \times 10^{50}$ erg/s in wave power reaching the shock over the course of the simulation.

Exactly what happens as the waves reach the shock is complicated but, in general, downward reflection of the waves at the shock is expected. Acoustic waves are reflected at the discontinuity in density, entropy, and flow velocity, due to the supersonic inflow velocity above the shock. Generally speaking, acoustic waves here are partially reflected (to inwardly propagating acoustic waves), or transformed into vorticity and entropy waves through perturbation of the shock. Wave amplitudes can be amplified by tapping the kinetic energy of mass falling onto the shock, hence we expect the wave pressure calculations below to be conservative estimates. The interaction of outgoing acoustic waves with the stalled shock has been studied extenstively in the context of the SASI (see, e.g., [7, 330–332]), but the particulars of the wave-shock interaction are beyond the scope of this study and left to future work. We also direct the interested reader to work by [304, 305, 333] for discussions on the interaction of waves with the stalled shock.

The momentum flux carried by the acoustic waves is imparted onto the shock as they reflect at it, just as photons impact momentum when they reflect at a surface. The waves therefore exert pressure on the shock, and a useful figure of merit to consider is the ratio of wave pressure P_{wave} to total fluid pressure at the shock. The momentum flux in acoustic waves is $L_{\mathrm{wave}}/(2c_s)$, and thus the wave pressure can be estimated from the heating rate;

$$P_{\mathrm{wave}} = \frac{L'_{\mathrm{heat}}}{4\pi r^2 c_s}\,, \tag{7.22}$$

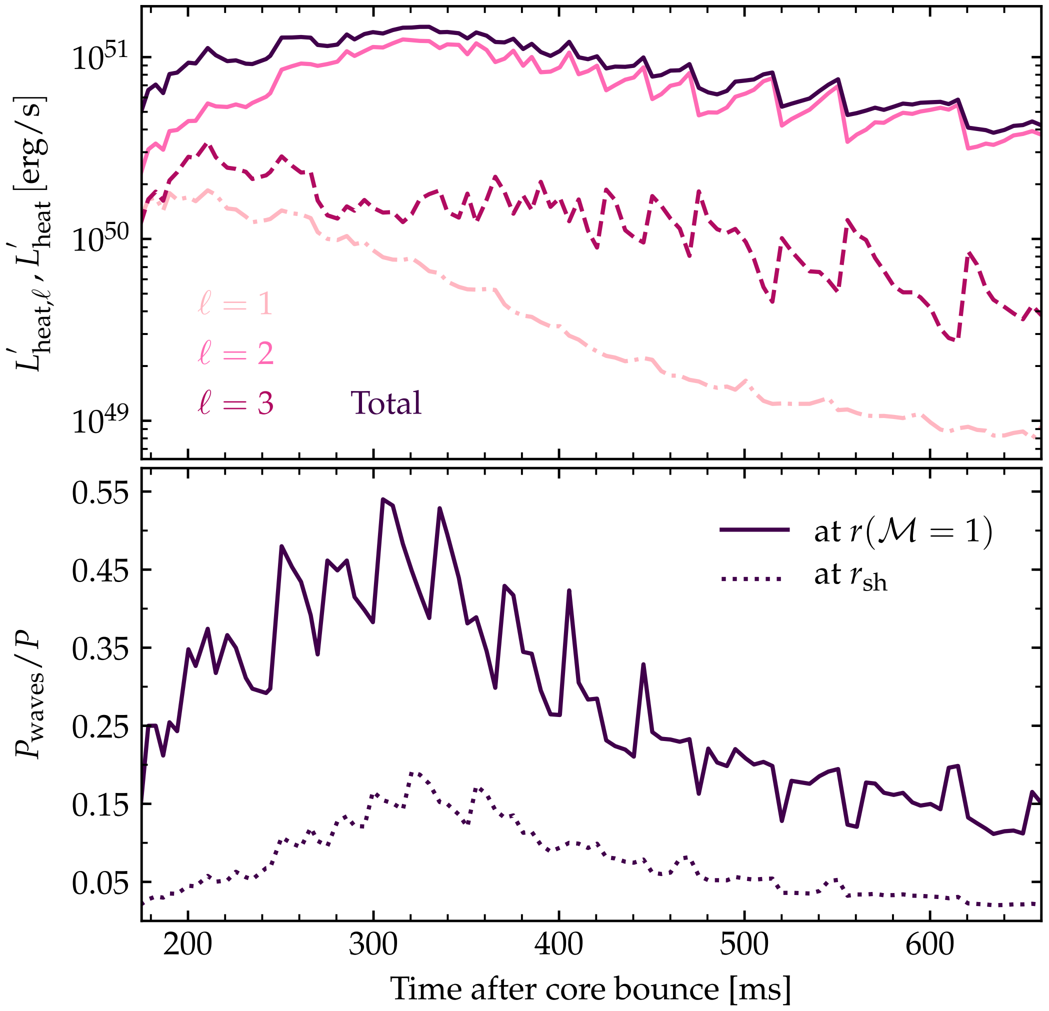

Figure 7.11: (Top panel) Temporal evolution of the net heating rates corrected for neutrino damping $L'_{\mathrm{heat}\,,\,\ell}$ in $\ell = 1$ (shown with a dash-dotted light pink line), $\ell = 2$ (shown with a solid mid pink line), and $\ell = 3$ (shown with a dashed deep pink line) waves. The total corrected heating rate L'_{heat}, summed over excited angular modes, is overlaid with a dark purple line. (Bottom panel) The ratio of the wave pressure P_{wave} (summed over excited modes) to the total pressure P_{wave}/P as a function of time, as measured where mach number $\mathcal{M} = 1$ (solid dark purple line), and at the shock radius r_{sh} (dotted dark purple line).

where we employ the energy transport rate as computed above, corrected for the effects of neutrino damping.

In the lower panel of Fig. 7.11, we show P_{wave}/P as a function of time, measured just exterior to the entropy discontinuity marking the shock (a lower bound), in addition to at the radius where $\mathcal{M} = 1$ (an upper bound). Below the entropy discontinuity, we see wave pressure may account for up to almost 20% of the total pressure after 325 ms post-bounce, falling to just a few percent by the end of our simulation. In contrast, where $\mathcal{M} = 1$, in excess of 30% of the total pressure as seen in waves from early times, rising to a maximum of over 50% of the total pressure contributed in waves between $300 - 350$ ms post-bounce. Between 500 ms through the end of the simulation, wave pressure ratios of order $10-20\%$ are consistently seen. We believe these estimates are relatively conservative, as wave pressure behind the shock may build up over time as a consequence of multiple interactions facilitated by wave reflection and/or multiple advective-acoustic cycles, similar to the SASI.

7.6 Discussion

Implications for CCSN explosions

It is important to distinguish our work from the so-called acoustic mechanism (see [226, 323]), as also discussed in Sec. 7.2. In the acoustic mechanism, PNS oscillations are driven by asymmetric accretion onto the outer PNS, or by the SASI (see [315]). These mechanisms essentially transfer kinetic energy from the accretion flow into the PNS and then back out toward the gain region, so there is no net transfer of energy from the PNS core outward. In our mechanism, wave energy excited by PNS convection is nearly independent of the accretion rate or asymmetry. Unlike the acoustic mechanism, the mechanism considered here can draw from the larger reservoir of PNS binding energy ($E \sim 5 \times 10^{53}$ erg), albeit inefficiently. More importantly, eave excitationa can persist for as long as the inner convective zone exists, which is likely for several seconds after core bounce [79, 334]. Consequently, wave power generated in this scenario could contribute to the explosion power for long periods of time, even after the explosion has been fully launched and accretion power is negligible.

The extent to which acoustic energy aids explosion energy was studied in detail by [335]. On its own, acoustic power nearing 10^{52} erg is required to drive an explosion, which is unlikely to be generated by PNS core convection. However, in realistic models with neutrino luminosities of several 10^{52} erg/s, less than 10^{51} erg/s of wave power could have a large effect, especially at late times when the mass accretion rate has declined. Hence, our predicted wave energy fluxes of $\sim 10^{51}$ erg/s could play a pivotal role in shock revival for some supernovae.

Another important effect of waves may be late time (beyond ~ 500 ms) energy deposition in the PNS wind. Once the shock has been driven to large radii, the waves will steepen into shocks as they propagate into the low-density PNS wind, thereby thermalising their energy in the inner explosion ejecta. Extrapolating Fig. 7.11 to late times, wave power of the order 10^{50} erg/s may be sustained for more than a second after bounce, potentially contributing as much as $\sim 10^{51}$ erg to the explosion energy. While some of this energy may well be lost to neutrino cooling, late-time wave energy deposition could significantly contribute to the final explosion energy. In light of the very low explosion energies ($E_{\mathrm{exp}} \sim$ few $\times 10^{50}$ erg) currently reached at the end of many CCSN simulations, this effect seems especially important. The extent to which wave effects will contribute to the explosion energy at late times will depend on how efficiently convectively excited gravity waves are transmitted into outgoing acoustic waves. This efficiency is dependent on the structure of the outer PNS at late times, which will be quite difference in the case of a successful explosion. As our simulations, which do not explode, cannot be used to compute this efficiency, we hope to quantify late time wave heating rates in future work.

A crucial implication of our study is that CCSN simulations that do notresolve the dynamics within the inner 20 km of the PNS may be missing an important source of explosion energy because they will not capture the effects of waves excited by convection in the PNS mantle. Indeed, many 3D and/pr long-running simulations (see, e.g., [43, 336, 337]) evolve the inner PNS in spherical symmetry to allow for longer timesteps to be taken. Other simulations (e.g., [338, 339]) do resolve the dynamics of the inner PNS, thought it is still not clear whether the 0.5 km resolution is sufficiently fine to accurately capture the effects of convective wave excitation and propagation. To help quantify the effects of waves, it would be interesting to compare simulations that evolve the inner PNS both with and without spherical symmetry. If waves are contributing to the explosion, we expect simulations that do resolve the dynamics of the inner PNS to explode more easily and with larger energies.

Energy fluxes from non-radial oscillations can be computed in simulations via

$$L_{\text{wave}} = \int dS \, \delta P \, \delta v_r \, . \tag{7.23}$$

Here, the integral is taken over a spherical surface area S, while δP and δv_r are the non-radial components of the pressure and radial velocity perturbations, respectively. Care should be taken to distinguish the upward wave energy flux from the downward energy and mass flux due to accretion. [336] examined the *downward* energy flux of gravity waves that are excited by the *outer* convection zone, finding downward energy fluxes as large as a few $\times 10^{50}$ erg/s in 2D simulations. While their 3D simulations find much smaller downward energy fluxes due to less violent and less coherent convective motions, those simulations did not resolve the inner PNS, and so the upward energy flux due to gravity waves excited by the inner PNS convection zone would have been missed. In general, both types of waves are expected to be present.

Gravity waves excited by PNS convection may be present in some simulations even if it is not recognised or discussed in corresponding papers. We expect non-horizontal motions of $\sim 10^3 - 10^4$ km/s (with somewhat smaller radial motions) due to gravity waves in the outer (stably stratified) region of the PNS, with larger motions at larger radii where the density is smaller. In the outer gravity wave cavity, the waves of interest have only one or two nodes and, hence, they may not appear very wavelike in simulations, perhaps instead looking more like a large-scale ringing of the PNS. We note that gravity waves have opposite radial group and phase velocities, hence waves that carry energy upwards have phases that propagate *downward*, which could easily be mistaken for downward propagating waves excited by convection and non-radial accretion from the overlying gain region. It is also possible that some vigorous motion in the gain region, usually attributed to neutrino-driven convection, could be caused partially by acoustic waves emerging from below.

Using simulations that resolved PNS convection, [233] found that inner PNS convections does indeed excite waves (although they did not quantify the hydrodynamic energy flux), and that these PNS motions can contribute the GW emission from CCSNe. Using the same runs as [338], [340] found that motions in the gain region helped excite a fundamental oscillation mode of the

PNS, which dominated the GW emission found by their simulations. The peak GW frequencies they find are roughly twice that of the gravity waves we expect to be excited by convection in the PNS mantle. As fundamental PNS modes are excited by waves from the outer convection zone (behind the shock) at early times (from $\sim$ 100 ms post-bounce), this higher frequency emission dominates the GW spectrum because the energy flux in GWs is strongly dependent on frequency ($\dot{E}_{\rm GW} \propto \omega^6$). At late times after neutrino heating has died down, it is possible that PNS oscillations excited by PNS convection (which will persist for several seconds as the PNS cools and contracts) could dominate the GW emission. Indeed if true, this could mirror the scenario we are proposing in this paper; at early times neutrino heating may dominate explosion dynamics (and the GW signature), but waves excited by convection in the PNS mantle could contribute significantly to explosion dynamics, PNS evolution, and consequently the GW emission beyond $\sim$ 400 ms post-bounce. Further investigations into wave heating from PNS convection will require simulations that resolve the PNS to evolve it from formation out to several seconds after core bounce.

Ours is not the first work to consider the impacts of convectively excited waves on CCSNe. [341] examined the impacts of convectively excited Alfvén waves on r-process nucleosynthesis in PNS winds. Wave heat deposited at the base of the PNS wind can help drive it outwards more rapidly, such that it maintains lower Y_e and produces more r-process elements. They found Alfvén wave heating may be important, but only for proto-magnetar-type remnants with magnetic fields of the order $B \sim 10^{15}$ G. Even then, they estimated wave heating rates of only $L \lesssim 10^{49}$ erg/s, roughly two orders of magnitude smaller than the wave heating estimates we present here. [342] found that Alfvén waves could revive the shock only for remnants with exceptionally large field strengths ($B \gtrsim 2 \times 10^{15}$ G) and perturbation amplitudes. Consequently, we believe that waves hydrodynamically excited by PNS convection are usually more important for both the explosion and r-process production than Alfvén waves. In light of our results, the effect of wave heating on nucleosynthesis in PNS winds should be reinvestigated.

Uncertainties

As explained in Sec. 7.4, we make the approximation that all wave flux excited by PNS convection is at the convective overturn frequency ω_{con} and that the angular wave spectrum is flat in modes $\ell \in [1, \dots, \ell_c]$. While the spectral behaviour of waves excited in this way is not well understood, our prescription is rooted in the assertions made in [306, 307, 319], on the basis of bulk Reynolds stresses driving convective wave excitation. The propagation path of the excited waves, as shown in Fig. 7.5, is clearly frequency dependent, a statement quantified with the fraction of wave flux transmitted from gravity waves to acoustic waves in the outer PNS as a function of frequency shown in Fig. 7.6. Based on these figures, it would appear that emission at higher frequencies, as argued for in [310, 343] on the basis of plume incursion driving convective wave excitation, may slightly increase the fraction of transmitted wave flux. As a consequence, despite their somewhat crude and uncertain nature, we believe our estimates of the wave flux excited by PNS convection are conservative. More importantly, we see from Fig. 7.5 that the transmitted wave flux may be higher or lower at different wave frequencies for different values of ℓ, but integrating over a broad frequency spectrum will yield wave fluxes of similar magnitude to our rough estimates.

Neutrino damping likely has a substantial impact on wave heating rates. As we have shown in Fig. 7.9, a sizeable fraction of the wave flux is likely to be damped away through increased neutrino energy losses in the marginally optically thin region between the shock and the neutrinosphere. Our estimates of neutrino damping, which are admittedly somewhat crude, use a WKB approximation for the waves (which is only marginally valid for low-order gravity waves), and do not accurately predict neutrino losses where the optical depth across a wavelength is near unity. Hence, a more careful assessment of neutrino damping of waves from CCSN simulations is warranted.

Given all emission at ω_{con} with a flat angular spectrum in $\ell \in [1, \dots, \ell_c]$, strong non-linear effects are likely to be important only for gravity waves in the PNS core at early times, and perhaps additionally for acoustic waves in the gain region on very close approach to the shock. Whilst non-linear damping in the core may prevent wave energy emitted into the core from escaping, the estimates for L_{heat} we present consider only outwardly propagating waves, and thus can only be increased by wave flux escaping from the inner core. Our estimates suggest that non-linear three-mode coupling, as discussed by [322], is marginally important for the waves we consider. Waves with lower ω and higher-order angular wavenumber ℓ are more susceptible to non-linear effects due to their larger radial wavenumbers $|k_{r,\ell}|$ and slower group velocities $v_{\mathrm{gr},\ell}$. If convection excites waves at predominantly lower frequencies (or higher ℓ than our estimates), three-mode coupling could reduce the wave flux transmitted into acoustic waves. Alternatively, convective excitation at higher frequency or lower ℓ could increase the transmitted wave flux. In the latter case, increased transmission of acoustic wave flux will increase the non-linearity of acoustic waves in the gain region, increasing the likelihood of wave damping through weak shock formation.

Beyond the points already highlighted here and previously alluded to, a crucial limitation underscoring this work is the failure of our simulations to explode. The thermodynamic structure of the accreting PNS, particularly in the immediate post-shock region, will be altered in the case of a successful explosion. Although this is unlikely to impact the development or persistence of convection in the PNS mantle over the timescales considered in this study, the propagation of waves through the outer PNS and the gain region is likely to be impacted. A quantitative evaluation of the effect on wave pressure and corrected heating rates are beyond the scope of this study, but should be considered in future work.

7.7 Conclusion

In the first few seconds after core collapse, energy transport by convectively excited waves from the inner PNS out toward the shock may have a substantial impact on whether a successful explosion occurs and, if so, the explosion energy. To quantify wave transport, we have modelled the core collapse of a $15\,M_\odot$ progenitor and followed post-bounce evolution for 660 ms. We used a spherically-symmetric, general relativistic hydrodynamics code employing mixing length theory prescription for convection [79, 316] to estimate wave generation rates, analyse wave propagation within the PNS, and compute wave eneryg fluxes behind the stalled shock.

Convection develops in the PNS mantle after around 200 ms post-bounce due to deleptonisation and entropy changes as the PNS cools and contracts. We see convective luminosities of $L_{\rm con} \sim 10^{53}$ erg/s across the inner convective region, of which a few 10^{51} erg/s is expected to be radiated outwards as gravity waves from the outer edge with frequencies near the convective turnover frequency $\omega_{\rm con}$, which we estimate to increase from $\sim 10^3$ rad/s to $\sim 4 \times 10^3$ rad/s over the course of the simulation. The convectively excited gravity waves encounter a relatively narrow evanescent region between the PNS and the gain region, with a large fraction of their energy ($T_\ell^2 \sim 1/3$) transmitted into acoustic waves that then propagate out toward the shock. In the post-shock region, we find net wave energy transport rates of roughly $L_{\rm heat} \sim 10^{51}$ erg/s sustained through the end of the simulation.

Neutrino damping of acoustic waves in the outer PNS is likely to be significant, with a substantial fraction of wave energy dissipated via escaping neutrinos. Accounting for the effects of neutrino damping, we still find wave heating rates in excess of 4×10^{50} erg/s sustained through the end of the simulation. While we do not expect non-linear effects to drastically alter our results, steepening of acoustic waves could cause energy deposition in the post-shock region, especially once the explosion commences and the shock moves outwards. Non-linear three-mode coupling in the outer PNS could moderately reduce the amount of wave energy escaping toward the gain region, particularly if the spectrum of waves excited by convection peaks at lower frequencies than we have assumed.

Although we don't expect wave energy transport to be the primary driving force behind the supernova explosion, our study here shows that its impact is expected to be highly significant, contributing as much as 50% of the pressure upon the shock. As many configurations of core collapse exist perilously close to the threshold between collapse and explosion (see, e.g., [24, 344]), waves may play a crucial role in many events. Furthermore, since wave heating from PNS convection extends to late times (i.e., beyond 500 ms post-bounce) and falls off at a slower rate than neutrino heating, wave energy may significantly contribute to the final explosion energy. Future simulations can better quantify the impact of waves, and we encourage CCSN modellers to attempt ot resolve the inner PNS in order to capture wave excitation and propagation from convection in the PNS mantle. Additionally, we suggest a re-examination of the hydrodynamic energy flux out of the PNS, as convectively excited waves may well be present in some existing simulations, but could be unrecognised, or even mistaken for downgoing waves.

The physics governing CCSNe is rich and diverse, encompassing turbulent hydrodynamic instabilities and complex radiative transfer of neutrinos. In the absence of unlimited computational resources, the extent to which these systems can be modelled is constrained by the approximations used to make such studies viable. Wave physics in itself is a complex field which is not fully understood, and thus our results are both estimative and subject to a number of uncertainties which have been outlined in this study and can be improved upon with further investigation. Nevertheless, it is clear that the accurate quantification of the impact of wave heating from PNS convection on the revival of the stalled supernova shock is vital to developing a comprehensive understanding of the CCSN explosion mechanism.

8 Prospects for core-collapse supernova science over the next thirty years

"But I don't want to go among mad people," Alice remarked.
"Oh, you can't help that," said the Cat: "we're all mad here. I'm mad. You're mad."
"How do you know I'm mad?" said Alice.
"You must be," said the Cat, "or you wouldn't have come here."
–Lewis Carroll, *Alice in Wonderland*

[1] R. X. Adhikari, P. Ajith, et al. Astrophysical science metrics for next-generation gravitational-wave detectors. ArXiv e-prints, 1905.02842 (2019). Submitted to Class. Quantum Grav., available at `https://arxiv.org/abs/1905.02842`.
SEG performed all calculations related to stellar collapse, and wrote all manuscript text in the supernova sections.

[2] S. E. Gossan, E. D. Hall, and S. Nissanke. Prospects for core-collapse supernova science with the next generation of ground-based gravitational wave detectors (2019). In preparation; to be submitted to Astrophys. J..

8.1 Motivation

With the GW era well underway, the natural next step is to consider what lies ahead. As established in Chapter 4, GW astronomers interested in observing CCSNe are limited to sources within just a few kpc for the most part with the second-generation of GW detectors. While rapid rotation of the precollapse core can push this hypothetical horizon distance out throughout the galaxy and Magellanic Clouds for the $\sim 1\%$ of progenitors thought to possess appreciable angular momentum, the CCSN rate within 100 kpc is just a couple per century at best. These (perhaps dismal) prospects for observing GWs from CCSNe can be attributed primarily to two issues; (i) the relatively feeble GW emission from PNS formation and early evolution (in comparison with GWs from compact binary inspiral, merger, and ringdown), in addition to (ii) the small fraction of optimal SNR recoverable for GWs from CCSNe using the current generation of excess-power search algorithms. With these very problems in mind, the goal of this Chapter is to explore the potential for improving observational prospects for GWs from CCSNe over the next thirty years through both next-generation instrumental techniques and development of targeted search pipelines optimised with the signal morphology of GWs from CCSNe in mind.

The rest of this Chapter is organised as follows. In Sec. 8.2, we introduce three proposed third-generation detectors currently in the design stage. In Sec. 8.3, we discuss recent advances in computational modelling of CCSNe, augmenting the waveform catalogs considered in previous Chapters with new samples drawn from state-of-the-art simulations. In Sec. 8.4, we use new waveforms introduced to explore the baseline sensitivity of the third-generation detectors to GWs from CCSNe, before considering specifically the improvements in sensitivity to be gleaned by changing the detector configuration in the context of LIGO Voyager in Sec. 8.5. In Sec. 8.6, we outline the limitations of our approach and discuss the potential for augmenting sensitivity to GWs from CCSNe through development of more sophisticated search techniques algorithms, before concluding in Sec. 8.7.

8.2 Third generation of ground-based GW detectors

In this Section, we discuss the prospective third-generation ground-based GW detectors.

Sensitivity of the current generation of ground-based GW detectors is limited by seismic motion and thermal noise in the suspensions at low frequency ($\lesssim$ 15 Hz), Brownian thermal noise in the mirror coatings around 100 Hz, and quantum shot noise at higher frequencies. Below 10 Hz, construction of underground GW detectors may be crucial to sidestep seismic noise. Beyond this, use of seismometers to estimate and subtract noise borne of Newtonian gravity gradient effects (much akin to the employ of adaptive optics systems in ground-based optical telescopes) will improve sensitivity prospects in the low frequency limit (see, e.g. [85, 345, 346]). Around 100 Hz, limitations from coating Brownian noise can be circumvented through cryogenic cooling of test masses.

LIGO Voyager [347, 348] is a proposed next-generation detector design to replace the Advanced LIGO interferometers. Sensitivity improvements over Advanced LIGO are achieved through employment of more massive mirrors composed of silicon, operation at cryogenic temperatures, augmented laser power, and use of squeezed light.

Einstein Telescope [349, 350] is a proposed next-generation European detector, composed of a 10 km detector formed from three co-located interferometers arranged in triangular geometry and to be built underground.

Cosmic Explorer [351] is a proposed next-generation detector with 40 km arms. Sensitivity above 10 Hz is bounded by quantum noise, with Newtonian noise dominating at lower frequencies.

In Tab. 8.1, we show parameters characterising detector configurations for LIGO Voyager, Cosmic Explorer, and Einstein Telescope, alongside those for Advanced LIGO for context. For the timescales over which these detectors are expected to be constructed and come online, we refer the interested reader to [351, 352].

Parameter	Advanced LIGO	LIGO Voyager	Einstein Telescope	Cosmic Explorer
Arm length	4 km	4 km	10 km	40 km
Laser wavelength	1064 nm	2000 nm	1064 nm	1550 nm
Beam radius	6.2 cm	8.4 cm	9 cm	14 cm
Test mass	39.6 kg	200 kg	200 kg	320 kg
Temperature	300 K	123 K	290 K	123 K
Squeeze factor	n/a	10 dB	10 dB	10 dB

Table 8.1: Parameters characterising interferometer design for Advanced LIGO, LIGO Voyager, Einstein Telescope, and Cosmic Explorer [348, 351].

In Fig. 8.1, we show the strain noise ASDs for LIGO Voyager, Einstein Telescope, and Cosmic Explorer, alongside the ASDs for Advanced LIGO and the Advanced LIGO+ configuration for context.

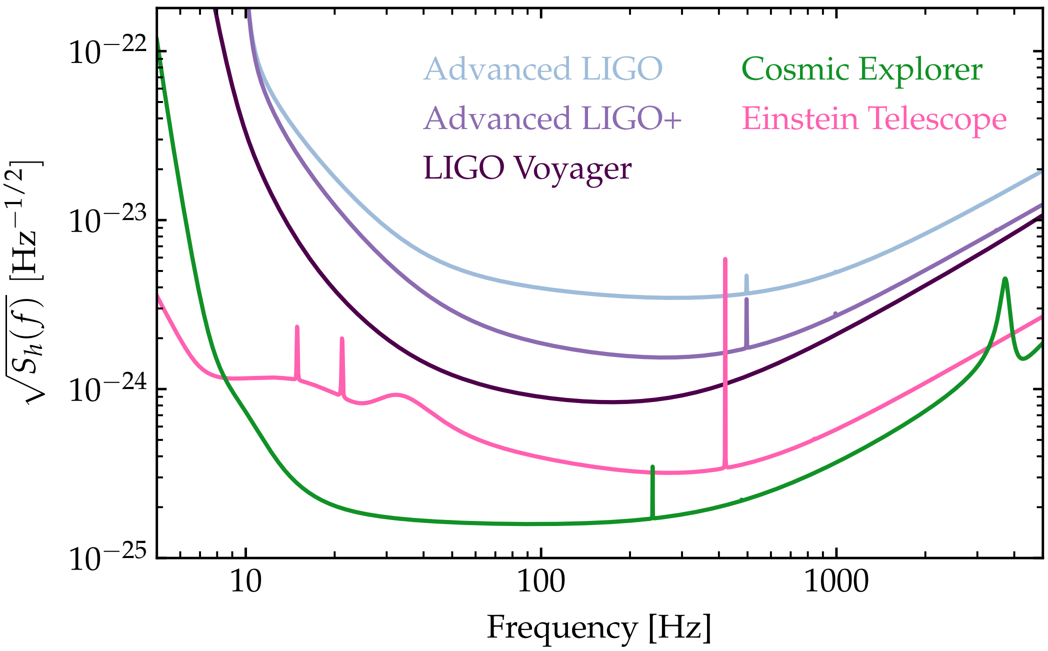

Figure 8.1: Amplitude spectral densities (ASDs) for proposed third generation detectors LIGO Voyager, Einstein Telescope, and Cosmic Explorer. For context, the ASDs for Advanced LIGO and the Advanced LIGO+ configuration (technically a 2.5-generation detector) are shown.

8.3 Waveforms

Following previous chapters, we consider GW emission from garden-variety CCSNe (dominated by PNS oscillations excited by convection and the SASI) and more extreme CCSNe originating from rapidly-rotating progenitors (GW emission from collapse, bounce, and ringdown of millisecond PNSs). Further to these, we consider low frequency emission from GW memory effects originating from aspherical neutrino emission, as well as high frequency emission from the ringdown of BHs formed in collapsar-type systems thought to be associated with long GRBs. We augment our waveform catalogs with new signals from state-of-the-art simulations, which we describe below.

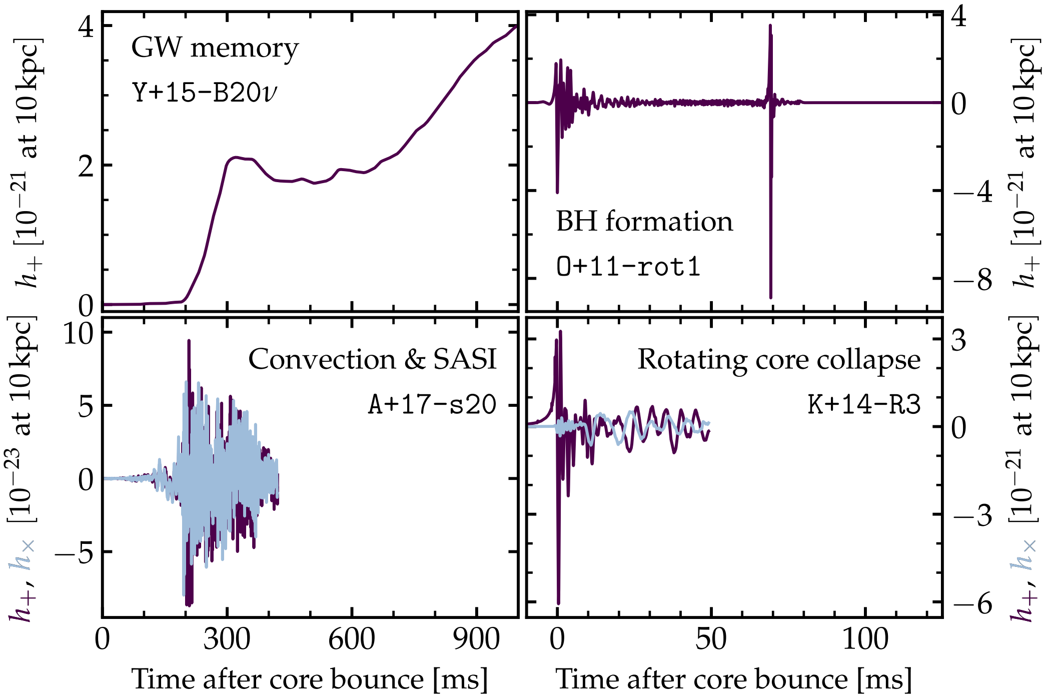

Figure 8.2: GW strain as seen by an equatorial observer at 10 kpc for GW memory (upper left panel; model `Y+15-B20`ν [47]), BH formation (upper right panel; model `O+11-rot1` [72]), PNS oscillations excited by convection and the SASI (lower left panel; model `A+17-s20` [233]), and post-bounce ringdown of millisecond PNS (lower right panel; model `K+14-R3`).

GW memory

Thus far we have considered GWs that return spacetime to its original state after propagating through. Some GW emission, however, imprints a permanent non-oscillatory offset on spacetime after its passage; a so-called 'memory' effect. GW memory (see, e.g, [353, 354]) is difficult to detect with ground-based detectors, as the rise time over which this DC offset builds up is of order seconds if not longer. In the context of CCSNe, anisotropic neutrino emission (see, e.g., [45–47, 197, 355, 356]) and aspherical explosive outflows of matter and magnetic stresses (from, for example, jet-like dynamics; see [357–359]) may source memory effects that produce observables around $(1-10)$ Hz.

For the purposes of this study, we draw waveforms from the ab-initio axisymmetric CCSN simulations presented by Yakunin *et al.* [47]. The authors employ the `CHIMERA` code to evolve four non-rotating progenitors with ZAMS mass $\{12, 15, 20, 25\}\, M_\odot$ in Newtonian self-gravity with relativistic corrections, multi-frequency neutrino treatment through the ray-by-ray approximation with weak-interaction physics, and using the LS220 EOS [198] to close the system of equations. Specifically, we consider the GW signal from aspherical neutrino emission for the $12\, M_\odot$ and $20\, M_\odot$ progenitors (labelled B12-WH07-neutrino and B20-WH07-neutrino respectively by the authors in [47]), which we hereafter denote `Y+15-B12`ν and `Y+15-B20`ν in this chapter. In the upper left panel of Fig. 8.2, we show the GW strain as seen by an equatorial observer $h_{+,\mathrm{eq}}$ at 10 kpc for `Y+15-B20`ν.

Black hole formation

We have often discussed in this thesis the GW signature from core collapse assuming that the stalled shock is indeed revived, but this is not necessarily the case. For progenitors of ZAMS mass $\lesssim 40 M_\odot$, BH formation can occur through fallback accretion onto the PNS should the stalled shock not be revived in a timely fashion. The timescale from the initial core collapse to delayed BH formation is dependent on the accretion rate onto the PNS (influenced by the properties of the progenitor star), the angular momentum of the PNS, and the nuclear matter EOS, but is typically around $\sim (0.5 - 3)$ s (see, e.g, [49, 68–70]). The GW signature of BH formation is a characteristic short burst and ringdown. The peak ringdown frequency is inversely proportional to the mass of the nascent BH, with typical ringdown spectra for stellar mass BH formation peaking around several kilohertz [27, 49, 71, 72].

In very massive progenitors ($M_{\mathrm{ZAMS}} \gtrsim (60 - 70)\, M_\odot$), a BH will be formed within timescales of a few hundred milliseconds, even if the progenitor core possesses significant angular momentum. Such systems have oft been discussed in connection to the collapsar model for LGRBs (see, e.g. [206, 360] for original literature), in which a nascent BH surrounded by an accretion disk formed from fallback material powers jet-like, bipolar outflows. GW emission may arise in a number of different ways from collapsar-type systems (see, e.g., [63, 72, 207, 361, 362]), a couple of which have already been discussed in Chap. 4 in the context of prospects for observational model exclusion for CCSNe within a few Mpc. Here, we consider two models from the general-relativistic axisymmetric study of Ott *et al.* [72], in which the collapse and evolution of a $75\, M_\odot$ progenitor with several different rotation profiles imposed is followed using the `Zelmani` CCSN code [21]. Specifically, we employ two waveforms from simulations in which the progenitor has an initial central velocity of 1 rad/s and 2 rad/s, which we hereafter denote `O+11-rot1` and `O+11-rot2`, respectively. In the upper right panel of Fig. 8.2, we show the GW strain as seen by an equatorial observer at 10 kpc for the `O+11-rot1` model.

Convection & SASI

As discussed previously (see Chap. 3, Chap. 4, and Chap. 5), for CCSNe borne of precollapse cores with periods exceeding a few tens of seconds, GW emission is dominated by oscillations of the nascent PNS, excited by convective plumes and hydrodynamic waves striking the PNS and causing it to ring up. The peak frequency of emission naturally follows the dominant PNS surface g-mode frequency, which increases quasi-linearly with time from $\sim (100-200)$ Hz to over 1 kHz as the PNS accretes fallback material, contracts, and deleptonises, although it has been shown that a broad and complex spectrum of oscillations is typically excited (see, e.g., [44, 48, 233, 344]). Strong fluid downflows from development of the SASI can modify the accretion rate at the PNS, inducing quadrupolar oscillations around $(100-200)$ Hz at later times (after a few hundred milliseconds), where the emission frequency is related to the characteristic frequency of the advective-acoustic cavity in which the SASI develops (see, e.g., [25, 42]).

We sample here broadly from the literature, choosing six waveforms from three different studies. In addition to the `müller1`, `müller2`, and `müller3` waveforms introduced in Chap. 4, we draw models from the three-dimensional general-relativistic studies presented by Andresen *et al.* [233] and Kuroda *et al.* [230]. From Andresen *et al.* [233], who treat neutrino transport through a multi-group ray-by-ray approximation, we choose model s20 (hereafter denoted `A+17-s20`), which follows the core collapse and post-bounce evolution of a progenitor with $M_{\mathrm{ZAMS}} = 20\,M_{\odot}$ and the LS220 EOS. From Kuroda *et al.* [230], who employ an M1 closure approximation to account for neutrino effects, we choose models SFHx and TM1 (hereafter denoted `K+16-SFHx` and `K+16-TM1`, respectively), which evolve a progenitor star with $M_{\mathrm{ZAMS}} = 15\,M_{\odot}$ and either the SFHx EOS [363] or TM1 EOS [364]. In the lower left panel of Fig. 8.2, we show the GW strain as seen by an equatorial observer at 10 kpc for the `A+17-s20` model.

Rapidly-rotating core collapse

As explored extensively throughout this thesis (see, e.g., Chap. 3, Chap. 4, Chap. 5, and Chap. 6), rotating progenitors yield CCSNe in which GW emission is dominated by collapse, bounce, and ringdown of the core. Centrifugal affects cause oblate deformation of the PNS, which produces a large quadrupole moment. For precollapse cores characterised by extremely rapid rotation and/or strongly differential rotation profiles, non-axisymmetric dynamics may develop at later times due to development of co-rotation, secular, or dynamic fluid instabilities (see, e.g., [65, 66]).

In addition to the `sch1` and `sch2` waveforms introduced in Chap. 4, we employ a rapidly rotating model from the three-dimensional general-relativistic simulations with approximate neutrino treatement of a $15M_\odot$ progenitor carried out by Kuroda *et al.* [66]. Specifically, we consider the R3 model (hereafter denoted `K+14-R3`), which evolves the aforementioned progenitor with a cylindrical rotation profile characterised by central angular velocity π rad/s imposed. In the lower right panel of Fig. 8.2, we show the GW strain for `K+14-R3` as seen by an equatorial observer at 10 kpc .

8.4 Baseline detectability

In the absence of a more robust, astrophysically-motivated figure of merit to characterise the detectability of GWs from CCSNe, we employ the optimal SNR $\langle \rho_{10\,\mathrm{kpc}} \rangle$, averaged over orientation of the source frame with respect to an observer at 10 kpc. While the SNR recovered using an excess-power analysis pipeline is undoubtably a small fraction of the matched-filter SNR, our goal predominantly in this Section (and the next) is to establish improvements in detectability yielded by more sensitive detectors and advances in instrument science. A discussion on the potential to improve detectability of GWs from CCSNe through development and application of more sophisticated signal analysis techniques is postponed to Sec. 8.6.

In Table 8.2, we present $\langle \rho_{10\,\mathrm{kpc}} \rangle$ for the waveforms introduced in Sec. 8.3 in the context of the hypothetical detectors discussed in Sec. 8.2.

Waveform	$\langle \rho_{10\,\mathrm{kpc}} \rangle_{\mathrm{aLIGO}}$	$\langle \rho_{10\,\mathrm{kpc}} \rangle_{\mathrm{aLIGO+}}$	$\langle \rho_{10\,\mathrm{kpc}} \rangle_{\mathrm{Voy}}$	$\langle \rho_{10\,\mathrm{kpc}} \rangle_{\mathrm{ET}}$	$\langle \rho_{10\,\mathrm{kpc}} \rangle_{\mathrm{CE}}$
Y+15-B12ν	19.70	39.45	75.91	222.53	726.87
Y+15-B20ν	16.54	33.11	63.73	187.15	610.04
sch1	74.38	168.74	287.87	810.67	1323.57
sch2	77.12	169.10	287.53	807.71	1309.20
K+14-R3	30.48	70.03	123.72	334.85	651.83
müller1	3.74	8.42	15.39	40.83	96.84
müller2	2.89	6.14	11.47	31.74	90.33
müller3	2.49	5.75	10.31	28.16	62.55
A+17-s20	5.58	12.46	21.95	59.87	121.04
K+16-TM1	8.43	18.59	32.14	88.63	158.38
K+16-SFHx	12.48	27.32	47.75	130.04	245.81
O+11-rot1	11.77	25.69	43.84	122.31	201.00
O+11-rot2	30.91	67.21	114.84	320.13	525.22

Table 8.2: Optimal SNRs for the waveforms considered given a fiducial distance of $10\,\mathrm{kpc}$, averaged over orientation of the source frame with respect to an observer, in the context of future ground-based GW detectors Advanced LIGO+ (aLIGO+), LIGO Voyager (Voy), Einstein Telescope (ET), and Cosmic Explorer (CE). For reference, the angle-averaged optimal SNRs in the context of Advanced LIGO (aLIGO) are also shown.

We see that upgrading the aLIGO detectors to the 2.5G aLIGO+ configuration will more than double the angle-averaged matched-filter SNR for the waveforms considered. Comparatively, LIGO Voyager is expected to yield yet another factor of two improvement in detectability, resulting in SNRs a factor $\sim 4-5$ greater than for Advanced LIGO. For proposed detectors Einstein Telescope and Cosmic Explorer, we note that angle-averaged SNRs are increased by factors of $\sim 10-12$ and $\sim 16-26$ respectively compared with Advanced LIGO. While we remind the reader that $\langle\rho_{10\,\mathrm{kpc}}\rangle$ values presented here are representative more of hypothetical upper bounds than realistic metrics for detectability, the trends of improved sensitivity exhibited are expected to map across to detectability with excess-power pipelines well.

Using these findings to extrapolate the results presented in Chap. 4, GWs from CCSNe borne of non-rotating progenitors will likely be detectable throughout the galaxy with Einstein Telescope, and perhaps even out to the Magellanic Clouds with Cosmic Explorer. Considering now CCSNe from rotating progenitors, LIGO Voyager is expected to be able to detect GWs from even slowly to moderately rotating precollapse cores out to the Magellanic Clouds. For rapidly rotating CCSNe, Einstein Telescope should be able to observe GWs beyond M31, with Cosmic Explorer extending the horizon distance even further to a couple of megaparsecs. At these distances, the CCSN rate is of order several per year, potentially yielding the opportunity to routinely constrain progenitor rotation with GW observations.

We note that these extrapolations are based on the ability to recover just a small fraction of the matched-filter SNR through excess-power searches. As noted previously in this thesis, development of targeted search methods GWs from CCSNe (based on signal morphology) to improve the fraction of signal SNR recovered can push the horizon distance out further still. We discuss the prospects for this in Sec. 8.6.

8.5 Impact of detector configuration

While the third-generation interferometers are still in concept stage, it is instructive to quantify the impact of altering detector configuration on the sensitivity to one's favourite astrophysical source. In Sec. 3.2, we discussed sources of noise limiting the sensitivity of GW interferometers. We explore here, in the context of LIGO Voyager, the impact of configuration changes on the detector sensitivity to GWs from CCSNe.

Explicitly, we consider the following noise sources:

- **NN**: Newtonian noise, originating from fluctuations in the local Newtonian gravitational potential, produces test mass accelerations that affect sensitivity below $\sim 40\,\mathrm{Hz}$. Use of seismometers can allow offline estimation and subtraction of Newtonian noise contributions to increase sensitivity (see, e.g. [85, 365]).
- **SEI**: Seismic noise, borne of ground vibrations and internal noise in active isolation systems, causes motion of test masses between $5 - 50\,\mathrm{Hz}$. It is typically mitigated through multiple layers of active and passive seismic isolation [366].
- **SUS**: At low frequencies, mirror suspension fibres contribute Brownian thermal noise. Incremental progress may be made through continued research in suspension design (see, e.g, [367]) and materials science.
- **SPOT/CTN**: Around $100\,\mathrm{Hz}$, the noise floor is limited by Brownian thermal noise in mirror coatings [368]. The noise spectrum from this source scales inversely with diameter of the laser beam and mechanical quality factor Q of the coating.
- **SQZ**: Both radiation pressure and shot noise can be reduced at by increasing quantum squeezing. While it's likely the impact on the noise floor will have some frequency dependence [369], we naively assume broadband improvement for the purpose of this study.
- **POW**: Augmenting the laser power increases radiation pressure noise and reduces shot noise. We note that thermal wavefront distortion effects due to increased heating of the mirror are neglected here.
- **FCL**: Degradation of squeezed light can be reduced by increasing the optical filter cavity length (see, e.g., [370]) to improve broadband sensitivity.
- **MASS**: Quantum radiation pressure can be reduced by increasing the mass of the mirrors. While this is likely to also have an effect on the

suspension thermal noise, we neglect this effect for the purposes of this study.

In Fig. 8.3, we show the contributions of these outlined noise components to the overall noise floor in the context of Advanced LIGO and prospective detector LIGO Voyager.

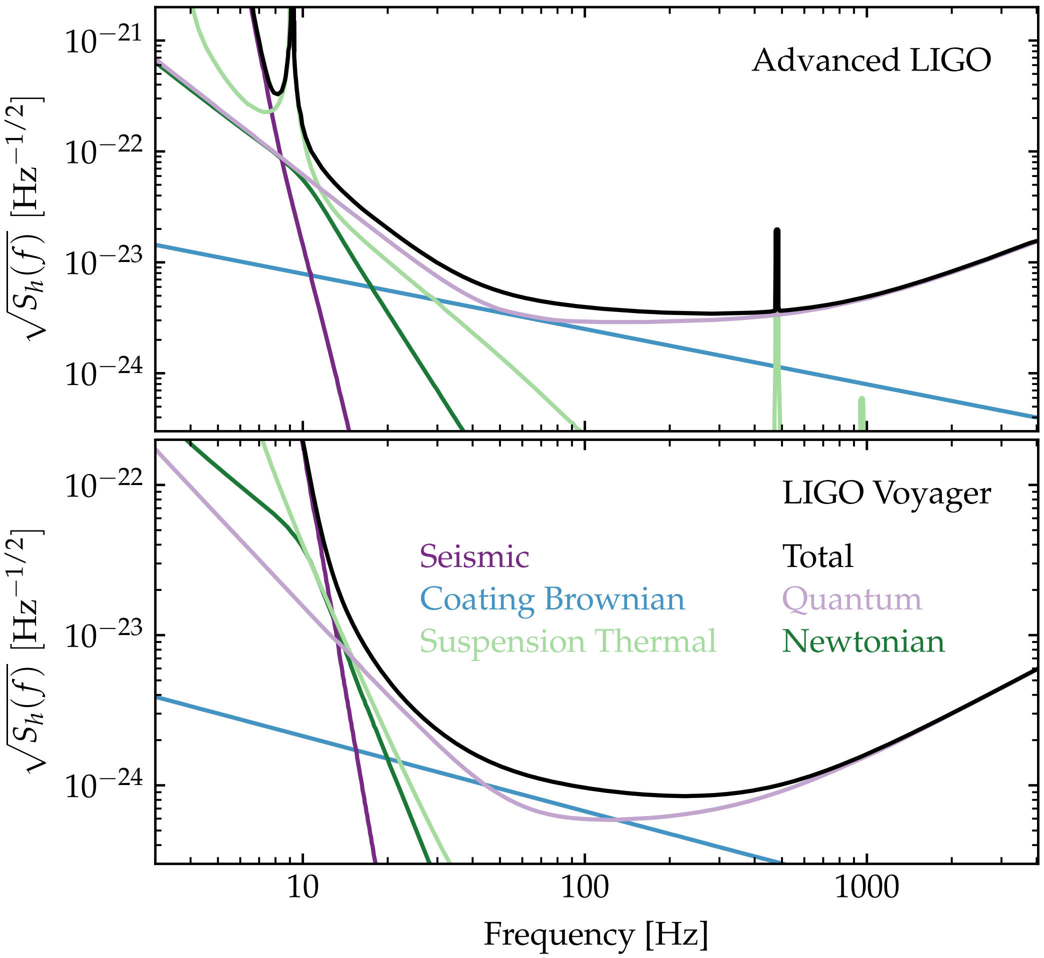

Figure 8.3: The strain noise ASDs for contributions from Newtonian noise, seismic noise, Brownian thermal noise in the suspensions, Brownian thermal noise in mirror coatings, and the quantum noise floor in the context of Advanced LIGO (top panel) and LIGO Voyager (bottom panel).

Using the matched-filter SNR employed in the previous Section as a metric for detectability of given waveform families, we construct a Jacobian to relate improvements in sensitivity to changes in parameters controlling the aforementioned sources of interferometer noise. For each noise source highlighted, we vary the component PSD by 20% and compute the angle-averaged matched-filter SNR for each waveform for a hypothetical source at 10 kpc, $\langle \rho_{10\,\mathrm{kpc}} \rangle$. Weighting the change in SNR by the 20% perturbation in component PSD, we establish a figure-of-merit to determine the relative impact of changing the detector configuration on the sensitivity to GWs from CCSNe.

In Tab. 8.3, we show the weighted improvement in $\langle \rho_{10\,\mathrm{kpc}} \rangle$ obtained through the eight changes in configuration outlined above, for all waveforms considered.

Waveform	**NN**	**SEI**	**SUS**	**SPOT/CTN**	**SQZ**	**POW**	**FCL**	**MASS**
Y+15-B12ν	4.22×10^{-3}	3.93×10^{-4}	1.00×10^{-2}	3.14×10^{-1}	-2.18×10^{-2}	3.40×10^{-1}	2.20×10^{-1}	-1.86×10^{-1}
Y+15-B20ν	4.18×10^{-3}	3.89×10^{-4}	1.00×10^{-2}	3.14×10^{-1}	-2.19×10^{-2}	3.40×10^{-1}	2.20×10^{-1}	-1.86×10^{-1}
sch1	2.43×10^{-7}	1.14×10^{-8}	1.09×10^{-6}	7.49×10^{-2}	7.03×10^{-1}	3.81×10^{-1}	-8.73×10^{-4}	-1.84×10^{-3}
sch2	4.42×10^{-7}	1.40×10^{-8}	2.22×10^{-6}	5.99×10^{-2}	7.38×10^{-1}	3.99×10^{-1}	-7.69×10^{-4}	-2.65×10^{-3}
K+14-R3	1.98×10^{-5}	4.95×10^{-7}	8.17×10^{-5}	2.21×10^{-1}	5.04×10^{-1}	2.82×10^{-1}	-4.10×10^{-3}	-4.28×10^{-2}
müller1	4.92×10^{-4}	4.19×10^{-5}	1.23×10^{-3}	3.28×10^{-1}	3.58×10^{-1}	2.14×10^{-1}	-8.59×10^{-3}	-9.46×10^{-2}
ott	1.28×10^{-7}	4.30×10^{-9}	3.37×10^{-6}	1.63×10^{-1}	5.84×10^{-1}	3.20×10^{-1}	-2.31×10^{-3}	-1.48×10^{-2}
A+17-s20	1.85×10^{-4}	9.08×10^{-6}	6.14×10^{-4}	1.88×10^{-1}	5.52×10^{-1}	3.09×10^{-1}	-5.15×10^{-3}	-5.31×10^{-2}
K+16-TM1	6.94×10^{-7}	1.33×10^{-8}	2.16×10^{-5}	1.33×10^{-1}	6.39×10^{-1}	3.51×10^{-1}	-2.67×10^{-3}	-3.31×10^{-2}
K+16-SFHx	7.20×10^{-7}	1.76×10^{-8}	2.75×10^{-5}	1.79×10^{-1}	5.83×10^{-1}	3.24×10^{-1}	-3.87×10^{-3}	-5.21×10^{-2}
O+11-rot1	1.81×10^{-7}	3.55×10^{-9}	1.76×10^{-6}	7.33×10^{-2}	7.18×10^{-1}	3.89×10^{-1}	-9.13×10^{-4}	-3.20×10^{-3}
O+11-rot2	5.70×10^{-7}	1.32×10^{-8}	2.98×10^{-6}	7.08×10^{-2}	7.22×10^{-1}	3.91×10^{-1}	-8.76×10^{-4}	-2.82×10^{-3}

Table 8.3: Fractional change in angle-averaged SNR for a source at 10 kpc $\langle \rho_{10\,\mathrm{kpc}} \rangle$ weighted by change in detector configuration for all waveforms considered.

8.6 Discussion

In this Section, we address the uncertainties and limitations of the research presented here, before musing on what the future for the multimessenger astronomy with CCSNe.

As explained previously, we employ the angle-averaged matched-filter SNR as a figure of metric for detectability. While this is an unachievable goal due to the stochastic nature of GWs from CCSNe, it is a useful metric as it depends only on the signal morphology and the sensitivity of a particular detector. As our primary goal here has been to establish the improvements in sensitivity to GWs from CCSNe to be gleaned with proposed next-generation detectors and changes in detector configuration, it is prudent to employ a figure of merit independent of the ability of a particular excess-power pipeline to extract signal from noise.

Realistically, the true sensitivity of a detector network to a given astrophysical source is dependent not only on the baseline of detector noise, but also on the data quality and the signal analysis toolkit used to recover astrophysical transient signals. As discussed in Chap. 4, non-stationary and non-Gaussian behaviour of detector data undoubtedly impacts the prospects for detection and source inference. Though beyond the scope of this study, it will be crucial in the future to understand the influence of glitchy data and, in particular, the morphology of noise transients, on the sensitivity of a proposed next-generation detector network to GWs from CCSNe.

Beyond data quality considerations, improving the current excess-power searches to increase recovered signal SNR for CCSNe in the context of even Gaussian noise will be crucial to maximising the scientific potential for multimessenger observations of the next nearby CCSN. Improved search methods for GWs from CCSNe are likely to focus on recovering excess power along preferred time-frequency tracks. The dominant source of GWs from CCSNe is oscillations of the PNS excited by turbulent convection in the gain region and PNS mantle. Oscillation modes of compact objects are well defined, and tracking the evolution of the peak frequency of GW emission is directly related to the PNS evolution, specifically the PNS compactness and mass-accretion rate, as a function of time (see, e.g., [45, 371]). Developing phenomenological models to tie time-frequency tracks to tangible physical parameters to be extracted is just one way to probe the landscape of nascent NSs [48, 249].

8.7 Conclusions

We have explored the prospects for multimessenger astrophysics with CCSNe over the next thirty years. In the context of proposed GW observatories from the future third-generation of ground-based interferometers, we investigated observational prospects for GWs from CCSNe using waveforms from state-of-the-art simulations modelling GW emission from BH formation, aspherical neutrino emission, memory effects, in addition to the PNS formation and early evolution scenarios considered elsewhere in this thesis. We investigate how changes in interferometer configuration affects the broadband sensitivity to GWs from CCSNe for LIGO Voyager. Beyond this, we deliberate on the capacity for improving observational prospects through refinement of search pipelines and harnessing augmented neutrino detection capabilities.

Implementation of improved experimental techniques in the next generation of ground-based GW detectors yields broadband gains in sensitivity to astrophysical sources. Upgrading the Advanced LIGO detectors to the 2.5G Advanced LIGO+ configuration more than doubles the angle-averaged optimal SNR for GWs from CCSNe for all emission scenarios considered. For the third-generation detectors considered, we find SNRs increased by factors $\sim 4-5$, $\sim 10-12$, and $\sim 16-26$ for LIGO Voyager, Einstein Telescope, and Cosmic Explorer, respectively, in comparison to the Advanced LIGO baseline. Restating this result in a perhaps less esoteric manner, GWs from garden-variety CCSNe may be detectable with an excess-power search pipeline out to $\sim 10\,\mathrm{kpc}$ with LIGO Voyager, throughout the galaxy with Einstein Telescope, and possibly out to the Large Magellanic Cloud with Cosmic Explorer. From CCSNe borne of rapidly rotating progenitors, GWs are likely to be observable with excess-power searches throughout the Magellanic Clouds with LIGO Voyager, in M31 with Einstein Telescope, and out to a couple of Mpc with Cosmic Explorer.

Relating this to the broader goal of simulation results motivating multimessenger observation strategies and vice versa, it is clear that an impass has been reached with respect to optimising detection and post-observation inference techniques for GWs from CCSNe. While the third-generation of ground-based detectors will undoubtably increase the horizon distance for observing GWs from CCSNe, further sensitivity gains can yielded through development of targeted signal extraction techniques to improve the recovered SNR over that currently achievable with excess-power pipelines. Explicitly, understanding the underlying physics governing the time-frequency evolution of PNS oscillations is crucial not only to this goal, but additionally provides a built-in method to robustly constrain source properties for even garden-variety CCSNe.

To conclude, we reiterate the unparalleled opportunity to probe the dynamics driving stellar explosions through multimessenger observations of the next galactic CCSN, which we explore further in [372]. While limited for most CCSNe to within a few kiloparsecs for GW observations with the current generation of detectors, LIGO Voyager will extend our our observational horizon to 10 kpc , the fiducial distance considered in the context of galactic CCSNe. Einstein Telescope and Cosmic Explorer will push this horizon further still, ensuring observation of GWs from CCSNe throughout the galaxy and LMC respectively are not out of reach.

9 Conclusions

Today, we escape. We escape.

–Radiohead, *Exit Music (For A Film)*

The core collapse of massive stars produces a rich and diverse population of energetic explosions, marking the birth of compact objects from their nuclear burning progenitors. Governed by a complex interplay of general relativity, neutrino radiation hydrodynamics, and nuclear physics (to name just a few) over length scales spanning almost twenty orders of magnitude, these cosmic laboratories offer an unparalleled opportunity to probe fundamental physics in extreme conditions. While EM observations, originating far from the central engine, provide only second-hand information on the explosion mechanism, GWs and neutrinos are emitted from deep within central regions of the CCSN impenetrable by photons. Multi-messenger observations of CCSNe, interpreted in the context of predictions from computational simulations, provide a direct view of the explosion dynamics and the nascent compact object.

Our comprehension, however, of the dynamics driving these explosions is far from complete. The same intricacies that make CCSN physics so intruiging render the task of accurately modelling CCSNe a challenge of Gordian proportions. In the absence of unlimited computational resources, implementation of approximate treatments for the true source physics become a necessity. This in turn presents its own problems, as the impact of said approximations on simulation outputs is not thoroughly understood. In this way, predictions for observational signatures of CCSNe obtained from simulations are almost a fourth messenger of sorts; crucial to improving our understanding of CCSN physics by informing observational strategies, but to be interpreted with caution and in the context of poorly constrained systematic uncertainties. In this thesis, we have taken steps to investigate the potential for probing CCSN physics with multimessenger astronomy over the next thirty years. In this conclusion, we summarise the research presented in previous chapters and discuss the impact of these results on the field in the context of future directions to explore.

Tackling first the issue of detection, we develop an astrophysically-motivated search protocol for GWs from CCSNe, harnessing electromagnetic and neutrino counterparts to refine temporal and spatial localisation with the goal of maximising search sensitivity. We outline an injection procedure for unpolarised GW signals to account for uncertainty in source frame orientation, making realistic sensitivity studies for GW waveform predictions from 3D CCSN simulations feasible for the first time. By recolouring long stretches of publicly-available detector data taken by the first generation of ground-based GW interferometers, we make it possible for groups to study the impact of non-Gaussian, non-stationary noise on detection and inference methods for GWs from CCSNe in the context of second-generation of detectors. Employing these tools, we present a detailed investigation into the sensitivity of Advanced LIGO and Advanced Virgo to both realistic GW signals produced by CCSN simulations and more speculative analytic models so far observationally unconstrained. We show that observation of GWs from the core collapse of non-rotating progenitors is likely limited to within a few kiloparsecs, while GWs from CCSNe borne of rapidly rotating precollapse cores should be detectable throughout the galaxy and perhaps out to the Magellanic Clouds. Additionally, we demonstrate the potential for observational exclusion of more speculative GW emission scenarios out to a few megaparsecs. Beyond this, we are working to develop of publicly-available tools to enable interested parties to augment their own sensitivity studies with more realistic method. We note that a subset of these methods have already been employed in searches for GWs from CCSNe with the first- and second-generation LIGO-Virgo detectors.

We turn our attention to the prospects for post-detection source inference, focusing particularly on the feasibility of distinguishing between CCSNe from non-rotating and rapidly rotating progenitors from GW observations alone, in addition to constraining the angular momentum distribution of the precollapse core for the latter case. We extend the `SMEE` pipeline established by Logue *et al.* [58], introducing functionality to consider multiple-detector networks, inject unpolarised GW signals, and employ realistic noise. We find that CCSNe from rapidly rotating progenitors are distinguishable throughout the galaxy, while for their non-rotating, garden-variety counterparts, the potential is less promising. Limitations abound due to the small number of GW waveforms from three-dimensional simulations modelling the core collapse of non-rotating progenitors. Large differences in the nature of turbulent convection and the standing accretion-shock instability (SASI) between two and three dimensions make basis vectors constructed from linearly polarised waveform catalogs obtained through axisymmetric simulations unsuitable for reconstruction of realistic GW observations from garden-variety CCSNe. Combined with fundamental analysis limitations due to the stochastic nature of the GW phase evolution from non-rotating CCSNe, we conclude that future studies should focus instead on modelling the more robust time-frequency evolution of the GW signature.

For the more deterministic GW signature from rotating core collapse, we carry out general-relativistic simulations in axisymmetry of the collapse, bounce, and early ringdown of many made-to-measure rotating progenitors to investigate the dependence of the GW emission on the angular momentum distribution in the precollapse core. We find strong dependence of the GW signature on the total rotation of the core, with some non-negligible impact from the degree of differential rotation limited to rapidly rotating progenitors. Developing two proof-of-principle concept studies to investigate the viability of constraining the angular momentum distribution of the precollapse core from GW observations alone, we show that the total core rotation may be constrained to within 20% for galactic sources. For the differential rotation length scale, it is likely that only strong differential rotation in the limit of extremely rapidly rotating cores may be distinguished, with the caveat that uncertainties in the nuclear matter EOS or inner core electron fraction may complicate even this possibility. We posit that better understanding of these issues is needed for a more sophisticated analysis, and suspect more heuristic semi-analytic modelling techniques are better suited to this problem.

One constant throughout all these studies is the PNS, the formation and evolution of which dominates characteristics of the GW and neutrino signatures from CCSNe. In the interest of reducing computational expense, approximations masking hydrodynamic effects within the PNS are often implemented, but the impact of doing so is poorly understood. We consider wave-driven energy transport from convection in the PNS mantle, and investigate its impact in the context of shock revival. Using spherically-symmetric general-relativistic simulations with multi-group neutrino transport, we estimate heating rates in the post-shock region, finding in excess of several 10^{50} erg/s from around 200 ms post-bounce, persisting through the end of our simulation. While not the dominant mechanism driving revival of the stalled shock, wave heating may provide crucial aid to producing an explosion in many progenitors featured in CCSN simulation literature that exist at the bifurcation between failed and successful explosion. While some approximate scheme to encompass the effects of wave heating in simulations could be developed, we propose the more appropriate course of action is for future simulations to better resolve non-radial hydrodynamics in the PNS.

Relating this to the broader goal of simulation results motivating multi-messenger observation strategies and vice versa, it is clear that an impass has been reached with respect to optimising detection and post-observation inference techniques for GWs from CCSNe. While the third-generation of ground-based detectors will undoubtably increase the horizon distance for observing GWs from CCSNe, it is clear that there are sensitivity gains to be achieved through development of targeted signal extraction techniques, explicitly with the goal of improving the fraction of signal SNR recoverable in comparison with excess-power pipelines. Explicitly, understanding the underlying physics governing the time-frequency evolution of PNS oscillations is crucial not only to this goal, but additionally provides a built-in method to robustly constrain source properties for even garden-variety CCSNe.

Above all, the goal of these investigations is to maximise the scientific potential to be gleaned from multimessenger observations of CCSNe. Looking forward, there is much to be done by both the source modelling and signal analysis communities. With no anticipation of unlimited computational resources on the horizon, the importance of establishing both a qualitative and quantitative understanding of the impact physical approximations have on the dynamics and observables of numerical studies cannot be overstated. Interdisciplinary collaboration has been, and will continue to be, invaluable for developing a comprehensive picture of the CCSN explosion mechanism across the vast parameter space occupied by precollapse progenitor stars. To this end, we have endeavoured in this thesis to develop open-source tools, promote accessibility of CCSN research to interested parties; we heartily encourage our colleagues to follow suit. The next galactic CCSN has already exploded, and we cannot afford to wait.

Bibliography

[1] T. E. Oliphant. *A guide to NumPy*. 2006 (cit. on p. x).

[2] E. Jones, T. Oliphant, P. Peterson, et al. *SciPy: Open source scientific tools for Python*. [Online; accessed <today>]. 2001 (cit. on p. x).

[3] J. D. Hunter. Matplotlib: A 2D graphics environment. Computing in Science & Engineering 9 (3) (2007), pp. 90–95 (cit. on p. x).

[4] C. Prescod-Weinstein. *Decolonising Science Reading List* (cit. on p. xi).

[5] W. Baade and F. Zwicky. On Super-novae. Proc. Natl. Acad. Sci. 20 (1934), pp. 254–259 (cit. on pp. xiii, 77).

[6] B. P. Abbott, R. Abbott, et al. Multi-messenger Observations of a Binary Neutron Star Merger. Astrophys. J. 848, L12 (2017) (cit. on pp. xiii, 4, 38).

[7] T. Foglizzo, P. Galletti, et al. Instability of a Stalled Accretion Shock: Evidence for the Advective-Acoustic Cycle. Astrophys. J. 654 (2007), pp. 1006–1021 (cit. on pp. 3, 130, 151).

[8] K. Hirata, T. Kajita, M. Koshiba, et al. Observation of a neutrino burst from the supernova SN1987A. Phys. Rev. Lett. 58 (1987), pp. 1490–1493 (cit. on pp. 4, 35, 38, 43, 78).

[9] R. M. Bionta, G. Blewitt, C. B. Bratton, et al. Observation of a neutrino burst in coincidence with supernova 1987A in the Large Magellanic Cloud. Phys. Rev. Lett. 58 (1987), pp. 1494–1496 (cit. on pp. 4, 35, 38, 78).

[10] B. P. Abbott, LIGO Scientific Collaboration, Virgo Collaboration, et al. GW170817: Observation of Gravitational Waves from a Binary Neutron Star Inspiral. Phys. Rev. Lett. 119, 161101 (2017) (cit. on pp. 4, 38).

[11] K. S. Thorne and R. D. Blandford. *Modern Classical Physics: Optics, Fluids, Plasmas, Elasticity, Relativity, and Statistical Physics*. Princeton University Press, 2017, p. 1528. ISBN: 9780691159027 (cit. on p. 7).

[12] S. L. Shapiro and S. A. Teukolsky. *Black holes, white dwarfs, and neutron stars: The physics of compact objects*. John Wiley & Sons, Inc., 1983, p. 663 (cit. on pp. 7, 113).

[13] J. Creighton and W. Anderson. *Gravitational-Wave Physics and Astronomy: An Introduction to Theory, Experiment and Data Analysis*. Wiley-VCH, 2011. ISBN: 978-3527408863 (cit. on pp. 7, 27, 29).

[14] S. A. Richers. Neutrino Radiation Transport and Other Topics in High Energy Density Astrophysics. PhD thesis. California Institute of Technology, 2018 (cit. on pp. 7, 14, 127).

[15] E. D. Hall. Long-baseline laser interferometry for the detection of binary black-hole mergers. PhD thesis. California Institute of Technology, 2017 (cit. on pp. 7, 29).

[16] R. L. Arnowitt, S. Deser, and C. W. Misner. Canonical analysis of general relativity. *Recent Developments in General Relativity*. Warsaw: Polish Scientific Publishers, 1962, p. 127 (cit. on p. 10).

[17] H. Dimmelmeier, N. Stergioulas, and J. A. Font. Non-linear axisymmetric pulsations of rotating relativistic stars in the conformal flatness approximation. Mon. Not. Roy. Astron. Soc. 368 (2006), pp. 1609–1630 (cit. on pp. 10, 11).

[18] J. R. Wilson, G. J. Mathews, and P. Marronetti. Relativistic numerical model for close neutron-star binaries. Phys. Rev. D 54 (1996), pp. 1317–1331 (cit. on p. 11).

[19] C. D. Ott, H. Dimmelmeier, A. Marek, et al. 3D Collapse of Rotating Stellar Iron Cores in General Relativity Including Deleptonization and a Nuclear Equation of State. Phys. Rev. Lett. 98 (26), 261101 (2007) (cit. on pp. 11, 21, 53, 79, 102).

[20] C. W. Misner, K. S. Thorne, and J. A. Wheeler. *Gravitation*. W. H. Freeman and Co., 1973 (cit. on pp. 11, 48, 81).

[21] C. Reisswig, C. D. Ott, et al. Gravitational wave extraction in simulations of rotating stellar core collapse. Phys. Rev. D 83, 064008 (2011) (cit. on pp. 11, 108, 168).

[22] F. Banyuls, J. A. Font, et al. Numerical $(3+1)$ General Relativistic Hydrodynamics: A Local Characteristic Approach. Astrophys. J. 476 (1997), pp. 221–231 (cit. on p. 12).

[23] R. W. Lindquist. Relativistic transport theory. Ann. Phys. 37 (1966), pp. 487–518 (cit. on p. 13).

[24] L. F. Roberts, C. D. Ott, et al. General-Relativistic Three-Dimensional Multi-group Neutrino Radiation-Hydrodynamics Simulations of Core-Collapse Supernovae. Astrophys. J. 831, 98 (2016) (cit. on pp. 14, 131, 159).

[25] T. Kuroda, T. Takiwaki, and K. Kotake. A New Multi-energy Neutrino Radiation-Hydrodynamics Code in Full General Relativity and Its Application to the Gravitational Collapse of Massive Stars. Astrophys. J. Supp. Ser. 222, 20 (2016) (cit. on pp. 14, 21, 168).

[26] S. Richers, H. Nagakura, et al. A Detailed Comparison of Multidimensional Boltzmann Neutrino Transport Methods in Core-collapse Supernovae. Astrophys. J. 847, 133 (2017) (cit. on pp. 14, 96, 104, 115, 127, 128).

[27] T. Kuroda, K. Kotake, et al. A full general relativistic neutrino radiation-hydrodynamics simulation of a collapsing very massive star and the formation of a black hole. Mon. Not. Roy. Astron. Soc. 477 (2018), pp. L80–L84 (cit. on pp. 14, 23, 167).

[28] M. Shibata, K. Kiuchi, et al. Truncated Moment Formalism for Radiation Hydrodynamics in Numerical Relativity. Progr. Theor. Exp. Phys. 125 (2011), pp. 1255–1287 (cit. on p. 14).

[29] G. N. Minerbo. Maximum entropy Eddington factors. J. Quant. Spectrosc. Radiat. Transfer 20 (1978), pp. 541–545 (cit. on p. 14).

[30] P. B. Demorest, T. Pennucci, et al. A two-solar-mass neutron star measured using Shapiro delay. Nature 467 (2010), pp. 1081–1083 (cit. on pp. 15, 16).

[31] J. Antoniadis, P. C. C. Freire, et al. A Massive Pulsar in a Compact Relativistic Binary. Science 340 (2013), p. 448 (cit. on pp. 15, 16).

[32] E. Fonseca, T. T. Pennucci, et al. The NANOGrav Nine-year Data Set: Mass and Geometric Measurements of Binary Millisecond Pulsars. Astrophys. J. 832, 167 (2016) (cit. on p. 15).

[33] M. Oertel, M. Hempel, et al. Equations of state for supernovae and compact stars. Rev. Mod. Phys. 89, 015007 (2017) (cit. on p. 15).

[34] A. W. Steiner, M. Hempel, and T. Fischer. Core-collapse Supernova Equations of State Based on Neutron Star Observations. Astrophys. J. 774, 17 (2013) (cit. on p. 15).

[35] J. M. Lattimer. The Nuclear Equation of State and Neutron Star Masses. Ann. Rev. Nuc. Par. Sci. 62 (2012), pp. 485–515 (cit. on p. 15).

[36] J. M. Lattimer. Neutron stars and the dense matter equation of state. Astrophys. Space Sci. 336 (2011), pp. 67–74 (cit. on p. 15).

[37] S. Typel, M. Oertel, and T. Klähn. CompOSE CompStar online supernova equations of state harmonising the concert of nuclear physics and astrophysics compose.obspm.fr. Phys. Part. Nuclei 46 (2015), pp. 633–664 (cit. on pp. 16, 107).

[38] H.-T. Janka. Neutrino Emission from Supernovae. *Handbook of Supernovae*. Springer International Publishing, 2017, p. 1575. ISBN: 978-3-319-21845-8 (cit. on pp. 18, 23).

[39] P. Cerda-Duran and N. Elias-Rosa. Neutron Stars Formation and Core Collapse Supernovae. Vol. 457. 2018, p. 1 (cit. on p. 18).

[40] A. Juodagalvis, K. Langanke, et al. Improved estimate of electron capture rates on nuclei during stellar core collapse. Nuc. Phys. A 848 (2010), pp. 454–478 (cit. on p. 18).

[41] K. G. Balasi, K. Langanke, and G. Martínez-Pinedo. Neutrino-nucleus reactions and their role for supernova dynamics and nucleosynthesis. Progr. Part. Nucl. Phys. 85 (2015), pp. 33–81 (cit. on p. 18).

[42] T. Foglizzo, R. Kazeroni, J. Guilet, et al. The Explosion Mechanism of Core-Collapse Supernovae: Progress in Supernova Theory and Experiments. Publ. Astron. Soc. Aust. 32 (2015), p. 17 (cit. on pp. 20, 21, 78, 168).

[43] B. Müller. The Core-Collapse Supernova Explosion Mechanism. Vol. 329. IAU Symp. 2017 (cit. on pp. 20, 78, 129, 154).

[44] J. W. Murphy, C. D. Ott, and A. Burrows. A Model for Gravitational Wave Emission from Neutrino-Driven Core-Collapse Supernovae. Astrophys. J. 707 (2009), pp. 1173–1190 (cit. on pp. 20–22, 81, 83, 168).

[45] B. Müller, H.-T. Janka, and A. Marek. A New Multi-dimensional General Relativistic Neutrino Hydrodynamics Code of Core-collapse Supernovae. III. Gravitational Wave Signals from Supernova Explosion Models. Astrophys. J. 766, 43 (2013) (cit. on pp. 20, 21, 166, 176).

[46] K. N. Yakunin, P. Marronetti, et al. Gravitational waves from core collapse supernovae. Class. Quantum Grav. 27 (19), 194005 (2010) (cit. on pp. 20, 50, 52, 166).

[47] K. N. Yakunin, A. Mezzacappa, et al. Gravitational wave signatures of ab initio two-dimensional core collapse supernova explosion models for 12-25 $M_\odot$ stars. Phys. Rev. D 92 (8), 084040 (2015) (cit. on pp. 20, 79, 166, 167).

[48] V. Morozova, D. Radice, et al. The Gravitational Wave Signal from Core-collapse Supernovae. Astrophys. J. 861, 10 (2018) (cit. on pp. 21, 168, 177).

[49] P. Cerdá-Durán, N. DeBrye, et al. Gravitational Wave Signatures in Black Hole Forming Core Collapse. Astrophys. J. Lett. 779, L18 (2013) (cit. on pp. 21–23, 167).

[50] H. Sotani and T. Takiwaki. Gravitational wave asteroseismology with protoneutron stars. Phys. Rev. D 94, 044043 (2016) (cit. on p. 21).

[51] K. Kotake, W. Iwakami, et al. Stochastic Nature of Gravitational Waves from Supernova Explosions with Standing Accretion Shock Instability. Astrophys. J. Lett. 697 (2009), pp. L133–L136 (cit. on pp. 21, 79).

[52] H. Dimmelmeier, C. D. Ott, et al. Gravitational wave burst signal from core collapse of rotating stars. Phys. Rev. D 78 (6), 064056 (2008) (cit. on pp. 21, 52, 78, 82, 83, 102, 104–106, 111, 115).

[53] C. D. Ott. TOPICAL REVIEW: The gravitational-wave signature of core-collapse supernovae. Class. Quantum Grav. 26 (6), 063001 (2009) (cit. on p. 21).

[54] J. Fuller, M. Cantiello, et al. The Spin Rate of Pre-collapse Stellar Cores: Wave-driven Angular Momentum Transport in Massive Stars. Astrophys. J. 810, 101 (2015) (cit. on pp. 21, 114, 132).

[55] T. Z. Summerscales, A. Burrows, et al. Maximum Entropy for Gravitational Wave Data Analysis: Inferring the Physical Parameters of Core-Collapse Supernovae. Astrophys. J. 678, 1142-1157 (2008) (cit. on p. 21).

[56] I. S. Heng. Rotating stellar core-collapse waveform decomposition: a principal component analysis approach. Class. Quantum Grav. 26 (2009), p. 105005 (cit. on pp. 21, 79).

[57] C. Röver, M.-A. Bizouard, et al. Bayesian reconstruction of gravitational wave burst signals from simulations of rotating stellar core collapse and bounce. Phys. Rev. D 80 (10), 102004 (2009) (cit. on pp. 21, 79).

[58] J. Logue, C. D. Ott, et al. Inferring core-collapse supernova physics with gravitational waves. Phys. Rev. D 86 (4), 044023 (2012) (cit. on pp. 21, 79, 181).

[59] M. C. Edwards, R. Meyer, and N. Christensen. Bayesian parameter estimation of core collapse supernovae using gravitational wave simulations. Inverse Probl. 30, 114008 (2014) (cit. on p. 21).

[60] E. Abdikamalov, S. Gossan, et al. Measuring the angular momentum distribution in core-collapse supernova progenitors with gravitational waves. Phys. Rev. D 90 (4), 044001 (2014).
SEG led the signal analysis and detectability studies using waveforms produced by simulations ran by EA and AM, and wrote around one third of the manuscript. (cit. on pp. 21, 89).

[61] W. J. Engels, R. Frey, and C. D. Ott. Multivariate regression analysis of gravitational waves from rotating core collapse. Phys. Rev. D 90, 124026 (2014) (cit. on p. 21).

[62] S. Richers, C. D. Ott, et al. Equation of state effects on gravitational waves from rotating core collapse. Phys. Rev. D 95, 063019 (2017) (cit. on p. 21).

[63] C. L. Fryer, D. E. Holz, and S. A. Hughes. Gravitational Wave Emission from Core Collapse of Massive Stars. Astrophys. J. 565 (2002), pp. 430–446 (cit. on pp. 21, 167).

[64] C. D. Ott, S. Ou, et al. One-armed Spiral Instability in a Low-T/|W| Postbounce Supernova Core. Astrophys. J. Lett. 625 (2005), pp. L119–L122 (cit. on pp. 21, 53).

[65] S. Scheidegger, S. C. Whitehouse, et al. Gravitational waves from supernova matter. Class. Quantum Grav. 27 (11), 114101 (2010) (cit. on pp. 21, 52, 53, 78, 96, 104, 128, 169).

[66] T. Kuroda, T. Takiwaki, and K. Kotake. Gravitational wave signatures from low-mode spiral instabilities in rapidly rotating supernova cores. Phys. Rev. D 89 (4), 044011 (2014) (cit. on pp. 21, 53, 78, 79, 101, 102, 128, 169).

[67] T. Takiwaki and K. Kotake. Anisotropic emission of neutrino and gravitational-wave signals from rapidly rotating core-collapse supernovae. Mon. Not. Roy. Astron. Soc. 475 (2018), pp. L91–L95 (cit. on pp. 21, 23, 96).

[68] E. O'Connor and C. D. Ott. Black Hole Formation in Failing Core-Collapse Supernovae. Astrophys. J. 730, 70 (2011) (cit. on pp. 22, 55, 107, 167).

[69] D. Clausen, A. L. Piro, and C. D. Ott. The Black Hole Formation Probability. Astrophys. J. 799, 190 (2015) (cit. on pp. 22, 23, 167).

[70] M. Ugliano, H.-T. Janka, et al. Progenitor-explosion Connection and Remnant Birth Masses for Neutrino-driven Supernovae of Iron-core Progenitors. Astrophys. J. 757, 69 (2012) (cit. on pp. 22, 167).

[71] K.-C. Pan, C. Mattes, et al. The impact of different neutrino transport methods on multidimensional core-collapse supernova simulations. J. Phys. G: Nucl. Phys. 46 (2019), p. 014001 (cit. on pp. 23, 96, 167).

[72] C. D. Ott, C. Reisswig, et al. Dynamics and Gravitational Wave Signature of Collapsar Formation. Phys. Rev. Lett. 106 (16), 161103 (2011) (cit. on pp. 23, 166, 167).

[73] Y. Sekiguchi and M. Shibata. Formation of Black Hole and Accretion Disk in a Massive High-entropy Stellar Core Collapse. Astrophys. J. 737, 6 (2011) (cit. on p. 23).

[74] S. E. Woosley, A. Heger, and T. A. Weaver. The evolution and explosion of massive stars. Rev. Mod. Phys. 74 (2002), pp. 1015–1071 (cit. on p. 23).

[75] A. Heger, C. L. Fryer, et al. How Massive Single Stars End Their Life. Astrophys. J. 591 (2003), pp. 288–300 (cit. on p. 23).

[76] L. F. Roberts and S. Reddy. Neutrino Signatures from Young Neutron Stars. *Handbook of Supernovae*. Springer International Publishing, 2017, p. 1605. ISBN: 978-3-319-21845-8 (cit. on p. 23).

[77] A. Mirizzi, I. Tamborra, H.-T. Janka, et al. Supernova neutrinos: production, oscillations and detection. Nuovo Cimento Rivista Serie 39 (2016), pp. 1–112 (cit. on pp. 23, 44).

[78] C. D. Ott, E. Abdikamalov, et al. Correlated gravitational wave and neutrino signals from general-relativistic rapidly rotating iron core collapse. Phys. Rev. D 86 (2), 024026 (2012) (cit. on pp. 23, 102, 105, 107).

[79] L. F. Roberts. A new code for proto-neutron star evolution. Astrophys. J. 755 (2012), pp. 126–146 (cit. on pp. 24, 135, 153, 158).

[80] S. J. Smartt. Progenitors of Core-Collapse Supernovae. Ann. Rev. Astron. Astroph. 47 (2009), pp. 63–106 (cit. on pp. 25, 44, 45).

[81] M. D. Kistler, W. C. Haxton, and H. Yüksel. Tomography of Massive Stars from Core Collapse to Supernova Shock Breakout. Astrophys. J. 778, 81 (2013) (cit. on pp. 25, 26, 39).

[82] R. X. Adhikari. Gravitational radiation detection with laser interferometry. Rev. Mod. Phys. 86 (2014), pp. 121–151 (cit. on pp. 25, 27, 29, 30, 41).

[83] B. S. Sathyaprakash and B. F. Schutz. Physics, Astrophysics and Cosmology with Gravitational Waves. Living Rev. Relat. 12, 2 (2009), p. 2 (cit. on p. 28).

[84] N. Christensen. Measuring the stochastic gravitational-radiation background with laser-interferometric antennas. Phys. Rev. D 46 (1992), pp. 5250–5266 (cit. on p. 28).

[85] J. C. Driggers. Noise Cancellation for Gravitational Wave Detectors. PhD thesis. California Institute of Technology, 2015 (cit. on pp. 29, 163, 172).

[86] V. B. Braginsky and F. Y. Khalili. Low noise rigidity in quantum measurements. Phys. Lett. A 257 (1999), pp. 241–246 (cit. on p. 30).

[87] A. Buonanno and Y. Chen. Quantum noise in second generation, signal-recycled laser interferometric gravitational-wave detectors. Phys. Rev. D 64, 042006 (2001) (cit. on p. 30).

[88] A. Buonanno and Y. Chen. Signal recycled laser-interferometer gravitational-wave detectors as optical springs. Phys. Rev. D 65, 042001 (2002) (cit. on p. 30).

[89] H. J. Kimble, Y. Levin, et al. Conversion of conventional gravitational-wave interferometers into quantum nondemolition interferometers by modifying their input and/or output optics. Phys. Rev. D 65, 022002 (2001) (cit. on p. 30).

[90] O. Miyakawa, R. Ward, R. Adhikari, et al. Measurement of optical response of a detuned resonant sideband extraction gravitational wave detector. Phys. Rev. D 74, 022001 (2006) (cit. on p. 30).

[91] D. Martynov, H. Miao, H. Yang, et al. Exploring the sensitivity of gravitational wave detectors to neutron star physics. arXiv e-prints (2019) (cit. on p. 30).

[92] R. Tso, D. Gerosa, and Y. Chen. Optimizing LIGO with LISA forewarnings to improve black-hole spectroscopy. arXiv e-prints (2018) (cit. on p. 30).

[93] B. P. Abbott, R. Abbott, R. Adhikari, et al. LIGO: the Laser Interferometer Gravitational-Wave Observatory. Rep. Prog. Phys. 72 (7), 076901 (2009) (cit. on pp. 30, 41).

[94] T. Accadia, F. Acernese, et al. Virgo: a laser interferometer to detect gravitational waves. J. Inst. 7 (2012), p. 3012 (cit. on pp. 30, 31).

[95] H. Grote and LIGO Scientific Collaboration. The GEO 600 status. Class. Quantum Grav. 27 (8), 084003 (2010) (cit. on p. 30).

[96] B. Willke, P. Ajith, B. Allen, et al. The GEO-HF project. Class. Quantum Grav. 23 (2006), S207–S214 (cit. on p. 30).

[97] M. Ando, K. Arai, R. Takahashi, et al. Stable Operation of a 300-m Laser Interferometer with Sufficient Sensitivity to Detect Gravitational-Wave Events within Our Galaxy. Phys. Rev. Lett. 86 (2001), pp. 3950–3954 (cit. on p. 30).

[98] G. M. Harry (for the LIGO Scientific Collaboration). Advanced LIGO: the next generation of gravitational wave detectors. Class. Quantum Grav. 27 (8) (2010), p. 084006 (cit. on p. 30).

[99] F. Acernese, M. Agathos, K. Agatsuma, et al. Advanced Virgo: a second-generation interferometric gravitational wave detector. Class. Quantum Grav. 32 (2), 024001 (2015) (cit. on pp. 31, 47).

[100] K. Somiya. Detector configuration of KAGRA-the Japanese cryogenic gravitational-wave detector. Class. Quantum Grav. 29 (12), 124007 (2012) (cit. on p. 31).

[101] Y. Aso, Y. Michimura, K. Somiya, et al. Interferometer design of the KAGRA gravitational wave detector. Phys. Rev. D 88 (4), 043007 (2013) (cit. on p. 31).

[102] T. Akutsu, M. Ando, S. Araki, et al. Construction of KAGRA: an underground gravitational-wave observatory. Progr. Theor. Exp. Phys. 013F01 (2018) (cit. on p. 31).

[103] B. Iyer et al. *LIGO-India, Proposal of the Consortium for Indian Initiative in Gravitational-wave Observations (IndIGO)*. Tech. rep. LIGO-M1100296-v2. IndIGO and LIGO Scientific Collaboration, 2011 (cit. on p. 31).

[104] B. P. Abbott, R. Abbott, et al. Prospects for Observing and Localizing Gravitational-Wave Transients with Advanced LIGO and Advanced Virgo. Living Rev. Relat. 19, 1 (2016) (cit. on p. 31).

[105] K. Scholberg. Supernova Neutrino Detection. Ann. Rev. Nuc. Par. Sci. 62 (2012), pp. 81–103 (cit. on pp. 32–34).

[106] K. Nakamura. Review of Particle Physics. J. Phys. G: Nucl. Phys. 37, 075021 (2010) (cit. on p. 32).

[107] E. N. Alekseev, L. N. Alekseeva, et al. Possible detection of a neutrino signal on 23 February 1987 at the Baksan underground scintillation telescope of the Institute of Nuclear Research. Sov. Phys. JETP Lett. 45 (1987), p. 589 (cit. on p. 36).

[108] M. Aglietta, B. Alpat, et al. The most powerful scintillator supernovae detector: LVD. Nuovo Cimento A Ser. 105 (1992), pp. 1793–1804 (cit. on p. 36).

[109] G. Alimonti, C. Arpesella, H. Back, et al. The Borexino detector at the Laboratori Nazionali del Gran Sasso. Nucl. Instr. Meth. Phys. Res. A 600 (2009), pp. 568–593 (cit. on p. 36).

[110] A. Suzuki. Present Status of KamLAND. Nuc. Phys. B Proc. Suppl. 77 (1999), pp. 171–176 (cit. on p. 36).

[111] The NOvA Collaboration and D. Ayres. NOvA Proposal to Build a 30 Kiloton Off-Axis Detector to Study Neutrino Oscillations in the Fermilab NuMI Beamline. arXiv e-prints, hep-ex/0503053 (2005), hep–ex/0503053 (cit. on p. 36).

[112] J. P. Ochoa-Ricoux. The Daya Bay Neutrino Oscillation Experiment. Nuc. Phys. B Proc. Suppl. 217 (2011), pp. 140–142 (cit. on p. 36).

[113] M. Ikeda, A. Takeda, et al. Search for Supernova Neutrino Bursts at Super-Kamiokande. Astrophys. J. 669 (2007), pp. 519–524 (cit. on p. 36).

[114] R. Abbasi, Y. Abdou, T. Abu-Zayyad, et al. IceCube sensitivity for low-energy neutrinos from nearby supernovae. Astron. Astrophys. 535, A109 (2011) (cit. on p. 36).

[115] C. A. Duba, F. Duncan, et al. HALO: the helium and lead observatory for supernova neutrinos. Vol. 136. 2008 (cit. on p. 36).

[116] M. Soderberg. MicroBooNE: A New Liquid Argon Time Projection Chamber Experiment. Vol. 1189. 2009, pp. 83–87 (cit. on p. 36).

[117] J. F. Beacom and P. Vogel. Can a supernova be located by its neutrinos? Phys. Rev. D 60, 033007 (1999) (cit. on p. 37).

[118] R. Tomàs, D. Semikoz, et al. Supernova pointing with low- and high-energy neutrino detectors. Phys. Rev. D 68, 093013 (2003) (cit. on p. 37).

[119] V. Brdar, M. Lindner, and X.-J. Xu. Neutrino astronomy with supernova neutrinos. J. Cosmol. Astropart. Phys. 2018, 025 (2018) (cit. on p. 37).

[120] N. Panagia. Distance to SN 1987 A and the LMC. Vol. 190. 1999, p. 549. ISBN: 1-58381-021-8 (cit. on p. 38).

[121] L. Wang and J. C. Wheeler. Spectropolarimetry of Supernovae. Ann. Rev. Astron. Astroph. 46 (2008), p. 433 (cit. on pp. 39, 79).

[122] R. Chornock, A. V. Filippenko, W. Li, et al. The Transitional Stripped-envelope SN 2008ax: Spectral Evolution and Evidence for Large Asphericity. Astrophys. J. 739, 41 (2011) (cit. on pp. 39, 79).

[123] N. Smith, S. B. Cenko, et al. SN 2010jp (PTF10aaxi): a jet in a Type II supernova. Mon. Not. Roy. Astron. Soc. 420 (2012), p. 1135 (cit. on pp. 39, 79, 100).

[124] B. Sinnott, D. L. Welch, A. Rest, et al. Asymmetry in the Outburst of SN 1987A Detected Using Light Echo Spectroscopy. Astrophys. J. 767, 45 (2013) (cit. on pp. 39, 79).

[125] S. E. Boggs, F. A. Harrison, et al. ^{44}Ti gamma-ray emission lines from SN1987A reveal an asymmetric explosion. Science 348 (2015), pp. 670–671 (cit. on pp. 39, 79).

[126] K. Kotake, K. Sumiyoshi, S. Yamada, et al. Core-collapse supernovae as supercomputing science: A status report toward six-dimensional simulations with exact Boltzmann neutrino transport in full general relativity. Progr. Theor. Exp. Phys. 2012, 01A301 (2012), p. 301 (cit. on p. 39).

[127] H.-T. Janka. Explosion Mechanisms of Core-Collapse Supernovae. Ann. Rev. Nuc. Par. Sci. 62 (2012), p. 407 (cit. on pp. 39, 78, 129).

[128] C. D. Ott, E. Abdikamalov, et al. General-relativistic Simulations of Three-dimensional Core-collapse Supernovae. Astrophys. J. 768, 115 (2013) (cit. on pp. 39, 50, 52, 79).

[129] J. C. Dolence, A. Burrows, J. W. Murphy, et al. Dimensional Dependence of the Hydrodynamics of Core-collapse Supernovae. Astrophys. J. 765, 110 (2013) (cit. on p. 39).

[130] F. Hanke, B. Müller, et al. SASI Activity in Three-dimensional Neutrino-hydrodynamics Simulations of Supernova Cores. Astrophys. J. 770, 66 (2013) (cit. on p. 39).

[131] P. Mösta, S. Richers, C. D. Ott, et al. Magnetorotational Core-collapse Supernovae in Three Dimensions. Astrophys. J. Lett. 785, L29 (2014) (cit. on pp. 39, 101).

[132] S. M. Couch and E. P. O'Connor. High-resolution Three-dimensional Simulations of Core-collapse Supernovae in Multiple Progenitors. Astrophys. J. 785, 123 (2014) (cit. on p. 39).

[133] E. J. Lentz, S. W. Bruenn, W. R. Hix, et al. Three-dimensional Core-collapse Supernova Simulated Using a $15M_{\odot}$ Progenitor. Astrophys. J. Lett. 807, L31 (2015) (cit. on p. 39).

[134] T. Melson, H.-T. Janka, and A. Marek. Neutrino-driven Supernova of a Low-mass Iron-core Progenitor Boosted by Three-dimensional Turbulent Convection. Astrophys. J. Lett. 801, L24 (2015) (cit. on p. 39).

[135] K. Kotake. Multiple physical elements to determine the gravitational-wave signatures of core-collapse supernovae. C. R. Phys. 14 (2013), pp. 318–351 (cit. on pp. 39, 102, 117).

[136] S. van den Bergh and G. A. Tammann. Galactic and Extragalactic Supernova Rates. Ann. Rev. Astron. Astroph. 29 (1991), p. 363 (cit. on pp. 39, 43).

[137] E. Cappellaro, M. Turatto, S. Benetti, et al. The Rate of Supernovae - Part Two - the Selection Effects and the Frequencies Per Unit Blue Luminosity. Astron. Astrophys. 273 (1993), p. 383 (cit. on p. 39).

[138] G. A. Tammann, W. Loeffler, and A. Schroeder. The Galactic supernova rate. Astrophys. J. Supp. Ser. 92 (1994), p. 487 (cit. on pp. 39, 43).

[139] W. Li, R. Chornock, et al. Nearby supernova rates from the Lick Observatory Supernova Search - III. The rate-size relation, and the rates as a function of galaxy Hubble type and colour. Mon. Not. Roy. Astron. Soc. 412 (2011), p. 1473 (cit. on p. 39).

[140] R. Diehl, H. Halloin, K. Kretschmer, et al. Radioactive ^{26}Al from massive stars in the Galaxy. Nature 439 (2006), pp. 45–47 (cit. on p. 39).

[141] S. M. Adams, C. S. Kochanek, et al. Observing the Next Galactic Supernova. Astrophys. J. 778, 164 (2013) (cit. on pp. 39, 42, 43).

[142] D. Maoz and C. Badenes. The supernova rate and delay time distribution in the Magellanic Clouds. Mon. Not. Roy. Astron. Soc. 407 (2010), pp. 1314–1327 (cit. on p. 39).

[143] F. X. Timmes and S. E. Woosley. Gamma-Ray Line Signals from 26Al and 60Fe in the Galaxies of the Local Group. Astrophys. J. Lett. 481 (1997), p. L81 (cit. on p. 39).

[144] H. A. Thronson Jr., D. A. Hunter, et al. Submillimeter continuum emission from galaxies - Star formation and the interstellar medium in the local group dwarf IC 10. Astrophys. J. 355 (1990), p. 94 (cit. on p. 39).

[145] K. Gill, M. Zanolin, et al. Prospects for Gravitational Wave Searches for Core-Collapse Supernovae within the Local Universe. (LIGO-P1500232-v4) (). In preparation. (cit. on p. 39).

[146] S. Ando, J. F. Beacom, and H. Yüksel. Detection of Neutrinos from Supernovae in Nearby Galaxies. Phys. Rev. Lett. 95 (17), 171101 (2005), p. 171101 (cit. on p. 39).

[147] M. D. Kistler, H. Yüksel, S. Ando, et al. Core-collapse astrophysics with a five-megaton neutrino detector. Phys. Rev. D 83 (12), 123008 (2011) (cit. on p. 39).

[148] M. T. Botticella, S. J. Smartt, et al. A comparison between star formation rate diagnostics and rate of core collapse supernovae within 11 Mpc. Astron. Astrophys. 537, A132 (2012) (cit. on p. 39).

[149] S. Mattila, T. Dahlen, A. Efstathiou, et al. Core-collapse Supernovae Missed by Optical Surveys. Astrophys. J. 756, 111 (2012) (cit. on p. 39).

[150] L. A. Wainstein and V. D. Zubakov. *Extraction of Signals from Noise*. Prentice-Hall, Englewood Cliffs, NJ, USA, 1962 (cit. on p. 40).

[151] W. G. Anderson, P. R. Brady, et al. Excess power statistic for detection of burst sources of gravitational radiation. Phys. Rev. D 63 (4) (2001), p. 042003 (cit. on p. 40).

[152] A. Viceré. Optimal detection of burst events in gravitational wave interferometric observatories. Phys. Rev. D 66 (6), 062002 (2002) (cit. on p. 40).

[153] J. Sylvestre. Optimal generalization of power filters for gravitational wave bursts from single to multiple detectors. Phys. Rev. D 68 (10) (2003), p. 102005 (cit. on p. 40).

[154] J. Abadie et al. All-sky search for gravitational-wave bursts in the second joint LIGO-Virgo run. Phys. Rev. D 85 (12 2012), p. 122007 (cit. on pp. 40, 56, 60).

[155] J. Abadie, B. P. Abbott, et al. All-sky search for gravitational-wave bursts in the first joint LIGO-GEO-Virgo run. Phys. Rev. D 81 (10), 102001 (2010) (cit. on p. 40).

[156] J. Abadie, B. P. Abbott, et al. Search for Gravitational Waves Associated with Gamma-Ray Bursts during LIGO Science Run 6 and Virgo Science Runs 2 and 3. Astrophys. J. 760, 12 (2012) (cit. on p. 40).

[157] J. e. a. (S. C. Abadie. Implications for the Origin of GRB 051103 from LIGO Observations. Astrophys. J. 755, 2 (2012) (cit. on p. 40).

[158] J. e. a. (S. C. Abadie. Search for Gravitational Wave Bursts from Six Magnetars. Astrophys. J. Lett. 734, L35 (2011) (cit. on p. 40).

[159] M. Was, P. J. Sutton, et al. Performance of an externally triggered gravitational-wave burst search. Phys. Rev. D 86 (2), 022003 (2012) (cit. on pp. 40, 58).

[160] B. P. Abbott, R. Abbott, et al. Search for gravitational-wave bursts in the first year of the fifth LIGO science run. Phys. Rev. D 80 (10), 102001 (2009) (cit. on p. 40).

[161] J. Abadie, B. P. Abbott, R. Abbott, et al. Calibration of the LIGO gravitational wave detectors in the fifth science run. Nucl. Instr. Meth. Phys. Res. A 624 (2010), pp. 223–240 (cit. on pp. 40, 64).

[162] P. Astone, M. Bassan, E. Coccia, et al. Analysis of 3 years of data from the gravitational wave detectors EXPLORER and NAUTILUS. Phys. Rev. D 87 (8), 082002 (2013) (cit. on p. 41).

[163] A. Vinante and AURIGA Collaboration. Present performance and future upgrades of the AURIGA capacitive readout. Class. Quantum Grav. 23 (2006), S103–S110 (cit. on p. 41).

[164] O. D. Aguiar, J. J. Barroso, N. C. Carvalho, et al. Status Report of the Schenberg Gravitational Wave Antenna. Vol. 363. J. Phys. Conf. Ser. 2012 (cit. on p. 41).

[165] J. Aasi, J. Abadie, B. P. Abbott, et al. Characterization of the LIGO detectors during their sixth science run. Class. Quantum Grav. 32 (11), 115012 (2015) (cit. on pp. 41, 64).

[166] J. Aasi, J. Abadie, B. P. Abbott, et al. The characterization of Virgo data and its impact on gravitational-wave searches. Class. Quantum Grav. 29 (15), 155002 (2012) (cit. on pp. 41, 47).

[167] L. Blackburn, L. Cadonati, S. Caride, et al. The LSC glitch group: monitoring noise transients during the fifth LIGO science run. Class. Quantum Grav. 25 (18), 184004 (2008) (cit. on p. 41).

[168] T. B. Littenberg and N. J. Cornish. Separating gravitational wave signals from instrument artifacts. Phys. Rev. D 82 (10), 103007 (2010) (cit. on p. 41).

[169] J. Powell, D. Trifirò, et al. Classification methods for noise transients in advanced gravitational-wave detectors. Class. Quantum Grav. 32 (21), 215012 (2015) (cit. on pp. 41, 97).

[170] R. Biswas, L. Blackburn, J. Cao, et al. Application of machine learning algorithms to the study of noise artifacts in gravitational-wave data. Phys. Rev. D 88 (6) (2013), p. 062003 (cit. on p. 41).

[171] G. S. F. Center. *Lambda Tools Coordinate Conversions* (cit. on p. 42).

[172] J. R. Thorstensen, R. A. Fesen, and S. van den Bergh. The Expansion Center and Dynamical Age of the Galactic Supernova Remnant Cassiopeia A. Astron. J. 122 (2001), pp. 297–307 (cit. on p. 42).

[173] R. C. Kennicutt Jr. and P. W. Hodge. H II regions and star formation in the Magellanic Clouds. Astrophys. J. 306 (1986), pp. 130–141 (cit. on p. 42).

[174] G. de Vaucouleurs, A. de Vaucouleurs, and H. G. Corwin. *Second Reference Catalogue of Bright Galaxies*. Austin: University of Texas Press, 1976 (cit. on pp. 42, 43).

[175] B. P. Schmidt, R. P. Kirshner, and R. G. Eastman. Expanding photospheres of type II supernovae and the extragalactic distance scale. Astrophys. J. 395 (1992), pp. 366–386 (cit. on p. 43).

[176] G. Pietrzyński, D. Graczyk, et al. An eclipsing-binary distance to the Large Magellanic Cloud accurate to two per cent. Nature 495 (2013), pp. 76–79 (cit. on p. 43).

[177] I. N. Evans, F. A. Primini, et al. The Chandra Source Catalog. Astrophys. J. Supp. Ser. 189 (2010), pp. 37–82 (cit. on p. 43).

[178] I. D. Karachentsev, V. E. Karachentseva, et al. A Catalog of Neighboring Galaxies. Astron. J. 127 (2004), pp. 2031–2068 (cit. on p. 43).

[179] B. Arbutina, D. Urošević, and B. Vukotić. High supernova rate and enhanced star-formation triggered in M81-M82 encounter. Vol. 237. IAU Symp. 2007, pp. 391–391 (cit. on p. 43).

[180] N. Jackson, R. A. Battye, et al. A survey of polarization in the JVAS/CLASS flat-spectrum radio source surveys - I. The data and catalogue production. Mon. Not. Roy. Astron. Soc. 376 (2007) (cit. on p. 43).

[181] B. A. Jacobs, L. Rizzi, et al. The Extragalactic Distance Database: Color-Magnitude Diagrams. Astron. J. 138 (2009), pp. 332–337 (cit. on p. 43).

[182] S. Mattila and W. P. S. Meikle. Supernovae in the nuclear regions of starburst galaxies. Mon. Not. Roy. Astron. Soc. 324 (2001), pp. 325–342 (cit. on p. 43).

[183] L. Colina and D. Perez-Olea. On the origin of the radio emission in IRAS galaxies with high and ultrahigh luminosity - The starburst-AGN controversy. Mon. Not. Roy. Astron. Soc. 259 (1992), pp. 709–724 (cit. on p. 43).

[184] A. Brunthaler, I. Martí-Vidal, et al. VLBI observations of SN 2008iz. I. Expansion velocity and limits on anisotropic expansion. Astron. Astrophys. 516, A27 (2010) (cit. on p. 43).

[185] S. J. Fossey, B. Cooke, et al. Supernova 2014J in M82 = PSN J09554214+6940260. CBET 3792 (2014) (cit. on p. 43).

[186] Y. Cao, M. M. Kasliwal, et al. Classification of Supernova in M82 as a young, reddened Type Ia Supernova. ATel 5786 (2014) (cit. on p. 43).

[187] P. Antonioli, R. Tresch Fienberg, et al. SNEWS: the SuperNova Early Warning System. New J. Phys. 6 (2004), p. 115 (cit. on p. 44).

[188] G. Pagliaroli, F. Vissani, E. Coccia, et al. Neutrinos from Supernovae as a Trigger for Gravitational Wave Search. Phys. Rev. Lett. 103 (3), 031102 (2009) (cit. on p. 44).

[189] T. Fischer, S. C. Whitehouse, et al. Protoneutron star evolution and the neutrino-driven wind in general relativistic neutrino radiation hydrodynamics simulations. Astron. Astrophys. 517, A80 (2010) (cit. on p. 44).

[190] J. Wallace, A. Burrows, and J. C. Dolence. Detecting the Supernova Breakout Burst in Terrestrial Neutrino Detectors. Astrophys. J. 817, 182 (2016) (cit. on pp. 44, 86).

[191] A. V. Filippenko. Optical Spectra of Supernovae. Ann. Rev. Astron. Astroph. 35 (1997), pp. 309–355 (cit. on pp. 44, 45).

[192] L.-X. Li. Shock breakout in Type Ibc supernovae and application to GRB 060218/SN 2006aj. Mon. Not. Roy. Astron. Soc. 375 (2007), pp. 240–256 (cit. on pp. 44, 75).

[193] C. D. Matzner and C. F. McKee. The Expulsion of Stellar Envelopes in Core-Collapse Supernovae. Astrophys. J. 510 (1999), pp. 379–403 (cit. on p. 45).

[194] S. Gezari, D. O. Jones, N. E. Sanders, et al. GALEX Detection of Shock Breakout in Type IIP Supernova PS1-13arp: Implications for the Progenitor Star Wind. Astrophys. J. 804, 28 (2015) (cit. on p. 45).

[195] V. Morozova, A. L. Piro, M. Renzo, et al. Light Curves of Core-collapse Supernovae with Substantial Mass Loss Using the New Open-source SuperNova Explosion Code (SNEC). Astrophys. J. 814, 63 (2015) (cit. on pp. 45, 75).

[196] P. Ajith, M. Boyle, D. A. Brown, et al. Data formats for numerical relativity waves. arXiv:0709.0093v3 (2007) (cit. on pp. 49, 53, 55).

[197] E. Müller, H.-T. Janka, and A. Wongwathanarat. Parametrized 3D models of neutrino-driven supernova explosions. Neutrino emission asymmetries and gravitational-wave signals. Astron. Astrophys. 537, A63 (2012) (cit. on pp. 50, 52, 166).

[198] J. M. Lattimer and F. Douglas Swesty. A generalized equation of state for hot, dense matter. Nuc. Phys. A 535 (1991), pp. 331–376 (cit. on pp. 52, 82, 106, 114, 120, 126, 135, 167).

[199] D. Lai. Secular bar-mode evolution and gravitational waves from neutron stars. Vol. 575. AIP Conf. Proc. 2001, pp. 246–257 (cit. on p. 53).

[200] C. D. Ott, A. Burrows, et al. The Spin Periods and Rotational Profiles of Neutron Stars at Birth. Astrophys. J. Supp. Ser. 164 (2006), p. 130 (cit. on pp. 53, 101, 102, 111).

[201] E. Balbinski. A new shear instability in rotating, self-gravitating, perfect fluids. Mon. Not. Roy. Astron. Soc. 216 (1985), pp. 897–908 (cit. on p. 53).

[202] A. L. Watts, N. Andersson, and D. I. Jones. The Nature of Low T/|W| Dynamical Instabilities in Differentially Rotating Stars. Astrophys. J. 618 (2005), pp. L37–L40 (cit. on p. 53).

[203] C. D. Ott. *GWs from Barmode Instabilities*. Tech. rep. LIGO-T1000553-v2. LIGO Scientific Collaboration, 2010 (cit. on pp. 53, 56).

[204] K. S. Thorne. Gravitational radiation. *Three Hundred Years of Gravitation*. Ed. by S. W. Hawking and W. Israel. 1987, pp. 330–458 (cit. on pp. 53, 55).

[205] H.-T. Janka, K. Langanke, A. Marek, et al. Theory of core-collapse supernovae. Phys. Rep. 442 (2007), pp. 38–74 (cit. on pp. 55, 78, 79).

[206] S. E. Woosley and J. S. Bloom. The Supernova Gamma-Ray Burst Connection. AIP Conf. Proc. 836 (2006), pp. 398–407 (cit. on pp. 55, 101, 167).

[207] A. L. Piro and E. Pfahl. Fragmentation of Collapsar Disks and the Production of Gravitational Waves. Astrophys. J. 658 (2007), pp. 1173–1176 (cit. on pp. 55, 56, 167).

[208] R. Perna, P. J. Armitage, and B. Zhang. Flares in Long and Short Gamma-Ray Bursts: A Common Origin in a Hyperaccreting Accretion Disk. Astrophys. J. Lett. 636 (2006), p. L29 (cit. on p. 55).

[209] L. Santamaria and C. D. Ott. *GWs from Accretion Disk Instabilities*. Tech. rep. LIGO-T1100093-v2. LIGO Scientific Collaboration, 2011 (cit. on p. 55).

[210] J. Abadie, B. P. Abbott, et al. All-sky search for periodic gravitational waves in the full S5 LIGO data. Phys. Rev. D 85, 022001 (2012) (cit. on p. 56).

[211] M. Was. Searching for gravitational waves associated with gamma-ray bursts in 2009-2010 ligo-virgo data. PhD thesis. Université Paris Sud - Paris XI, 2011 (cit. on p. 57).

[212] P. J. Sutton, G. Jones, S. Chatterji, et al. X-Pipeline: an analysis package for autonomous gravitational-wave burst searches. New J. Phys. 12, 053034 (2010) (cit. on pp. 57, 58).

[213] S. Klimenko, S. Mohanty, M. Rakhmanov, et al. Constraint likelihood analysis for a network of gravitational wave detectors. Phys. Rev. D 72 (12), 122002 (2005) (cit. on p. 58).

[214] S. Klimenko, S. Mohanty, M. Rakhmanov, et al. Constraint likelihood method: generalization for colored noise. J. Phys. Conf. Ser. 32 (2006), pp. 12–17 (cit. on p. 58).

[215] P. R. Brady, J. D. E. Creighton, and A. G. Wiseman. Upper limits on gravitational-wave signals based on loudest events. Class. Quantum Grav. 21 (2004), S1775–S1781 (cit. on p. 58).

[216] R. Biswas, P. R. Brady, et al. The loudest event statistic: general formulation, properties and applications. Class. Quantum Grav. 26, 175009 (2009) (cit. on p. 58).

[217] S. Chatterji, A. Lazzarini, L. Stein, et al. Coherent network analysis technique for discriminating gravitational-wave bursts from instrumental noise. Phys. Rev. D 74 (8), 082005 (2006) (cit. on p. 59).

[218] M. Vallisneri, J. Kanner, et al. The LIGO Open Science Center. J. Phys. Conf. Ser. 610 (1) (2015), p. 012021 (cit. on pp. 59, 88).

[219] K. Cannon, R. Cariou, et al. Toward Early-warning Detection of Gravitational Waves from Compact Binary Coalescence. Astrophys. J. 748, 136 (2012) (cit. on p. 60).

[220] S. Privitera, S. R. P. Mohapatra, et al. Improving the sensitivity of a search for coalescing binary black holes with nonprecessing spins in gravitational wave data. Phys. Rev. D 89, 024003 (2014) (cit. on p. 60).

[221] P. Kalmus. Search for Gravitational Wave Bursts from Soft Gamma Repeaters. PhD thesis. Columbia University, 2009 (cit. on p. 64).

[222] M. C. Bersten, O. Benvenuto, and M. Hamuy. Hydrodynamical Models of Type II Plateau Supernovae. Astrophys. J. 729, 61 (2011) (cit. on p. 75).

[223] J. B. Kanner, T. B. Littenberg, et al. Leveraging waveform complexity for confident detection of gravitational waves. Phys. Rev. D 93 (2), 022002 (2016) (cit. on p. 76).

[224] R. Schaeffer, Y. Declais, and S. Jullian. The neutrino emission of SN1987A. Nature 330 (1987), pp. 142–144 (cit. on p. 78).

[225] A. Burrows, L. Dessart, et al. Multi-dimensional explorations in supernova theory. Phys. Rep. 442 (2007), pp. 23–37 (cit. on p. 79).

[226] A. Burrows, E. Livne, et al. A New Mechanism for Core-Collapse Supernova Explosions. Astrophys. J. 640 (2006), pp. 878–890 (cit. on pp. 79, 133, 153).

[227] A. Burrows, E. Livne, et al. Features of the Acoustic Mechanism of Core-Collapse Supernova Explosions. Astrophys. J. 655 (2007), pp. 416–433 (cit. on pp. 79, 101).

[228] D. S. Sivia and J. Skilling. *Data Analysis: A Bayesian Tutorial*. Oxford University Press, 2006. ISBN: 9780198568315 (cit. on pp. 79, 85, 87).

[229] J. Skilling. Nested Sampling. Vol. 735. AIP Conf. Proc. 2004, pp. 395–405 (cit. on pp. 79, 85, 123).

[230] T. Kuroda, K. Kotake, and T. Takiwaki. A New Gravitational-wave Signature from Standing Accretion Shock Instability in Supernovae. Astrophys. J. Lett. 829, L14 (2016) (cit. on pp. 79, 168).

[231] M. Shibata and Y.-I. Sekiguchi. Three-dimensional simulations of stellar core collapse in full general relativity: Nonaxisymmetric dynamical instabilities. Phys. Rev. D 71 (2), 024014 (2005) (cit. on p. 79).

[232] S. Scheidegger, T. Fischer, et al. Gravitational waves from 3D MHD core collapse simulations. Astron. Astrophys. 490 (2008), pp. 231–241 (cit. on p. 79).

[233] H. Andresen, B. Müller, et al. Gravitational wave signals from 3D neutrino hydrodynamics simulations of core-collapse supernovae. Mon. Not. Roy. Astron. Soc. 468 (2017), pp. 2032–2051 (cit. on pp. 79, 155, 166, 168).

[234] K. Kotake, W. Iwakami-Nakano, and N. Ohnishi. Effects of Rotation on Stochasticity of Gravitational Waves in the Nonlinear Phase of Core-collapse Supernovae. Astrophys. J. 736, 124 (2011) (cit. on p. 79).

[235] J. Veitch, V. Raymond, B. Farr, et al. Parameter estimation for compact binaries with ground-based gravitational-wave observations using the LALInference software library. Phys. Rev. D 91 (4), 042003 (2015) (cit. on pp. 79, 85).

[236] J. W. Murphy and A. Burrows. BETHE-Hydro: An Arbitrary Lagrangian-Eulerian Multidimensional Hydrodynamics Code for Astrophysical Simulations. Astrophys. J. Supp. Ser. 179 (2008), pp. 209–241 (cit. on p. 81).

[237] S. E. Woosley and A. Heger. Nucleosynthesis and remnants in massive stars of solar metallicity. Phys. Rep. 442 (2007), pp. 269–283 (cit. on pp. 81, 82, 104, 105).

[238] H. Dimmelmeier, J. A. Font, and E. Müller. Relativistic simulations of rotational core collapse II. Collapse dynamics and gravitational radiation. Astron. Astrophys. 393 (2002), pp. 523–542 (cit. on pp. 82, 106).

[239] H. Dimmelmeier, J. Novak, J. A. Font, et al. Combining spectral and shock-capturing methods: A new numerical approach for 3D relativistic core collapse simulations. Phys. Rev. D 71 (6), 064023 (2005) (cit. on pp. 82, 106, 123).

[240] H. Shen, H. Toki, et al. Relativistic equation of state of nuclear matter for supernova and neutron star. Nuc. Phys. A 637 (1998), pp. 435–450 (cit. on pp. 82, 107, 108, 114, 120, 126).

[241] H. Shen, H. Toki, et al. Relativistic Equation of State of Nuclear Matter for Supernova Explosion. Progr. Theor. Phys. 100 (1998), pp. 1013–1031 (cit. on p. 82).

[242] R. Essick, S. Vitale, et al. Localization of Short Duration Gravitational-wave Transients with the Early Advanced LIGO and Virgo Detectors. Astrophys. J. 800, 81 (2015) (cit. on p. 86).

[243] T. Hastie, R. Tibshirani, and J. H. Freidman. *The Elements of Statistical Learning: Data Mining, Inference, and Prediction*. Springer series in statistics, 2001. ISBN: 9780387952840 (cit. on p. 87).

[244] R. Kazeroni, B. K. Krueger, et al. The non-linear onset of neutrino-driven convection in two- and three-dimensional core-collapse supernovae. Mon. Not. Roy. Astron. Soc. 480 (2018), pp. 261–280 (cit. on p. 96).

[245] T. Takiwaki, K. Kotake, and Y. Suwa. A Comparison of Two- and Three-dimensional Neutrino-hydrodynamics Simulations of Core-collapse Supernovae. Astrophys. J. 786, 83 (2014) (cit. on p. 96).

[246] S. M. Couch. On the Impact of Three Dimensions in Simulations of Neutrino-driven Core-collapse Supernova Explosions. Astrophys. J. 775, 35 (2013) (cit. on pp. 96, 130).

[247] R. M. Cabezón, K.-C. Pan, et al. Core-collapse supernovae in the hall of mirrors. A three-dimensional code-comparison project. Astron. Astrophys. 619, A118 (2018) (cit. on p. 96).

[248] O. Just, R. Bollig, et al. Core-collapse supernova simulations in one and two dimensions: comparison of codes and approximations. Mon. Not. Roy. Astron. Soc. 481 (2018), pp. 4786–4814 (cit. on p. 96).

[249] A. Torres-Forné, P. Cerdá-Durán, et al. Towards asteroseismology of core-collapse supernovae with gravitational wave observations - II. Inclusion of space-time perturbations. Mon. Not. Roy. Astron. Soc. 482 (2019), pp. 3967–3988 (cit. on pp. 97, 177).

[250] A. Passamonti, N. Andersson, and W. C. G. Ho. Buoyancy and g-modes in young superfluid neutron stars. Mon. Not. Roy. Astron. Soc. 455 (2016), pp. 1489–1511 (cit. on p. 97).

[251] J. Fuller, H. Klion, et al. Supernova seismology: gravitational wave signatures of rapidly rotating core collapse. Mon. Not. Roy. Astron. Soc. 450 (2015), pp. 414–427 (cit. on pp. 97, 126, 128).

[252] J. R. Westernacher-Schneider. Turbulence, Gravity, and Multimessenger Asteroseismology. PhD thesis. The University of Guelph, 2018 (cit. on p. 97).

[253] J. Powell, A. Torres-Forné, et al. Classification methods for noise transients in advanced gravitational-wave detectors II: performance tests on Advanced LIGO data. Class. Quantum Grav. 34 (3), 034002 (2017) (cit. on p. 97).

[254] G. S. Bisnovatyi-Kogan. The Explosion of a Rotating Star As a Supernova Mechanism. Astron. Lett. 47 (1970), p. 813 (cit. on p. 101).

[255] J. M. LeBlanc and J. R. Wilson. A Numerical Example of the Collapse of a Rotating Magnetized Star. Astrophys. J. 161 (1970), p. 541 (cit. on p. 101).

[256] J. C. Wheeler, I. Yi, et al. Asymmetric Supernovae, Pulsars, Magnetars, and Gamma-Ray Bursts. Astrophys. J. 537 (2000), pp. 810–823 (cit. on p. 101).

[257] J. C. Wheeler, D. L. Meier, and J. R. Wilson. Asymmetric Supernovae from Magnetocentrifugal Jets. Astrophys. J. 568 (2002), pp. 807–819 (cit. on p. 101).

[258] P. Mösta, C. D. Ott, et al. A large-scale dynamo and magnetoturbulence in rapidly rotating core-collapse supernovae. Nature 528 (2015), pp. 376–379 (cit. on p. 101).

[259] B. D. Metzger, D. Giannios, et al. The protomagnetar model for gamma-ray bursts. Mon. Not. Roy. Astron. Soc. 413 (2011), pp. 2031–2056 (cit. on p. 101).

[260] M. R. Drout, A. M. Soderberg, et al. The First Systematic Study of Type Ibc Supernova Multi-band Light Curves. Astrophys. J. 741, 97 (2011) (cit. on p. 101).

[261] N. Smith, W. Li, et al. Observed fractions of core-collapse supernova types and initial masses of their single and binary progenitor stars. Mon. Not. Roy. Astron. Soc. 412 (2011), pp. 1522–1538 (cit. on p. 101).

[262] M. Modjaz. Stellar forensics with the supernova-GRB connection. Astron. Nachr. 332 (2011), pp. 434–447 (cit. on p. 101).

[263] J. Hjorth and J. S. Bloom. The Gamma-Ray Burst - Supernova Connection. *Gamma-Ray Bursts*. Ed. by C. Kouveliotou, R. A. M. J. Wijers, and S. Woosley. Vol. 51. Cambridge University Press, 2012. Chap. 9, pp. 169–190 (cit. on p. 101).

[264] A. Heger, S. E. Woosley, and H. C. Spruit. Presupernova Evolution of Differentially Rotating Massive Stars Including Magnetic Fields. Astrophys. J. 626 (2005), pp. 350–363 (cit. on pp. 101, 103).

[265] S. A. Balbus and J. F. Hawley. A powerful local shear instability in weakly magnetized disks. I - Linear analysis. II - Nonlinear evolution. Astrophys. J. 376 (1991), pp. 214–233 (cit. on p. 101).

[266] M. Obergaulinger, P. Cerdá-Durán, et al. Semi-global simulations of the magneto-rotational instability in core collapse supernovae. Astron. Astrophys. 498 (2009), pp. 241–271 (cit. on p. 101).

[267] S. Akiyama, J. C. Wheeler, et al. The Magnetorotational Instability in Core-Collapse Supernova Explosions. Astrophys. J. 584 (2003), pp. 954–970 (cit. on p. 101).

[268] J. Fuller, D. Lecoanet, et al. Angular Momentum Transport via Internal Gravity Waves in Evolving Stars. Astrophys. J. 796, 17 (2014) (cit. on pp. 101, 103, 132).

[269] S. E. Woosley and A. Heger. The Progenitor Stars of Gamma-Ray Bursts. Astrophys. J. 637 (2006), pp. 914–921 (cit. on pp. 101, 103, 104).

[270] S.-C. Yoon, N. Langer, and C. Norman. Single star progenitors of long gamma-ray bursts. I. Model grids and redshift dependent GRB rate. Astron. Astrophys. 460 (2006), pp. 199–208 (cit. on p. 101).

[271] S. E. de Mink, N. Langer, et al. The Rotation Rates of Massive Stars: The Role of Binary Interaction through Tides, Mass Transfer, and Mergers. Astrophys. J. 764, 166 (2013) (cit. on pp. 101, 103).

[272] R. Kazeroni, J. Guilet, and T. Foglizzo. Are pulsars spun up or down by SASI spiral modes? Mon. Not. Roy. Astron. Soc. 471 (2017), pp. 914–925 (cit. on p. 101).

[273] L. Dessart, E. O'Connor, and C. D. Ott. The Arduous Journey to Black Hole Formation in Potential Gamma-Ray Burst Progenitors. Astrophys. J. 754, 76 (2012) (cit. on p. 102).

[274] S. Scheidegger, R. Käppeli, et al. The influence of model parameters on the prediction of gravitational wave signals from stellar core collapse. Astron. Astrophys. 514, A51 (2010) (cit. on p. 102).

[275] N. Andersson, V. Ferrari, et al. Gravitational waves from neutron stars: promises and challenges. Gen. Rel. Gravit. 43 (2011), pp. 409–436 (cit. on p. 102).

[276] E. B. Abdikamalov, C. D. Ott, et al. Axisymmetric general relativistic simulations of the accretion-induced collapse of white dwarfs. Phys. Rev. D 81 (4), 044012 (2010) (cit. on pp. 102, 105, 106, 111, 116, 123).

[277] A. Heger, N. Langer, and S. E. Woosley. Presupernova Evolution of Rotating Massive Stars. I. Numerical Method and Evolution of the Internal Stellar Structure. Astrophys. J. 528 (2000), pp. 368–396 (cit. on p. 103).

[278] T. Zwerger and E. Mueller. Dynamics and gravitational wave signature of axisymmetric rotational core collapse. Astron. Astrophys. 320 (1997), pp. 209–227 (cit. on p. 104).

[279] J. L. Friedman, J. R. Ipser, and L. Parker. Rapidly rotating neutron star models. Astrophys. J. 304 (1986), pp. 115–139 (cit. on p. 105).

[280] M. Shibata and Y.-I. Sekiguchi. Gravitational waves from axisymmetric rotating stellar core collapse to a neutron star in full general relativity. Phys. Rev. D 69 (8), 084024 (2004) (cit. on p. 106).

[281] P. Cerdá-Durán, G. Faye, et al. CFC+: improved dynamics and gravitational waveforms from relativistic core collapse simulations. Astron. Astrophys. 439 (2005), pp. 1033–1055 (cit. on p. 106).

[282] C. D. Ott, H. Dimmelmeier, A. Marek, et al. Rotating collapse of stellar iron cores in general relativity. Class. Quantum Grav. 24 (2007), S139–S154 (cit. on p. 106).

[283] E. O'Connor and C. D. Ott. A new open-source code for spherically symmetric stellar collapse to neutron stars and black holes. Class. Quantum Grav. 27 (11), 114103 (2010) (cit. on pp. 106, 107).

[284] H. Shen, H. Toki, et al. Relativistic Equation of State for Core-collapse Supernova Simulations. Astrophys. J. Supp. Ser. 197, 20 (2011) (cit. on pp. 107, 108, 114, 120, 126).

[285] M. Liebendörfer, M. Rampp, et al. Supernova Simulations with Boltzmann Neutrino Transport: A Comparison of Methods. Astrophys. J. 620 (2005), pp. 840–860 (cit. on p. 107).

[286] C. D. Ott, A. Burrows, et al. Gravitational Waves from Axisymmetric, Rotating Stellar Core Collapse. Astrophys. J. 600 (2004), pp. 834–864 (cit. on p. 111).

[287] H. Dimmelmeier, C. D. Ott, et al. Generic Gravitational-Wave Signals from the Collapse of Rotating Stellar Cores. Phys. Rev. Lett. 98 (25), 251101 (2007) (cit. on p. 111).

[288] H. A. Bethe. Supernova mechanisms. Rev. Mod. Phys. 62 (4 1990), pp. 801–866 (cit. on p. 111).

[289] R. Mönchmeyer, G. Schaefer, et al. Gravitational waves from the collapse of rotating stellar cores. Astron. Astrophys. 246 (1991), pp. 417–440 (cit. on p. 111).

[290] C. W. Helstrom. Fundamental limitations on the detectability of electromagnetic signals. Int. J. Theo. Phys. 1 (1968), pp. 37–50 (cit. on pp. 117, 118).

[291] C. D. Ott, A. Burrows, et al. Two-Dimensional Multiangle, Multigroup Neutrino Radiation-Hydrodynamic Simulations of Postbounce Supernova Cores. Astrophys. J. 685 (2008), pp. 1069–1088 (cit. on p. 117).

[292] D. Shoemaker. Tech. rep. LIGO-T0900288-v3. LIGO Scientific Collaboration, 2010 (cit. on p. 118).

[293] H. Dimmelmeier, J. A. Font, and E. Müller. Relativistic simulations of rotational core collapse I. Methods, initial models, and code tests. Astron. Astrophys. 388 (2002), pp. 917–935 (cit. on p. 123).

[294] T. Takiwaki, K. Kotake, and Y. Suwa. Three-dimensional simulations of rapidly rotating core-collapse supernovae: finding a neutrino-powered explosion aided by non-axisymmetric flows. Mon. Not. Roy. Astron. Soc. 461 (2016), pp. L112–L116 (cit. on p. 128).

[295] H.-T. Janka, T. Melson, and A. Summa. Physics of Core-Collapse Supernovae in Three Dimensions: A Sneak Preview. Ann. Rev. Nuc. Par. Sci. 66 (2016), pp. 341–375 (cit. on p. 129).

[296] A. Burrows, D. Vartanyan, et al. Crucial Physical Dependencies of the Core-Collapse Supernova Mechanism. Space Sci. Rev. 214, 33 (2018), p. 33 (cit. on p. 129).

[297] E. Abdikamalov, C. D. Ott, D. Radice, et al. Neutrino-driven Turbulent Convection and Standing Accretion Shock Instability in Three-dimensional Core-collapse Supernovae. Astrophys. J. 808, 70 (2015) (cit. on p. 130).

[298] D. Radice, S. M. Couch, and C. D. Ott. Implicit large eddy simulations of anisotropic weakly compressible turbulence with application to core-collapse supernovae. Comp. Astr. Cosm. 2, 7 (2015) (cit. on p. 130).

[299] S. M. Couch and C. D. Ott. The Role of Turbulence in Neutrino-driven Core-collapse Supernova Explosions. Astrophys. J. 799, 5 (2015) (cit. on p. 130).

[300] M. Liebendörfer. A Simple Parameterization of the Consequences of Deleptonization for Simulations of Stellar Core Collapse. Astrophys. J. 633 (2005), pp. 1042–1051 (cit. on p. 130).

[301] J. Nordhaus, A. Burrows, et al. Dimension as a Key to the Neutrino Mechanism of Core-collapse Supernova Explosions. Astrophys. J. 720 (2010), pp. 694–703 (cit. on p. 130).

[302] F. Hanke, A. Marek, et al. Is Strong SASI Activity the Key to Successful Neutrino-driven Supernova Explosions? Astrophys. J. 755 (2012), p. 138 (cit. on p. 131).

[303] S. M. Couch, E. Chatzopoulos, et al. The Three-dimensional Evolution to Core Collapse of a Massive Star. Astrophys. J. Lett. 808, L21 (2015), p. L21 (cit. on p. 131).

[304] E. Abdikamalov, A. Zhaksylykov, et al. Shock-turbulence interaction in core-collapse supernovae. Mon. Not. Roy. Astron. Soc. 461 (2016), pp. 3864–3876 (cit. on pp. 131, 151).

[305] E. Abdikamalov, C. Huete, et al. Turbulence Generation by Shock-Acoustic-Wave Interaction in Core-Collapse Supernovae. arXiv e-prints (2018) (cit. on pp. 131, 151).

[306] P. Goldreich and P. Kumar. Wave generation by turbulent convection. Astrophys. J. 363 (1990), pp. 694–704 (cit. on pp. 132, 137, 157).

[307] P. Kumar, S. Talon, and J.-P. Zahn. Angular Momentum Redistribution by Waves in the Sun. Astrophys. J. 520 (1999), pp. 859–870 (cit. on pp. 132, 157).

[308] S. Talon, P. Kumar, and J.-P. Zahn. Angular Momentum Extraction by Gravity Waves in the Sun. Astrophys. J. Lett. 574 (2002), pp. L175–L178 (cit. on p. 132).

[309] T. M. Rogers, D. N. C. Lin, and H. H. B. Lau. Internal Gravity Waves Modulate the Apparent Misalignment of Exoplanets around Hot Stars. Astrophys. J. Lett. 758, L6 (2012) (cit. on p. 132).

[310] T. M. Rogers, D. N. C. Lin, et al. Internal Gravity Waves in Massive Stars: Angular Momentum Transport. Astrophys. J. 772 (2013), p. 21 (cit. on pp. 132, 139, 157).

[311] C. A. Meakin and D. Arnett. Turbulent Convection in Stellar Interiors. I. Hydrodynamic Simulation. Astrophys. J. 667 (2007), pp. 448–475 (cit. on p. 132).

[312] E. Quataert and J. Shiode. Wave-driven mass loss in the last year of stellar evolution: setting the stage for the most luminous core-collapse supernovae. Mon. Not. Roy. Astron. Soc. 423 (2012), pp. L92–L96 (cit. on p. 132).

[313] J. Fuller. Pre-supernova outbursts via wave heating in massive stars - I. Red supergiants. Mon. Not. Roy. Astron. Soc. 470 (2017), pp. 1642–1656 (cit. on pp. 132, 144).

[314] L. Dessart, A. Burrows, et al. Multidimensional Radiation/Hydrodynamic Simulations of Proto-Neutron Star Convection. Astrophys. J. 645 (2006), pp. 534–550 (cit. on p. 132).

[315] S. Yoshida, N. Ohnishi, and S. Yamada. Excitation of g-Modes in a Proto-Neutron Star by the Standing Accretion Shock Instability. Astrophys. J. 665 (2007), pp. 1268–1276 (cit. on pp. 132, 153).

[316] L. F. Roberts. private communication. 2017 (cit. on pp. 135, 158).

[317] D. Mihalas and B. Weibel-Mihalas. *Foundations of radiation hydrodynamics*. Oxford University Press, 1984. ISBN: 9780195034370 (cit. on p. 135).

[318] A. S. Schneider, L. F. Roberts, and C. D. Ott. Open-source nuclear equation of state framework based on the liquid-drop model with Skyrme interaction. Phys. Rev. C 96, 065802 (2017) (cit. on p. 135).

[319] D. Lecoanet and E. Quataert. Internal gravity wave excitation by turbulent convection. Mon. Not. Roy. Astron. Soc. 430 (2013), pp. 2363–2376 (cit. on pp. 137, 139, 157).

[320] L.-A. Couston, D. Lecoanet, et al. The energy flux spectrum of internal waves generated by turbulent convection. J. Fluid Mech. 854, R3 (2018), R3 (cit. on pp. 137, 139).

[321] L. Alvan, A. S. Brun, and S. Mathis. Theoretical seismology in 3D: nonlinear simulations of internal gravity waves in solar-like stars. Astron. Astrophys. 565, A42 (2014) (cit. on p. 139).

[322] N. N. Weinberg and E. Quataert. Non-linear saturation of g-modes in proto-neutron stars: quieting the acoustic engine. Mon. Not. Roy. Astron. Soc. 387 (2008), pp. L64–L68 (cit. on pp. 144, 149, 150, 158).

[323] A. Burrows, S. Reddy, and T. A. Thompson. Neutrino opacities in nuclear matter. Nuc. Phys. A 777 (2006), pp. 356–394 (cit. on pp. 145, 153).

[324] S. Maddox. *Project Title*. `https://github.com/scott-maddox/fdint`. 2017 (cit. on p. 145).

[325] T. Fukushima. *Precise and fast computation of generalized Fermi-Dirac integral by parameter polynomial approximation*. Tech. rep. 2014 (cit. on p. 145).

[326] T. Fukushima. Precise and fast computation of inverse Fermi-Dirac integral of order 1/2 by minimax rational function approximation. Appl. Math. Comp. 259 (2015), pp. 698–707 (cit. on p. 145).

[327] T. Fukushima. Precise and fast computation of Fermi-Dirac integral of integer and half integer order by piecewise minimax rational approximation. Appl. Math. Comp. 259 (2015), pp. 708–729 (cit. on p. 145).

[328] A. J. Barker and G. I. Ogilvie. Stability analysis of a tidally excited internal gravity wave near the centre of a solar-type star. Mon. Not. Roy. Astron. Soc. 417 (2011), pp. 745–761 (cit. on p. 147).

[329] J. Fuller and S. Ro. Pre-supernova outbursts via wave heating in massive stars - II. Hydrogen-poor stars. Mon. Not. Roy. Astron. Soc. 476 (2018), pp. 1853–1868 (cit. on p. 148).

[330] T. Foglizzo. A Simple Toy Model of the Advective-Acoustic Instability. I. Perturbative Approach. Astrophys. J. 694 (2009), pp. 820–832 (cit. on p. 151).

[331] J. Guilet, J. Sato, and T. Foglizzo. The Saturation of SASI by Parasitic Instabilities. Astrophys. J. 713 (2010), pp. 1350–1362 (cit. on p. 151).

[332] J. Guilet and T. Foglizzo. On the linear growth mechanism driving the standing accretion shock instability. Mon. Not. Roy. Astron. Soc. 421 (2012), pp. 546–560 (cit. on p. 151).

[333] C. Huete, E. Abdikamalov, and D. Radice. The impact of vorticity waves on the shock dynamics in core-collapse supernovae. Mon. Not. Roy. Astron. Soc. 475 (2018), pp. 3305–3323 (cit. on p. 151).

[334] A. Burrows. Convection and the mechanism of type II supernovae. Astrophys. J. Lett. 318 (1987), pp. L57–L61 (cit. on p. 153).

[335] A. Harada, H. Nagakura, et al. A Parametric Study of the Acoustic Mechanism for Core-collapse Supernovae. Astrophys. J. 839, 28 (2017) (cit. on p. 153).

[336] B. Müller. The dynamics of neutrino-driven supernova explosions after shock revival in 2D and 3D. Mon. Not. Roy. Astron. Soc. 453 (2015), pp. 287–310 (cit. on pp. 154, 155).

[337] B. Müller, T. M. Tauris, et al. Three-dimensional simulations of neutrino-driven core-collapse supernovae from low-mass single and binary star progenitors. Mon. Not. Roy. Astron. Soc. 484 (2019), pp. 3307–3324 (cit. on p. 154).

[338] A. Burrows, D. Radice, and D. Vartanyan. Three-Dimensional Supernova Explosion Simulations of 9-, 10-, 11-, 12-, and 13-$M_\odot$ Stars. Mon. Not. Roy. Astron. Soc. (2019) (cit. on pp. 154, 155).

[339] D. Vartanyan, A. Burrows, et al. A successful 3D core-collapse supernova explosion model. Mon. Not. Roy. Astron. Soc. 482 (2019), pp. 351–369 (cit. on p. 154).

[340] D. Radice, E. Abdikamalov, et al. Turbulence in core-collapse supernovae. J. Phys. G: Nucl. Phys. 45 (2018), p. 053003 (cit. on p. 155).

[341] B. D. Metzger, T. A. Thompson, and E. Quataert. Proto-Neutron Star Winds with Magnetic Fields and Rotation. Astrophys. J. 659 (2007), pp. 561–579 (cit. on p. 156).

[342] T. K. Suzuki, K. Sumiyoshi, and S. Yamada. Alfvén Wave-Driven Supernova Explosion. Astrophys. J. 678, 1200-1206 (2008) (cit. on p. 156).

[343] C. Pinçon, K. Belkacem, and M. J. Goupil. Generation of internal gravity waves by penetrative convection. Astron. Astrophys. 588, A122 (2016), A122 (cit. on p. 157).

[344] B. Müller, T. Melson, et al. Supernova simulations from a 3D progenitor model - Impact of perturbations and evolution of explosion properties. Mon. Not. Roy. Astron. Soc. 472 (2017), pp. 491–513 (cit. on pp. 159, 168).

[345] J. Harms, F. Acernese, et al. Characterization of the seismic environment at the Sanford Underground Laboratory, South Dakota. Class. Quantum Grav. 27 (22) (2010), p. 225011 (cit. on p. 163).

[346] M. G. Beker, J. F. J. van den Brand, and D. S. Rabeling. Subterranean ground motion studies for the Einstein Telescope. Class. Quantum Grav. 32 (2) (2015), p. 025002 (cit. on p. 163).

[347] R. X. Adhikari, N. Smith, et al. *LIGO Voyager upgrade: Design concept*. 2018 (cit. on p. 163).

[348] R. X. Adhikari, P. Ajith, et al. Astrophysical science metrics for next-generation gravitational-wave detectors. ArXiv e-prints, 1905.02842 (2019). Submitted to Class. Quantum Grav., available at `https://arxiv.org/abs/1905.02842`.
SEG performed all calculations related to stellar collapse, and wrote all manuscript text in the supernova sections. (cit. on pp. 163, 164).

[349] S. Hild, M. Abernathy, F. Acernese, et al. Sensitivity studies for third-generation gravitational wave observatories. Class. Quantum Grav. 28 (9), 094013 (2011) (cit. on p. 163).

[350] M. Punturo, M. Abernathy, F. Acernese, et al. The Einstein Telescope: a third-generation gravitational wave observatory. Class. Quantum Grav. 27, 194002 (2010) (cit. on p. 163).

[351] B. P. Abbott, R. Abbott, et al. Exploring the sensitivity of next generation gravitational wave detectors. Class. Quantum Grav. 34, 044001 (2017) (cit. on pp. 163, 164).

[352] E. D. Hall and M. Evans. Metrics for next-generation gravitational-wave detectors. arXiv e-prints, arXiv:1902.09485 (2019), arXiv:1902.09485 (cit. on p. 163).

[353] V. B. Braginskii and K. S. Thorne. Gravitational-wave bursts with memory and experimental prospects. Nature 327 (1987), pp. 123–125 (cit. on p. 166).

[354] M. Favata. The gravitational-wave memory effect. Class. Quantum Grav. 27, 084036 (2010) (cit. on p. 166).

[355] K. N. Yakunin, A. Mezzacappa, et al. The Gravitational Wave Signal of a Core Collapse Supernova Explosion of a 15M$_ $ Star. arXiv e-prints (2017) (cit. on p. 166).

[356] A. Marek, H.-T. Janka, and E. Müller. Equation-of-state dependent features in shock-oscillation modulated neutrino and gravitational-wave signals from supernovae. Astron. Astrophys. 496 (2009), pp. 475–494 (cit. on p. 166).

[357] M. Obergaulinger, M. A. Aloy, and E. Müller. Axisymmetric simulations of magneto-rotational core collapse: dynamics and gravitational wave signal. Astron. Astrophys. 450 (2006), pp. 1107–1134 (cit. on p. 166).

[358] M. Obergaulinger, M. A. Aloy, et al. Axisymmetric simulations of magnetorotational core collapse: approximate inclusion of general relativistic effects. Astron. Astrophys. 457 (2006), pp. 209–222 (cit. on p. 166).

[359] T. Takiwaki and K. Kotake. Gravitational Wave Signatures of Magnetohydrodynamically Driven Core-collapse Supernova Explosions. Astrophys. J. 743, 30 (2011) (cit. on p. 166).

[360] A. I. MacFadyen, S. E. Woosley, and A. Heger. Supernovae, Jets, and Collapsars. Astrophys. J. 550 (2001), pp. 410–425 (cit. on p. 167).

[361] A. Corsi and P. Mészáros. Gamma-ray Burst Afterglow Plateaus and Gravitational Waves: Multi-messenger Signature of a Millisecond Magnetar? Astrophys. J. 702 (2009), pp. 1171–1178 (cit. on p. 167).

[362] A. L. Piro and E. Thrane. Gravitational Waves from Fallback Accretion onto Neutron Stars. Astrophys. J. 761, 63 (2012) (cit. on p. 167).

[363] A. W. Steiner, J. M. Lattimer, and E. F. Brown. The Neutron Star Mass-Radius Relation and the Equation of State of Dense Matter. Astrophys. J. 765, L5 (2013) (cit. on p. 168).

[364] M. Hempel and J. Schaffner-Bielich. A statistical model for a complete supernova equation of state. Nuc. Phys. A 837 (2010), pp. 210–254 (cit. on p. 168).

[365] J. Harms. Terrestrial Gravity Fluctuations. /lrr 18, 3 (2015), p. 3 (cit. on p. 172).

[366] F. Matichard, B. Lantz, et al. Seismic isolation of Advanced LIGO: Review of strategy, instrumentation and performance. Class. Quantum Grav. 32, 185003 (2015) (cit. on p. 172).

[367] A. V. Cumming, L. Cunningham, et al. Silicon mirror suspensions for gravitational wave detectors. Class. Quantum Grav. 31, 025017 (2014) (cit. on p. 172).

[368] S. Reid and I. W. Martin. Development of Mirror Coatings for Gravitational Wave Detectors. Coatings 6 (4) (2016), p. 61. ISSN: 2079-6412 (cit. on p. 172).

[369] H. Miao, H. Yang, et al. Quantum limits of interferometer topologies for gravitational radiation detection. Class. Quantum Grav. 31, 165010 (2014) (cit. on p. 172).

[370] M. Evans, L. Barsotti, et al. Realistic filter cavities for advanced gravitational wave detectors. Phys. Rev. D 88, 022002 (2013) (cit. on p. 172).

[371] H. Sotani, T. Kuroda, et al. Probing mass-radius relation of protoneutron stars from gravitational-wave asteroseismology. Phys. Rev. D 96, 063005 (2017) (cit. on p. 176).

[372] S. E. Gossan, E. D. Hall, and S. Nissanke. Prospects for core-collapse supernova science with the next generation of ground-based gravitational wave detectors (2019). In preparation; to be submitted to Astrophys. J..
(cit. on p. 178).